LIGHT ECHO STUDIES IN ACTIVE GALACTIC NUCLEI AND THEIR APPLICATION FOR DISTANCE MEASUREMENT

Thesis submitted in partial fulfilment of the requirements
for the award of the degree of

Doctor of Philosophy

by

Vikram Kumar Jaiswal

Under the Guidance of

Prof. Bożena Czerny

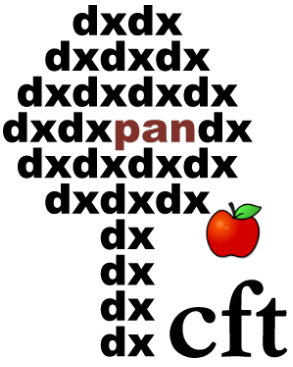

Center for Theoretical Physics, Polish Academy of Sciences

September 5, 2025

Dedicated to my beloved parents.

Declaration

I hereby declare that this thesis represents my work between 2021 and 2025, when I was a doctoral student at the Center for Theoretical Physics PAS under the supervision of Prof. Bożena Czerny. No part of this thesis has been submitted for any other degree application.

I confirm that I have obtained the consent of all co-authors for the inclusion of the publications listed below in this dissertation and for the use of the results therein in my doctoral proceedings.

The thesis includes the following works:

- Vikram Kumar Jaiswal, Raj Prince, Swayamtrupta Panda, Bożena Czerny *Modeling time delays from two reprocessors in active galactic nuclei*, DOI: 10.1051/0004-6361/202244352
- Vikram Kumar Jaiswal, Amit Kumar Mandal, Raj Prince, Ashwani Pandey, Mohammad Hassan Naddaf, Bożena Czerny, Swayamtrupta Panda, Francisco Pozo Nu, *Application of the FRADO model of BLR formation to the Seyfert galaxy NGC 5548 and the first step toward determining the Hubble constant*, arXiv:2410.03597(accepted for publication).
- Vikram Kumar Jaiswal, Bożena Czerny, *Testing the extended corona model with the optical/UV reverberation mapping of the accretion disk*, arXiv:2501.00806(submitted)

My contributions to the above articles are as follows:

- The general idea of the project - the use of the continuum time delay from two reprocessors in active galaxies to measure the Hubble constant - was formulated in the grant proposals of the supervisor. I was responsible for putting that into realization. My key part was to design the architecture of the code calculating the time delay, and then to write it and test. The code is written in Fortran90,

has a modular form, and it calculates the respocessing of the corona emission by the accretion disk and by the broad line region (BLR). I developed a few versions of the code, suitable for the goals formulated in the three presented works, they differed in the description of the BLR as well as of the corona.

- **Paper 1:** I implemented a simple description of the BLR time profile of the response in the form of analytical shape (Gaussian, half-Gaussian etc.). For the reprocessing mechanism, I used simple scattering, representing both BLR clouds and intra-cloud medium. I compared my simulations of the combined disk + BLR responce with the results available in the literature which included only the disk reprocessing. I saw that large corona height is not strongly different from disk + corona reprocessing as the predicted time delay does not have the imprinted atomic patters. I also modeled full lightcurves - for the emitter I used stochastic lightcurve (generating code provided by Supervisor), I calculated the disk+BLR lightcurves and calculated the delay numerically, using standard ICCF method like done in the data. In this way I could evaluate the role of the observational sampling of the lightcurve. I wrote most of the text, and in was later polished with the help of the supervisor.

- **Paper 2:** Paper II was much more complex. In search for atomic imprints on the time delay I introduced an option for the wavelength-dependent contribution from the BLR. This was done in two steps. First, I calculated the BLR time response profile from the 3-D distribution of BLR clouds. This distribution was calculated by one the team members at the basis of FRADO model - dynamics of the clouds calculated from radiation pressure acting on dust who provided me with the cloud positions and velocities. Having that, I calculated the time delay for the adopted viewing angle, and the line profile (this was for test purposes). Next I used the public code CLOUDY to calculate the radiative transfer in a representative clouds. At this point the team selected a specific object - NGC 5548 - for modelling, as well as a specific set of data for this object. I thus tested the CLOUDY options and by comparing preliminary results to the data and the recomendations in the literature I selected the local cloud density at $10^{11} particles/cm^2$ in further computations. At this stage the BLR contribution in my code started to show the imprints of the atomic data since the combined delayed flux at a give wavelength depended on the sum of

the disk plus BLR emission containing Balmer and Paschen edge, and various emission lines. I searched the literature for a geometrical models of the NGC 5548 and I selected three promissing options. They required additional code modification - allowing for a color correction to the local black body temperature and creation of an inner disk gap which would be filled with the disk with a warm corona. I tested combined modelling for model A and B, but only model C was general enough and provided satisfactory fit to the data. The spectral fitting required additionally the warm corona Comptonization code (it was provided by the supervisor) as well as the starlight shape (provided by another team member). Having a best fit for model C, I was able to disentangle the disk and the BLR contribution to the time delay, and at this basis I analytically determined the tentative value of the Hubble constant (section 5.1) which was already a considerable improvement in comparison to disk-based estimate (without BLR) of Cackett et al. (2007) for this source. Next step - development of the automatically fitting procedure based on my code and all the other elements - was made by the team and used in Sect. 6.2. I drafted the text, and I made most (although not all) plots for this paper, and later the team considerably contributed to the text and Discussion. I also made tests of shielding which did not enter into the published work but now are enclosed as an Appendix for later consideration.

- **Paper 3:** In Paper III I basically returned to the code version from Paper I and focused on the possible vertical extension of the irradiating source. It was motivated by the fact that in the literature the quoted values of the corona were small when recovered from X-ray reverberation and quite heigh when determined from optical/UV delay. I introduced a two-point corona (one - heigh, one - low height) and using simulated lightcurves I aimed to see of they differ from a single point corona. I proposed an efficient method of comparison but the differences expected in the UV/optical monitoring did not seem easily detectable in the typically available data. I wrote most of the text which was later consulted with my supervisor.

Other contributions

In the course of my studies, I contributed to the following publications, which are not part of this thesis:

- Bożena Czerny, Shulei Cao, **Vikram Kumar Jaiswal**, Vladimír Karas, Narayan Khadka, Mary Loli Martínez-Aldama, Mohammad Hassan Naddaf, Swayamtrupta Panda, Francisco Pozo Nuñez, Raj Prince, Bharat Ratra, Marzena Sniegowska, Zhefu Yu, Michal Zajaček *"Accretion disks, quasars and cosmology: meandering towards understanding"*,
DOI: 10.1007/s10509-023-04165-7

- Bożena Czerny, Michal Zajaček, Mohammad-Hassan Naddaf, Marzena Sniegowska, Swayamtrupta Panda, Agata Różańska, Tek P. Adhikari, Ashwani Pandey, **Vikram Kumar Jaiswal**, Vladimír Karas, Abhijeet Borkar, Mary Loli Martínez-Aldama, Raj Prince *"Dusty plasma in active galactic nuclei"*,
DOI: 10.1140/epjd/s10053-023-00630-8

- Narayan Khadka, Michal Zajaček, Raj Prince, Swayamtrupta Panda, Bożena Czerny, Mary Loli Martínez-Aldama, **Vikram Kumar Jaiswal**, Bharat Ratra *"Quasar UV/X-ray relation luminosity distances are shorter than reverberation-measured radius-luminosity relation luminosity distances"*,
DOI: 10.1093/mnras/stad1040

- Ashwani Pandey, Bożena Czerny, Swayamtrupta Panda, Raj Prince, **Vikram Kumar Jaiswal**, Mary Loli Martinez-Aldama, Michal Zajaček, Marzena Śniegowska *"Broad-line region in active galactic nuclei: Dusty or dustless?"*,
DOI: 10.1051/0004-6361/202347819

- Michal Zajaček, Swayamtrupta Panda, Ashwani Pandey, Raj Prince, Alberto Rodríguez-Ardila, **Vikram Jaiswal**, Bożena Czerny, Krzysztof Hryniewicz, Maciej Urbanowicz, Piotr Trzcionkowski, Marzena Śniegowska, Zuzanna Fałkowska, Mary Loli Martínez-Aldama, Norbert Werner *"UV FeII emission model of HE 0413-4031 and its relation to broad-line time delays"*,
DOI: 10.1051/0004-6361/202348172

- M. Zajaček, B. Czerny, **V. K. Jaiswal**, M. Štolc, V. Karas, A. Pandey, D. R. Pasham, M. Śniegowska, V. Witzany, P. Suková, F. Münz, N. Werner, J. Řípa, J. Merc, M. Labaj, P. Kurfürst, J. Krtička *"Science with a Small Two-Band UV-Photometry Mission III: Active Galactic Nuclei and Nuclear Transients"*, DOI: 10.1007/s11214-024-01062-5

Acknowledgements

I would like to begin by expressing my deepest gratitude for the opportunity to pursue my Ph.D at the Centre for Theoretical Physics of the Polish Academy of Sciences (CFT PAN). I feel truly fortunate to have had the guidance of my supervisor, **Prof. Bozena Czerny**, throughout this journey. Her unwavering support, patience, and encouragement have been invaluable to me. She has an exceptional ability to explain complex ideas in a simple and accessible way, which has helped me overcome many challenges during my research. I am sincerely grateful for her mentorship, kindness, and dedication, without which this work would not have been possible.

I would also like to extend my heartfelt thanks to my professors, **Prof. Marek Demiański**, **Prof. Miljenko Cemeljic**, **Prof. Krzysztof Mizerski**, **Prof. Mariusz Białecki**, and **Prof. Krzysztof Kochanek**, whose lectures I had the privilege of attending during my doctoral studies. Their teaching not only broadened my academic perspective but also provided me with clear insights that greatly enriched my research. Each lecture served as a source of inspiration and deepened my understanding of the field.

I am also grateful to my colleagues, **Dr. Tae-Hun Lee**, **Dr. Raj Prince**, **Dr. Ashwani Pandey**, **Dr. Swayamtrupta Panda**, **Dr. Mohamad Naddaf**, **Joseph Saji**, and **Pulkit Ojha** and members of the institute with whom I had the chance to engage in occasional discussions. These conversations, both formal and informal, were moments I truly enjoyed. They not only made my academic journey more lively and fulfilling but also often offered new perspectives and ideas that supported the development of this thesis.

A very special note of thanks goes to **Dr. Amit Kumar Mandal**, who guided me like a second Ph.D. supervisor. His constant support, patience, and willingness to answer even my simplest questions made a significant difference in my research journey. I am deeply indebted to him for his generosity in sharing knowledge and for being a source of encouragement throughout this work.

I would also like to acknowledge the members of the institute **secretariat**, whose assistance with administrative tasks and formal paperwork made my stay much easier. Their timely support in handling these matters was greatly appreciated.

I am also thankful to the **IT team** for their help in resolving computer and network issues whenever they arose. Their prompt assistance ensured a smooth working environment during my time at the institute.

I would like to extend my heartfelt acknowledgement to **Prashant Singh**, my best friend since school days, who has always stood by me and guided me like a brother in life. Along with him, I am truly grateful to **Nilakatha Tripathy, Avni Parmar, Shubhi Parolia, and Kamal Bora**, who were always present whenever I needed them and whose friendship means a great deal to me.

Finally, I would like to express my deepest gratitude to my family—my mother, father, and sister—for their unconditional love and support. A very special acknowledgement goes to my brother, who has been like a gravitational force holding our family together. I also feel blessed by the presence of my niece, **Mahi Jaiswal**, and my two nephews, **Chirag Jaiswal** and **Shivik Jaiswal**, whose presence carries a very deep meaning in my life. Without the constant encouragement, strength, and love of my family, it would have been impossible for me to reach where I am today.

Abstract

Light echo studies, usually referred to as reverberation mapping in active galactic nuclei(AGN) is an indirect but powerful method for investigating the structure of the central engine. Instead of relying on spatial resolution, it makes use of time delays between variations at different wavelengths, which are generally interpreted as high-energy photons from the corona being reprocessed by the accretion disk. These so-called continuum lags are widely used to estimate disk sizes. However, many recent studies have reported lags that are larger, or more complex, than predicted by the thin-disk standard model. This thesis investigates the origin of these discrepancies by developing models that include additional sources of reprocessing.

The first part of the work focuses on building such a model, starting from the lamp-post geometry and extending it to include the contribution of the broad-line region (BLR). A series of simulations shows that scattering in the BLR can enhance the observed lag amplitude and produce signatures that closely resemble those generated by increasing the coronal height. This degeneracy complicates reliable disk-size estimates. We also find that the cadence and duration of monitoring campaigns strongly affect lag recovery, with short baselines in particular leading to underestimated values.

The second part of this work applies a physically motivated BLR model to the well-studied AGN NGC 5548. The model is based on the Failed Radiatively Accelerated Dusty Outflow (FRADO) framework of the physically motivated formation of BLR coupled with spectral calculations of BLR reprocessing from the radiative transfer code (CLOUDY). In combination with the accretion disk, this approach reproduces both the observed spectral energy distribution and the pattern of multi-band lags. As a further outcome, the model provides an estimate of the source distance and, from this, a tentative value for the Hubble constant.

The final part of this work looks at the effect of a vertically extended corona by adopting a two-lamppost setup. Our simulations show that reverberation signal of AGN is found to be very similar to that of a single source placed at the average height, with no clear distinction between the two cases. For systems that are both

very massive and slowly accreting, some differences do appear, although they remain small.

The results of the presented PhD thesis indicate that continuum reverberation is shaped by a combination of disk reprocessing, and BLR reprocessing. Including these effects in the models helps to explain why many measured lags differ from the thin-disk predictions. As a pilot study, the method was applied to NGC 5548, where the combined disk+BLR model reproduced both the spectrum and the observed lag pattern. The next step would be extend this approach to a larger set of AGN, which will make it possible to test the model more broadly and improve its use for studying accretion and cosmology.

Streszczenie

Badania echa świetlnego, zazwyczaj określane jako mapowanie reverberacyjne w aktywnych jądrach galaktyk (AGN), stanowią pośrednią, lecz potężną metodę badania struktury centralnego silnika. Zamiast polegać na rozdzielczości przestrzennej, metoda ta wykorzystuje opóźnienia czasowe pomiędzy zmianami obserwowanymi przy różnych długościach fal, co jest zazwyczaj interpretowane jako ponowne przetwarzanie wysokoenergetycznych fotonów z korony przez dysk akrecyjny. Tego typu tzw. opóźnienia ciągłe są powszechnie stosowane do szacowania rozmiarów dysku. Jednak wiele najnowszych badań wykazało, że obserwowane opóźnienia są większe lub bardziej złożone, niż przewiduje standardowy model cienkiego dysku. Niniejsza rozprawa bada źródła tych rozbieżności, rozwijając modele uwzględniające dodatkowe źródła reprocessingu.

Pierwsza część pracy koncentruje się na budowie takiego modelu, rozpoczynając od geometrii typu lamp-post i rozszerzając ją o wkład obszaru linii szerokich (BLR). Seria symulacji pokazuje, że rozpraszanie w BLR może zwiększać obserwowaną amplitudę opóźnień oraz generować sygnały bardzo podobne do tych powstających przy zwiększeniu wysokości korony. Ta niejednoznaczność utrudnia wiarygodne oszacowania rozmiaru dysku. Stwierdzono również, że częstotliwość i czas trwania kampanii obserwacyjnych silnie wpływają na odzyskiwanie opóźnień, a szczególnie krótkie okresy bazowe prowadzą do zaniżonych wartości.

Druga część pracy wykorzystuje fizycznie uzasadniony model BLR w odniesieniu do dobrze przebadanej aktywnej galaktyki NGC 5548. Model ten opiera się na koncepcji *Failed Radiatively Accelerated Dusty Outflow* (FRADO), opisującej fizycznie motywowany mechanizm powstawania BLR, sprzężony z obliczeniami widmowymi reprocessingu BLR przy użyciu kodu transferu promieniowania CLOUDY. W połączeniu z dyskiem akrecyjnym podejście to pozwala odtworzyć zarówno obserwowaną dystrybucję energetyczną widma, jak i wzór opóźnień wielopasmowych. Dodatkowym wynikiem modelu jest oszacowanie odległości do źródła, a na tej podstawie wstępna wartość stałej Hubble'a.

Ostatnia część pracy analizuje wpływ rozciągłej pionowo korony poprzez zastosowanie konfiguracji z dwoma źródłami typu lamp-post. Symulacje pokazują, że sygnał reverberacyjny AGN jest bardzo podobny do tego, który powstaje w przypadku pojedynczego źródła umieszczonego na średniej wysokości, bez wyraźnych różnic pomiędzy obiema sytuacjami. Dla układów bardzo masywnych i wolno akreujących pojawiają się pewne różnice, lecz pozostają one niewielkie.

Wyniki przedstawionej rozprawy doktorskiej wskazują, że opóźnienia ciągłe kształtowane są przez kombinację reprocesowania promieniowania w dysku i BLR. Uwzględnienie tych efektów w modelach pomaga wyjaśnić, dlaczego wiele zmierzonych opóźnień odbiega od przewidywań cienkodyskowych. Jako badanie pilotażowe metoda została zastosowana do NGC 5548, gdzie połączony model dysk+BLR odtworzył zarówno widmo, jak i obserwowany kształt opóźnień. Kolejnym krokiem będzie rozszerzenie tego podejścia na większy zbiór AGN, co umożliwi szersze przetestowanie modelu i poprawi jego zastosowanie do badań akrecji oraz w kosmologii.

Contents

List of Figures

List of Tables

Chapter 1

Active Galactic Nuclei

1.1 Introduction

Astrophysical systems such as gamma–ray bursts (GRBs), active galactic nuclei (AGN), X–ray binaries, protoplanetary disks, and tidal disruption events look different, but they are all powered by the same basic process: accretion of matter onto a compact object. The main difference between these systems is their physical scale.

In accretion, gas falls toward the central object and transforms gravitational potential energy into kinetic energy, heat, and radiation. The gas, however, usually carries angular momentum, which prevents direct infall. If we assume a Keplerian disk, in which the rotational velocity at a given distance is determined solely by the gravitational force of the compact object, the azimuthal velocity and the specific angular momentum (angular momentum per unit mass) are given by

$$v_\phi(r) = \sqrt{\frac{GM}{r}}, \tag{1.1}$$

$$j(r) = r v_\phi = \sqrt{GMr}. \tag{1.2}$$

From the equation 1.2, it is apparent that angular momentum, which is also a conserved quantity, increases with radius. In order for accretion to take place, transferring the angular momentum is the only solution. Transport of angular momentum can happen in different ways: through viscosity (Shakura and Sunyaev, 1973), turbulence, magnetic instabilities such as the magnetorotational instability (MRI; Balbus and Hawley, 1991, 1998), or disk winds and outflows (Blandford and Payne, 1982). The ideal situation, where pressure forces are negligible and central gravity dominates, is a thin Keplerian disk. Disks in real systems, particularly AGN, may differ from this simple model due to factors like thickness, magnetisation, or radiative inefficiency, which I will mention briefly in the coming sections.

1.2 History

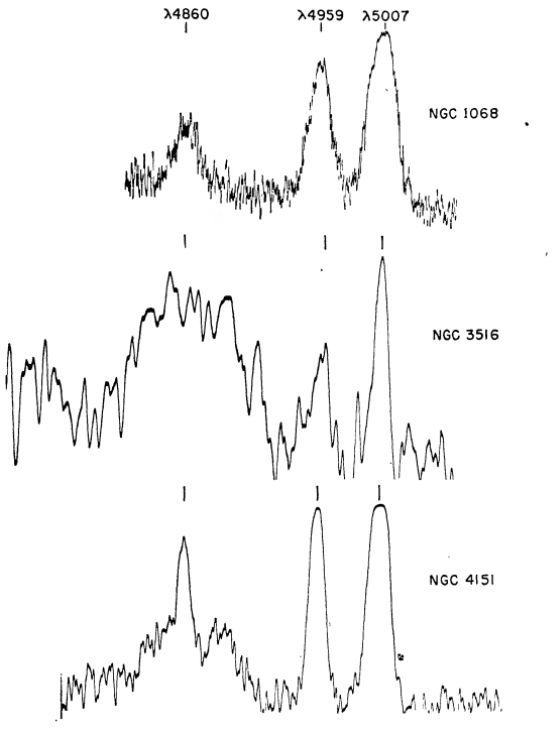

FIGURE 1.1: Emission lines generated from the original observations reported by Seyfert (1943).

The first step toward understanding active galactic nuclei (AGN) was made in 1909, when Edwin A. Fath used the 36-inch Crossley reflector at Lick Observatory to take the optical spectrum of NGC 1068. He found that the nucleus of this galaxy showed bright emission lines on top of a weak continuum, very different from the absorption features usually seen in stellar spectra (Fath, 1909). At that time, the origin of this emission was not understood.

In 1917, V. M. Slipher obtained higher quality spectra of 25 spiral nebulae, including NGC 1068. He confirmed the strong, narrow emission lines and also showed that NGC 1068 had a radial velocity of +1130 km/s, which was unusual compared with normal galaxies (Slipher, 1917).

In 1943, Carl K. Seyfert extended this work by showing that several spiral galaxies, again including NGC 1068, have nuclei with strong emission lines, as illustrated in figure 1.1. From the spectra of six galaxies, he reported both broad permitted lines and narrow forbidden lines on top of the stellar background. These galaxies became known as Seyfert galaxies (Seyfert, 1943).

Another breakthrough happened in 1963, when Maarten Schmidt obtained an optical spectrum of the radio source 3C 273 and realized that the strange emission lines were simply Doppler redshifted Balmer hydrogen emission lines (Schmidt, 1963). The source was found to have a redshift of 0.16, and this finding confirmed the identification of a quasar, and transformed the understanding of extragalactic astronomy.

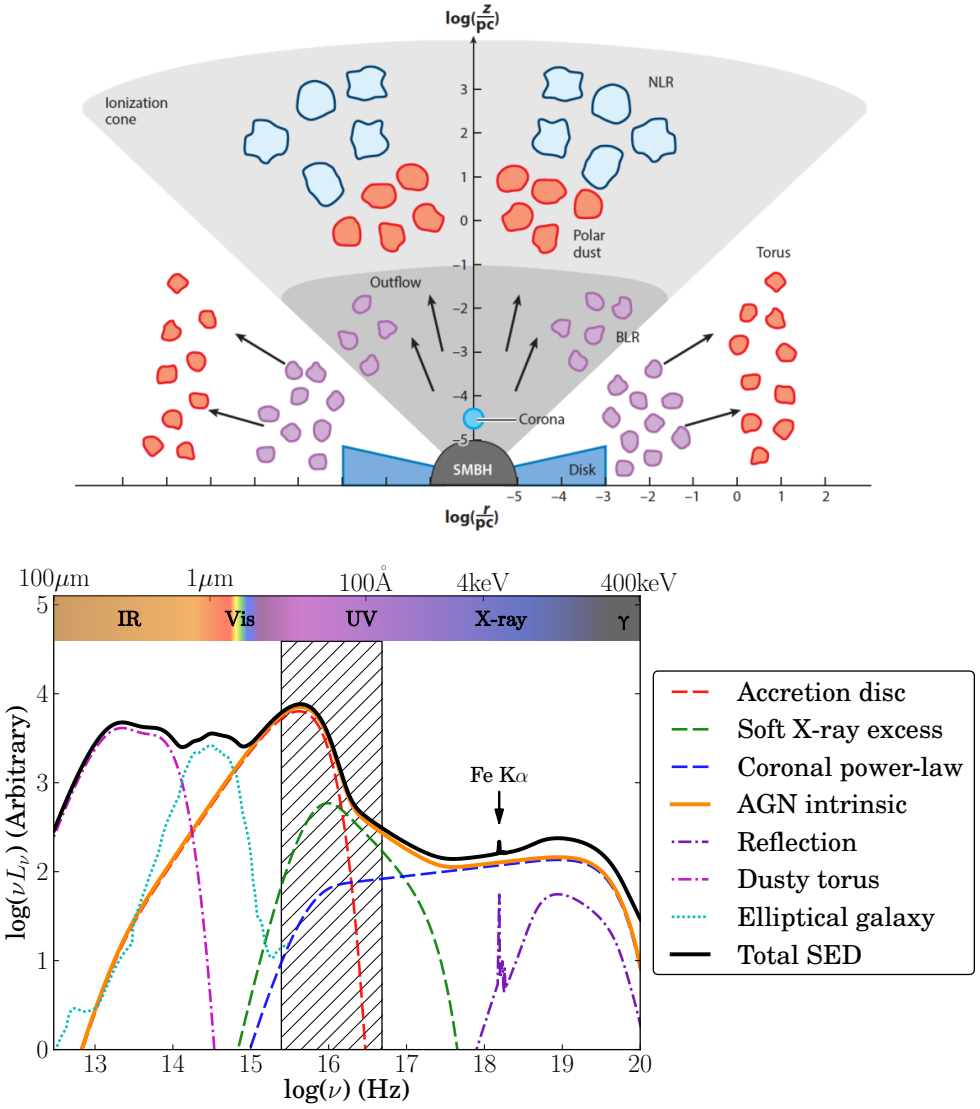

FIGURE 1.2: **Top:** Illustration of the primary structural components of an active galactic nucleus (AGN), as described in unification models (adapted from Hickox and Alexander 2018). **Bottom:** Representative spectral energy distribution (SED) of an AGN, decomposed into contributions from the accretion disk, dust, and host galaxy (adapted from Collinson et al. 2017).

1.3 Components of AGN

The term *active galactic nucleus* (AGN) is a broad label for galaxies whose central black holes are actively accreting gas. Seyfert galaxies are one example, but other well-known classes include quasars, radio galaxies, and blazars, among others. What distinguishes these categories are mainly their luminosities, spectral characteristics, and the viewing angle toward the nucleus. In particular, obscuration by gas and dust, together with orientation effects, plays a major role in how an AGN appears (Antonucci, 1993; Urry and Padovani, 1995). Table 1.1 gives a summary of the main classes. In the chapters that follow, the terms *Seyfert galaxy* and *AGN* will occasionally be used interchangeably.

Figure 1.2 illustrates both the structure and the broadband emission of an AGN. At the center lies a supermassive black hole encircled by an accretion disk. Surrounding the disk is the broad-line region (BLR), and farther out a dusty torus together with the narrow-line region (NLR). In many systems, relativistic jets are also launched, extending to scales far beyond the host galaxy. Each of these components contributes to a different part of the observed SED, and their roles will be discussed in more detail in the following sections.

1.3.1 Supermassive Black Holes (SMBHs)

While the SMBH itself contributes no radiation directly to the SED, it acts as the central engine, creating the deep gravitational potential well into which gas and dust fall and accrete. This process of *accretion* converts gravitational potential energy into radiation. As material spirals closer to the black hole, friction and compression heat the gas, producing the luminous accretion disk observed in AGN.

The luminosity L produced by such a system is connected to the mass accretion rate $\dot{M}$ through

$$L = \eta \dot{M} c^2, \tag{1.3}$$

where η represents the radiative efficiency. Rearranging gives

$$\dot{M} = \frac{L}{\eta c^2}. \tag{1.4}$$

Assume an AGN with efficiency $\eta \sim 0.1$. A luminosity $L \sim 10^{46}\,\mathrm{erg\,s^{-1}}$ then requires an accretion rate of roughly

$$\dot{M} \sim 1.8\,M_\odot\,\mathrm{yr}^{-1}.$$

To understand efficiency, assume a gas of mass m falling into a black hole of mass M down to radius r would release

$$\Delta U \sim \frac{GMm}{r}. \tag{1.5}$$

For continuous accretion, the corresponding rate is

$$\frac{dU}{dt} \sim \frac{GM\dot{M}}{r}. \tag{1.6}$$

Comparing with $L = \frac{dU}{dt} = \eta \dot{M} c^2$ yields

$$\eta \sim \frac{GM}{rc^2}. \tag{1.7}$$

In this sense, the efficiency is tied to the **compactness** of the central object, given by the ratio M/r. More compact systems allow more efficient conversion

of accreted mass into radiation. For gas reaching within a few Schwarzschild radii ($R_s = 2GM/c^2$), efficiencies of order $\eta \approx 0.1$ are achieved, making accretion onto SMBHs one of the most powerful energy-generation mechanisms in nature.

In addition to efficiency, there is also a theoretical upper limit on the luminosity that can be sustained. This is the **Eddington luminosity**, obtained by equating the outward radiation pressure (acting on electrons through Thomson scattering) to the inward pull of gravity (acting on protons). For a spherical system of ionized hydrogen, the limit is

$$L_E = \frac{4\pi GMm_p c}{\sigma_T}, \tag{1.8}$$

where m_p is the proton mass and σ_T the Thomson cross-section. If $L > L_E$, radiation pressure would exceed gravity, disrupting steady inflow. The Eddington luminosity therefore sets a natural ceiling on the radiative output of quasars and AGN for a given black hole mass.

Another defining property of a black hole is the *event horizon*, the surface from which not even light can escape. For a non-rotating black hole this is set by the Schwarzschild radius,

$$R_s = \frac{2GM}{c^2}. \tag{1.9}$$

The Schwarzschild metric, which describes the spacetime outside such a mass, is given by

$$ds^2 = \left(1 - \frac{2GM}{c^2 r}\right) c^2 dt^2 - \left(1 - \frac{2GM}{c^2 r}\right)^{-1} dr^2 - r^2 \left(d\theta^2 + \sin^2\theta \, d\phi^2\right). \tag{1.10}$$

where

- ds^2: spacetime interval,
- t: coordinate time,
- r, θ, ϕ: spherical spatial coordinates,
- G: gravitational constant,
- M: mass of the object,
- c: speed of light.

For $r > R_s$, the metric describes the exterior spacetime for any spherically symmetric mass distribution, while at $r = R_s$, the event horizon is located. From the Schwarzschild metric, the innermost stable circular orbit (ISCO) for a non-rotating black hole lies at $r = 3R_s$. Inside this radius, circular orbits are unstable and matter rapidly plunges into the black hole. For rotating (Kerr) black holes, the ISCO depends on the dimensionless spin parameter a (with $0 \leq a \leq 1$). In the case of a maximally rotating Kerr black hole ($a = 1$), the ISCO shrinks to $r \simeq 0.5\, R_s$ for co-rotating orbits, while for counter-rotating orbits it moves outward to $r \simeq 4.5\, R_s$ (Bambi, 2020).

The first dynamical evidence for a stellar-mass black hole came from the X-ray binary Cygnus X-1, where orbital studies of the companion star pointed to a compact object with several solar masses (Webster and Murdin, 1972; Bolton, 1972). Observational evidence for SMBHs followed soon after. Photometric modeling of the nuclear light distribution in M87 implied the presence of a supermassive object with a mass of order $\sim 5 \times 10^9\, M_\odot$ confined within 100 pc, providing some of the earliest compelling evidence for a massive black hole in a galactic nucleus (Young et al., 1978).

When direct dynamical measurements are not possible, black hole masses are estimated using host galaxy correlations. The two most common are the M–σ relation

and the M–$M_{\rm bulge}$ relation. The M–σ relation connects the black hole mass to the velocity dispersion of stars in the galaxy bulge (Ferrarese and Merritt, 2000; Tremaine et al., 2002). The M–$M_{\rm bulge}$ relation instead links the black hole mass to the stellar mass or luminosity of the bulge. The first evidence for a connection between black hole mass and bulge mass came from dynamical modeling of nearby galaxies (Magorrian et al., 1998). A more precise calibration of this M–$M_{\rm bulge}$ relation was later established using improved data (Häring and Rix, 2004).

For AGN, indirect methods such as *reverberation mapping* (chapter 2) are commonly employed. Under the assumption of virialized motion, the black hole mass can be expressed in terms of broad-line region (BLR) cloud velocities and the radius–luminosity (R–L) relation (Kaspi et al., 2000). The empirical R–L relation derived by Kaspi et al. (2000) is given by:

$$R_{\rm BLR} = 32.9 \left(\frac{\lambda L_\lambda (5100\,\text{Å})}{10^{44}\,\mathrm{erg\,s^{-1}}} \right)^{0.7} \quad \text{light-days.} \tag{1.11}$$

Subsequently, single-epoch virial mass estimators were developed, combining this relation with the full width at half maximum (FWHM) of broad emission lines such as Hβ, Mg II, and C IV. Several studies (e.g., Wandel et al., 1999; Vestergaard and Peterson, 2006) derived widely used calibrations based on Hβ. One common form is:

$$\log_{10}\left(\frac{M_{\rm BH,virial}}{M_\odot}\right) = 0.91 + 0.5\log_{10}\left(\frac{L_{5100}}{10^{44}\,\mathrm{erg\,s^{-1}}}\right) + 2\log_{10}\left(\frac{\mathrm{FWHM(H}\beta)}{1000\,\mathrm{km\,s^{-1}}}\right). \tag{1.12}$$

Analogous relations have been developed for Hα (Greene and Ho, 2005), C IV λ1549 (Vestergaard, 2002; Vestergaard and Peterson, 2006), and Mg II λ2798 (McLure and Jarvis, 2002; Wang et al., 2009).

Other specialized methods can also be used to measure black hole masses. For example, water megamaser emission, from circumnuclear disks, can be mapped very accurately, allowing Keplerian rotation curves to be modeled, as in NGC 4258 (Miyoshi et al., 1995). Gravitational lensing provides another case: in the lens system PMN J1632–0033, a faint central image was detected and used to place an upper limit of $\lesssim 2 \times 10^8\, M_\odot$ on the black hole mass (Winn et al., 2004). More recently, the Event Horizon Telescope has imaged the region around SMBHs such as M87, making it possible to determine their masses directly from black hole shadow observations (Event Horizon Telescope Collaboration et al., 2019a,b).

1.4 Accretion disk

Gas falling toward a compact object generally has non-zero angular momentum. Because of this, the gas cannot fall in directly but instead forms a rotating structure. Angular momentum is gradually transported outward by viscosity, magnetic instabilities, or winds, while mass moves inward and gravitational energy is converted into radiation (Shakura and Sunyaev, 1973; Balbus and Hawley, 1991, 1998; Blandford and Payne, 1982).

As the gas spirals inward, gravitational potential energy is converted into kinetic and thermal energy. The gas is heated and radiates in optical, ultraviolet, and X-ray bands. Because of angular momentum conservation, the inflow settles into a flattened accretion disk instead of a free fall. Different regimes of accretion lead to different types of disks. At low accretion rates, the flow can become an **advection-dominated accretion flow (ADAF)**, where most of the energy is advected inward rather than radiated (Narayan and Yi, 1994). At very high accretion rates close to the Eddington limit, radiation pressure produces a **slim disk** (Abramowicz et al.,

1988). In other regimes, **thick disks** (Abramowicz et al., 1978) or **magnetically arrested disks (MADs)** (Narayan et al., 2003; Tchekhovskoy et al., 2011) are relevant, especially in connection with jet production. In this thesis, I focus on the standard **Shakura–Sunyaev thin disk model**, which assumes a geometrically thin, optically thick disk and will be described in the next section.

1.4.1 Shakura–Sunyaev Accretion Disk Model

The model assumes a disk that is **geometrically thin** and **optically thick**. Angular momentum transport is described by an effective viscous stress. Shakura and Sunyaev (1973) introduced the α**-prescription**, writing the stress as

$$T_{r\phi} = \alpha P_{\rm tot},$$

where $P_{\rm tot}$ is the total pressure and α is a dimensionless constant. The corresponding kinematic viscosity is

$$\nu = \alpha c_s H, \tag{1.13}$$

with c_s the sound speed and H the disk scale height.

The energy flux from the disk surface at radius R is

$$F(R) = \frac{3GM\dot{M}}{8\pi R^3}\left[1 - \left(\frac{R_{ISCO}}{R}\right)^{1/2}\right]. \tag{1.14}$$

This expression assumes a steady-state disk where gravitational energy released at each radius is radiated locally. The result does not depend on the detailed origin of viscosity.

In Newtonian gravity this form is valid. In general relativity, the flux is modified by correction factors (Novikov and Thorne, 1973; Page and Thorne, 1974):

$$F(R) = \frac{3GM\dot{M}}{8\pi R^3} f(R), \tag{1.15}$$

where $f(R)$ vanishes at the ISCO. For a Schwarzschild black hole the ISCO is at $R = 3R_s$. For Kerr black holes the ISCO moves inward for prograde orbits and outward for retrograde orbits.

The effective temperature of the disk is given by

$$T_{\text{eff}}(R) = \left(\frac{F(R)}{\sigma}\right)^{1/4}, \tag{1.16}$$

with σ the Stefan–Boltzmann constant. Each annulus radiates approximately as a blackbody. The sum of all annuli produces a multi-temperature spectrum that peaks in the ultraviolet and extends to optical and infrared. The disk contribution appears in the SED shown in figure 1.2.

The disk alone does not reach temperatures high enough to produce hard X-rays. The X-ray spectrum is due to *reflection and reprocessing* of photons from the corona. Part of the coronal radiation is reflected by the disk, producing a hard X-ray excess. Another part is absorbed, and photons above 7.1 keV can eject K-shell electrons from iron atoms. Two outcomes are possible:

1. The Auger effect, where the excess energy ejects another electron.
2. Emission of a fluorescent Fe Kα photon at 6.4 keV, a ubiquitous feature of AGN spectra (figure 1.2).

1.5 Corona

The corona is a high-energy region located above the accretion disk, and it plays a central role in producing the X-ray emission of AGN. It is often described in terms of two components: a **hot corona** and a **warm corona**.

The hot corona is an *optically thin* plasma with temperatures of 10^{8-9} K. Electrons in this region are highly energetic, and X-rays are produced through *inverse Comptonization* of thermal photons from the inner accretion disk. The geometry of the hot corona is not well constrained and is model dependent. Suggested configurations include a compact "lamp-post" above the black hole (Martocchia and Matt, 1996; Miniutti and Fabian, 2004), or extended structures (Haardt and Maraschi, 1991). Recent observations also suggest that the corona may vary over time; for example, Kara et al. (2019) report changes in coronal geometry in the stellar-mass black hole transient MAXI J1820+070, possibly linked to evolving conditions in the inner accretion flow or magnetic field structure.

The emission from the hot corona is usually described by a power-law spectrum:

$$F(E) = A_X E^{-\Gamma} \quad (\text{photons s}^{-1}\ \text{cm}^{-2}\ \text{keV}^{-1}), \tag{1.17}$$

where A_X is a normalization constant, E is the photon energy, and Γ is the photon index. This power-law emission is represented by the dashed blue line in the bottom panel of figure 1.2.

An important feature of AGN X-ray spectra is the deviation from a pure power-law below $\sim$ 2 keV, known as the **soft excess** (Turner and Pounds, 1988). One explanation is a **warm corona**: an optically thick, low-temperature medium located

near the disk, which Comptonizes disk photons into soft X-rays (Petrucci et al., 2018).

Alternative explanations for the soft excess have also been proposed. In the **reflection model**, the soft excess arises from reflection of hard X-rays by the accretion disk (Crummy et al., 2006; Jiang et al., 2019). In the **complex absorption model**, the apparent soft X-ray excess is produced by partially ionized, velocity-smeared absorption along the line of sight, possibly associated with a disk wind (Gierliński and Done, 2004). While this scenario can in principle mimic a soft excess, it requires extreme smearing and is not favored compared to reflection or warm-Comptonization. The relative contribution of these mechanisms is still debated, but it is clear that both hot and warm coronae are essential for shaping the observed AGN X-ray spectrum.

1.6 Torus

A dusty torus, composed of gas and dust, looks like a doughnut (Antonucci, 1993), and the very high column density of the torus completely blocks the bright light from the center. Studies using mid-infrared (MIR) imaging have shown that this torus is optically thick and can extend between 0.1 and 10 parsecs (Packham et al., 2005; Radomski et al., 2008).

The dust sublimation radius sets the inner edge of the torus, which also sets the outer edge of the broad line region (BLR). This radius is where dust grains reach their sublimation temperature, $T_{\rm sub}$, which is the highest temperature that dust can withstand before it evaporates. The size, composition, and local photon flux of the dust grains all affect the sublimation temperature. The mean sublimation radius,

$\langle R_{\rm sub} \rangle$, can be found by averaging over typical graphite grains in the interstellar medium Barvainis (1987).

$$\langle R_{\rm sub} \rangle \approx 0.5\, L_{46}^{1/2} \left(\frac{1800\,{\rm K}}{T_{\rm sub}} \right)^{2.6} f(\theta) \quad {\rm pc},$$

where

$\langle R_{\rm sub} \rangle$: mean dust sublimation radius (parsecs, pc)

L_{46} : AGN luminosity normalized to 10^{46} erg s^{-1}

$T_{\rm sub}$: dust sublimation temperature (Kelvin, K)

$f(\theta)$: angular-dependent factor accounting for radiation anisotropy

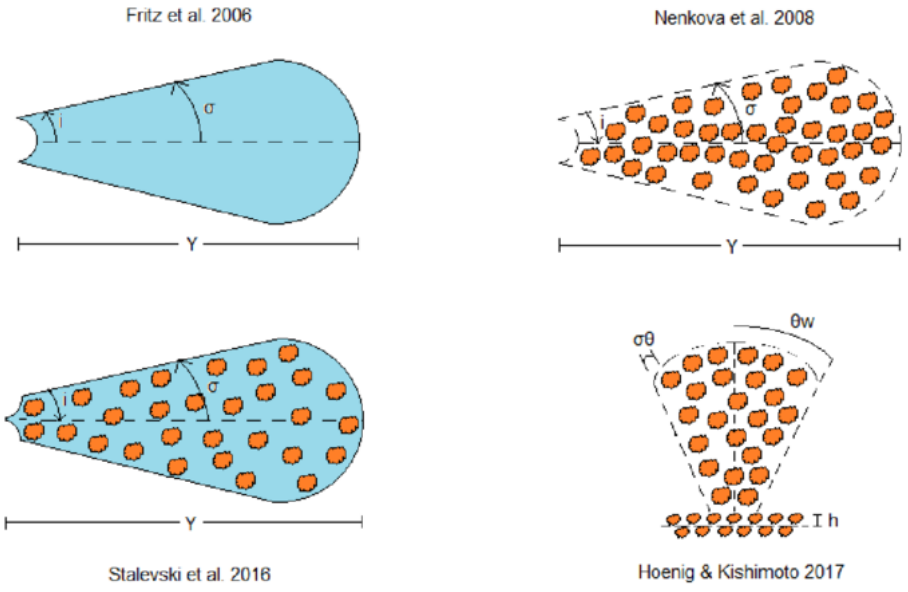

FIGURE 1.3: Illustration of different theoretical models for the structure of the AGN torus (adapted from Victoria-Ceballos et al. 2022).

The dusty torus in AGN can be described in different ways, as shown in figure 1.3.

In the *smooth torus* model, the dust and gas are assumed to follow a continuous distribution (Pier and Krolik, 1992; Fritz et al., 2006), with the temperature depending primarily on the distance from the black hole. The "clumpy torus" model (Nenkova et al., 2008a,b) assumes that the dust exists in dense clouds with gaps in between. These gaps let light travel through more freely, which means even clouds at the same distance from the black hole can have very different temperatures because some are shaded by others. Later, Stalevski et al. (2016) introduced a two-phase model that includes both clumps and a diffuse medium between them. This provides a description that sits between the smooth and clumpy pictures. More recently, Hönig and Kishimoto (2017) suggested a disk+outflow structure, where the torus is clumpy but also has a dusty wind in the polar direction.

The covering factor quantifies the fraction of the sky, from the black hole's perspective, that is blocked by the torus. Studies have shown that this covering factor varies widely across different AGN (Mateos et al., 2016). The SED contribution from the torus is in the IR window, as shown in figure 1.2. The dust around the AGN absorbs the intense ultraviolet and optical light coming from the center and then re-emits that energy as infrared radiation. The re-radiation happens at temperatures close to the dust sublimation limit, which is typically around 1500 K (Barvainis, 1987; Nenkova et al., 2008a).

1.7 Broad-Line Region (BLR)

The broad emission lines seen in the spectra of active galactic nuclei (AGN) were key to their discovery. These lines come from the Broad Line Region (BLR), which is made up of clouds of gas orbiting the central supermassive black hole at speeds

reaching up to 5000 $\mathrm{km\,s^{-1}}$ or even more. To an observer, these lines appear broadened because some clouds are moving away, stretching the light to longer wavelengths, while others move toward us, compressing the light. The BLR clouds are very dense, and the frequent collisions within them play a crucial role in producing strong permitted emission lines while suppressing forbidden lines (Osterbrock, 1989). The absence of forbidden lines, together with photoionization models, makes it possible to estimate the electron density in the BLR, which is found to be very high (Davidson and Netzer, 1979).

There are multiple models proposed to describe the geometry and dynamics of the BLR. Early models suggested that the BLR could be explained either as a flat and gravitationally bound disk (Perez et al., 1988; Kollatschny et al., 2014), or as a system made of discrete line-emitting clouds (Kwan and Krolik, 1981). In some AGN, the BLR gas shows signs of flowing inward toward the black hole (Gaskell, 2009), while in others, parts of the BLR are moving outward as an outflow (Emmering et al., 1992; Kollatschny, 2003). Such observations motivated the development of outflow-based models. For instance, Elvis (2000) proposed a funnel-shaped, radiatively driven disk wind in which the BLR clouds are embedded as a cooler phase of the flow. In this thesis, however, we focus on a related model, the Failed Radiatively Accelerated Dusty Outflow (FRADO) model proposed by Czerny and Hryniewicz (2011), which we adopt to generate the BLR response function (discussed in chapter 2).

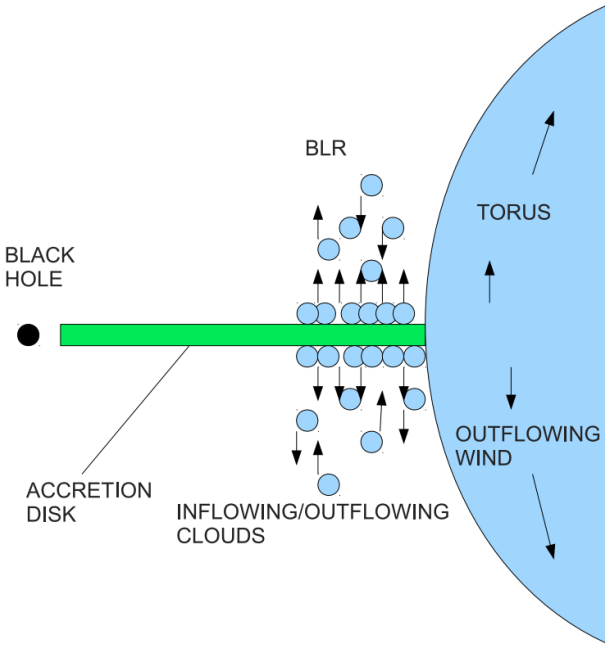

FIGURE 1.4: Illustration of the proposed mechanism for broad-line region (BLR) formation in active galactic nuclei, adapted from Czerny and Hryniewicz 2011.

1.7.1 Failed Radiatively Accelerated Dusty Outflow (FRADO) Model

The FRADO model (Czerny and Hryniewicz, 2011) provides a physical explanation for the origin of the Broad Line Region (BLR) in AGN. In this scenario, the key ingredient is dust formation in the outer regions of the accretion disk. The effective temperature of a thin disk at radius r is

$$T_{\rm eff}(r) = \left(\frac{3GM\dot{M}}{8\pi\sigma r^3} \right)^{1/4},$$

which decreases outward. At radii where $T_{\rm eff}(r) \lesssim T_{\rm sub} \sim 1000$–$1500$ K, dust can condense in the disk atmosphere. Once dust forms, the local disk radiation flux exerts an upward force

$$F_{\rm rad} = \frac{\kappa_{\rm d} F}{c},$$

where $\kappa_{\rm d}$ is the dust opacity and F the radiative flux. This competes with the vertical component of gravity from the central black hole,

$$F_{\rm grav} = \Omega_K^2 z, \quad \Omega_K = \sqrt{\frac{GM}{r^3}}.$$

If $F_{\rm rad} > F_{\rm grav}$ at the disk surface, dusty gas is lifted upward, initiating a vertical outflow. However, as the cloud rises, it becomes exposed to the intense UV radiation from the central engine. At some critical height $z_{\rm evap}$, the dust grains are heated above $T_{\rm sub}$ and evaporate, so that $\kappa_{\rm d} \to 0$ and the radiative driving vanishes. The gas then loses vertical support and falls back onto the disk, creating a "failed wind." This cycle of launching, sublimation, and fallback naturally produces a population of dense clumps moving mainly with Keplerian velocities but also showing vertical oscillations and signatures of inflow. Figure 1.4 illustrates the FRADO model.

With the help of reverberation mapping, a clear relation between the BLR size and the brightness of the accretion disk has been established (Kaspi et al., 2005). This relation shows that the BLR size scales with the AGN luminosity as $R \propto L^{0.5}$. Another important result from reverberation mapping is that **high-ionization emission lines respond more quickly** to changes in the central light source than low-ionization lines (Gaskell and Sparke, 1986; Clavel et al., 1991; Peterson et al., 1991). High-ionization lines are also observed to be **broader** than low-ionization lines, which indicates that the gas producing them is moving at higher velocities (Shuder, 1982; Wilkes, 1984; Espey et al., 1989). Since the orbital velocity decreases with radius, clouds located closer to the black hole must move faster. These inner clouds are the ones that emit high-ionization lines such as He II, He I, N V, and C IV, which therefore appear broader. By contrast, low-ionization lines including Mg II, Ca II, O I, and Fe II are narrower, consistent with their origin at larger radii where the gravitational potential is weaker and orbital velocities are lower. Taken together,

these observational trends and reverberation results provide strong evidence for an **ionization stratification** within the broad line region. In other words, different ions are not produced at random locations but instead trace a layered structure, with highly ionized species closer in and more weakly ionized species further out.

1.8 Narrow-Line Region (NLR)

In contrast to the BLR, the Narrow-Line Region (NLR) extends beyond the torus and can reach scales comparable to the host galaxy bulge (Ho, 2009). Since the NLR is located at very large distances from the black hole, gravity is no longer the dominant force; instead, the intense ionizing radiation from the central source plays the main role. Because the gas lies far from the black hole, it moves at much lower velocities, producing emission lines with widths of typically 200–500 $\mathrm{km\,s^{-1}}$. The relatively low density of the NLR allows forbidden transitions such as [O III] and [N II] to be observed. These transitions are considered "forbidden" only in high-density environments, where collisions suppress them; in the low-density NLR they occur efficiently. The NLR therefore contributes prominently to the optical spectrum of AGN through strong forbidden emission lines.

The size of the NLR scales with the strength of the [O III] emission line. Observations show that the radial extent of the NLR follows

$$R_{\mathrm{NLR}} \propto L^{\alpha}_{[\mathrm{O\,III}]},$$

where $L_{[\mathrm{O\,III}]}$ is the luminosity of the [O III] line and $\alpha \approx 0.5$ (Bennert et al., 2002; Schmitt et al., 2003; Netzer et al., 2004). Typical NLR sizes are comparable to the central bulge of the host galaxy, extending up to kiloparsec scales.

1.9 Jet

Among the AGN population, it has been observed that only about 10% are radio-loud, meaning they produce powerful relativistic jets, while the remaining 90% are radio-quiet (Padovani, 2011, 2016). These jets consist mainly of relativistic plasma and are launched from regions very close to the black hole. Observations further show that jets can propagates up to distance of 100kpc, and in doing so they can strongly influence both the host galaxy and the surrounding intracluster medium (Blandford et al., 2019).

The exact mechanism that produces jets is not fully understood. One idea is that magnetic fields connected to the accretion disk are wound up by rotation and direct the plasma outward (Blandford et al., 2019). Another model, the Blandford–Znajek process, extracts energy from the spin of the black hole through magnetic fields near the event horizon (Blandford and Znajek, 1977; Tchekhovskoy et al., 2011).

For synchrotron emission to occur, two key ingredients are required: relativistic charged particles and magnetic fields, both of which are present in jets. Therefore, the radiation from jets falls mostly in the non-thermal regime, with emission produced through the synchrotron process that spans a broad range of the spectrum, including radio, X-ray, and gamma-ray bands (Madejski and Sikora, 2016; Harris and Krawczynski, 2006). The spectrum power law can be written as:

$$S_\nu \propto \nu^\alpha, \tag{1.18}$$

where S_ν is the flux density at frequency ν, and α is the spectral index. A common way to classify jets is the Fanaroff–Riley scheme (Fanaroff and Riley, 1974). FR I

jets fade gradually with distance from the nucleus, whereas FR II jets end in bright hotspots where they collide with the surrounding medium.

1.10 AGN Unification

TABLE 1.1: Types of AGN based on observational properties(table is taken from Padovani (2016))

Class/Acronym	**Meaning**	**Main properties/reference**
Quasar	Quasi-stellar radio source (originally)	Radio detection no longer required
Sey1	Seyfert 1	FWHM $\geq 1,000$ km s^{-1}
Sey2	Seyfert 2	FWHM $<$ 1,000 km s^{-1}
QSO	Quasi-stellar object	Quasar-like, non-radio source
QSO2	Quasi-stellar object 2	High power Seyfert 2
RQ AGN	Radio-quiet AGN	see ref. 1
RL AGN	Radio-loud AGN	see ref. 1
Jetted	AGN with strong relativistic jets	see ref. 1
Non-jetted	AGN without strong relativistic jets	see ref. 1
Type 1	Seyfert 1 and quasars	
Type 2	Seyfert 2 and QSO2	
FR I	Fanaroff-Riley class I radio source	radio core-brightened (ref. 2)
FR II	Fanaroff-Riley class II radio source	radio edge-brightened (ref. 2)
BL Lac	BL Lacertae object	see ref. 3
Blazar	BL Lac and quasar	BL Lacs and FSRQs

Reference key: 1. Padovani (2016); 2. Fanaroff and Riley (1974); 3. Giommi et al. (2012)

The general picture of an active galactic nucleus (AGN) includes a supermassive black hole at the center, surrounded by an accretion disk, a system of rapidly moving gas clouds that form the broad-line region (BLR), a dusty torus on larger scales, slower-moving clouds that form the narrow-line region (NLR), and, in some cases, powerful jets. Table 1.1 shows the different types of AGN. Antonucci (1993) argued that Type 1 and Type 2 AGN can be explained within the same unified framework by orientation. If the torus is viewed edge-on, it blocks the accretion disk and BLR so that only the NLR is observed, giving the appearance of a Type 2 spectrum. When the nucleus is viewed more directly, the BLR and accretion disk are visible and the

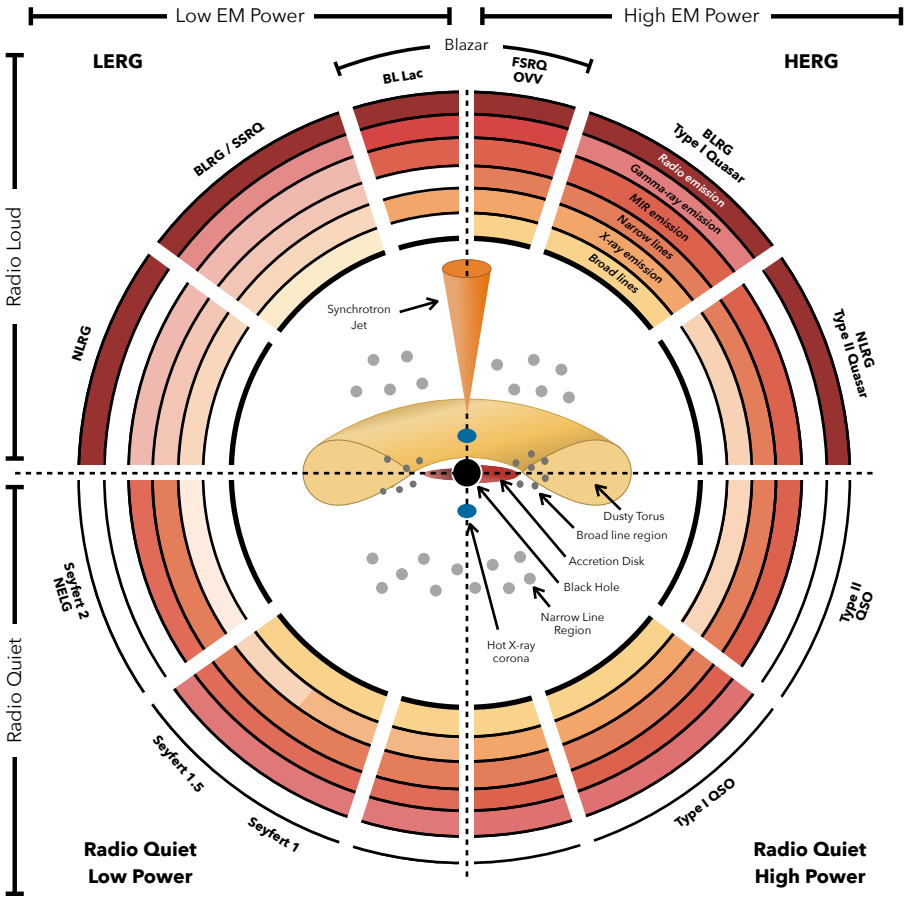

FIGURE 1.5: Schematic diagram of the orientation-dependent unification model for active galactic nuclei (AGN), adapted from Thorne et al. 2022.

object appears as a Type 1 AGN, as illustrated in figure 1.5. Importantly, the BLR does not vanish in Type 2 AGN but is simply hidden. Some of its radiation can escape along unobscured paths, scatter off electrons or dust, and reach the observer. Since scattering produces polarized light, broad emission lines from the BLR can still be detected in polarized spectra. This was first demonstrated in the seminal work of Antonucci and Miller (1985), who detected broad Balmer lines in the polarized spectrum of the Seyfert 2 galaxy NGC 1068. Another strong observational support for the unification-by-orientation model came when similar results were obtained (Miller and Goodrich, 1990; Tran et al., 1992) for other Seyfert 2 galaxies.

However, there are some observations that question the unification-by-orientation model. For example, the fraction of obscured AGN decreases with increasing luminosity (Lawrence, 1991; Simpson, 2005; Assef et al., 2013). This luminosity dependence is difficult to explain if orientation is the only factor, and it has motivated the "receding torus" model of Lawrence (1991), where the inner edge of the obscuring material depends on luminosity. In this picture, the dust sublimation radius grows as $R_{\rm sub} \propto L^{1/2}$ while the torus height remains fixed. As a result, the torus opening angle widens at high luminosities, reducing the covering factor of obscuration.

Narrow-line Seyfert 1 galaxies (NLS1s) form a subclass of Type 1 AGN characterized by unusually narrow broad emission lines (FWHM Hβ < 2000 km s^{-1}), strong Fe II emission, and rapid X-ray variability (Osterbrock and Pogge, 1985). In the simple orientation-based unification picture, such narrow broad lines would be unexpected, since viewing angle alone cannot systematically reduce BLR velocities. Instead, NLS1s are interpreted as systems with relatively low black hole masses accreting at high Eddington ratios, where the larger BLR radius leads to lower orbital velocities (Mathur, 2000).

Another major challenge to the simple unification scheme comes from the so-called changing-look AGN, seen both in X-rays (Matt et al., 2003) and in the optical (LaMassa et al., 2015), where objects transition between obscured and unobscured states or between Type 1 and Type 2 spectra on timescales of only a few years. Such rapid changes cannot be explained by a shift in orientation, which would require much longer timescales, but instead point to intrinsic variability in the central engine. Possible drivers include changes in the accretion rate or variations in obscuration along the line of sight, both of which can dramatically alter the appearance of the BLR and continuum emission.

At the population level, the fraction of obscured AGN is not fixed but evolves with redshift. Deep X-ray and infrared surveys show that obscured AGN reach their maximum space density at earlier cosmic times than unobscured AGN (Hasinger, 2008; Lacy et al., 2015). This evolutionary difference cannot be explained by orientation alone and suggests that the frequency of obscuration depends on the cosmic environment and accretion history, adding another dimension to AGN unification models.

In summary, orientation clearly plays a major role in shaping AGN spectra, as demonstrated by the detection of hidden BLRs in Type 2 sources. Nevertheless, luminosity, accretion rate, and cosmic epoch also strongly influence whether an AGN appears obscured or unobscured. A complete unification model must therefore combine orientation effects with intrinsic physical drivers of AGN structure and evolution.

Chapter 2

Reverberation mapping

2.1 Introduction

Chapter 1 discussed the basic structure and components of active galactic nuclei (AGN). In this chapter, I will focus on one of the most widely used techniques to study the unresolved central regions of AGNs: reverberation mapping (Blandford and Payne, 1982; Peterson, 1993). To explain the method and its practical applications, we will use NGC 5548 as a primary example, since this galaxy also serves as the basis for the modeling presented in chapter 5.

NGC 5548 is a Seyfert 1 galaxy at redshift $z \approx 0.017$ and is one of the most extensively observed AGNs to date. Over the past thirty years, it has been monitored across multiple wavelengths by space-based observatories such as the *Hubble Space Telescope* (HST), *Swift*, and *XMM-Newton*, as well as through long-term ground-based campaigns (Peterson et al., 2002; Bentz et al., 2009; De Rosa et al., 2015; Edelson et al., 2015). These efforts have produced high-cadence, multi-band data that make NGC 5548 an ideal case for studying time-dependent processes in AGNs.

This long-term monitoring has enabled detailed measurements of the broad-line region (BLR) geometry, ionization structure, and variability patterns. As a result, NGC 5548 plays a central role in the development of scaling relations for black hole mass estimates and remains the most important calibrator in reverberation mapping studies.

Even with decades of high-quality, multi-wavelength observations, the central regions of NGC 5548—such as the accretion disk, broad-line region, and dusty torus—remain unresolved by current telescopes. Their physical scales are simply too small and too distant to be directly imaged, even with the most advanced optical, infrared, or radio facilities available today.

This limitation raises an important question: what level of spatial resolution would be required to directly observe these inner structures? More importantly, are there indirect methods that can probe their structure and dynamics?

2.2 Optical Telescopes

The diffraction of light places a fundamental limit on the smallest angular scale that a telescope can resolve. Mathematically, this limit is expressed as

$$\theta = \frac{1.22\,\lambda}{D}, \tag{2.1}$$

where D is the telescope's aperture diameter, λ is the observation wavelength, and θ is the smallest resolvable angle (in radians).

As an example, consider the Gran Telescopio Canarias (GTC), which has a primary mirror of 10.4 m. At an observing wavelength of $\lambda = 500\,\mathrm{nm}\,(5 \times 10^{-7}\,\mathrm{m})$, the diffraction-limited resolution is

$$\theta = \frac{1.22 \times 5 \times 10^{-7}}{10.4} \approx 5.87 \times 10^{-8}\,\mathrm{radians}. \tag{2.2}$$

Converting this to arcseconds, using 1 radian = 206,265 arcseconds, gives

$$\theta \approx 0.012\,\mathrm{arcseconds}. \tag{2.3}$$

Thus, the GTC can at best achieve an angular resolution of about 0.012 arcseconds.

Now, let us translate this angular resolution into a physical length scale at the distance of NGC 5548, which is approximately 75 Mpc (or 2.31×10^{24} m). The corresponding linear size is

$$\text{linear size} = \theta \times D_{\text{distance}} = 5.87 \times 10^{-8} \times 2.31 \times 10^{24} \approx 1.34 \times 10^{17}\,\mathrm{m}. \tag{2.4}$$

Expressed in light-days, this becomes

$$\frac{1.34 \times 10^{17}}{2.59 \times 10^{13}} \approx 5{,}170\,\text{light-days}. \tag{2.5}$$

This scale is enormous compared with the compact regions of interest in AGN: the dusty torus spans only a few hundred light-days, the broad-line region (BLR) extends over just a few tens of light-days, and the accretion disk operates on scales of a few light-days. This simple calculation highlights the severe limitations of even the largest current optical telescopes in directly resolving these inner AGN structures.

Conversely, we can also invert the diffraction equation 2.1 to estimate the aperture size that would be required to spatially resolve each of these components.

2.2.1 Adopted Characteristic Length Scales

For consistency, all aperture calculations in this chapter are based on the following representative physical sizes:

- **Event horizon:** $R_{\mathrm{S}} = 3.0 \times 10^{10}\,\mathrm{m}$,
- **Accretion disk:** $L_{\mathrm{disk}} = 3.0 \times 10^{13}\,\mathrm{m}$,
- **Broad-line region (BLR):** $L_{\mathrm{BLR}} = 3.0 \times 10^{15}\,\mathrm{m}$,
- **Dusty torus:** $L_{\mathrm{torus}} = 2.6 \times 10^{16}\,\mathrm{m}$.

These characteristic scales are chosen as order-of-magnitude estimates consistent with reverberation mapping and interferometric observations of Seyfert galaxies. Unless otherwise noted, all subsequent telescope aperture requirements (tables 2.1–2.4) are derived using these values together with the diffraction formula (eq. 2.6).

Note: The calculations presented in this chapter assume an ideal case and omit effects such as scattering or absorption of light over cosmological distances, which in practice can affect observations.

2.2.2 Requirements for Hypothetical Apertures

To estimate the telescope diameters required to resolve different AGN structures, we invert the diffraction relation (eq. 2.6):

$$D_{\text{tel}} = \frac{1.22\,\lambda\,D_{\text{A}}}{L}, \tag{2.6}$$

where L is the physical size of the structure and D_{A} is the distance to the source. Using $\lambda = 5 \times 10^{-7}\,\text{m}$ and $D_{\text{A}} = 2.31 \times 10^{24}\,\text{m}$ (NGC 5548), we obtain table 2.1.

TABLE 2.1: Estimated telescope diameters required to resolve AGN components in NGC 5548 at 500 nm.

Component	Size (m)	Required Aperture (m)
Event Horizon	3.0×10^{10}	4.7×10^{7}
Accretion Disk	3.0×10^{13}	4.7×10^{4}
Broad-Line Region	3.0×10^{15}	4.7×10^{2}
Dusty Torus	2.6×10^{16}	5.4×10^{1}

The table 2.1 shows that while resolving the BLR would require telescope apertures of several hundred meters, imaging the black hole's event horizon or accretion disk would demand instruments larger than the Earth itself. The next generation of extremely large telescopes may, at best, approach the scale required to resolve the dusty torus.

To emphasize this limitation further, we can perform another simple experiment: hypothetically place the same source at increasing distances—that is, vary its redshift—and then calculate the telescope aperture required to resolve each AGN component at those distances.

2.2.3 Extension to Higher Redshifts

Adopting a flat ΛCDM cosmology with $H_0 = 69.6\,\mathrm{km\ s^{-1}\,Mpc^{-1}}$, $\Omega_m = 0.286$, and $\Omega_\Lambda = 0.714$, we extend this analysis to higher redshifts. The telescope apertures required to resolve different AGN components at 500 nm are calculated using the distances mentioned in table 2.2 and the results are in table 2.3.

TABLE 2.2: Angular-diameter distance D_A in a flat ΛCDM with $H_0 = 69.6$ km s^{-1} Mpc^{-1}, $\Omega_m = 0.286$, $\Omega_\Lambda = 0.714$.

z	D_A [Mpc]	D_A [Gpc]
0.05	197.8	0.198
0.10	372.3	0.372
0.20	685.9	0.686
0.30	926.5	0.927
0.40	1117.4	1.117
0.50	1269.9	1.270
0.70	1549.2	1.549
1.00	1757.9	1.758
1.50	1940.9	1.941
2.00	1921.0	1.921

TABLE 2.3: Telescope diameters (m) required to resolve AGN components at $\lambda = 500$

Redshift	Event Horizon	Accretion Disk	BLR	Dusty Torus
0.05	1.25e+08	1.25e+05	1.25e+03	1.44e+02
0.1	2.36e+08	2.36e+05	2.36e+03	2.73e+02
0.2	4.35e+08	4.35e+05	4.35e+03	5.02e+02
0.3	5.88e+08	5.88e+05	5.88e+03	6.78e+02
0.4	7.09e+08	7.09e+05	7.09e+03	8.18e+02
0.5	8.06e+08	8.06e+05	8.06e+03	9.30e+02
0.7	9.83e+08	9.83e+05	9.83e+03	1.13e+03
1.0	1.12e+09	1.12e+06	1.12e+04	1.28e+03
1.5	1.24e+09	1.24e+06	1.24e+04	1.42e+03
2.0	1.23e+09	1.23e+06	1.23e+04	1.39e+03

These calculations illustrate the severe limitations of direct imaging for AGN inner regions. Resolving structures smaller than the dusty torus remains far beyond

foreseeable optical technology. Indirect methods such as reverberation mapping therefore remain essential to probe AGN central engines.

In the following section, we repeat the same experiment in the near-infrared regime.

2.2.4 Near-Infrared Requirements

At a wavelength of $\lambda = 2.2\,\mu$m (K-band), the diffraction limit increases proportionally with wavelength. Applying the same approach as in the optical case, we can estimate the telescope diameters required to resolve key AGN structures. The results are shown in table 2.4.

TABLE 2.4: Telescope diameters (m) required to resolve AGN components at $\lambda = 2.2$ μm using the same cosmology.

Redshift	Event Horizon	Accretion Disk	BLR	Dusty Torus
0.05	5.51e+08	5.51e+05	5.51e+03	6.33e+02
0.1	1.04e+09	1.04e+06	1.04e+04	1.15e+03
0.2	1.91e+09	1.91e+06	1.91e+04	2.21e+03
0.3	2.58e+09	2.58e+06	2.58e+04	2.97e+03
0.4	3.11e+09	3.11e+06	3.11e+04	3.59e+03
0.5	3.53e+09	3.53e+06	3.53e+04	4.08e+03
0.7	4.31e+09	4.31e+06	4.31e+04	4.95e+03
1.0	4.93e+09	4.93e+06	4.93e+04	5.67e+03
1.5	5.48e+09	5.48e+06	5.48e+04	6.31e+03
2.0	5.43e+09	5.43e+06	5.43e+04	6.12e+03

As table 2.4 shows, even under optimistic assumptions, only the dusty torus falls within the potential reach of kilometer-scale infrared interferometry. Resolving the broad-line region remains extremely difficult, and accessing the inner accretion disk or the event horizon would still require telescope baselines far beyond current or near-future capabilities.

2.3 Conclusion

The calculations presented above clearly illustrate the immense challenge posed by direct spatial resolution of the innermost regions of active galactic nuclei such as NGC 5548. Across the electromagnetic spectrum—from optical through infrared to radio wavelengths—the telescope aperture sizes required to resolve fundamental components like the event horizon, accretion disk, broad-line region, or dusty torus at cosmological distances range from hundreds of meters to hundreds of thousands of kilometers. These scales vastly exceed the dimensions of any current or foreseeable human-made observatories, making direct imaging of these compact structures practically impossible with conventional telescopes.

Building a single telescope with such a large aperture is clearly impractical. A more realistic approach is to use two or more smaller telescopes and combine their signals through interferometry. In this case the resolution is set by $\theta \approx \lambda/B$, where B is the separation (baseline) between the telescopes. This method is already in common use: radio interferometers (e.g. VLA), optical/infrared arrays (e.g. VLTI), and even projects like the Event Horizon Telescope, which links radio dishes across the Earth. With VLTI, the GRAVITY instrument has already spatially resolved the BLR in some quasars and the hot dust torus in nearby AGNs, providing direct constraints on geometry and dynamics (Gravity Collaboration et al., 2018a; GRAVITY Collaboration et al., 2020; Gravity Collaboration et al., 2024; GRAVITY Collaboration et al., 2021, 2020). Its successor, GRAVITY+, will extend sensitivity and sky coverage, enabling such interferometric studies for larger samples of AGNs (Santos et al., 2025). In this way, interferometry is emerging as a unique complement to reverberation mapping and remains the only direct probe of AGN sub-parsec structure. There are also proposals to attempt interferometry at X-ray wavelengths in the future.

Even so, to resolve the innermost regions of AGN the required baselines remain very large, and interferometry brings its own technical difficulties. For extremely long baselines the signals must be combined in phase with very high timing precision. Although Infrared interferometry has already resolved the dusty torus and even the BLR in a few nearby AGN, extending such measurements to larger samples and higher redshifts remains a major challenge.

This severe constraint justifies the central role of *indirect observational techniques*, which do not rely on spatial resolution but instead exploit time resolution. The **reverberation mapping** stands out as the most effective tool to probe AGN inner structures. By using the time delays between continuum and line emission variations, it enables us to infer geometry, size, and kinematics of the BLR and accretion disk, and torus. In this context, reverberation mapping is not just a useful technique; it is a scientific necessity.

2.4 A General View of Reverberation Mapping

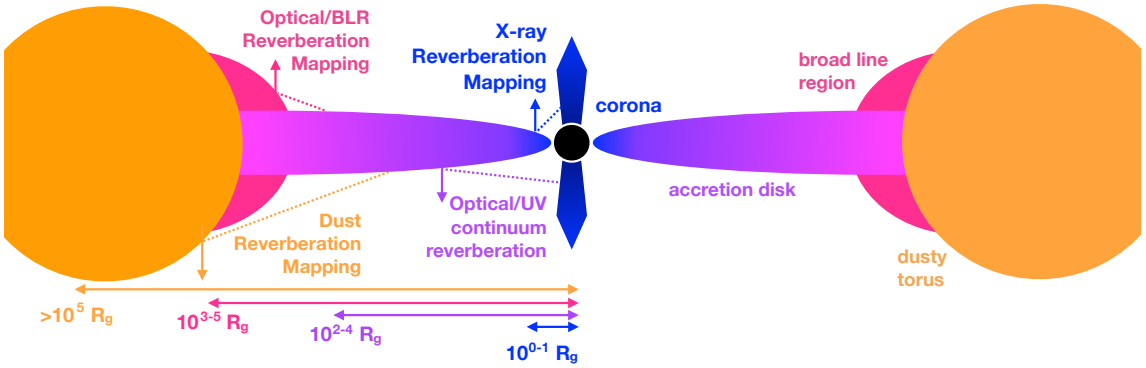

FIGURE 2.1: Comparison of the spatial scales probed by different reverberation mapping approaches, showing how each technique provides information on distinct regions of the active galactic nucleus (AGN) structure (adapted from Cackett et al. 2020).

At its core, reverberation mapping is built on a simple but powerful idea: we observe **two related light signals** — one acting as a *reference*, and the other as a *delayed signal* due to reprocessing by distant material.

- **Reference/Driving signal**: In X-ray reverberation mapping, the driving signal is the rapid variability from the compact corona, while in disk reverberation mapping it typically arises from X-ray or ultraviolet fluctuations in the inner accretion disk. For broad-line region (BLR) reverberation mapping, the accretion disk continuum serves as the driver, and in the infrared the same disk continuum drives the response of the dusty torus.

- **Delayed signal**: In X-ray reverberation mapping, the delayed signal arises from reflection off the inner accretion disk, producing features such as the iron Kα line and Compton hump. In disk reverberation mapping, the delay is seen as thermal reprocessing in the outer regions of the accretion disk. For BLR reverberation mapping, the delayed response is not limited to broad emission lines. It also includes a variable continuum component, which arises partly from scattering (primarily by free electrons) and partly from continuum emission processes in the ionized gas, dominated by hydrogen but with contributions from other ions as well. In infrared reverberation mapping, the delayed response arises from dust in the torus re-radiating absorbed disk continuum. The observed signal consists of a thermal continuum together with broad spectral features such as the silicate bands at 9.7 and 18 μm, which are produced by vibrational modes in the dust grains rather than by atomic line transitions.

This time delay τ corresponds to a light-travel distance $R = c \cdot \tau$, giving a direct measurement of the spatial scale of the reprocessing region. As illustrated in figure 2.1,

the region of an active galactic nucleus that can be probed with reverberation mapping depends on the observed part of the electromagnetic spectrum, with different wavebands providing access to distinct physical structures.

In reverberation mapping, the delayed signal reproduces the overall variability pattern of the driving signal but with two key modifications: it is shifted in time due to the finite light-travel distance, and it is smoothed or broadened as a consequence of the extended geometry of the reprocessing region. Consequently, the delayed light curve mirrors the driver, though its features appear later and less sharply defined. Formally, this behaviour is described as a convolution of the driving signal with a response function, $\Psi(\tau)$, which encapsulates the geometry and physical conditions of the reprocessing medium. If $F_{\rm i}(t)$ denotes the variable component of the continuum, the reprocessed signal $F_{\rm r}(t)$ can be expressed as

$$F_{\rm r}(t) = \int_0^{t_{\rm max}} \Psi(\tau)\, F_{\rm i}(t-\tau)\, d\tau. \tag{2.7}$$

The response function is a key element in reverberation mapping, since in principle it allows us to reconstruct the delayed signal directly from the driving light curve by convolution. There are two main ways to approach it. One is observational: this has been attempted most successfully in BLR reverberation mapping, where long monitoring campaigns make it possible to use inversion methods to estimate the transfer function. In other regimes, however, the response function cannot be directly determined. In X-ray reverberation mapping the delays are extremely short, making direct inversion impossible with current timing precision; instead, one measures frequency-dependent lags. In disk reverberation mapping the continuum delays are only of order hours to days, so in practice the data is used to generate lag spectrum rather than a full transfer function. In the infrared, by contrast, the

lags are very long (months to years) and light curves are sparsely sampled, so again only mean delays can usually be obtained.

The second approach is theoretical: here one models the system by introducing a short pulse of radiation and following how it is redistributed as it travels through the reprocessing medium. The geometry, orientation, and physical state of the material shape the form of the theoretical response function. Moreover, such modelling reveals which wavebands most effectively probe distinct AGN components: X-ray lags trace the innermost accretion disk, optical and ultraviolet lags map the broad-line region along with middle and outer disk, and infrared lags uncover the structure of the dusty torus. Thus, despite differences in observational regime, the underlying process of reverberation mapping is fundamentally the same: the delayed signal arises from the convolution of the driving light curve with the response function, making this framework a unified and powerful tool for investigating the central structures of active galaxies.

2.5 Lamp-post Model

Before discussing the different types of reverberation mapping, it is useful to introduce the lamp-post model, which is also a very important part of my research. This model is particularly relevant for both X-ray and disk reverberation studies. In this model, the corona is approximated as a compact source located on the spin axis above the black hole (Martocchia and Matt, 1996; Miniutti and Fabian, 2004), as illustrated in figure 2.2. A fraction of the coronal X-rays reaches the observer directly, while the rest illuminates the accretion disk. The illuminated photons are then reflected or reprocessed, imprinting characteristic spectral signatures before reaching the observer with a delay due to the additional light-travel path.

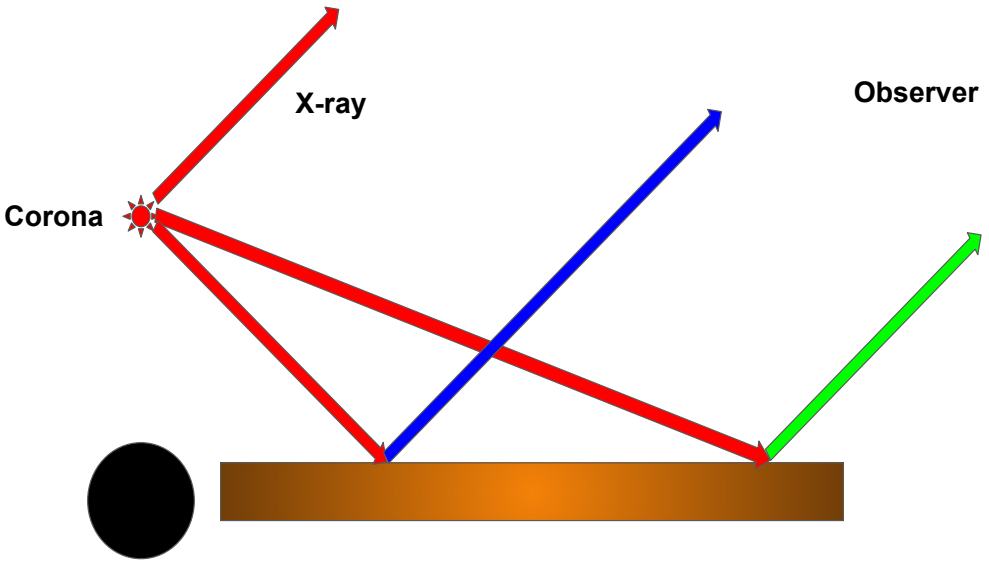

FIGURE 2.2: The lamp-post model of AGN emission, where a point-like X-ray corona situated on the rotation axis irradiates the surrounding accretion disk.

Although the lamp-post model is very simple to apply, the true geometry of the corona is still an open question. Observational and theoretical work has suggested that the corona may often be extended rather than point-like. Patchy or sandwich-like coronae covering parts of the disk were already proposed in the two-phase disk–corona model (Haardt and Maraschi, 1991, 1993). Microlensing studies of quasars indicate that the X-ray emitting region can be compact but not strictly point-like, implying a radial extent of a few to tens of gravitational radii (Chartas et al., 2009; Mosquera et al., 2013). Other scenarios favour vertically elongated or jet-like coronae, motivated by the apparent connection between coronal emission and the base of relativistic jets (Markoff et al., 2005; Wilkins et al., 2017). Outflowing corona models have also been invoked to explain weak reflection fractions, as bulk motion of the plasma can beam radiation away from the disk (Beloborodov, 1999). More recently, Kara et al. (2019) proposed that the geometry of the corona can also evolve with time, although the result was not for an AGN.

2.6 X-ray Reverberation Mapping: A Probe of the Inner Disk

X-ray reverberation mapping provides a unique window onto the innermost regions of active galactic nuclei (AGNs), on scales of only $\sim$ 10–20 $R_{\rm g}$ from the black hole. The accretion disk itself does not have enough temperature to emit X-rays directly; instead, thermal UV photons from the disk are upscattered to X-ray energies by inverse Comptonisation in the corona (Haardt and Maraschi, 1991). Some of these photons reach the observer directly, while others illuminate the disk. The reflected photons carry the imprint of absorption, fluorescence, Compton scattering, and thermalisation, producing characteristic spectral features in the observed X-ray spectrum.

The most prominent reflection signatures are the iron Kα complex and the Compton hump. The former consists of fluorescent lines from iron in different ionization states: 6.4 keV for neutral or weakly ionized gas, and 6.7 and 6.97 keV for He-like and H-like iron, respectively. The latter is a broad excess peaking at 20–30 keV (Risaliti et al., 2013; Parker et al., 2014; Walton et al., 2014; Marinucci et al., 2014). Both features are strongly modified by relativistic effects in the inner disk (Fabian et al., 1989). The line profile in particular is sensitive to black hole spin: faster spin reduces the innermost stable circular orbit, broadening the line (Reynolds, 2019).

Because reflected photons travel a longer path, they arrive with a delay relative to the direct coronal emission. As mentioned before, fourier-based methods are employed, allowing lags to be measured as a function of frequency. Measuring these delays converts into a light-travel distance, $R = c\tau$, directly probing the inner accretion flow. The breakthrough case was the $\sim$30 s soft lag in 1H 0707$-$495 (Fabian et al., 2009). Since then, lags have been detected in the soft X-ray band (Zoghbi et al., 2011; Cackett et al., 2013; Alston et al., 2014; De Marco et al., 2013), in the Fe Kα line

(Zoghbi et al., 2012; Kara et al., 2013b, 2016; Vincentelli et al., 2020), and even in the Compton hump above 10 keV using *NuSTAR* (Zoghbi et al., 2014; Kara et al., 2015). In some Seyfert galaxies, lags of tens of seconds have been observed, corresponding to only a few gravitational radii. Other techniques, such as microlensing (Chartas et al., 2009, 2012) and X-ray eclipses (Gallo et al., 2021), independently confirm that the X-ray emitting region is compact.

The X-ray reverberation mapping studies on multiple AGNs show that lags correlate with black hole mass (De Marco et al., 2013; Kara et al., 2016). The large scatter in this relation likely reflects differences in coronal size and geometry. For instance, in IRAS 13224−3809 the lag increases when the corona brightens (Kara et al., 2013a), consistent with models in which the coronal height grows with luminosity (Alston et al., 2020).

NGC 5548 is one of the best-monitored Seyfert galaxies. Observations with *XMM-Newton* and *Suzaku* reveal soft lags of a few hundred seconds and tentative Fe Kα lags of a few kiloseconds (De Marco et al., 2013; Cackett et al., 2014; Kara et al., 2016). Unlike narrow-line Seyfert 1 galaxies such as 1H 0707−495, however, NGC 5548 does not show a strongly broadened Fe Kα line; instead, the line core at 6.4 keV remains narrow, consistent with more distant reflection. Nevertheless, the reverberation delays imply reprocessing at radii of order 10–20 $R_{\rm g}$, reinforcing the view that X-ray reverberation mapping is a powerful probe of the innermost accretion flow.

2.7 UV/Optical Reverberation mapping

In contrast to X-ray reverberation mapping, which probes only the innermost few tens of gravitational radii, UV/optical reverberation mapping is sensitive to much

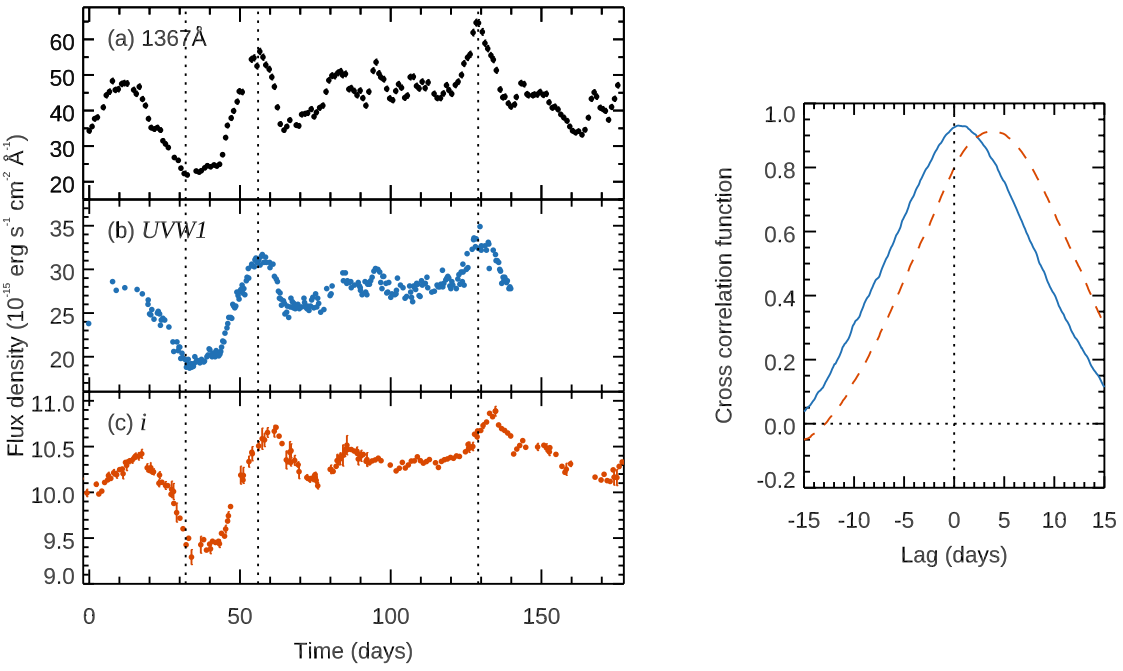

FIGURE 2.3: **Left:** Ground-based light curves of NGC 5548 at three wavelengths. **Right:** Cross-correlation functions (CCFs) computed with respect to the 1367 Å continuum: UVW1 (solid blue) and i band (orange dashed). (figure adapted from Fausnaugh et al. 2016)

larger radii in the accretion disk, typically 10^2–$10^4\,R_{\rm g}$. Shorter-wavelength UV photons are emitted from the hotter inner regions of the disk, while longer-wavelength optical and infrared photons come from cooler outer regions. This radial temperature gradient naturally determines the range of physical scales that can be studied with continuum reverberation mapping. Figure 2.3 illustrates this in NGC 5548, where variability at longer wavelengths clearly lags behind that at shorter wavelengths.

Theoretical expectations for these lags can be derived from the standard Shakura–Sunyaev thin-disk model. In this framework, the temperature profile of the disk is

$$T(R) \propto (M\dot{M})^{1/4} R^{-3/4},$$

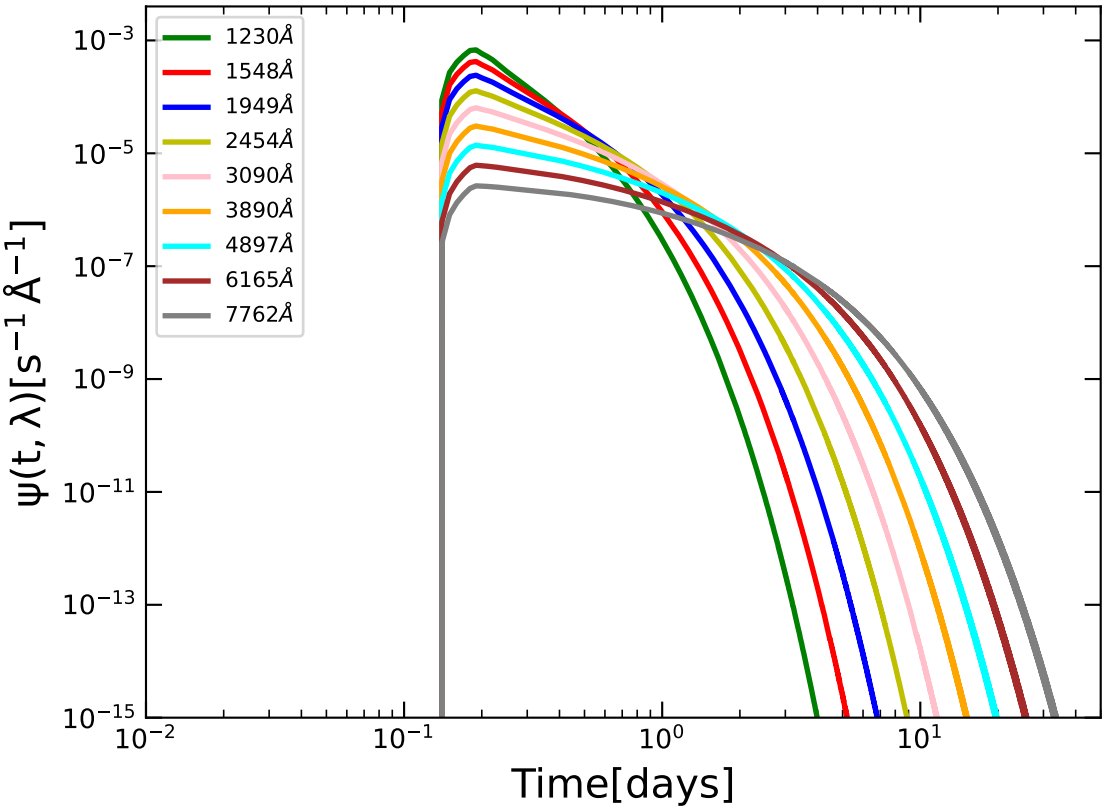

FIGURE 2.4: Response functions at multiple wavelengths predicted by the lamp-post model. Parameters used: $M_{\rm BH} = 5.0 \times 10^7\,M_\odot$, Eddington ratio = 0.015, lamp luminosity $L_X = 9.68 \times 10^{43}\,{\rm erg\,s^{-1}}$, height $h = 48.29\,r_g$, $R_{\rm in} = 6\,r_g$, $R_{\rm out} = 10000\,r_g$, and viewing angle $i = 40°$.

where $\dot{M}$ is the mass accretion rate. Since the observed lag corresponds to the light-travel time from radius R ($\tau = R/c$), and blackbody radiation obeys

$$\lambda \propto T^{-1},$$

we obtain the scaling relation

$$\tau(\lambda) \propto (M\dot{M})^{1/3}\lambda^{4/3}.$$

This expression predicts how the time delay should increase with wavelength in a standard thin disk.

The central aim of my PhD research was to investigate continuum reverberation mapping within the framework of the lamp-post model, as outlined in section 2.5. The physical picture is illustrated in figure 2.2. If the corona emits a short pulse of radiation, the innermost regions of the accretion disk receive and reprocess this signal before the more distant regions, simply due to the difference in light-travel times. For the observer, this sequence appears as emission from the inner disk (shown in blue) arriving first, followed by progressively delayed responses from the outer disk (shown in green). Thus, an initially sharp and compact pulse from the corona is observed as a broadened and stretched signal, since different annuli of the disk contribute at different times. This behaviour is described by the *response function*, which quantifies how the accretion disk reacts to an instantaneous flash of light from the corona, and is illustrated in figure 2.4.

There are two main points to notice in the response function. The first is that the curves for all wavelengths start at the same time. This happens because the accretion disk emits like a blackbody, so each part of the disk contributes some radiation across a wide range of wavelengths. The very hot inner regions emit strongly at short wavelengths but still contribute at longer ones as well. This means that every wavelength band receives an almost immediate signal from the inner disk, which is why the responses all begin together.

The second point is that the response becomes broader as the wavelength increases. UV light comes mostly from the hot, compact inner disk, giving a narrow response. In contrast, the optical bands are produced over a much larger area of the disk, where the cooler, outer regions dominate. Because of this, the response at long wavelengths is spread out over a wider range of times.

Once I generated the response function, I calculated the lag corresponding to each wavelength by using equation 2.8:

$$\tau(\lambda) = \frac{\int t\,\psi(t,\lambda)\,dt}{\int \psi(t,\lambda)\,dt}. \tag{2.8}$$

The launch of the *Swift* observatory provided a major opportunity for progress, as it enabled simultaneous monitoring of AGN in X-ray, ultraviolet (UV), and optical bands with high signal-to-noise. Early lag measurements from *Swift* showed that the delays between different wavelengths were significantly larger than those predicted by standard thin-disk theory (Shappee et al., 2014; McHardy et al., 2014).

This result was later confirmed by a large coordinated campaign on NGC 5548 that combined observations from *Swift*, the *Hubble Space Telescope*, and multiple ground-based facilities. The campaign showed that inter-band time delays are systematically larger than those predicted by the standard thin-disk model. In fact, the data suggest that the effective size of the accretion disk is about three times greater than expected from classical theory (Edelson et al., 2015; Fausnaugh et al., 2016). This discrepancy has become widely known as the *accretion disk size problem*.

The wavelength dependence of the delays is usually parameterized as

$$\tau(\lambda) = \tau_0 \left[\left(\frac{\lambda}{\lambda_0} \right)^{\beta} - 1 \right],$$

where λ_0 is the reference wavelength (typically the best-sampled band), τ_0 is the normalization, and $\beta = 4/3$ for a standard thin accretion disk.

The measured lags are almost always found to be larger by a factor of two to three (Shappee et al., 2014; McHardy et al., 2014; Edelson et al., 2015, 2017, 2019; Fausnaugh et al., 2016, 2018; Cackett et al., 2018, 2020; Pozo Nuñez et al., 2019; Jiang

et al., 2017; Mudd et al., 2018). These larger-than-expected delays suggest that the radius corresponding to a given temperature is greater than predicted by the thin-disk model. Independent evidence from gravitational microlensing has also indicated that the optical emission regions of quasars are larger than predicted by standard thin-disk theory, a point first discussed by Rauch and Blandford (1991) and confirmed in later systematic studies (Morgan et al., 2010).

There were many proposed models to explain the difference in measurements of the size of the accretion disk. For example, Dexter and Agol (2011) suggest that an accretion disk that is not uniform and changes over time can lead to longer lags than what standard models predict. Hall et al. (2018) pointed out that the emission should not be treated as a simple blackbody. A scattering atmosphere on top of the disk can shift the spectrum and change the temperature profile, which increases the delays. This is often described by introducing a colour-correction factor. Building on this, Kammoun et al. (2019, 2021a,b) showed that including such corrections in thin-disk models helps to match the longer lags seen in reverberation data. Along with colour correction, the larger height of the corona also helps to increase the delay.

In our work, we tried to resolve the disk size problem by including the contribution from the BLR. Some of the reprocessed light from the disk reaches the observer directly, while some is scattered and modulated by the emission profile of the BLR. The light emitted by the BLR is therefore delayed even further. We first modeled BLR reprocessing as a scattering process, with the BLR structure represented by a Gaussian or semi-Gaussian smearing (Paper 1). In Paper 2, we advanced the approach by incorporating radiative transfer within the clouds (using CLOUDY) and adopting the three-dimensional structure of the region from a physically motivated model (FRADO) (Czerny and Hryniewicz, 2011), as described in Chapter 3. When

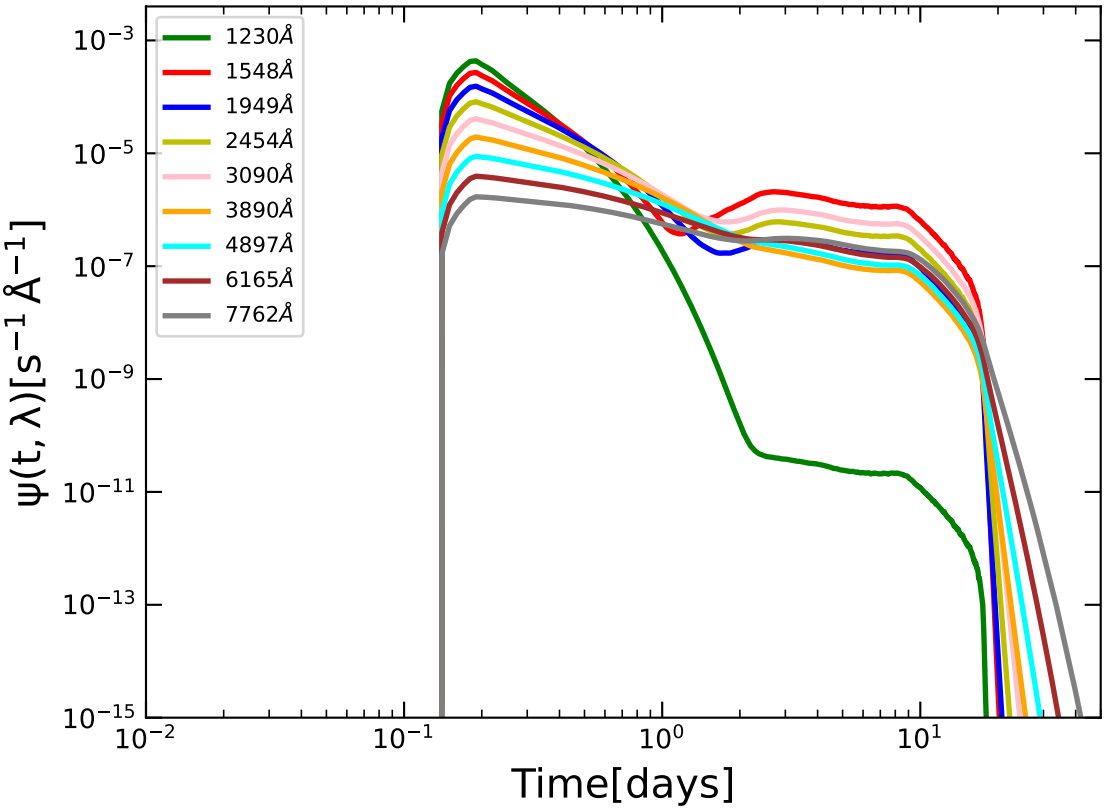

FIGURE 2.5: Response functions at multiple wavelengths predicted by the lamp-post model including the contribution from the BLR. Parameters used: $M_{\rm BH} = 5.0 \times 10^7\,M_\odot$, Eddington ratio $= 0.015$, lamp luminosity $L_X = 9.68 \times 10^{43}\,{\rm erg\,s^{-1}}$, height $h = 48.29\,r_g$, $R_{\rm in} = 6\,r_g$, $R_{\rm out} = 10000\,r_g$, $f_{\rm BLR} = 30\%$, and viewing angle $i = 40°$.

the BLR response function is added to the disk response function, the combined result is shown in figure 2.5. The second peak in the total response function arises from the BLR contribution, and as a result the overall response is more extended in the time domain, producing longer delays compared to the case with only the disk contribution. This is the way we address the disk size problem.

Another interesting test we performed, though not used in the fitting process, was to introduce shielding of the BLR clouds along the observer's line of sight using a cone-shaped geometry. As the cone's base becomes larger, an increasing fraction of clouds is hidden from the observer. Our aim was to study how this shielding affects

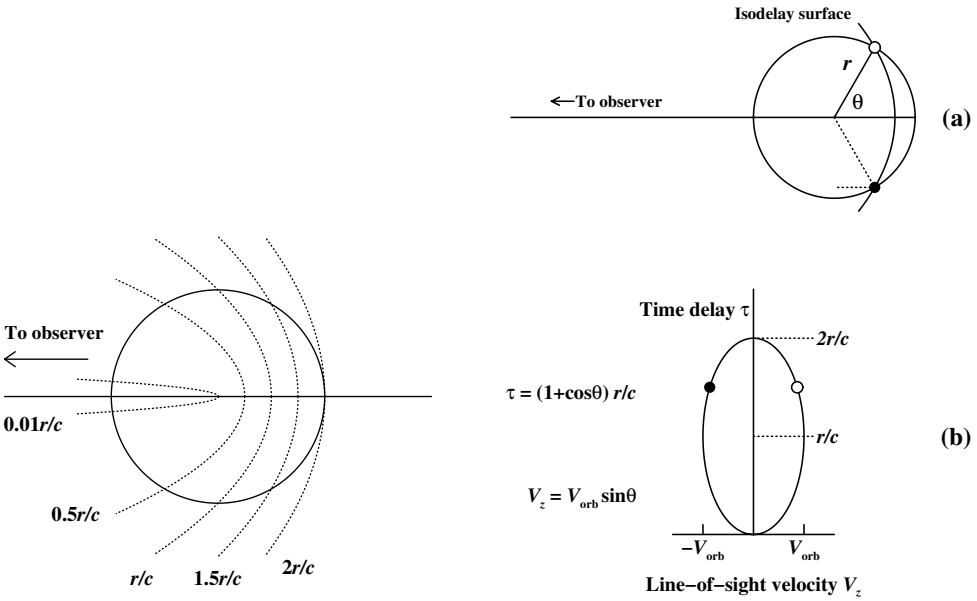

FIGURE 2.6: **Left:** Iso-delay curve, along which BLR clouds produce the same time lag. **Right:** Corresponding observed line-of-sight velocity distribution for clouds located on a given iso-delay curve. (figure adapted from Peterson 2001)

the BLR response function and the resulting emission profile. The outcomes of this test are presented in figures B.1 and B.2.

2.8 Broad-Line Region Reverberation Mapping

Blandford and Payne (1982) introduced the theory of reverberation (or echo) mapping as a powerful method to probe the geometry and kinematics of the broad-line region (BLR) in active galactic nuclei (AGN). The central idea is that continuum variations from the accretion disk act as a variable "lamp" that photoionizes the BLR gas. The BLR responds with a delayed change in its emission-line flux, and this delay encodes information about the spatial distribution of the gas.

As illustrated in figure 2.6, consider a short light pulse emitted from the center and a population of BLR clouds arranged on a thin ring at radius R. Since all clouds are at

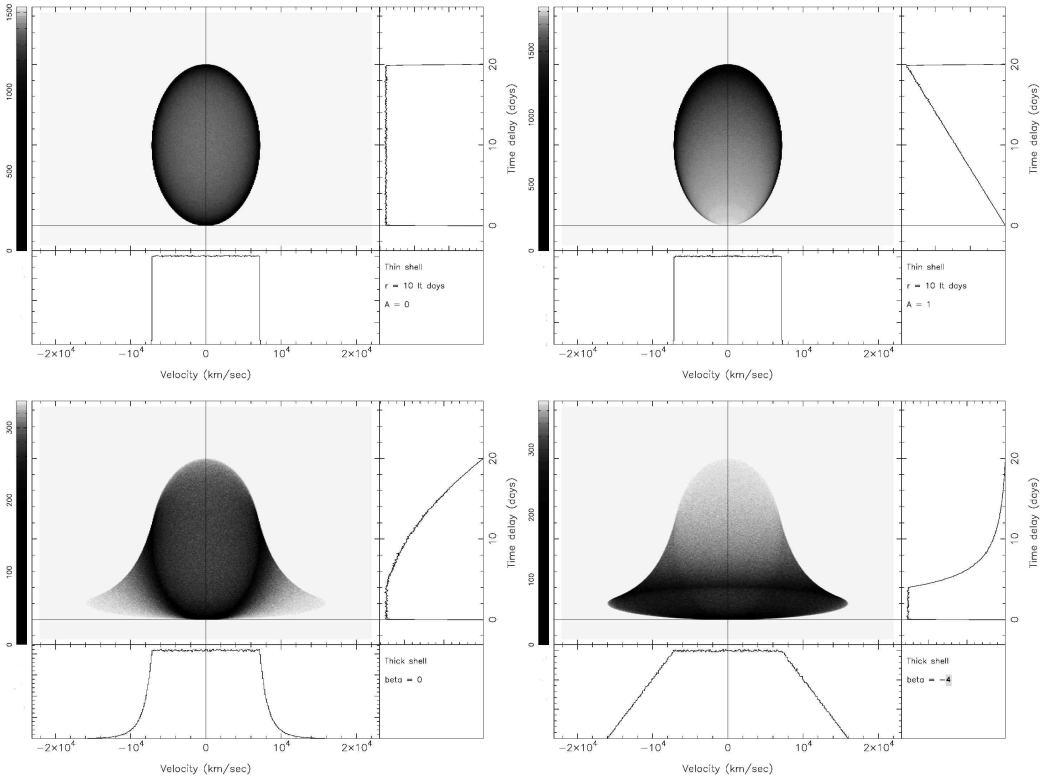

FIGURE 2.7: Each figure consists of three panels. **Upper left:** Two-dimensional transfer function (grayscale), showing the emission-line response as a function of line-of-sight velocity V_z and time delay τ. **Upper right:** One-dimensional transfer function obtained by integrating over V_z, representing the total line response as a function of time. **Lower:** Emission-line response integrated over time delay, corresponding to the variable component of the line profile. The different subfigures correspond to distinct geometries and parameters: **Top left:** Ring with anisotropy parameter $A = 0$ and responsivity index $\beta = 0$. **Top right:** Ring with $A = 1$, $\beta = 0$. **Bottom right:** Spherical shell with $A = 0$, $\beta = 0$. **Bottom left:** Spherical shell with $A = 0$, $\beta = -4$ (figure adapted from Peterson 2001).

the same distance from the center, they receive the continuum pulse simultaneously. However, the observer does not see their responses at the same time, because the reprocessed light must travel an additional distance from each cloud to the observer. The set of points that produce the same observed time delay defines an *iso-delay surface*. The minimum delay is $\tau = 0$, corresponding to the near-side cloud, where the continuum and line photons arrive together. The maximum delay is $\tau = 2R/c$, corresponding to the far-side cloud, where the line photon must travel an extra $2R$. Thus, the sharp input pulse is observed as a broadened response function extending

from 0 to $2R/c$.

In addition to delays, each cloud has a line-of-sight velocity V_z that depends on its orbital motion. Combining both effects yields the two-dimensional transfer function $\Psi(V_z, \tau)$, also known as the velocity–delay map, which describes the line response as a function of both V_z and τ. The one-dimensional transfer function $\Psi(\tau)$ is obtained by integrating over all velocities, and represents the total emission-line response as a function of lag.

Different BLR models produce different forms of $\Psi(\tau)$ as shown in figure 2.7. For a thin spherical shell with isotropic emission ($A = 0$), the response is flat between 0 and $2R/c$, since all delays are equally probable. If the emission is anisotropic ($A = 1$), with flux directed back toward the continuum source, near-side emission is suppressed and far-side emission dominates, producing a triangular response that rises linearly with τ. For a thick spherical shell extending from $r_{\rm in}$ to $r_{\rm out}$, the shape further depends on the radial responsivity index β, which parameterizes how the line emissivity depends on radius:

$$\epsilon(r) \propto r^{\beta}.$$

With $\beta = 0$, all radii contribute equally, yielding a broad response: flat from 0–$2r_{\rm in}/c$, then tapering smoothly to zero at $2r_{\rm out}/c$. With $\beta = -4$, the emissivity is strongly weighted toward the inner radii, so the response is sharply peaked at short delays. In summary, anisotropy controls the angular weighting of clouds, while the responsivity index β governs the radial weighting, together shaping the observed response functions.

Attempts to map the broad-line region (BLR) in active galactic nuclei (AGNs) through reverberation techniques began with the goal of measuring its response to

fluctuations in the central continuum. However, these early efforts were hampered by assumptions that overestimated the BLR's size. For example, it was found that the BLR size in NGC 4151 is under 30 light-days in multiple works (Cherepashchuk and Lyutyi, 1973; Antonucci and Cohen, 1983; Bochkarev, 1984). Initially, they accepted this discrepancy between theoretical and observational BLR size as the galaxy has low luminosity and large ionization parameter. But with the 4-year observation of Akn 120, a highly luminous source, the estimated BLR size was still smaller than the theoretical prediction (Peterson et al., 1985). Their findings revealed that predictions based on photoionization had overstated the BLR size by nearly an order of magnitude.

Later monitoring programs, especially AGN Watch, added more data over longer timescales. These studies didn't just confirm the smaller BLR size—they also showed that high-ionisation emission lines responded faster than low-ionisation emission lines (Peterson, 1993). This implied a layered or stratified BLR, where different lines are formed at different distances from the central source.

In order to understand this, the Locally Optimally Emitting Cloud (LOC) model was introduced (Baldwin et al., 1995). This model suggests that the BLR is made of many clouds with different densities and distances. Each line is strongest under certain conditions, so what we observe is a result of how these clouds are distributed. The LOC model is used today to explain the reverberation data.

With these developments, the next step was to attempt a direct recovery of the two-dimensional response function from observed data. I will discuss two approaches. Horne et al. (2021) developed a true non-parametric inversion of the reverberation equation using the maximum entropy method (MEMECHO), which reconstructs the velocity–delay map $\Psi(V_z, \tau)$ directly from the data with minimal assumptions. This approach yields empirical 2D response functions that reveal BLR structure, but its

resolution depends strongly on data quality. In contrast, Li and collaborators developed a Bayesian forward-modeling approach (Li et al., 2013, 2018). In this method, the BLR is described by a flexible parametric model in which the clouds can have different spatial distributions and dynamical states. Given a set of model parameters, synthetic velocity-resolved light curves are generated and then compared with the observed data. The comparison is carried out using Markov Chain Monte Carlo inference, which yields a posterior probability distribution for the physical BLR properties such as inclination, radial structure, and the balance between inflow and outflow. From these posterior samples, a model-based transfer function can be constructed. In this way, Horne's inversion technique directly reconstructs the transfer function from the data, while Li's method instead infers the BLR geometry and dynamics through parameterized modeling. Together, the two approaches provide complementary perspectives on the nature of the BLR.

Altogether, reverberation mapping remains a crucial tool—not just for mapping the BLR, but also for estimating black hole masses and understanding the gas conditions in the central regions of AGN.

2.8.1 Estimating Black Hole Mass from Reverberation

If we assume that BLR gas is orbiting the black hole, then the gravitational and centripetal forces must balance:

$$\frac{GM_{\rm BH}m}{R^2} = \frac{mV^2}{R}.$$

Solving this gives:

$$M_{\rm BH} = \frac{V^2 R}{G},$$

and since R can be written as $c\tau$ (where τ is the time delay from reverberation mapping), we get:

$$M_{\rm BH} = \frac{V^2(c\tau)}{G}.$$

To account for the unknown geometry and dynamics of the BLR, a factor f is used:

$$\boxed{M_{\rm BH} = f\frac{c\tau V^2}{G}}.$$

Using this formula, Peterson and Wandel (1999) estimated the mass of the black hole in NGC 5548, as well as for the sources NGC 3783 and NGC 7469 (Peterson and Wandel, 2000). Along with this, Peterson et al. (2004) suggested that to get an accurate mass, we should use the line width from the variable part, as this variable part is contributed by the virialised BLR clouds. High-ionisation lines usually have shorter delays and broader profiles than low-ionisation lines, which fits well with a virialised BLR and supports the use of reverberation for black hole mass estimates (Peterson and Wandel, 2000; Kollatschny et al., 2001).

2.8.2 The Radius-Luminosity Relationship

One of the most useful outcomes of BLR reverberation mapping is the radius–luminosity ($R - L$) relation, which connects the BLR size to the luminosity of the AGN (Koratkar and Gaskell, 1991; Kaspi et al., 2000, 2005). For the Hβ line, once host galaxy light is removed, the relation roughly follows $R \propto L^{1/2}$ (Bentz et al., 2006, 2009, 2013). This trend has been backed up by microlensing studies (Guerras et al., 2013) and direct interferometric measurements, such as those from the GRAVITY instrument (Gravity Collaboration et al., 2018b).

The $R - L$ relation makes it possible to estimate black hole masses using just a single AGN spectrum (Shen et al., 2011). If we know the AGN's luminosity, we can estimate R, measure the broad-line width, and plug the values into the virial formula with an appropriate f factor (Vestergaard and Peterson, 2006).

While Hβ has been the main focus, similar relations have also been developed for Mg II and C IV (Vestergaard and Peterson, 2006; Onken and Kollmeier, 2008; Woo et al., 2018), which helps extend mass estimates to higher redshifts where Hβ shifts out of the optical window. These scaling relations are key for tracing black hole growth over cosmic time.

2.9 Dust Reverberation Mapping in Active Galaxies

Dust reverberation mapping provides a means to probe scales beyond $\sim 10^5\, R_{\rm g}$. In active galaxies, the near-infrared emission is dominated by hot dust heated by the intense radiation coming from the center (Landt et al., 2011, 2019). Dust can survive only below its sublimation temperature, typically in the range 1300–2000 K. At higher temperatures the grains are destroyed, which sets an effective inner boundary to the dusty region. Because dust reprocesses variations in the continuum with a light-travel delay, the time lag between the driving optical/UV signal and the near-infrared response provides a direct measure of the dust sublimation radius (Clavel et al., 1989; Suganuma et al., 2006).

Early reverberation studies established that this dusty region, often identified with the "torus," extends on scales up to $\sim$1 light year. They also revealed a luminosity-dependent size relation, in which the dust radius increases with the AGN brightness.

More recent work has shown that the dust is systematically closer to the black hole than early measurements suggested, likely because large graphite grains can withstand higher temperatures and thus survive at smaller radii (Oknyanskij and Horne, 2001; Kishimoto et al., 2007; Burtscher et al., 2016).

Systematic monitoring has further demonstrated that the dust reverberation radius is typically a factor of $\sim$4 larger than the characteristic radius of the BLR, consistent with a stratified structure of the circumnuclear medium. On yet larger scales, the narrow-line region extends to parsecs or tens of parsecs, where variability occurs on timescales of years to decades (Koshida et al., 2014; Netzer, 2015; Peterson et al., 2013). Together, these results emphasize both the hierarchical structure of AGN environments and the need for long-term, high-cadence monitoring to map the interplay between dust, gas, and radiation around supermassive black holes.

Chapter 3

Hubble Constant Estimation

3.1 Introduction

The Hubble constant, H_0, is one of the most important parameters in cosmology as it brings the information about the present rate of cosmic expansion. Knowing its value helps us pin down both the age of the universe and what might happen to it in the far future. The problem is that different ways of measuring H_0 do not agree, and this mismatch is what people usually call the *Hubble tension*.

To give two examples, the *Planck* satellite, which measures the cosmic microwave background, finds $H_0 = 67.4 \pm 0.5$ km/s/Mpc (Planck Collaboration et al., 2020). By contrast, when astronomers build the distance ladder using Cepheid variables and Type Ia supernovae, the result comes out closer to 73 ± 1.04 km/s/Mpc (Riess et al., 2022). The estimates from these and other techniques, together with their uncertainties, are summarized in figure 3.1, which clearly illustrates the ongoing Hubble tension. The fact that these values are inconsistent has led to two main lines of thought: either there are still unaccounted-for systematics, or new physics

is required to explain the difference (Abdalla et al., 2022; Di Valentino et al., 2021; Hu and Wang, 2023; Efstathiou, 2025). There are three broad families of methods for estimating H_0: distance ladder techniques based on stellar and supernova calibrators, early universe probes such as the CMB and baryon acoustic oscillations that rely on the sound horizon, and one-step methods including strong gravitational lensing, megamasers, and gravitational-wave standard sirens. Since each of these approaches comes with its own strengths and challenges, a more complete discussion can be found in recent reviews such as Perivolaropoulos (2024). In this chapter, after briefly introducing these existing methods, I will describe the methodology for using reverberation mapping of active galactic nuclei as an additional route to estimate the Hubble constant.

3.2 Distance Ladder

In cosmology, one of the classic approaches to measuring the expansion rate is the so-called distance ladder. The idea is simple but applied in stages, often described as three different *rungs*. The first step relies on nearby distance markers, for example Cepheid variables, Mira variables, Tip of the Red Giant Branch (TRGB), etc . These sources provide a means to measure distances reliably up to ∼10 Mpc. The second stage takes those calibrations and uses them to standardize Type Ia supernovae, which then extend the scale much farther, to several tens of megaparsecs. Finally, in the third stage, the calibrated supernovae are applied to galaxies in the smooth Hubble flow. This provides a way to link observations at larger redshifts directly to H_0 (Freedman et al., 2001; Riess et al., 2016; Freedman et al., 2025; Riess et al., 2022). In this way the ladder gives an independent path to the Hubble constant that does not depend on early universe physics.

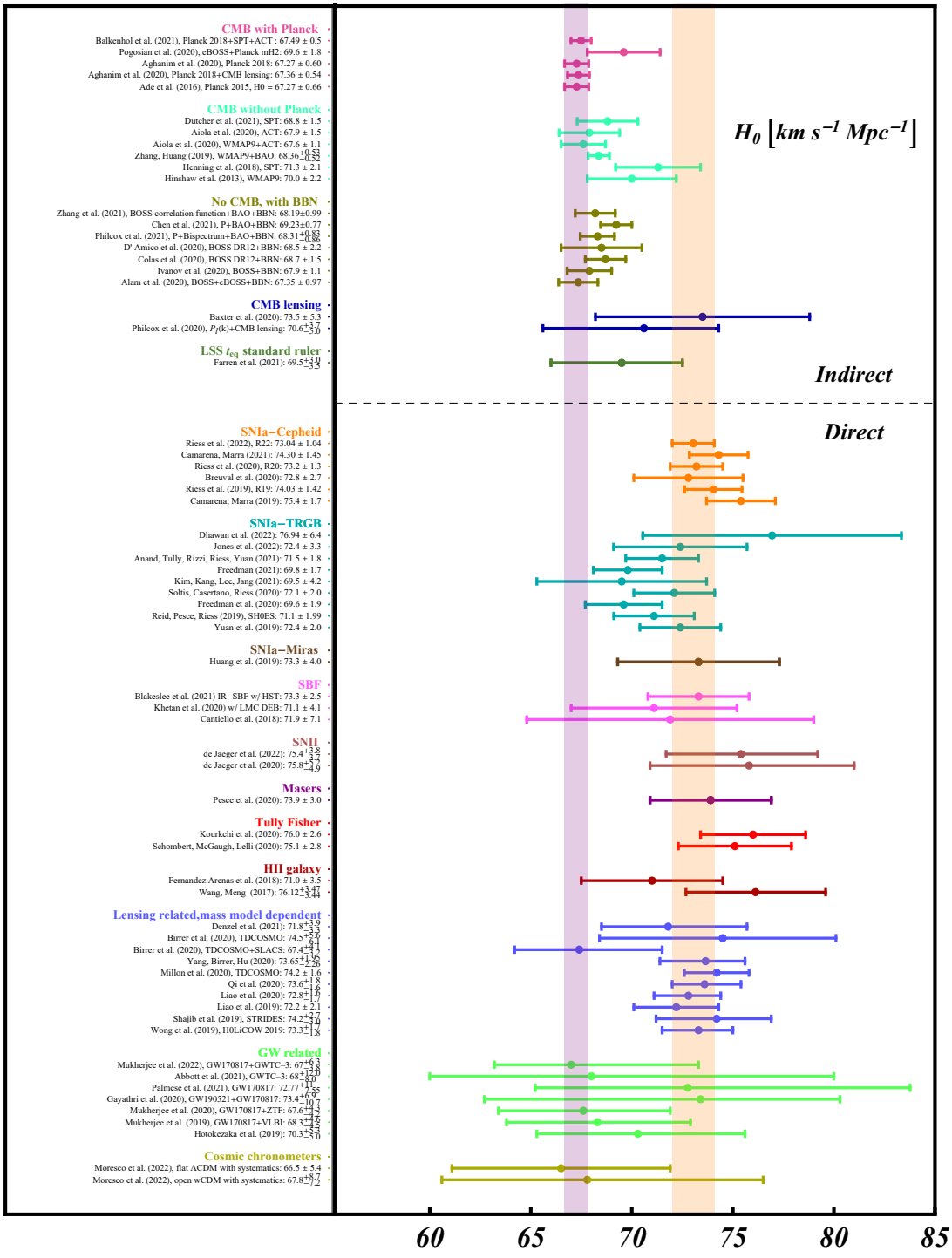

FIGURE 3.1: Illustration of the Hubble tension, adapted from Abdalla et al. 2022.

3.2.1 First Rung: Local Distance Indicators

The lowest step of the distance ladder is built from nearby stellar indicators whose distances can be tied directly to geometric measurements. These form the reference scale for all higher rungs and are generally applicable within ∼10 Mpc. The main classes of indicators include:

- **Cepheid Variables** Cepheids are pulsating supergiant stars whose light output changes regularly with time. Their intrinsic luminosity is linked to the pulsation period and chemical composition through the Period–Luminosity–Metallicity (PLZ) law:

$$M_\lambda = a_\lambda \log P + b_\lambda + c_\lambda [\mathrm{Fe/H}] + d_\lambda. \tag{3.1}$$

  The metallicity index is defined as

$$[\mathrm{Fe/H}] = \log_{10}\left(\frac{N_{\mathrm{Fe}}}{N_{\mathrm{H}}}\right)_{\mathrm{star}} - \log_{10}\left(\frac{N_{\mathrm{Fe}}}{N_{\mathrm{H}}}\right)_{\odot}. \tag{3.2}$$

- **Tip of the Red Giant Branch (TRGB):** When low-mass stars climb the red giant branch and ignite helium in their cores, they show a sharp cutoff in brightness. This feature, visible in the I-band luminosity function, provides a stable reference. It is commonly expressed as:

$$M_I^{\mathrm{TRGB}} = a\,[\mathrm{Fe/H}] + b, \tag{3.3}$$

  with a and b determined empirically (Freedman et al., 2020a,b). TRGB distances are particularly valuable because they are less sensitive to dust and chemical abundance compared with Cepheids.

- **Mira Variables** Miras are long-period stars on the asymptotic giant branch. In the near-infrared, their brightness correlates tightly with pulsation period via:

$$M_K = a \log P + b, \tag{3.4}$$

where M_K is the absolute K-band magnitude (Huang, 2024). Their strong infrared emission makes them effective distance tracers, especially in galaxies that lack Cepheids.

- **JAGB Stars (J-band Asymptotic Giant Branch)** A subset of carbon-rich AGB stars has an almost uniform luminosity in the J-band, approximated by:

$$M_J \approx \text{constant}. \tag{3.5}$$

These stars stand out clearly in near-infrared color–magnitude diagrams, are bright, and are relatively unaffected by dust, making them useful complementary indicators (Madore and Freedman, 2020).

The calibration of all the methods in rung 1 uses a few highly reliable geometric distance anchors. These include parallaxes from the *Gaia* mission, water maser measurements in the galaxy NGC 4258, and eclipsing binaries in the Large Magellanic Cloud. With these anchors providing the absolute scale, the first rung establishes the foundation on which the rest of the cosmic distance ladder is constructed.

3.2.2 Second Rung: Type Ia Supernovae

For this we find a galaxy containing the first rung source and supernova 1a. The role of the second rung is to calibrate the absolute magnitude of type Ia supernovae (SNe Ia) by using calibrated first rung. All supernova does not have same

peak brightness but their variation can be well predicted using Phillips relation. Observationally, supernovae that are intrinsically brighter decline more slowly after maximum light, producing broader light curves, while fainter events fade more rapidly. This correlation allows astronomers to correct for brightness differences and use SNe Ia as standardized candles for distance measurements (Phillips, 1993).

In practice, the observed peak magnitude m_B is standardized via Tripp relation (Tripp, 1998)

$$m_{B,\mathrm{corr}} \;=\; m_B \;+\; \alpha\, x_1 \;-\; \beta\, c\,, \tag{3.6}$$

where x_1 is the stretch (light-curve width) and c is the color; α and β are determined from global fits to supernova samples.

To set the absolute luminosity scale, one uses nearby galaxies that host both a SN Ia and a first-rung distance indicator (Cepheids, TRGB, Miras, or JAGB). If the host has distance modulus μ_{host}, the standardized absolute magnitude is

$$M_B \;=\; m_{B,\mathrm{corr}} \;-\; \mu_{\mathrm{host}}\,. \tag{3.7}$$

This calibration fixes the intrinsic luminosity of standardized SNe Ia and prepares them for use at much larger distances

3.2.3 Third Rung: Hubble-Flow Supernovae

The purpose of the third rung is to transform the calibrated luminosity of SNe Ia into a direct measurement of the Hubble constant. From rung 2 we have already established the standardized absolute magnitude M_B. For each Hubble-flow SN Ia, the two directly measured observables are the corrected apparent magnitude $m_{B,\mathrm{corr}}$ and the redshift z.

$$m^{\mathrm{th}}(z) \;=\; M_B \;+\; 5\log_{10}\!\left[cz\left(1+\tfrac{1-q_0}{2}z\right)\right] \;+\; 5\log_{10}\!\left(\frac{c/H_0}{1\,\mathrm{Mpc}}\right) \;+\; 25, \tag{3.8}$$

where q_0 is the deceleration parameter.

In this framework, M_B fixes the intrinsic luminosity scale (from Rung 2), while $m_{B,\mathrm{corr}}$ and z are measured for each supernova. The only free parameter that vertically shifts the magnitude–redshift relation is H_0. By fitting the observed magnitudes $m_{B,\mathrm{corr}}$ as a function of z to the model $m^{\mathrm{th}}(z)$ in equation (3.8), one extracts H_0 with high statistical precision. By using equation 3.8, there are two ways to estimate hubble constant either for fixed q_0 (Riess et al., 2021) or by simultaneously fitting q_0 and Hubble constant (Camarena and Marra, 2021). Because SNe Ia remain visible to hundreds of megaparsecs, this rung extends far beyond Cepheids or TRGB stars

.

3.3 One-Step (Direct) Methods

The distance ladder depends on several layers of calibration, each building on the previous one. Direct, or one-step, methods take a different route: they try to measure the Hubble constant in a single step. These methods rely on physical systems whose geometry or dynamics can be modeled well enough to give either an absolute distance or a fixed length scale. The appeal is that they do not rely on nearby stellar populations. The downside is that the objects are rare and the measurements often noisier, so the statistical errors are larger. Even so, they provide an important independent check on the distance ladder. The most widely used examples are outlined below.

- **Time Delays in Strong Lenses:** A massive foreground galaxy can bend the light of a background quasar to form multiple images. Because each image follows a different path through the lens and experiences a different gravitational potential, the light does not arrive simultaneously. The observed delay between two images, Δt_{AB}, is expressed as

$$\Delta t_{AB} \;=\; \frac{D_{\Delta t}}{c}\,\Delta\phi_{AB}, \tag{3.9}$$

where $\Delta\phi_{AB}$ is the difference in the Fermat potential, c is the speed of light, and $D_{\Delta t}$ is the so-called time-delay distance defined by

$$D_{\Delta t} \;=\; (1+z_d)\,\frac{D_d\,D_s}{D_{ds}}, \tag{3.10}$$

with z_d the lens redshift and D_d, D_s, and D_{ds} the angular-diameter distances to the lens, to the source, and between them. These angular-diameter distances depend on the cosmological expansion history, and therefore on the Hubble constant. By measuring the delays and modeling the lens potential, one can estimate H_0. Such analyses have been successfully demonstrated by collaborations including H0LiCOW and TDCOSMO (Birrer et al., 2020; Millon et al., 2020).

- **Megamasers:** Water megamasers are luminous maser sources located in the accretion disks of some active galactic nuclei. Their emission at 22 GHz arises from molecules orbiting the central supermassive black hole. Using very long baseline interferometry (VLBI), both the sky positions of the maser spots and their line-of-sight velocities can be measured. The orbital motion follows Kepler's law,

$$v^2 \;=\; \frac{GM}{r}, \tag{3.11}$$

where v is the orbital velocity, r the orbital radius, and M the central mass. The angular separation θ of the maser spots gives the apparent size of the disk. By combining the physical size from Kepler's law with the angular size, one obtains the distance D to the galaxy through

$$r = \theta D. \tag{3.12}$$

With the recession velocity of the galaxy, v_H, corrected for local motions, the Hubble constant follows directly as

$$H_0 = \frac{v_H}{D}. \tag{3.13}$$

This method estimate the H_0, independent of both the cosmic distance ladder and the CMB sound horizon (Gao et al., 2016).

- **Cosmic Chronometers:** Massive galaxies that have stopped forming stars can serve as natural clocks for cosmology. If one compares two such galaxies at close redshifts, the small difference in their stellar ages, Δt, can be linked to the corresponding redshift gap, Δz. This gives a direct estimate of the expansion rate at that epoch,

$$H(z) = -\frac{1}{1+z}\frac{\Delta z}{\Delta t}. \tag{3.14}$$

In practice, the method relies on precise stellar population dating, but it has the advantage of measuring $H(z)$ directly without assuming a full cosmological model (Moresco, 2023).

- **Gravitational Waves:** Mergers of compact objects, such as binary neutron stars, emit gravitational waves whose waveform directly reveals the luminosity

distance, d_L. The observed amplitude decreases with distance, so the signal acts as a "standard siren." From the redshift of the host galaxy, one can then obtain the Hubble constant in a single step. This is expressed through Hubble's law,

$$H_0 \approx \frac{cz}{d_L}, \tag{3.15}$$

where c is the speed of light, z is the redshift of the host galaxy, and d_L is the luminosity distance inferred from the gravitational-wave signal. This method bypasses the intermediate calibrations of the distance ladder and provides a direct, physics-based estimate of H_0 (Abbott et al., 2023).

3.4 Early Universe Methods

A complementary route to the Hubble constant looks not at nearby galaxies but at relics from the early universe. Here the relevant ruler is the sound horizon, the maximum distance acoustic waves in the photon–baryon fluid could travel before recombination. Two main probes are used: the cosmic microwave background (CMB) and baryon acoustic oscillations (BAO). Both rely on the ΛCDM model, but within that framework they deliver extremely precise values for H_0.

- **CMB Sound Horizon:** Prior to decoupling, photons and baryons oscillated together, producing a characteristic scale

$$r_s = \int_{z_{\rm rec}}^{\infty} \frac{c_s(z)}{H(z)}\, dz, \tag{3.16}$$

where c_s is the sound speed. This length is observed through the angular size of the first acoustic peak in the CMB,

$$\theta_s = \frac{r_s}{D_A(z_{\rm rec})}, \tag{3.17}$$

with $D_A(z_{\rm rec})$ the angular diameter distance to the surface of last scattering. Measurements from Planck space telescope determine θ_s with exquisite accuracy, giving $H_0 \simeq 67.4 \pm 0.5$ km/s/Mpc (Planck Collaboration et al., 2020).

- **Baryon Acoustic Oscillations (BAO):** The same acoustic physics also leaves an imprint on the clustering of galaxies at lower redshifts, visible as a preferred separation scale (the BAO feature). It is commonly expressed through the ratio of a distance measure $D_V(z)$ to the sound horizon r_s,

$$\frac{D_V(z)}{r_s} = \left[(1+z)^2 D_A^2(z)\,\frac{cz}{H(z)}\right]^{1/3}\frac{1}{r_s}, \tag{3.18}$$

where $D_V(z)$ combines transverse and radial distances. Since r_s is fixed by early universe physics, BAO measurements provide geometric distance information that, when combined with a cosmological model, can be extrapolated to $z = 0$ to give the present-day expansion rate H_0 (Aubourg et al., 2015). Current BAO results are most robust at intermediate redshifts ($0.2 \lesssim z \lesssim 2$).

3.5 Continuum Reverberation Mapping Framework for H_0 Estimation

This section outlines the methodology used to estimate the Hubble constant by modelling continuum reverberation mapping. As an example, I consider the observed lag spectrum and spectral energy distribution (SED) of the source

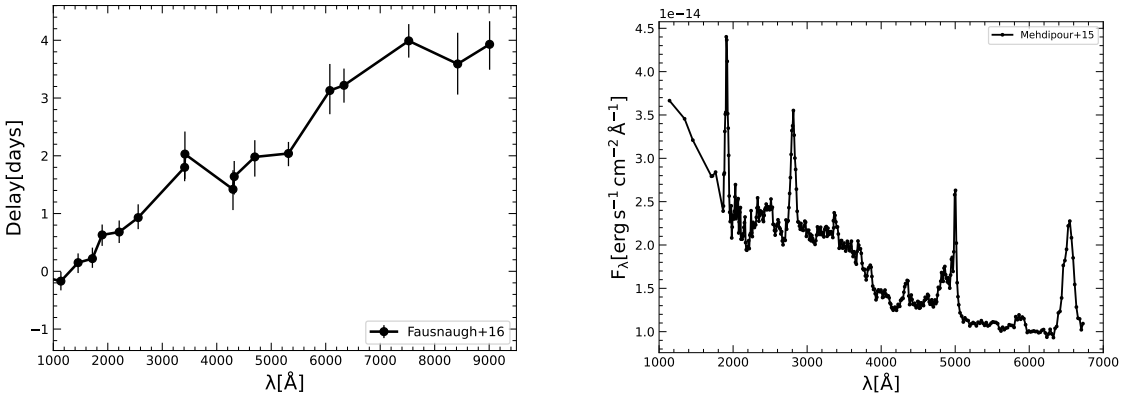

FIGURE 3.2: Two-panel illustration of the observed lag spectrum (left)(Fausnaugh et al. (2016)) and SED (right)(Mehdipour et al. (2015)) for NGC 5548.

NGC 5548, shown in figure 3.2. Although the procedure can be broken into four steps in principle, my analysis follows a three-step modelling sequence, with the final step used to estimate H_0.

3.5.1 Step 1:: Disk-only delays

As described in section 2.5, the starting point is the lamp-post model, which provides the accretion-disk response function. From this, I calculate the expected time delay as a function of wavelength, under the assumption that the lag originates solely from the disk. For the spectral energy distribution (SED), I estimate the energy contribution in each band from disk emission alone. The corresponding fits to the lag and SED are shown in red in figure 3.3. It is immediately evident that the disk-only model fails to fully reproduce either the lag spectrum or the SED.

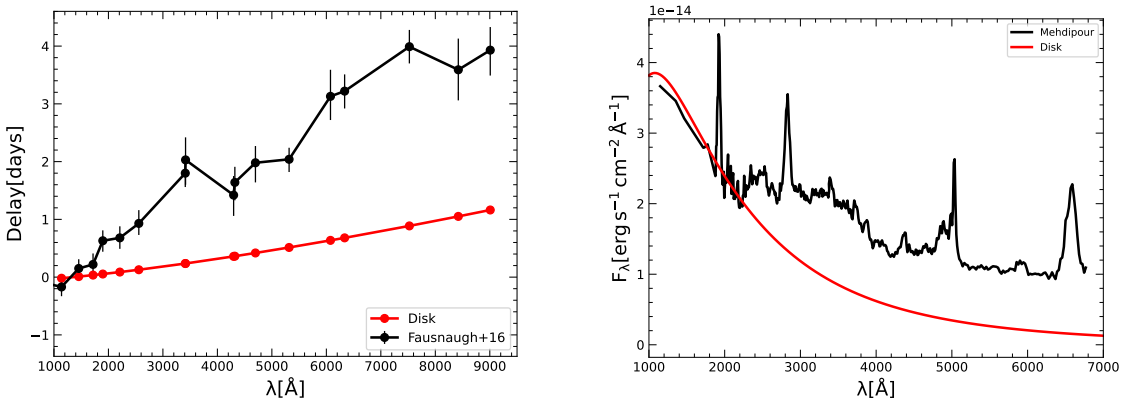

FIGURE 3.3: Model fits for the disk-only case: lag spectrum (left) and spectral energy distribution (SED, right).

3.5.2 Step 2:: Disk + BLR Lag Distribution in FRADO

The second step introduces the role of the broad-line region (BLR). Not all photons from the accretion disk reach the observer directly: a fraction is intercepted by BLR clouds. The purpose of the BLR response function is solely to introduce an additional delay through reprocessing, as some photons first travel to the BLR before reaching the observer. The effect is an extra lag component superimposed on the disk response, producing a secondary peak in the total response function that appears later in time. In paper-1, it was described as Gaussian or half Gaussian but in paper-2 more advanced method is use.

To describe this process, we employ the FRADO framework, which predicts the spatial distribution and trajectories of BLR clouds from global AGN parameters such as black hole mass and accretion rate (Czerny and Hryniewicz, 2011; Naddaf et al., 2021). From the FRADO cloud distribution, we calculate the light-travel delays associated with individual clouds and combine them to form a lag distribution, or BLR response function. This function, therefore, captures only the timing signature of the BLR as a whole.

$$\psi(\lambda, t) = (1 - f_{\rm BLR})\, \psi_d(\lambda, t) + f_{\rm BLR} \int_{t_0}^{t_{\rm max}} \psi_d(\lambda, t - t')\, \psi_{\rm BLR}(t')\, dt' \tag{3.19}$$

where:

- $\psi(\lambda, t)$: total response function at wavelength λ and time t,
- $\psi_d(\lambda, t)$: disk response function,
- $\psi_{\rm BLR}(t')$: BLR response function as a function of delay time t',
- $f_{\rm BLR}$: fractional contribution of BLR

Using equation 3.19, we convolve the FRADO based BLR response with the disk response which yields a total response profile that includes a tunable BLR contribution ($f_{\rm BLR}$) representing covering factor. As shown in figure 3.4, incorporating the BLR in this way improves the agreement between the model and the observed lag spectrum, particularly at longer wavelengths where the disk-only model falls short but still fails to reproduce the lag in 2000–4000 range. Also, this step does not alter the shape of the spectral energy distribution, as the BLR contribution here only introduces extra delays for a fraction of the disk photons. To refine the model further, we need to introduce a wavelength-dependent weighting of the BLR response, which is provided in the next step by incorporating the emission spectrum predicted with CLOUDY.

3.5.3 Step 3:: Disk + Full BLR Contribution (FRADO + CLOUDY)

$$\psi(\lambda, t) = (1 - f_{\rm BLR})\, \psi_d(\lambda, t) + f_{\rm BLR}\, \epsilon(\lambda) \int_{t_0}^{t_{\rm max}} \psi_d(\lambda, t - t')\, \psi_{\rm BLR}(t')\, dt' \tag{3.20}$$

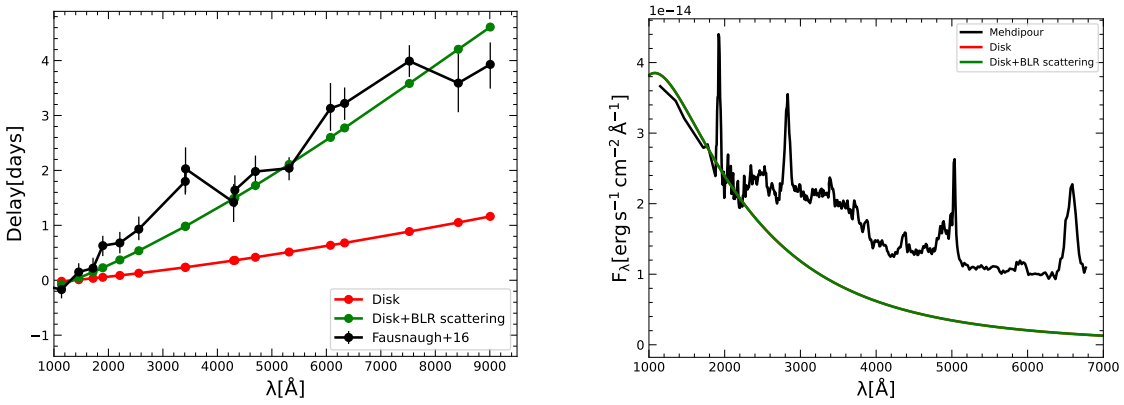

FIGURE 3.4: Fits to the lag spectrum (left) and spectral energy distribution (SED, right) for the disk plus Broad-Line Region (BLR) reprocessing model.

The third step introduces the spectral contribution of the BLR in addition to its timing signature. To do that, we select a representative cloud for which the radiative transfer is calculated with CLOUDY code (Chatzikos et al., 2023). This gives us the spectral shape of the BLR emission which is encoded as $\epsilon(\lambda)$. Comparing the total response function in equation 3.19 and equation 3.20, the key difference is the presence of the factor $\epsilon(\lambda)$, which encodes the wavelength-dependent emissivity of the BLR. This key difference will control the magnitude of second peak based on wavelength in response function as shown in figure 2.7. While FRADO provides the geometry and timing distribution of the clouds, it does not predict their detailed emission spectrum. For this, we rely on the photoionization code CLOUDY.

Given the incident radiation from the central source and the physical conditions of the BLR gas—such as density, column density, metallicity, and distance—CLOUDY self-consistently computes the emergent spectrum. This includes both continuum and line emission, capturing characteristic features such as the Balmer and Paschen jumps, diffuse recombination continua, and strong hydrogen lines like Hβ. In principle, the radiative transfer should be calculated for many clouds but it was beyond the scope of the project.

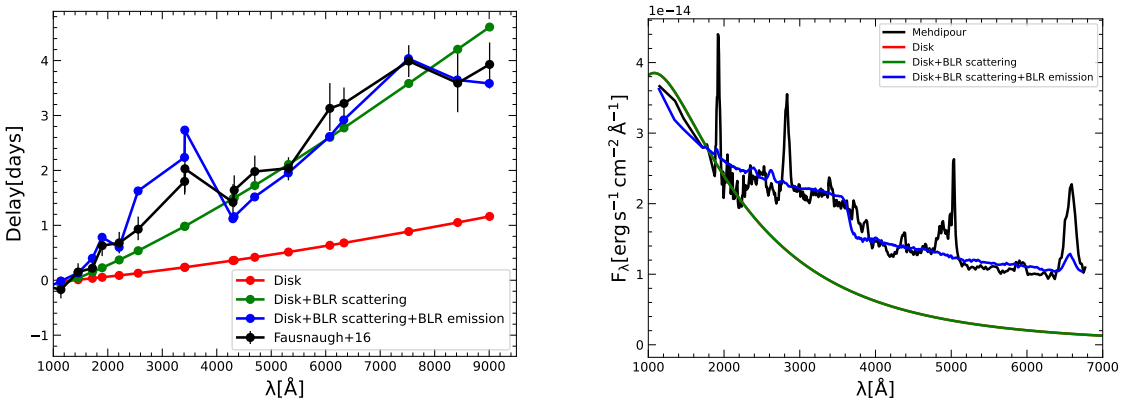

FIGURE 3.5: Lag spectrum (left) and spectral energy distribution (SED, right) for the final model, which combines disk emission, BLR reprocessing based on the FRADO framework, and the full emission profile (lines and diffuse continuum) calculated using CLOUDY.

By combining the intrinsic disk emission, the BLR timing contribution predicted by FRADO, and the wavelength-dependent emissivity from CLOUDY, we obtain a model that simultaneously reproduces the observed lag spectrum and the spectral energy distribution, As shown in figure 3.5. At this stage, the agreement with the data improves significantly: the lag spectrum is matched across the optical and UV bands, and the SED now exhibits the characteristic BLR-induced features that were previously missing. This integrated approach demonstrates that both the timing and the spectral properties of the BLR must be included for a realistic description of continuum reverberation. In the final fits, we also account for the host-galaxy starlight and the contribution of the warm corona to ensure a complete representation of the observed spectrum.

3.5.4 Step 4:: Estimating the Hubble constant

In the three steps above, we outlined how the contributions from the disk and BLR are incorporated so that both the lag spectrum and the SED can be fitted

simultaneously. The final step is to estimate the Hubble constant. For this purpose, the model parameters are divided into two groups: fixed and free (see table 1 in chapter 5). Fixed parameters are those that can be constrained directly from observations, such as the black hole mass, while free parameters are those that must be varied to obtain an optimal fit.

The redshift of a source can be determined from emission line, preferentially from NLR. Once the redshift is known, the luminosity distance can be calculated within the standard ΛCDM cosmological framework. This distance serves as the reference, or canonical, distance. Combining this reference distance with the observed flux then allows us to infer the intrinsic luminosity of the source. However, we do not use this distance and luminosity directly in the fitting procedure. Instead, we use them to rescale the intrinsic luminosity for different trial luminosity distances according to the relation eq. 3.21.

$$\frac{L_{\rm ref}}{D^2_{\rm ref}} = \frac{L_{\rm new}}{D^2_{\rm new}}, \tag{3.21}$$

where $L_{\rm ref}$ and $D_{\rm ref}$ are the intrinsic luminosity and luminosity distance at the reference redshift, and $L_{\rm new}$ and $D_{\rm new}$ are the corresponding values for the trial luminosity distance.

For our simulations, we run the model over a grid of assumed luminosity distances: 50, 54, 58, 62, 66, 70, 74, 78, 82, 86, 90, 94, 98, and 102 Mpc. For each distance, we compute the corresponding intrinsic luminosity and prepare an input file containing both the fixed and free parameters.

The code is first run with the prepared input, which produces the model lag profile and SED. It also reports χ^2 values separately for the lag, for the SED, and for the total combined χ^2. After this initial step, one of the free parameters is adjusted—say the accretion rate—by testing both a slightly larger and a

slightly smaller value. The same is done for other parameters, such as the height of the corona. Each new run gives updated χ^2 values, and the parameter set with the lowest value is carried forward. This cycle continues until further changes no longer improve the fit, which we take as a sign that the solution has converged for that assumed luminosity distance.

The whole process is carried out for every trial luminosity distance. Each distance yields a "best" fit, though not all are equally successful. For instance, as shown figure A.1 and A.2, at 50 Mpc the SED is fitted well but the lag is not, while at 102 Mpc the lag is acceptable but the SED fit is poor. To decide which solution is preferred, we rely on the combined χ^2, which balances both constraints. For NGC 5548, the minimum combined χ^2 is obtained at 74 Mpc, corresponding to a Hubble constant of about $H_0 \approx 66.8\ \mathrm{km\,s^{-1}\,Mpc^{-1}}$.

Chapter 4

Paper-1

4.1 Introduction

This chapter focuses at how time delays in UV/optical continuum of active galactic nuclei (AGNs) vary with wavelength. We estimated the lags using lamp-post model through two methods: by response function calculations and by light curve simulation. To simulate real conditions, scattering from the broad line region (BLR) is also considered. Including the BLR contribution not only lengthens the overall observed lag but also alters the delay pattern. Interestingly, the effect of BLR scattering can resemble what would be seen if the X-ray source were positioned higher above the black hole These results emphasize that BLR scattering must be taken into account in continuum reverberation mapping of AGNs. Doing so is essential both for understanding the physics of accretion and for improving the use of AGNs as distance indicators.

A&A 670, A147 (2023)
https://doi.org/10.1051/0004-6361/202244352

Astronomy & Astrophysics

Modeling time delays from two reprocessors in active galactic nuclei

Vikram Kumar Jaiswal[1], Raj Prince[1], Swayamtrupta Panda[2,1,⋆], and Bożena Czerny[1]

[1] Center for Theoretical Physics, Polish Academy of Sciences, Al. Lotników 32/46, 02-668 Warsaw, Poland
e-mail: vkj005@gmail.com
[2] Laboratório Nacional de Astrofísica – MCTIC, R. dos Estados Unidos, 154 – Nações, Itajubá, MG 37504-364, Brazil

Received 24 June 2022 / Accepted 20 December 2022

ABSTRACT

Context. Continuum time delays from accretion disks in active galactic nuclei (AGNs) have long been proposed as a tool for measuring distances to monitored sources. However, the method faces serious problems as a number of effects must be taken into account, including the contribution from the broad line region (BLR).
Aims. In this paper, we model the expected time delays when both the disk reprocessing of the incident X-ray flux and further reprocessing by the BLR are included, with the aim to see whether the two effects can be disentangled.
Methods. We used a simple response function for the accretion disk, without relativistic effects, and we used a parametric description to account for the BLR contribution. We included only the scattering of the disk emission by the BLR inter-cloud medium. We also used artificial light curves with one-day samplings to check whether the effects are likely to be seen in real data.
Results. We show that the effect of the BLR scattering on the predicted time delay is very similar to the effect of the rising height of the X-ray source, without any BLR contribution. This brings additional degeneracy for potential applications in the future, when attempting to recover the parameters of the system from the observed time delays in a specific object. Both effects, however, modify the slope of the delay-versus-wavelength curve when plotted in log space, which opens a way to obtaining bare disk time delay needed for cosmology. In addition, when the disk irradiation is strong, the modification of the predicted delay by the BLR scattering and by X-ray source height become considerably different. In this regard, simulations of the expected bias are also presented.

Key words. accretion, accretion disks – quasars: general – galaxies: active

1. Introduction

The standard ΛCDM cosmological model is currently under vigorous discussion and testing via a state-of-the-art approach based on current and upcoming astronomical instruments (Freedman 2017). This global model describes the evolution of the entire Universe, so the measurements of the global model parameters should give the same values independently of how and where they are measured. One such parameter is the current (i.e., at redshift zero) expansion rate of the Universe, the Hubble constant, H_0. However, the local direct measurements based on SN Ia, calibrated predominantly with Cepheid stars, give average values of H_0 of the order of $74\,\mathrm{km\,s^{-1}Mpc^{-1}}$ (e.g., $H_0 = 74.03 \pm 1.42\,\mathrm{km\,s^{-1}Mpc^{-1}}$, Riess et al. 2019; $H_0 = 73.2 \pm 1.3\,\mathrm{km\,s^{-1}\,Mpc^{-1}}$, Riess et al. 2021). At the same time, measurements of the cosmic microwave background (CMB) properties imply $67.4 \pm 0.5\,\mathrm{km\,s^{-1}\,Mpc^{-1}}$ (Planck Collaboration VI 2020) when the standard ΛCDM is used to derive H_0. In the observational cosmology this discrepancy in the Hubble constant is known as Hubble Tension. The detection of Hubble tension suggests a need of different cosmological model to explain the local universe. However, before going into detail of deriving a different cosmological model, we have to be very sure that the tension really exists – hence, a range of different independent methods is required to probe it. A similar tension between the *Planck* results and the local measurements shows up for most (and quite numerous) methods (for the most recent comprehensive review, see Di Valentino et al. 2021, in particular Fig. 1 therein). However, the disagreement is not at all that clear since the systematic errors in each method are difficult to assess.

Therefore, a relatively simple and direct method, which would not require the involvement of the distance ladder would be extremely useful to fix the problem. One such method is the one based on continuum time delays in accretion disks in active galactic nuclei (AGNs), proposed by Collier et al. (1999; see also Oknyanskij 1999 for a torus-based version of the idea). The method is effectively based on measuring the size of the accretion disk at different wavelengths and comparing it with the classical accretion disk model of Shakura & Sunyaev (1973). This comparison, due to a specific scaling of both the monochromatic flux and the effective temperature with the product of the black hole mass and accretion rate (see e.g., Panda et al. 2018), allows us to get the distance to the source directly, from the measured time delay τ between the two wavelengths and the observed monochromatic flux, f_ν, at one of these wavelengths, without any hidden dependence on the black hole mass and accretion rate. The time delay, τ, as predicted by the theory, depends on the wavelength λ as $\tau \propto \lambda^{4/3}$, and the proportionality coefficient is also strictly predicted by the theory. This coefficient contains the observed flux and the distance, thus offering the possibility to obtain the redshift-independent distance to the source knowing the time delays and observed fluxes.

Observational monitoring of several sources confirmed the expected delay pattern (e.g., Collier et al. 1999; Cackett et al. 2007; Pozo Nuñez et al. 2019; Lobban et al. 2020), specifically,

⋆ CNPq Fellow.

A&A 670, A147 (2023)

the proportionality: $\tau \propto \lambda^{4/3}$. However, the observationally determined proportionality constant was frequently deemed as being much too high (by some 40% up to a factor of a few) in comparison with the theory, that is, when the standard cosmology was used (e.g., Collier et al. 1999; Cackett et al. 2007; Lobban et al. 2020; Guo et al. 2022a) and the narrow filters used by Pozo Nuñez et al. (2019) did not help. Some sources have found a good agreement with expectations, particularly if the height of the irradiating source and/or the extended character of the reprocessor are included (Kammoun et al. 2021a); some authors have found a disagreement only at a single wavelength band, close to the Balmer edge (e.g., Edelson et al. 2015; Kammoun et al. 2019; McHardy et al. 2018; Cackett et al. 2018, 2020; Hernández Santisteban et al. 2020). Hints of a considerable problem with regard to the contribution from the more distant reprocessing region, namely, the broad line region (BLR), have appeared (Chelouche et al. 2019). In his most recent paper, Netzer (2022) concluded that (for sources analysed by him) most of the reprocessing actually happens in the BLR region, making a continuum time delay longer than the predicted value from the disk itself. A similar suggestion was made earlier by Lawther et al. (2018) for the case of NGC 5548. If this is true, it is very difficult to disentangle the BLR time delay with the continuum disk time delay – hence, these objects cannot be used for the cosmological purpose. The source of contamination comes, apart from strong emission lines, also from broadband spectral features such as the Fe II pseudo-continuum and the Balmer continuum (Wills et al. 1985). The problems of reconciling the disk size with the standard model also appeared in microlensing studies (Rauch & Blandford 1991; Mosquera et al. 2013), but the presence of the additional reprocessing medium most likely solves this problem as well.

In the present paper, we model the combined reprocessing by two media: an accretion disk and the extended BLR, with the aim to find a way to disentangle efficiently these two effects. Finally, we aim to use these results to reconstruct the disk time delay.

2. Method

We performed a set of numerical simulations that allows us to see whether the adopted geometry for the disk and the BLR region can be recovered in measurements of the time delays. We created artificial light curves to mimic the incident radiation, assumed a set of parameters describing the disk and BLR reprocessing, and, finally, calculated the time delays using interpolated cross-correlation function (ICCF) method to see whether the geometry can be determined and, in particular, the conditions under which the time delay related to the accretion disk alone can be recovered in such simulations.

2.1. Incident light curve simulation

According to the general picture used in the description of the disk reprocessing, we assume that variable X-ray emission is responsible for the variability of the disk emission (Rokaki et al. 1993).

We modeled the lightcurve using the algorithm of Timmer & Koenig (1995; hereafter, the TK method), which is based on the adopted shape of the power spectrum. We modeled the X-ray power spectrum as a broken power law, with two breaks and three slopes. The higher frequency break has been relatively well studied for a number of AGNs. For a given set of source parameters, the relation between the black hole mass, the Eddington rate, and the position of the break is given by McHardy et al. (2006). Older and newer measurements are roughly consistent with this law (e.g., Czerny et al. 1999, 2001; Markowitz 2010). For the slopes, we assumed −2, −1, and 0, respectively. For the lower frequency break, we assumed that its timescale is by a factor of 100 longer than the short timescale break. This is somewhat arbitrary, since the long timescale trends are not well measured. Alternatively, we could use a bending power law as, for example, in Georgakakis et al. (2021). The normalization of the power spectrum is then adjusted to the required level of the source variability. This model is certainly better than a damped random walk (DRW), corresponding to a single break and slopes −2 and 0, proposed by Kelly et al. (2009) for modeling the optical variability of AGNs. As shown by Yu et al. (2022), more advanced models are needed for precise description of quasar variability in Stripe 82. For our purposes, TK method is satisfactory, as it broadens the frequency range in comparison to DRW.

2.2. Accretion disk reprocessing

Our description of the disk reprocessing is relatively simple. For the geometry, we assumed a simple lamppost model that represents the X-ray corona, namely, one that is frequently adopted for the disk reprocessing in compact X-ray binaries and AGNs (e.g., Martocchia & Matt 1996; Miniutti & Fabian 2004; Niedźwiecki et al. 2016), and the disk height is neglected. We do not include general relativity (GR) effects and we assume perfect thermalization of the incident radiation. Once the X-ray photon hits the disk all the radiation get absorbed by the disk which increases the disk temperature locally. Thus, in our model, we do not consider any energy-dependent reflection as in Kammoun et al. (2019) but all the incident emission is absorbed by the disk and gets reprocessed.

The response of the disk to the variable irradiation was recently studied in much more detail by Kammoun et al. (2019, 2021b). Their approach included numerous effects, such as the assumption of the Kerr metric in the description of the disks, full GR treatment of the photon propagation, and energy-dependent reflection of the X-rays by the disk surface. We do not aim to achieve such a detailed approach here. Instead, we adopt the rather simple approach of Shakura & Sunyaev (1973) for the disk and geometrical optics, where a perfect thermalization of the incident X-ray flux is considered. In creating our software, we aim to check qualitatively the effect of the second reprocessor on the measured time delay and we do it not only with the use of the transfer function approach, but also with the use of artificial light curves simulating the data cadence and quality. In such cases, we simply carry out a direct calculation of a sequence of disk reactions to variable irradiation by X-ray flux, where the incident flux can vary with arbitrarily large amplitudes.

Our numerical scheme is thus different from the one used by Kammoun et al. (2019, 2021b). We first set the radial grid covering the accretion disk between $R_{\rm isco}$ and $R_{\rm out}$ by a variable sample size. The radial bin size is quasi-logarithmic, to allow for a proper resolution at the inner parts. Specifically, we define this grid by the following formula, $\mathrm{d}R = 0.085 * (\frac{R}{R_{\rm isco}})^{0.85}$, and for each "$R$," we also increase the grid step in angular (ϕ) direction by $\mathrm{d}\phi = \frac{1.5700}{N_{\rm div}}$. For a given R and ϕ, we calculate the Cartesian (x, y) coordinate in the disk plane, and the surface element, $\mathrm{d}s = R * \mathrm{d}R * \mathrm{d}\phi * R_g * R_g$. The disk height is neglected, that is, we assume $z = 0$. For a given x, y coordinate, we calculate the total delay $\tau_{\rm total}(x, y)$. This delay is the sum of time $\tau_d(r)$ taken by photon to reach the given disk location from corona, located at the height, H, along the symmetry axis to accretion disk, and the

time to reach observer after disk reprocessing, $\tau_{\rm do}(x, y)$. For convenience, we define this last time delay with respect to the plane crossing the equatorial plane at $R_{\rm out}$, $\phi = 0$, and perpendicular to the direction towards the observer. This delay depends on the inclination angle i, the corona height, the position on the accretion disk, and the black hole mass. All the delays are calculated with respect to the photon generated from the corona.

Once we have the total delay $\tau(r)$ for a differential disk elements, we calculate the new temperature from the total flux, F, the sum of flux generated from the non-irradiated disk, and irradiation. We thus used the following expression:

$$F(r, t + \tau_d(r)) = \left(\frac{3GM\dot{M}}{8\pi r^3}\left(1 - \sqrt{\frac{6}{r}}\right)\right) + \left(\frac{L_x(t)h}{4\pi r^3}\right). \quad (1)$$

The local temperature at each moment is calculated from the local flux assuming a blackbody emission:

$$T_{\rm eff}(r, t + \tau_d(r)) = \left[\left(\frac{3GM\dot{M}}{8\pi r^3\sigma_{\rm B}}\left(1 - \sqrt{\frac{6}{r}}\right)\right) + \left(\frac{L_x(t)h}{4\pi r^3\sigma_{\rm B}}\right)\right]^{\frac{1}{4}}, \quad (2)$$

where $\sigma_{\rm B}$ is the Boltzmann constant. We do not include the color correction, which would affect the normalization of the time delay but does not affect the basic trends with the parameters that are the topic of our study. However, the inclusion of the color correction indeed makes all the delays longer, which is critical for actual data fitting.

From Planck's formula, we can generate the entire spectrum for the given differential area only to store it in a photon table, which is a 2D matrix $\mathbf{P}(\mathbf{t}', \lambda)$, using a determined time delay appropriate for the disk position and wavelength. Every flux element of the photon table has a unique delay and a wavelength λ. We chose the values of λ from 1000–10 000 Å for the simulation, using a logarithmic scale grid for selection. The time delay step is either linear or logarithmic, depending on the need.

We assume that the incident light curve is provided with equal bin size, Δt. We treat such a light curve as a histogram, which is a step function with Δt. Thus, the time bin size of the photon table matches the resolution of the incident light curve and the time span must be long enough to cover the duration of the incident lightcurve, $t_{\rm irrad}$. For each incident light curve bin, we include this uncertainty of Δt of the photons arrival when locating the flux contribution into the photon table. We first performed the loop with respect to incident light curve bins for a given location at the disk, and then repeated the process for all the elements of the disk surface, thus creating the lightcurve expected from the irradiated disk, equivalent to:

$$L_{\rm disk}(\lambda, t) = \frac{1}{\Delta_t}\int_{t_{\rm min}}^{t_{\rm irrad}}\int_{S_{\rm disk}} B_\lambda(T_{\rm eff}(r, (t^{'} - \tau_{\rm do}(x, y))))\mathrm{d}s\mathrm{d}t^{'}, \quad (3)$$

for a very dense grid.

We can calculate the response function of the disk, ψ_d, which is a very useful concept if the response of the medium is linear (see e.g., Eq. (9) of Peterson 1993). In this case, we replace the light curve $L_X(t)$ with a very short impulse of duration of one second, and we normalize the result based on the incident bolometric luminosity:

$$\psi_d(t, \lambda) = \frac{1}{\Delta_t L_x}\int_{S_{\rm disk}} B_\lambda(T_{\rm eff}(r(, t^{'} - \tau_{\rm do}(x, y))))\mathrm{d}s. \quad (4)$$

We do not subtract the flux from the non-irradiated disk, since we do not aim to linearize the equation and, in general, $\psi(t, \lambda)$ depends on the parameters, including L_x, which is a function of time. When generating the response function, we used two types of time bins: linear and logarithmic – as the linear time bin failed to capture the smallest delays created by the disk elements close to the black hole.

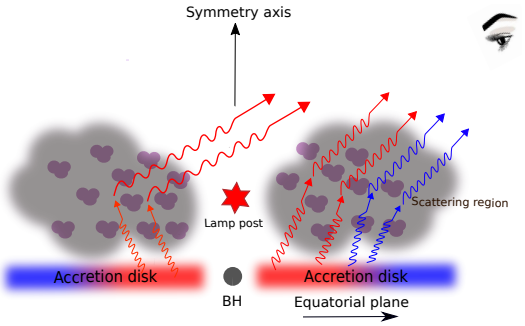

Fig. 1. Geometry of the reprocessing by the extended disk and extended BLR. We include only the scattering from the inter-cloud medium.

To create the disk light curves from the incident X-ray light curves, we generally do not use the concept of response function as defined by Eq. (4), but we calculate the result directly from Eq. (3). In this approach, the amplitude of the irradiating flux can be arbitrarily large in comparison with the locally dissipated radiation flux.

2.3. Second reprocessor

The BLR is a secondary medium responsible for the reprocessing of the irradiating flux (Lawther et al. 2018; Korista & Goad 2019; Chelouche et al. 2019; Netzer 2022). This medium is the source of the emission lines and the emission line time delays have been measured by many authors since many years using the reverberation mapping technique (e.g., Blandford & McKee 1982; Peterson 1988, 1993; Kaspi et al. 2000; Peterson et al. 2004; Bentz et al. 2013; Du et al. 2014; Grier et al. 2017; Martínez-Aldama et al. 2019; Du & Wang 2019; Panda et al. 2019; Zajaček et al. 2021). This process has mostly been modeled and measured as an independent process, neglecting the disk reprocessing. However, as pointed recently by many authors (Korista & Goad 2001, 2019; Netzer 2022; Guo et al. 2022b), BLR is also the source of diffuse continuum, including Balmer continuum and scattering, which also vary – this, together with some level of line contamination affects the measured continuum time delays.

In this paper, we focus on the simplest aspect of the BLR, which is electron scattering of the photons by the inter-cloud BLR medium. Such a process does not imprint any characteristic features as a function of wavelength but can effectively modify the predicted net time delay between the two continuum bands. The schematic illustration of the geometry is shown in Fig. 1. We include this effect through the Thomson scattering approximation. This means that the scattering does not change the photon frequency.

In order to model the scattering effect, we used a simple analytical parametrization of the response of the second reprocessor, $\psi_{\rm BLR}$. There are no simple direct observational determinations of such a response, but we can look for suitable parameters by looking at the measured responses for Hβ lines (e.g., Grier et al. 2013; Xiao et al. 2018; Du et al. 2018) and assume that the

A&A 670, A147 (2023)

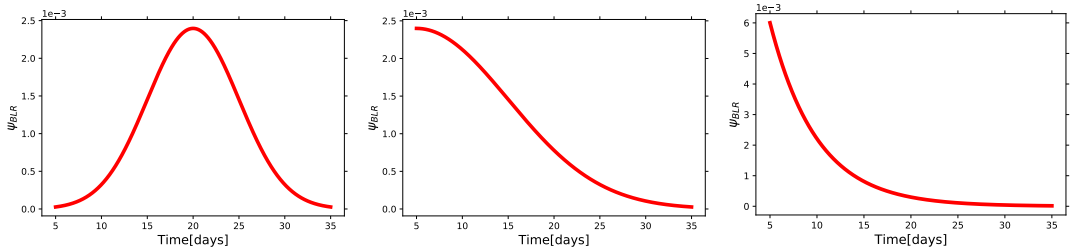

Fig. 2. BLR response function shapes used in this paper. Left panel: full Gaussian ($\tau_{\rm peak}$ = 20 days, σ = 5 days). Middle panel: half-Gaussian ($\tau_{\rm peak}$ = 5 days, σ = 10 days). Right panel: exponential decay ($\tau_{\rm peak}$ = 5, decay rate = 0.1). In all three cases, t_0 = 5 days, $t_{\rm max}$ = 35 days.

inter-cloud medium follows a similar distribution. Thus, for the shape of this function, we assumed one symmetric function in the form of a Gaussian and two asymmetric functions: half-Gaussian and an exponential decay. The peak location of the function in the time axis is given by $T_{\rm peak}$. The non-zero contribution is included starting at a specific time delay t_0 up to $t_{\rm max}$. The width of the Gaussian, σ, or the decay timescale of the exponential ($t_{\rm decay}$) are the parameters of the model. Exemplary shapes are presented in Fig. 2. We assume the same shape of the $\psi_{\rm BLR}$ for all the disk photons, independently from their wavelength and location on the accretion disk.

In the case of the presence of the second reprocessor, we introduce a parameter $f_{\rm BLR}$ which weights the relative contribution from the two regions. The parameter $f_{\rm BLR}$ accounts for the fraction of photons scattered by the inter-cloud medium and introduces an additional time delay. The factor $(1 - f_{\rm BLR})$ represents the fraction of disk photons that reaches the observer without any scattering or additional time delay. In case of $f_{\rm BLR}$ different from zero the total time delay is a combination of two processes: initial delay due to light travel time from the X-ray source to the disk and the extra time delay due to scattering in extended BLR inter-cloud medium.

The assumption of extended BLR medium modeled $\psi_{\rm BLR}$ implies that the final result is a convolution of these two effects:

$$\psi(\lambda, t) = (1 - f_{\rm BLR})\psi_d(\lambda, t) + f_{\rm BLR} \int_{t_0}^{t_{\rm max}} \psi_d(\lambda, t')\psi_{\rm BLR}(t')\mathrm{d}t'. \quad (5)$$

The value of $f_{\rm BLR}$ can vary from 0 (no BLR reprocessing) to 1 (no disk reprocessing). The usually expected value is rather in the range from 0.1 to 0.3, if measured by an estimated solid angle of the BLR. However, fully ionized medium can have a different spatial distribution than the BLR denser clouds.

If we aim to calculate the effect of reprocessing from the long X-ray lightcurve, we apply the response function directly to our photon table $\mathbf{P(t', \lambda)}$, using the same parameter $f_{\rm BLR}$: a fraction of $(1 - f_{\rm BLR})$ remains unchanged and the fraction of $f_{\rm BLR}$ is smeared by $\psi_{\rm BLR}(t)$.

2.4. Time delay measurements

We considered two mathematical approaches to determine the expected time delay. In the first method, we use a single flare event (not a delta function but of final duration of 1 s), we determined the response function by the disk for the corresponding parameters and we eventually added the response function of the second reprocessor. In this case (see Sect. 2.4.1), the whole light curve is not created, so this method is most accurate but does not adequately represent how the time delay is measured in the actual observational data. In the second approach, we created a realistically sampled light curve (incident and in each of the bands), and the time delay is measured using methods comparing the two light curves (see Sect. 2.4.2). Independently from the method, all delays are always measured with respect to the X-ray flare event.

2.4.1. Single-event delay

In the case of a single event, we constructed the standard response function ψ for the accretion disk with the lamp post geometry (see Sect. 2.2), combined it with properly normalized response function from the second reprocessor, and calculated the expected time delay using the formula (Koratkar & Gaskell 1991):

$$\tau(\lambda) = \frac{\int t\psi(t, \lambda)\mathrm{d}t}{\int \psi(t, \lambda)\mathrm{d}t}. \quad (6)$$

Computations in this case require much denser time grids in comparison with the computations for long X-ray light curves (see Sect. 2.2), since the onset of the reprocessed flare has to be well resolved in this case and that happens very close to the black hole.

2.4.2. Realistic light curves

In this case, we simulated the entire incident radiation curve, with realistic sampling, and determined the observed continuum curves at selected wavelengths. Three methods are most frequently adopted: interpolated cross-correlation function, ICCF (Peterson 1993; Sun et al. 2018), JAVELIN (Zu et al. 2011, 2013, 2016), and χ^2 (Czerny et al. 2013; Bao et al. 2022). In the present paper, we concentrate on the first one (ICCF), which brings rather stable results.

2.5. Mkn 110 as a motivation for the adopted parameters in simulations

Complex variability was recently discussed in detail for the source Mkn 110 (Vincentelli et al. 2021). So, in order to put our simulations onto realistic footing, we predominantly focus on parameters well representing this source and the light curve duration and spacing characteristic for this source. Mkn 110 (Markaryan 1969) is a well-studied nearby optically bright, radio-intermediate ($R \approx 1.6$) narrow-line Seyfert 1 galaxy (NLS1s) at a redshift $z = 0.036$ (see e.g., Dasgupta & Rao 2006). As implied by the relativistically broadened X-ray emission line (O VII), the cold, standard disk extends there at least up to 20–100r_g (Reeves et al. 2021) and Fe Kα line study implied

that the cold disk down to $1.24r_g$ is needed (Mantovani et al. 2016), although we note that such a fit was achieved for unlikely inclination of 80 deg. A more recent study of combined data from *XMM-Newton* and *NuSTAR* gave more conservative values of $\sim 20r_g$ (Porquet et al. 2021). The level of polarization in the optical band in this source is low (~0.5%, Afanasiev et al. 2019), but the low polarization does not necessarily imply the low optical depth of the scattering medium (e.g., Śniegowska et al. 2022) and the presence of very highly ionized medium is revealed through the presence of Fe XXVI emission line (Mantovani et al. 2016). The viewing angle is estimated at 18.0 ± 3.1 deg. (Afanasiev et al. 2019). The black hole mass in this source was estimated to be $2\times10^7 M_\odot$ (Bentz & Katz 2015) and also adopted by Vincentelli et al. (2021). Older measurements have claimed a higher value, $1.2 \times 10^8\ M_\odot$, and even larger values has been determined from the recent polarization method, $\log M = 8.32 \pm 0.21\ M_\odot$ (Afanasiev et al. 2019). The source has been monitored with Neil Gehrels Swift Observatory (Gehrels et al. 2004), with a cadence roughly once per day, for about 200 days, and we adopted this setup in our simulations. A detailed disk reverberation is studied by Vincentelli et al. (2021), using good cadence data from Neil Gehrels Swift Observatory and LCO network and they found the variability on two different time scales in Mkn 110. The variability time scale below ten days is mostly consistent with accretion disk reverberation with a maximum two-day lag between the shortest wavelength ($W2$ band) and longest z-band. On the longer time scale they found that the g-band lags the hard X-ray (from BAT) by ten days and a similar lag was also observed between the z- and g-band which is not consistent with the disk reverberation. The author proposed that the longer time scale and higher time delay can be due to the contamination from the diffuse emission of the BLR. Vincentelli et al. (2022) also discussed the effect of X-ray luminosity on the lag spectra. During the low X-ray luminosity state, they do not observe any u-band excess and negative time lag excess as frequently seen in many AGNs. However, at high a X-ray luminosity state, the u-band excess is visible, which is dedicated to the diffuse BLR emission. However, these authors also argue that the excess lag in X-ray can also be explained by moving the corona to farther distances. In the same sense, our study also sees the possibility to disentangle the BLR and corona height contribution in order to explain the disk reverberation.

3. Results

We presents the result of our project aimed at testing the time delay in the presence of the two reprocessors using simulated light curves. This allows us to test under which circumstances, if at all, the time delays from the disk alone can be recovered.

3.1. Response function of the disk and single event delay

We first calculated one example of the response function, that is, the result of the reprocessing of the delta signal from the X-ray lamp by the disk, without any presence from the second reprocessor. Such computations require much denser grids in space and time as specified in Sect. 2.2 to adequately see the onset of the radiation. For this exercise, we used the accretion disk model with the following parameters: $M = 10^8\ M_\odot$, $L/L_{\rm Edd} = 1$, lamp height of $H = 5R_g$, the lamp luminosity of $L_X = 10^{40}\,{\rm erg\,s^{-1}}$, and the viewing angle of $i = 30$ deg. All the delays are calculated with respect to the corona. Although we can generate a response function for any wavelength, we usually store and show

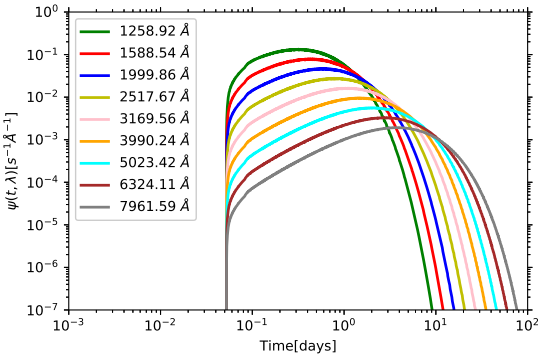

Fig. 3. Response function shapes for the accretion disk at selected wavelengths (see text). Parameters: black hole mass = $10^8\ M_\odot$, Eddington ratio = 1.0, $L_X = 10^{40}\,{\rm erg\,s^{-1}}$, height: $h = 5r_g$, and viewing angle: $i = 30$ degrees.

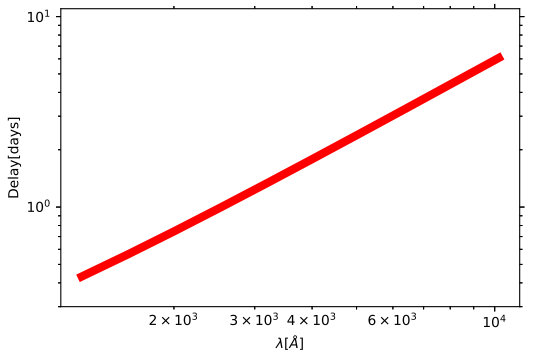

Fig. 4. Time delays calculated from the disk response functions from Fig. 3. Parameters as in Fig. 3.

the response function only for nine values of λ, from 1258.92 Å (response1) to 7961.59 Å (response9), adopting a constant logarithmic step. We show the results in Fig. 3. The overall shape is similar to the responses derived by Kammoun et al. (2021b), although we do not have GR corrections. We comment more quantitatively on this issue in Appendix A.

We calculated the centroid times of all response functions using Eq. (6). The results (see Fig. 4) are consistent with the simple analytic formula of Collier et al. (1999). We also compared the normalization of the best fit $\tau \propto \lambda^{4/3}$ trend with the expectations from Collier et al. (1999). Their formula contains an unspecified factor X which accounts for the peak contribution to the total emission from a given radius through a scaling of $X = hc/(kT\lambda)$, which they estimated to be of the order of 3-4. Our value, derived from numerical computations, gives $X = 2.47$, much lower than the factor suggested by Collier et al. (1999), but higher than the semi-analytical relation ($X = 1.65$) proposed by Siemiginowska & Czerny (1989).

3.2. Response function from two reprocessors and single event delay

We go on to calculate the time delay from Eq. (6) as a function of the wavelength, for a combined disk and BLR effect and for several values of the parameter $f_{\rm BLR}$.

A&A 670, A147 (2023)

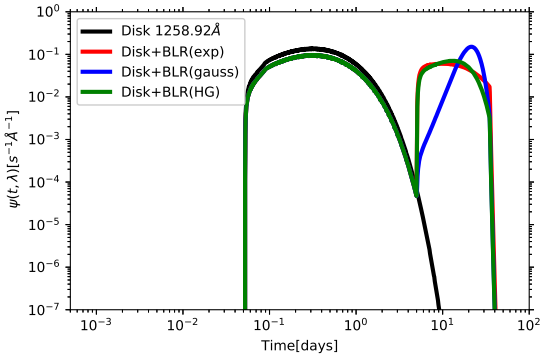

Fig. 5. Comparison between disk response function and disk plus BLR response function for different BLR profiles (Gaussian, half-Gaussian, and exponential; see Fig. 2), and 30% BLR contribution is used. Parameters: black hole mass $10^8\,M_\odot$, Eddington ratio = 1.0, $L_X = 10^{40}$ erg s^{-1}, height $h = 5r_g$, viewing angle $i = 30$ degrees.

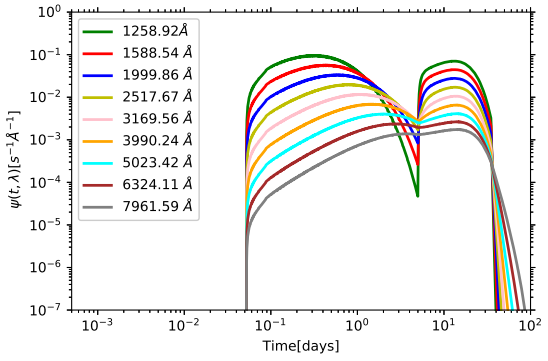

Fig. 6. Combined response function, disk plus BLR, for BLR profile half-Gaussian (see middle panel in Fig. 2) at selected wavelengths. Parameters: black hole mass $10^8\,M_\odot$, Eddington ratio = 1.0, $L_X = 10^{40}$ erg s^{-1}, height $h = 5r_g$, viewing angle $i = 30$ degree, $f_{\rm BLR} = 30\%$.

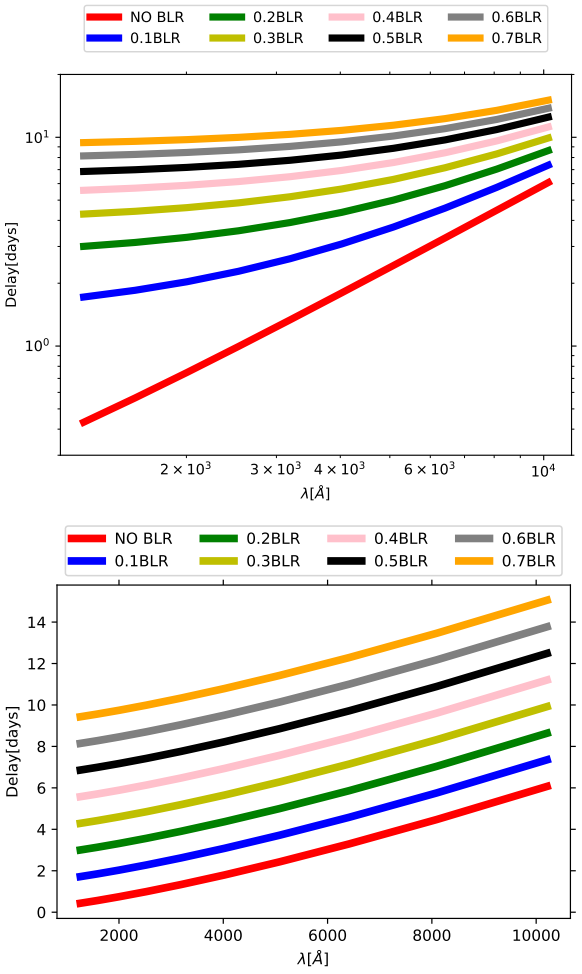

Fig. 7. Delay for all response function with different BLR percentage contribution for BLR profile half-Gaussian (see middle panel in Fig. 2). Upper panel: log scale, lower panel: linear scale. Parameters: black hole mass $10^8\,M_\odot$, Eddington ratio = 1.0, $L_X = 10^{40}$ erg s^{-1}, height $h = 5r_g$, viewing angle $i = 30$ degree.

The exemplary response functions for the two reprocessor setup is shown in Fig. 5. We plot the shape for the shortest wavelength only, but for three shapes of the BLR response illustrated in Fig. 2.

We see that in the two-reprocessor setup, the combined response has two peaks and the shape of the new response depend on the adopted description of the BLR. In Fig. 6, we plot the response functions for representative wavelengths, selecting half-Gaussian (Fig. 2, middle panel) that represents the BLR. We see that the deep valley between the two peaks becomes more shallow when we go towards longer wavelengths and, finally, the two-peak structure disappears. We note that the dependence of the time delay on wavelengths at the longest time delay is not due to wavelength-dependent effect in BLR itself (as we assume Thomson scattering in the inter-cloud medium), but it is due to the fact that those are photons generated at large disk radii, with the delay generated between the X-ray source and their origin and the net effect is a convolution, as given by Eq. (5).

Next, for the same parameters, we calculated the time delays from two reprocessors. The results are shown in Fig. 7. For $f_{\rm BLR} = 0$ the usual $\tau \propto \lambda^{4/3}$ is recovered. Now we add an offset in the Eq. (5), which corresponds to the fraction of BLR. The time delay for different contribution of BLR is estimated and in the linear scale the delays at higher BLR contribution are just shifted with respect to $f_{\rm BLR} = 0$ (lower panel of Fig. 7). However, the result appears to be very interesting when we plot the time delays in log-log space (upper panel of Fig. 7). With increasing $f_{\rm BLR}$, we obtain more shallower relations than the standard one. So, not only does the time delay become longer overall due to the extra scattering in the BLR region, but also the slope of the relation changes. In the extreme case, when the disk contribution becomes small and most of the photons are actually scattered, the delay only weakly depends on the wavelength. However, some dependence on the wavelength would remain even for 100% BLR contribution since the photons (before going on to the observer) are first reprocessed in the disk with a wavelength-dependent delay. It is important to note that the change of the slope is actually seen only if we use log-log plot.

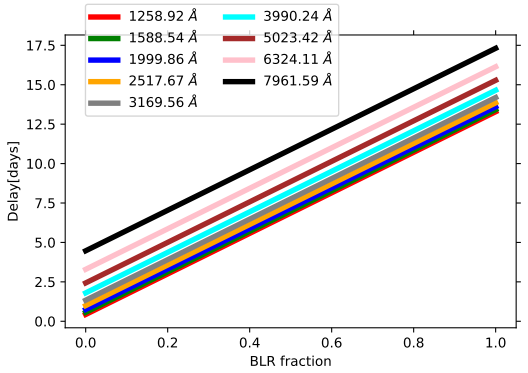

Fig. 8. Time delay as a function of the BLR contribution for exemplary wavelengths. For BLR profile, we used half-Gaussian as shown in the middle panel Fig. 2. Model parameters are as in Fig. 7.

It is also interesting to show the dependence of the time delay at selected wavelengths, but as a function of BLR contribution. Netzer (2022) argued (partially following Lawther et al. 2018) that the delay from two reprocessors is a linear combination of the two time delays (disk and BLR) weighted with the flux contribution. We plot the expectations from our model in Fig. 8. The plot supports the claim of the linear dependence of the time delay on the BLR contribution for all wavelengths if this contribution comes from scattering. The dependence is indeed linear, with the time delay plot shifted up with the increase in the wavelength.

The contribution from the scattering by the inter-cloud medium in BLR can thus easily account for too large disk sizes claimed from the data. In addition, the change of the delay shape shown in Fig. 7 might, in principle, reveal this effect in the data. However, Kammoun et al. (2021a) were able to fit well the observational data for a number of sources at the expense of postulating large height of the illuminating source. Thus, our more general model – which includes the arbitrary lamppost height and arbitrary contamination by the disk photon scattering – might be degenerate with respect to these two parameters and, in the data fitting in the future, we will not be able to discriminate among them. In order to address this problem in advance, in our simulations, we calculated the effect of these two parameters for a range of lamppost source luminosities.

First, we assumed a very faint lamppost of 10^{40} erg s^{-1}, and we repeated the disk delay computations for several height values and compared the results with the expected time delay for small height but with BLR contribution. We see that a change of the lamppost height leads to a flattening of the delay curve, as shown by Kammoun et al. (2021b). In particular, Fig. 18 of their paper shows that the effect is very similar to the introduction of the BLR scattering.

The curvature introduced to the delay curves in low-luminosity case is actually very similar in the case of an increased height or some BLR scattering (see Fig. 9, upper panel). It is a serious source of the degeneracy in the future data fitting, although the relative importance of the two effects depends strongly on the parameters. For example, from our standard model (σ = 10 days, $L_X = 10^{40}$ erg s^{-1}, the contribution of BLR just ~7% gives the same effect as moving the lamp height from 5 to 100R_g, and smaller values of σ further reduce this factor.

Next, we repeated the simulations for the incident X-ray flux to 30% of the disk bolometric luminosity. Such high luminosity

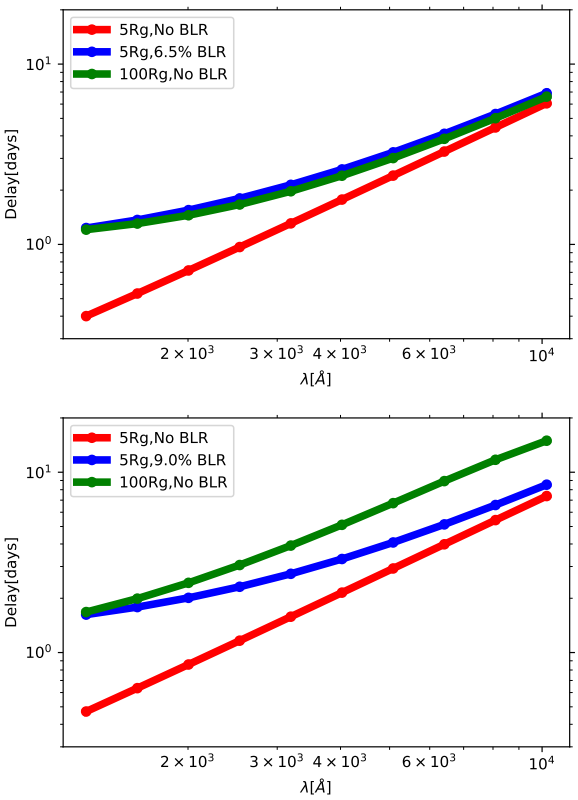

Fig. 9. Time delay as a function of the wavelength for models with different lamppost height and for no BLR and for BLR contribution. For the BLR profile, we used a half-Gaussian, as shown in the middle panel of Fig. 2. Model parameters (top): black hole mass $10^8\,M_\odot$, $L/L_{\rm Edd}$ = 1, inclination angle 30 degree, and luminosity of the corona is 10^{40} erg s^{-1}. Model parameters (bottom): black hole mass $10^8\,M_\odot$, $L/L_{\rm Edd}$ = 1, inclination angle 30 degree, and luminosity of the corona is 3.78×10^{46} erg s^{-1}.

($L_X \sim 3 \times 10^{46}$ erg^{-1}) brings different result: 9% BLR contribution delay is only matched at the smallest wavelength, not at longer wavelengths. Thus, the overall curvature becomes different (see Fig. 9, lower panel), which opens up the possibility to differentiate the effect of the height from the effect of the BLR scattering in the data. This shows that for X-ray-bright sources, we can differentiate between the lamppost height and the BLR contamination if the data is of sufficient quality, but it might be much more difficult for X-ray weak sources.

3.3. Time delays from light curves

In the case of observational data, we do not have a direct insight into the response function; however, some techniques allow us to recover it from the data. The observed light curves depend not only on the system parameters, but also on the sampling, while the measured time delay depends not only on the light curves but on the method to determine the time delay. Therefore, we repeated our experiment from Sects. 3.1 and 3.2, using the long artificial light curves with different adopted power and data sampling. As a standard, we adopted the frequency break timescale of 75 days, sampling of one day, and the ICCF method.

A&A 670, A147 (2023)

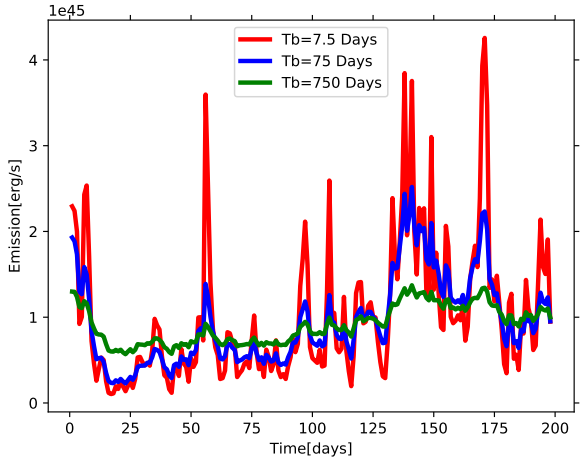

Fig. 10. Different X-ray light curve generated for different breaking time. Red, blue, and green are for breaking times of 7.5 days, 75 days, and 750 days, respectively.

Computations are based on ten statistical realizations of the process, allowing us to show the errors representing the dispersion, namely, a likely error in a single measurement.

3.3.1. Role of the frequency break in the power spectrum in disk time delay measurement

First, again for test purposes, we calculated the examples of X-ray light curves representing different intrinsic timescales assumed in parametrization of the power spectrum. We adopted the time step of one day, duration of 200 days, and the irradiating X-ray lightcurve was calculated as described in Sect. 2.1. We assumed the level of X-ray variability of set by normalized dispersion of 0.3 in the whole light curve of duration of 10^8 s. The examples of the light curve for three values of the high frequency break are shown in Fig. 10. We see that a small value for the timescale corresponding to the frequency break gives much sharper values of the curve peaks and much higher variability amplitude in a period of 200 days (i.e., much shorter than the whole curve duration). All three curves were obtained from the same value of the parameter initializing random generator – for a better comparison.

The X-ray curve seems more smooth when the timescale corresponding to high frequency break is longer, but otherwise, the geometry of the system is not affected. In order to check whether this indeed could affect the measured time delay, we calculated the delay for the three values of the frequency breaks, using ICCF. The results are shown in Fig. 11.

Comparing the time delays obtained from the light curves to the delays calculated directly from the response function (Fig. 4, upper panel), we see that for a black hole mass, $10^8\ M_\odot$, the time delays are relatively well recovered only in the case of a 75-day characteristic time variability (middle panel of Fig. 11). When variability is faster, the numerically calculated time delays are systematically much too short in comparison with expectations. If the variability timescales are longer, the numerical delays are marginally consistent with expectations within an error, but they again locate themselves systematically below the expected values. At the shortest wavelengths, even the optimum variability timescale underestimates the delay, but this is directly caused by

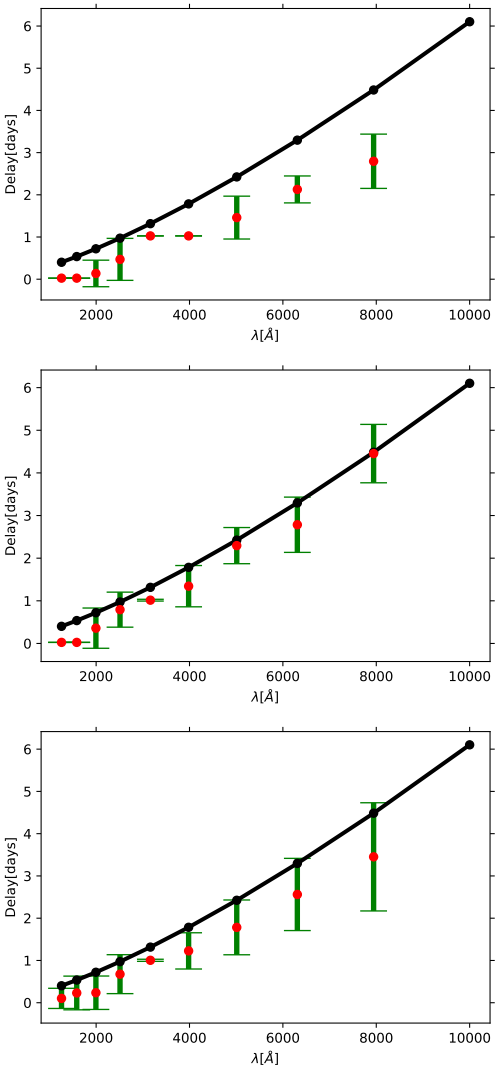

Fig. 11. Time delay as a function of the wavelength calculated with ICCF method from the artificial light curves for the frequency break corresponding to timescales of 7.5 day (upper panel), 75 days (second panel), and 750 days (third panel). Model parameters: black hole mass $10^8\ M_\odot$, Eddington ratio = 1.0, corona height = $5r_g$, inclination angle = 30 degree, and luminosity is on the order of 10^{45} erg s^{-1}. Black points and continuous line represents the delays expected from the disk response function.

the adopted one-day sampling which is not enough to resolve the innermost part of the disk. Increasing the incident X-ray flux to $\sim 3 \times 10^{46}$ erg s^{-1} does not improve the results. We discuss the issue later.

This trend to obtain numerically the time delays which are shorter than expected is rather interesting and potentially important for actual data analysis. The optimum characteristic variability of 75 days is within the duration of the total lightcurve of ~150 days, so characteristic peaks are a few and apparently well sampled. If the actual timescale is much longer than the total observing time, we may have no strong features to rely on for

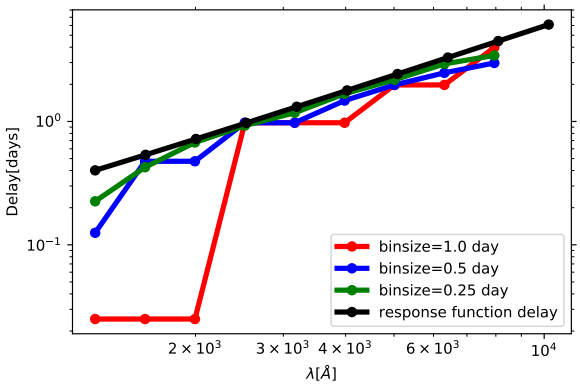

Fig. 12. Time delay as a function of the wavelength calculated with ICCF method from the artificial light curves for different bin size. Black curve is expected delay from the response function. Model parameters: black hole mass $10^8\,M_\odot$, Eddington ratio = 1.0, corona height = $5r_g$, inclination angle = 30 degrees, and luminosity is on the order of 10^{45} erg s^{-1}.

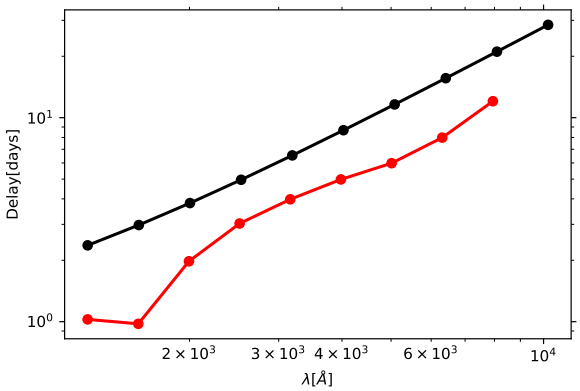

Fig. 13. Time delay from a bare disk as a function of the wavelength calculated with ICCF method from the artificial light curves. Model parameters: black hole mass $10^9\,M_\odot$, Eddington ratio = 1.0, corona height = $5r_g$, inclination angle = 30 degrees, luminosity is of the order of 10^{45} erg s^{-1}, and the frequency break corresponding to 75 days.

time delay measurement. Indeed, if we use the light curves of the duration of 1000 days (again, with a one-day sampling) and the remaining parameters unchanged, the agreement between the numerical results and predictions is much better. Additionally, the asymmetry in the time reprocessing by the disk can also contribute if there are only very few strong peaks in both curves. On the other hand, if the characteristic timescale is much shorter than the total observing run and the sampling rate is not very dense the curve is too noisy. It might thus be recommended to check the characteristic timescale in the data (e.g., using the structure function) and compare it to the derived time delay in order to additionally discuss the potential bias in the time lag determination.

3.3.2. Bin size effect in the disk time delay measurements

As we show in Fig. 11, the prediction of the delays from the simulated light curves systematically underestimate the delay by ∼30% at 4000 Å, and the effect is stronger at the shortest wavelengths.

In order to see whether this is the result of inadequate sampling, we repeated the analysis for just one frequency break corresponding to 75 days, but for an increased data sampling and keeping the total length of the curves unchanged – effectively increasing the number of observational points. The effect is shown in Fig. 12. Indeed, with the denser sampling the numerical light curve time delay was systematically approaching the expected response of the disk. Already, the sampling of 0.5 day was enough to measure well the time delay at 2000 Å and longer wavelengths, for the adopted black hole mass of $10^8\,M_\odot$. The shorter wavelengths ∼1000 Å would require still denser sampling, as even 0.25 of a day would still underestimate the delay almost by a factor of 2.

3.4. Time sampling and the black hole mass

The sampling rate of the lightcurve must be adjusted to the source parameters. Our previous discussion focused on $10^8\,M_\odot$ black hole mass. However, if we increase the black hole mass by a factor of 10, the delays are still not well recovered at the shortest wavelengths as shown in Fig. 13. However, at longer wavelengths, the delay is comparable to the value expectations based on the response function and the slope is well recovered (see Fig. 4). Thus, for a larger mass, a one-day sampling is fully adequate.

3.5. The influence of stochastic approach on time delay with BLR contribution

In the case of the analytical (response function) approach, the presence of the additional scattering in the BLR resulted in a simple shift in the net time delay, as expected previously (e.g., Netzer 2022; Lawther et al. 2018). However, the stochastic light curve approach may not preserve such a simple trend in all parameter range. We selected the timescale break of 75 days, since it was working relatively well for the disk delay, and we adopted a one-day sampling which was adequate at longer wavelengths. The resulting light curves thus become distorted (smoothed and shifted) by the BLR (as illustrated in Fig. 14). Smoothing is clearly stronger when the width of the BLR response function is larger.

We now calculate the time delay using those stochastic curves. We noticed that the numerically calculated time delay does not increase with $f_{\rm BLR}$ up to the critical moment when $f_{\rm BLR}$ crosses (unrealistic) value of 50%. This is in contrast to expectations based on the response function approach. The peak in the combined response function is still due to the disk for smaller values of $f_{\rm BLR}$, which is apparently confusing in terms of the numerical method. We see the same effect for the other values of the width of the Gaussian. It may indicate that in real data analysis, we would actually be recovering the disk delay, independently of the BLR contamination.

However, the symmetric Gaussian shape for the BLR response is unlikely, so we repeated the same analysis for half-Gaussian shape. We found that for half-Gaussian shape the BLR contamination shows more similarity between the time delay predicted by response function and the stochastic prediction, although the determined lags are always below the ones expected from the combined response function.

We finally checked, in a systematic way, how the adopted width of the BLR response function affects the delay. This time

A&A 670, A147 (2023)

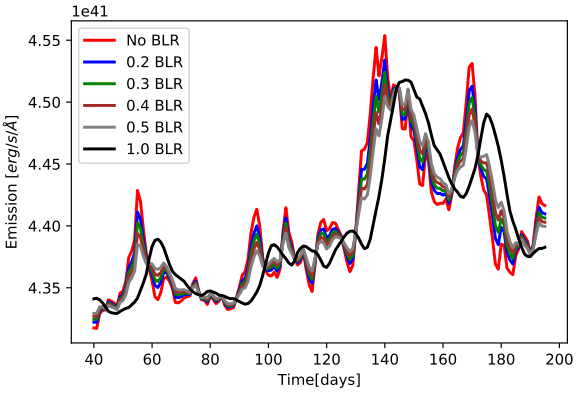

Fig. 14. Light curve for $\lambda = 1258.92$ Å generated for different BLR contribution. We used half-Gaussian for BLR profile $\sigma = 5$ days and we used an X-ray light curve for breaking time 75 days. Parameters: black hole mass $10^8\,M_\odot$, Eddington ratio = 1.0, height: $h = 5r_g$, and viewing angle: $i = 30$ degrees.

we performed ten simulations for each parameter set and the errors mark the dispersion. We illustrate the complex trend in the time delay with the change of the response model for BLR, σ, and $f_{\rm BLR}$ in Fig. 15.

We see that for a Gaussian shape the departure from the linear trend of the rise of the expected delay with the importance of the BLR contamination is strong. But most of the other shapes also predicted similar trend – the initial rise was slower than expected and only after crossing rather unrealistic level of BLR contribution (above 50%), the time delay flipped to values close to the BLR time delay. For example, when the departure between the measured time delay and the linear time delay is determined at 50% of the BLR contribution we see a delay longer by 33.88% (Gaussian), 28.85% (half-Gaussian), 15.01% (half-Gaussian2), 35.03% (half-Gaussian3), 25.62% (half-Gaussian4), and 0.66% (half-Gaussian5). We refer to the caption of Fig. 15 for the model parameters. Thus, no departure is seen for very wide asymmetric BLR response profile while narrow asymmetric or symmetric response show a considerable departure from a linear trend.

We see from the performed simulations that the measured time delay depends on the light curve properties as well as BLR response, and the dispersion in a single measurement is considerable. This means that when an actual reverberation mapping campaign is performed, corresponding to a single realization of our process, some modeling adjusted to the observational setup and source properties is useful for estimating the possibility of the systematic bias in the measured time delays.

4. Discussion

We studied the wavelength-dependent time delay of optical photons originating from the X-ray photons generated in the lamppost geometry above the AGN accretion disk and reprocessed by the surroundings. We included the photon thermalization and re-emission in the accretion disk, but we also allowed for an additional scattering of the generated optical photons by the inter-cloud medium of the BLR. Such a scattering does not change the photon energy but introduces an additional time delay with respect to the arrival of the primary X-ray emission as well as with respect to the unscattered optical photons. We constructed the response functions for the combined effect of the accretion disk and studied the time delays analytically, but we also constructed simulated X-ray light curves and their reprocessing.

The results based on the response function computations give a very smooth dependence on the model parameters. The most interesting result of this study is the modification of the time delay by the rising contribution of BLR scattering. This effect is difficult to distinguish from the effect of rising the height of the lamppost, without postulating any contribution from the BLR. In noticing the difference in the curvature of the time delay pattern is practically impossible even with high-quality data, if the mean incident X-ray flux is small in comparison with the disk bolometric luminosity. On one hand, this degeneracy between the lamppost height and the BLR contribution can account for surprisingly large heights obtained from data fitting. Kammoun et al. (2021a) successfully modeled the time delay in seven nearby AGNs, but the derived height of the lamppost ranged from $11.2R_g$ (for Mkn 509, maximally rotating black hole) to $\sim 75R_g$ for NGC 7469, independently from the spin. This is not consistent with many of the fits of the X-ray spectra that require low lamppost heights to model the relativistically broadened Kα line (e.g., Parker et al. 2014; Jiang et al. 2019; Walton et al. 2021). We have an independent insight into the geometry of the X-ray reprocessing from the measurement of the Kα line delays, and they rise with the black hole mass from ~100 to 1000 s for mass increasing from $10^6\,M_\odot$ to $10^8\,M_\odot$ (Kara et al. 2016); for $10^8\,M_\odot$, this implies a geometrical delay of $\sim 2R_g$. However, in the case of NGC 7469, the Kα line is broad (broadening velocity about 2700 km s^{-1}) but not relativistically distorted (Mehdipour et al. 2015), so it can come from the outer disk and/or BLR, so a large height is not in contradiction with the X-ray spectrum.

High values of the irradiating flux allow us to differentiate the delay curve shape caused by the increase of the lamppost height and by the BLR scattering. The question of whether such high values – namely, up to 30% of the disk bolometric luminosity – are possible is directly related to the question of the origin of the irradiating flux. Hard X-ray emission, as argued by Kubota & Done (2018), contributes less than 2% to the bolometric luminosity of bright AGNs, not containing inner ADAF. On the other hand, soft X-ray excess can contain much higher fraction of the total flux. The lamppost model is more likely to represent better the hard X-ray emission while the geometry of the soft X-ray emission is still under debate, but it is most likely a warm corona (e.g., Czerny et al. 2003; Różańska et al. 2015; Petrucci et al. 2020). However, studies of other geometries besides the lamppost is beyond the scope of the present paper.

In general, a potential data fitting of the time delay faces a number of degeneracies. As demonstrated by Kammoun et al. (2021a), independent information about the black hole mass and accretion rate would reduce it considerably; usually, estimates of the black hole mass, based on line widths, are available. Knowing the monochromatic flux, we can also estimate the accretion rate in a way that only weakly depends on the black hole spin. The viewing angle remains, however, an issue, since the monochromatic flux roughly depends on $\cos(i)$. However, a dusty or molecular torus limits the available viewing angles to between 0 and ~70° (e.g., Prince et al. 2022, and the references therein). The new degeneracy between the lamppost height, H_X, and the BLR contribution, $f_{\rm BLR}$, creates an additional issue. When the height is small and the high-quality X-ray data are available, we can independently estimate its height, but no such estimate is possible if the height is large and the relativistic distortion of the line is not strong.

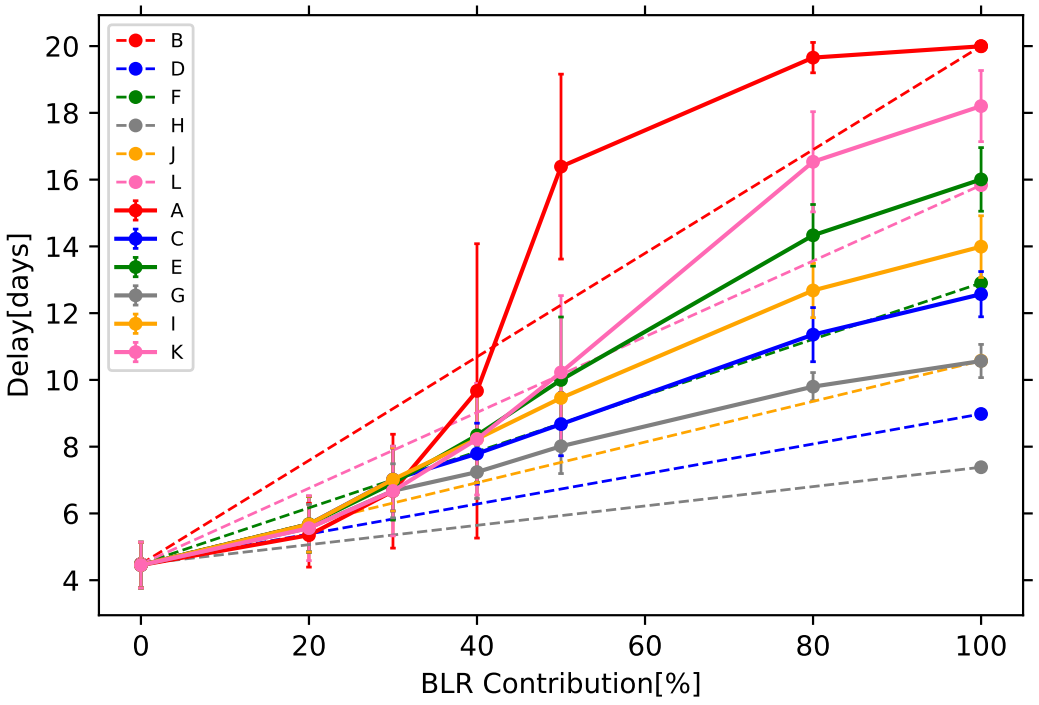

Fig. 15. Time delay as a function of BLR contribution for different BLR response functions. Dashed lines show the linear interpolation between the extreme cases of no BLR contribution to time delay and 100% of disk photons reprocessed by the BLR. Points show the intermediate delays calculated from stochastic light curves using ICCF between X-ray light curve and 7961.59 Å for different shapes of the BLR transfer function: A = Gaussian (τ_{peak} = 20, σ = 5); C = half-Gaussian (τ_{peak} = 5, σ = 5); E = half-Gaussian2 (τ_{peak} = 5, σ = 10); G = half-Gaussian3 (τ_{peak} = 5, σ = 3); K = half-Gaussian4 (τ_{peak} = 5, σ = 7); and I = half-Gaussian5 (τ_{peak} = 5, σ = 15). All values of τ_{peak} and σ given in days. Solid lines show the ICCF delay measured between X-ray light curve and 7961.59 Å light curve by varying the BLR contribution using different BLR response function (B = Gaussian, D = half-Gaussian, F = half-Gaussian2, H = half-Gaussian3, J = half-Gaussian4, and L = half-Gaussian5). All data points are summarized in Table 1.

Table 1. Simulated time lags for various shapes of response function and with different BLR contributions.

ψ_{BLR}	f_{BLR} = 0 (%)		f_{BLR} = 20 (%)		f_{BLR} = 30 (%)		f_{BLR} = 40 (%)		f_{BLR} = 50 (%)		f_{BLR} = 80 (%)		f_{BLR} = 100 (%)	
	τ	$\Delta\tau$	τ	$\Delta\tau$	τ	$\Delta\tau$	τ	$\Delta\tau$	τ	$\Delta\tau$	τ	$\Delta\tau$	τ	$\Delta\tau$
Gaussian	4.45	0.68	5.34	0.95	6.66	1.70	9.67	4.40	16.38	2.76	19.65	0.45	19.99	0.01
Half-Gaussian	4.45	0.68	5.67	0.83	7.01	0.94	7.79	0.91	8.67	0.94	11.3	0.81	12.5	0.67
Half-Gaussian2	4.45	0.68	5.67	0.83	6.9	1.1	8.34	1.4	9.99	1.88	14.3	0.92	16	0.95
Half-Gaussian3	4.45	0.68	5.56	0.7	6.67	0.8	7.23	0.79	8.01	0.81	9.79	0.42	10.5	0.49
Half-Gaussian4	4.45	0.68	5.67	0.83	7.01	0.94	8.22	1.3	9.45	0.83	12.6	0.81	13.9	0.92
Half-Gaussian5	4.45	0.68	5.55	0.97	6.67	1.34	8.22	1.67	10.2	2.29	16.5	1.5	18.2	1.06

Notes. The corresponding plot is shown in Fig. 15; τ is the delay measured in days between X-ray light curve and 7961.59 Å light curve, and $\Delta\tau$ is error in delay measured in days.

Perhaps, in the future, a more careful modeling of the disk reprocessing plus BLR scattering may help to ease the problem. In our simple code, indeed the effect of the height and the effect of BLR show similar trend for low X-ray luminosity; whereas, in Kammoun et al. (2021b), the disk height results in a convex-shape plot of the time delay versus wavelength, while in our simple model the pattern is concave both for height and BLR contribution. We think that the shape should actually be concave, and the convex shape results from too small outer radius adopted in the computations (see Appendix A). Repeating the calculations of the disk plus BLR scattering using full GR, X-ray reflection, and color correction to the temperature may reveal a systematic difference in the system reaction to these two parameters. In this case, the data fitting should not be done just using a power law part of the delay curve, as in Kammoun et al. (2021a), but the fits should include the full wavelength-dependent model with the curvature. Also, studies of the same source at different flux levels are very helpful in disentangling the lamp height and BLR effect, as argued by Vincentelli et al. (2022).

In the present study, we did not include the re-emission by the BLR clouds. Such emission has clear spectral signatures,

including the prominent Balmer edge (Lawther et al. 2018; Korista & Goad 2019; Chelouche et al. 2019; Netzer 2022). This effect is also important but, in principle, it is easier to include it later (in the data fitting), since the prominent Balmer edge should fit the corresponding drop in the time delay. In numerical computations of the reprocessed BLR component with the use of CLOUDY (Ferland et al. 2017) or equivalent code, the effect of scattering is included but only for (usually) constant density clouds, not accounting for the inter-cloud medium. Thus, the scattering effect can be more difficult to disentangle in the real data. Both broad band data, possibly dense in the wavelength (e.g., coming from specially designed narrow-band filter photometry, as used by Pozo Nuñez et al. 2019), but also very dense cadence is essential, as we can see from our experiments with the artificial light curves. Also, the broad wavelength coverage is very important since it allows to determine the shape of the relation more accurately and to improve the disentangling of the contributions from the disk and BLR. Finally, there are two other possible effects that could modify the delay obtained for the disk continuum: the disappearance of the inner cold disk and the disk winds, as argued by Zdziarski et al. (2022) – an insight into this issue could be expected from a fitting of the broadband spectra of the studied objects.

5. Conclusions

The results of our modeling of the X-ray reprocessing by the accretion disk, with the additional scattering of disk photons in the BLR region are as follows:

- For low-irradiating X-ray flux, the lamppost height and BLR contribution through scattering are degenerate;
- For high-irradiating flux, there is a difference in the curvature in delay versus wavelength plot that allows us to distinguish between the two effects – if the wavelength coverage is broad enough;
- The time delay rises linearly with the BLR contribution in the description, which uses the response function;
- When stochastic incident light curves are used, the time delay is aptly recovered only if the time-step of the curve is considerably denser than the characteristic variability timescale (set by the high-frequency break in the power spectrum) and when the total duration of the light curve is much longer than this timescale;
- In numerical stochastic incident light curves, this linear dependence is perturbed and the time delay rise is initially slower than linear, then rising rapidly with the BLR contribution;
- Our modeling shows that the results of the time delay based on a single observational campaign should be supplemented with simulations in order to identify the potential bias in measuring the time delays.

Acknowledgements. We are thankful to Elias Kammoun for helpful discussions, and to the anonymous referee for the comments which helped considerably to improve the manuscript. The project was partially supported by the Polish Funding Agency National Science Centre, project 2017/26/A/ST9/00756 (MAESTRO 9) and MNiSW grant DIR/WK/2018/12. SP acknowledges financial support from the Conselho Nacional de Desenvolvimento Científico e Tecnológico (CNPq) Fellowship (164753/2020-6). This project has received funding from the European Research Council (ERC) under the European Union's Horizon 2020 research and innovation program (grant agreement No. [951549]). RP and BC acknowledge the Czech-Polish mobility program (MŠMT 8J20PL037 and PPN/BCZ/2019/1/00069).

References

Afanasiev, V. L., Popović, L. Č., & Shapovalova, A. I. 2019, MNRAS, 482, 4985
Bao, D.-W., Brotherton, M. S., Du, P., et al. 2022, ApJS, 262, 14
Bentz, M. C., & Katz, S. 2015, PASP, 127, 67
Bentz, M. C., Denney, K. D., Grier, C. J., et al. 2013, ApJ, 767, 149
Blandford, R. D., & McKee, C. F. 1982, ApJ, 255, 419
Cackett, E. M., Horne, K., & Winkler, H. 2007, MNRAS, 380, 669
Cackett, E. M., Chiang, C.-Y., McHardy, I., et al. 2018, ApJ, 857, 53
Cackett, E. M., Gelbord, J., Li, Y.-R., et al. 2020, ApJ, 896, 1
Chelouche, D., Pozo Nuñez, F., & Kaspi, S. 2019, Nat. Astron., 3, 251
Collier, S., Horne, K., Wanders, I., & Peterson, B. M. 1999, MNRAS, 302, L24
Czerny, B., Schwarzenberg-Czerny, A., & Loska, Z. 1999, MNRAS, 303, 148
Czerny, B., Nikołajuk, M., Piasecki, M., & Kuraszkiewicz, J. 2001, MNRAS, 325, 865
Czerny, B., Nikołajuk, M., Różańska, A., et al. 2003, A&A, 412, 317
Czerny, B., Hryniewicz, K., Maity, I., et al. 2013, A&A, 556, A97
Dasgupta, S., & Rao, A. R. 2006, ApJ, 651, L13
Di Valentino, E., Mena, O., Pan, S., et al. 2021, CQG, 38, 153001
Du, P., & Wang, J.-M. 2019, ApJ, 886, 42
Du, P., Hu, C., Lu, K.-X., et al. 2014, ApJ, 782, 45
Du, P., Brotherton, M. S., Wang, K., et al. 2018, ApJ, 869, 142
Edelson, R., Gelbord, J. M., Horne, K., et al. 2015, ApJ, 806, 129
Freedman, W. L. 2017, Nat. Astron., 1, 0121
Ferland, G. J., Chatzikos, M., Guzmán, F., et al. 2017, Rev. Mex. Astron. Astrofis., 53, 385
Gehrels, N., Chincarini, G., Giommi, P., et al. 2004, ApJ, 611, 1005
Georgakakis, A., Papadakis, I., & Paolillo, M. 2021, MNRAS, 508, 3463
Grier, C. J., Peterson, B. M., Horne, K., et al. 2013, ApJ, 764, 47
Grier, C. J., Trump, J. R., Shen, Y., et al. 2017, ApJ, 851, 21
Guo, H., Barth, A. J., Korista, K. T., et al. 2022a, ApJ, 927, 60
Guo, W.-J., Li, Y.-R., Zhang, Z.-X., Ho, L. C., & Wang, J.-M. 2022b, ApJ, 929, 19
Hernández Santisteban, J. V., Edelson, R., Horne, K., et al. 2020, MNRAS, 498, 5399
Jiang, J., Walton, D. J., Fabian, A. C., & Parker, M. L. 2019, MNRAS, 483, 2958
Kammoun, E. S., Papadakis, I. E., & Dovčiak, M. 2019, ApJ, 879, L24
Kammoun, E. S., Dovčiak, M., Papadakis, I. E., Caballero-García, M. D., & Karas, V. 2021a, ApJ, 907, 20
Kammoun, E. S., Papadakis, I. E., & Dovčiak, M. 2021b, MNRAS, 503, 4163
Kara, E., Alston, W. N., Fabian, A. C., et al. 2016, MNRAS, 462, 511
Kaspi, S., Smith, P. S., Netzer, H., et al. 2000, ApJ, 533, 631
Kelly, B. C., Bechtold, J., & Siemiginowska, A. 2009, ApJ, 698, 895
Koratkar, A. P., & Gaskell, C. M. 1991, ApJS, 75, 719
Korista, K. T., & Goad, M. R. 2001, ApJ, 553, 695
Korista, K. T., & Goad, M. R. 2019, MNRAS, 489, 5284
Kubota, A., & Done, C. 2018, MNRAS, 480, 1247
Lawther, D., Goad, M. R., Korista, K. T., Ulrich, O., & Vestergaard, M. 2018, MNRAS, 481, 533
Lobban, A. P., Zola, S., Pajdosz-Śmierciak, U., et al. 2020, MNRAS, 494, 1165
Mantovani, G., Nandra, K., & Ponti, G. 2016, MNRAS, 458, 4198
Markaryan, B. E. 1969, Astrofizika, 5, 443
Markowitz, A. 2010, ApJ, 724, 26
Martínez-Aldama, M. L., Czerny, B., Kawka, D., et al. 2019, ApJ, 883, 170
Martocchia, A., & Matt, G. 1996, MNRAS, 282, L53
McHardy, I. M., Koerding, E., Knigge, C., Uttley, P., & Fender, R. P. 2006, Nature, 444, 730
McHardy, I. M., Connolly, S. D., Horne, K., et al. 2018, MNRAS, 480, 2881
Mehdipour, M., Kaastra, J. S., Kriss, G. A., et al. 2015, A&A, 575, A22
Miniutti, G., & Fabian, A. C. 2004, MNRAS, 349, 1435
Mosquera, A. M., Kochanek, C. S., Chen, B., et al. 2013, ApJ, 769, 53
Netzer, H. 2022, MNRAS, 509, 2637
Niedźwiecki, A., Zdziarski, A. A., & Szanecki, M. 2016, ApJ, 821, L1
Oknyanskij, V. L. 1999, Odessa Astron. Publ., 12, 99
Panda, S., Czerny, B., Adhikari, T. P., et al. 2018, ApJ, 866, 115
Panda, S., Martínez-Aldama, M. L., & Zajaček, M. 2019, Front. Astron. Space Sci., 6, 75
Parker, M. L., Wilkins, D. R., Fabian, A. C., et al. 2014, MNRAS, 443, 1723
Peterson, B. M. 1988, PASP, 100, 18
Peterson, B. M. 1993, PASP, 105, 247
Peterson, B. M., Ferrarese, L., Gilbert, K. M., et al. 2004, ApJ, 613, 682
Petrucci, P. O., Gronkiewicz, D., Rozanska, A., et al. 2020, A&A, 634, A85
Planck Collaboration VI. 2020, A&A, 641, A6
Porquet, D., Reeves, J. N., Grosso, N., Braito, V., & Lobban, A. 2021, A&A, 654, A89
Pozo Nuñez, F., Gianniotis, N., Blex, J., et al. 2019, MNRAS, 490, 3936
Prince, R., Hryniewicz, K., Panda, S., Czerny, B., & Pollo, A. 2022, ApJ, 925, 215

Rauch, K. P., & Blandford, R. D. 1991, ApJ, 381, L39
Reeves, J. N., Porquet, D., Braito, V., Grosso, N., & Lobban, A. 2021, A&A, 649, L3
Riess, A. G., Casertano, S., Yuan, W., Macri, L. M., & Scolnic, D. 2019, ApJ, 876, 85
Riess, A. G., Casertano, S., Yuan, W., et al. 2021, ApJ, 908, L6
Rokaki, E., Collin-Souffrin, S., & Magnan, C. 1993, A&A, 272, 8
Różańska, A., Malzac, J., Belmont, R., Czerny, B., & Petrucci, P. O. 2015, A&A, 580, A77
Shakura, N. I., & Sunyaev, R. A. 1973, A&A, 500, 33
Siemiginowska, A., & Czerny, B. 1989, MNRAS, 239, 289
Śniegowska, M., Panda, S., Czerny, B., et al. 2022, A&A, submitted [arXiv:2202.13839]
Sun, M., Grier, C. J., & Peterson, B. M. 2018, Astrophysics Source Code Library [record ascl:1805.032]
Timmer, J., & Koenig, M. 1995, A&A, 300, 707
Vincentelli, F. M., McHardy, I., Cackett, E. M., et al. 2021, MNRAS, 504, 4337
Vincentelli, F. M., McHardy, I., Hernández Santisteban, J. V., et al. 2022, MNRAS, 512, L33
Walton, D. J., Baloković, M., Fabian, A. C., et al. 2021, MNRAS, 506, 1557
Wills, B. J., Netzer, H., & Wills, D. 1985, ApJ, 288, 94
Xiao, M., Du, P., Lu, K.-K., et al. 2018, ApJ, 865, L8
Yu, W., Richards, G. T., Vogeley, M. S., Moreno, J., & Graham, M. J. 2022, ApJ, 936, 132
Zajaček, M., Czerny, B., Martinez-Aldama, M. L., et al. 2021, ApJ, 912, 10
Zdziarski, A. A., You, B., & Szanecki, M. 2022, ApJ, 939, L2
Zu, Y., Kochanek, C. S., & Peterson, B. M. 2011, ApJ, 735, 80
Zu, Y., Kochanek, C. S., Kozłowski, S., & Udalski, A. 2013, ApJ, 765, 106
Zu, Y., Kochanek, C. S., Kozłowski, S., & Peterson, B. M. 2016, ApJ, 819, 122

A&A 670, A147 (2023)

Appendix A: Comparison of results from our code and from Kammoun et al. (2019)

To test the importance of the effects neglected in our model, we calculated the model as closely as possible to the standard one of Kammoun et al. (2021b). We concentrate on the issue of the height effect on the measured delay. The result from our code is shown in Figure A.1. We use the parameters adopted by Kammoun et al. (2021b). We also included the color correction of 2.4 in this case, unlike in the other plots. We see that our code gives shorter time delays at the shortest wavelengths in comparison with Fig. 18 in Kammoun et al. (2021b), since GR effects are most important in the disk central regions. However, at the longest wavelengths, our delays are also somewhat shorter. The maximum delay is 1.7 days for $\lambda = 10^4$ Å as shown in Figure A.1, while in Kammoun et al. (2021b) in their Fig.18 the maximum delay for the same wavelength is approximately 2.8 days.

Since our plot with the color correction shows also traces of the convex shape, we carried out two experiments in order to understand better this trend. We calculated exemplary delay curves for a much higher incident luminosity and in this case, the effect of convex shape is even much stronger (see Figure A.1, middle panel). Since introducing the color correction and increasing the incident flux both lead to an increase in the disk temperature and the emission at a given wavelength comes with increasing disk radii, we checked whether the convex shape is not caused by adopting too small outer radius. Indeed, repeating the computations just for the high luminosity and the lamppost height of 100 R_g for two values of the disk outer radius (10^4 and $10^5 R_g$), we show that the convex shape is an artifact of an overly small outer radius value set in the model.

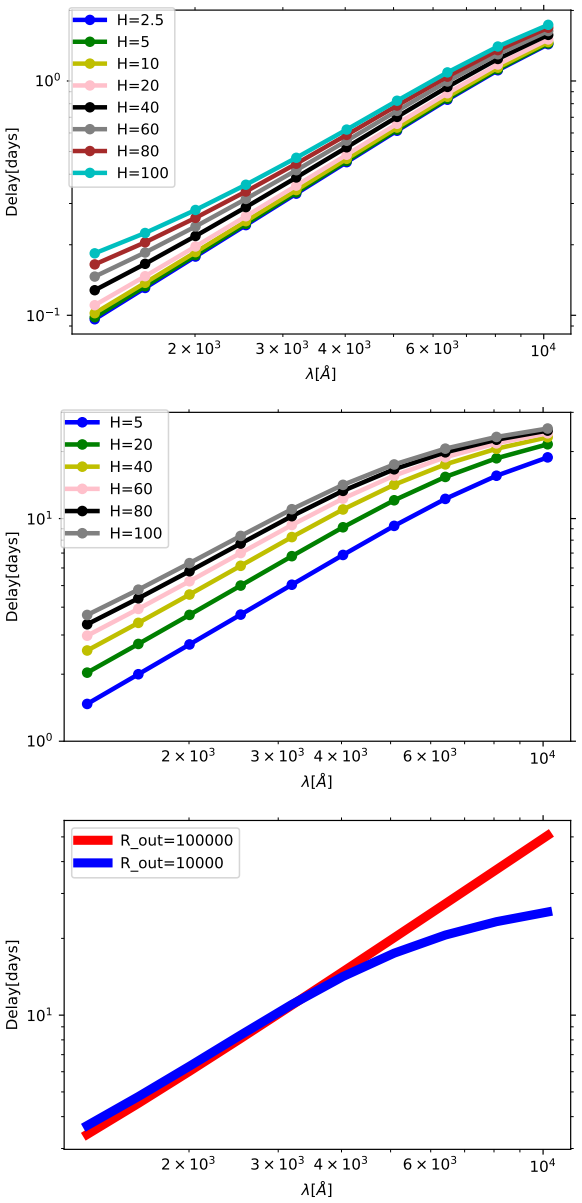

Fig. A.1. Comparision of delay plots. Upper panel: Delay curves from our code with the parameters: black hole mass = $10^7 M_\odot$, Eddington Ratio = 0.05, inclination angle = 40 degrees, color correction = 2.4, and X-ray source luminosity = 1.26×10^{43} erg s^{-1}. Middle panel: Black hole mass = $10^8 M_\odot$, Eddington Ratio = 1.0, inclination angle = 30 degrees, color correction = 2.4, and X-ray luminosity = 3.78×10^{46} erg s^{-1}. Lower panel: Same parameters as middle panel, only for corona height of $100 R_g$, but two different values of the disk outer radius.

Chapter 5

Paper-2

5.1 Introduction

This paper simultaneously fits the NGC 5548 delay spectra and SED by combining the contributions from the accretion disk and the broad line region (BLR). The BLR component is generated using the FRADO model together with the CLOUDY photoionization code. In this approach, a set of parameters is adopted. Some of them are fixed by independent observations, while others are kept free. The free parameters are varied systematically until the minimum chi-squared value is obtained. This procedure ensures that both the delay spectra and the spectral energy distribution are reproduced within observational uncertainties. From the best-fit model, the luminosity distance of the source is estimated directly, and the value of the Hubble constant, which is consistent with other cosmological measurements. This study serves as a pilot application of the method and demonstrates the possibility of using AGN continuum time delays for cosmological purposes.

Astronomy & Astrophysics manuscript no. main_rev3_no_color
August 13, 2025

Application of the FRADO model of BLR formation to the Seyfert galaxy NGC 5548 and the first step toward determining the Hubble constant

Vikram Kumar Jaiswal[1], Amit Kumar Mandal[1], Raj Prince[1,2], Ashwani Pandey[1,3], Mohammad Hassan Naddaf[4], Bożena Czerny[1], Swayamtrupta Panda[5,⋆], and Francisco Pozo Nuñez[6]

[1] Center for Theoretical Physics, Polish Academy of Sciences, Al. Lotników 32/46, 02-668 Warsaw, Poland
[2] Department of Physics, Institute of Science, Banaras Hindu University, Varanasi-221005, India
[3] Department of Physics and Astronomy, University of Utah, Salt Lake City, UT 84112, USA
[4] Institut d'Astrophysique et de Géophysique, Université de Liège Allée du six août 19c, B-4000 Liège (Sart-Tilman), Belgium
[5] International Gemini Observatory/NSF NOIRLab, Casilla 603, La Serena, Chile
[6] Astroinformatics, Heidelberg Institute for Theoretical Studies, Schloss-Wolfsbrunnenweg 35, 69118 Heidelberg, Germany

ABSTRACT

Context. The dynamical and geometric structures of the Broad Line Region (BLR), along with the origins of continuum time delays in active galaxies, remain topics of ongoing debate.
Aims. In this study, we aim to reproduce the observed broadband spectrum, the Hβ line delay, and the continuum time delays using our newly developed model for the source NGC 5548.
Methods. We adopt the standard accretion disk model, with the option of an inner hot flow, and employ the lamp-post model to account for disk irradiation. Additionally, we model the BLR structure based on radiation pressure acting on dust. The model is parameterized by the black hole mass, $M_{\rm BH}$ (which is fixed), the accretion rate, the viewing angle, the height of the lamp-post, the cloud density, and the cloud covering factor. The resulting continuum time delays arise from a combination of disk reprocessing and the reprocessing of a fraction of radiation by the BLR.
Results. Our model reasonably reproduces the observed broad-band continuum, the Hβ time delay, and the continuum inter-band time delays measured during the observational campaign. When the accretion rate is not constrained by the known distance to the source, our approach allows for a direct estimation of the distance. The resulting Hubble constant, $H_0 = 66.9^{+10.6}_{-2.1}$ km s^{-1} Mpc^{-1}, represents a significant improvement over previously reported values derived from continuum time delays in the literature.
Conclusions. This pilot study demonstrates that, with sufficient data coverage, it is possible to disentangle the time delays originating from the accretion disk and the BLR. This paves the way for effectively using inter-band continuum time delays as a method for determining the Hubble constant. Additionally, the findings provide strong support for the adopted model for the formation of the Hβ line.

Key words. Accretion, accretion disks, Galaxies: active

1. Introduction

The central components of active galactic nuclei (AGNs) include a massive black hole, a compact X-ray emitting region, a relatively cold Keplerian accretion disk, and the broad line region (BLR) (see, e.g., Krolik 1999a, for a basic compendium). The Keplerian disk serves as the primary source of continuum emission, while the BLR predominantly produces broad emission lines, along with a minor contribution to the continuum. In terms of spatial extent, the innermost regions of the accretion disk span approximately 10−100 gravitational radii (r_g), whereas the BLR extends outward at distances of order of $\sim 1000\ r_g$. Beyond the BLR, a dusty molecular torus is located at even larger radii ($\sim 10^4$ to $10^5 r_g$). Since the early studies of active galaxies by Seyfert (1943) and the discovery of quasars by Schmidt (1963), there has been tremendous progress in our understanding of the structure of AGNs (see e.g. Krolik 1999b, for a review).

The innermost regions of an AGN are too compact (~ a few microarcseconds in the case of BLR) to be spatially resolved directly. However, their structure can be probed using intrinsic flux variability. Among the various wavelengths, X-ray variability is the fastest, originating from the most compact region near the black hole. The reprocessing of this X-ray emission at longer wavelengths, observed through light echo studies, provides insights into the structure and dynamics of the surrounding material, a technique known as reverberation mapping (RM; Blandford & McKee 1982; Peterson 1993). RM has been widely applied to AGNs (Sergeev et al. 2005; McHardy et al. 2014; Mudd et al. 2018; Homayouni et al. 2019; Yu et al. 2020; Guo et al. 2022), particularly in studies of continuum variability, which is believed to arise from the irradiated accretion disk.

Although our understanding of AGN structure is still evolving, significant progress has enabled the exploration of AGNs as potential tools for cosmology. Unlike standard candles, AGNs exhibit luminosities that span several orders of magnitude. Nevertheless, the luminosity distance to individual AGNs can be estimated either through geometric methods or by standardizing them in a statistical sense (see e.g. Czerny et al. 2018, for reviews). Early successful approaches relied on the non-linear

⋆ Gemini Science Fellow

relation between UV and X-ray luminosities (Risaliti & Lusso 2015; Lusso et al. 2025), or the correlation between the BLR radius and the source luminosity (Martínez-Aldama et al. 2019; Cao et al. 2022, 2024, 2025). However, these methods require external scaling and, without it, can only constrain the curvature of the Hubble diagram. As such, they are not directly suitable for determining the Hubble constant.

The Hubble constant can instead be derived using strong gravitational lensing techniques (see Suyu et al. 2024, for a recent review), or through a combination of RM of the BLR with angular size measurements obtained from high-resolution interferometric observations (Li et al. 2022, 2025). While both methods are promising, they demand extensive, dedicated observational campaigns and are currently feasible only for a limited number of AGNs, specifically, nearby, bright sources at low redshift where sufficient spatial resolution can be achieved.

The primary goal of this work is to develop a practical method for measuring the Hubble constant using a single mean spectrum of an AGN combined with photometric RM results at multiple wavelengths. High-quality photometric RM measurements are already available for a number of sources (Fausnaugh et al. 2016; Cackett et al. 2018; Edelson et al. 2024; Prince et al. 2025), and a substantial influx of data is expected from large-scale time-domain surveys, such as the Zwicky Transient Facility (ZTF) and the Vera C. Rubin Observatory's Legacy Survey of Space and Time (LSST).

The idea of using photometric RM to measure the Hubble constant is not new; it was first proposed by Collier et al. (1999), but has yet to produce successful results. The method is based on the standard accretion disk model of Shakura & Sunyaev (1973), which predicts a direct relationship between the time delay at a given wavelength and the monochromatic luminosity: intrinsically brighter sources are physically larger and thus produce longer time delays. More specifically, the model anticipates that the time delays (τ) should scale with wavelength (λ) as $\tau \propto \lambda^{4/3}$. While all coefficients in this relation are determined by the model, the viewing angle (i) to the source remains a free parameter and must be estimated independently.

While observational results have roughly confirmed this trend, they have not matched the predicted normalization, as observed delays continue to exceed theoretical expectations (e.g. Cackett et al. 2007; Shappee et al. 2014; Kokubo 2018; Guo et al. 2022; Mandal et al. 2025). This discrepancy, known as the accretion disk size problem, was first recognized in optical microlensing studies of gravitationally lensed quasars (Morgan et al. 2010) and till recently remained an ongoing challenge in our understanding of AGN accretion disk structure.

Recent intensive RM campaigns (Edelson et al. 2015; De Rosa et al. 2015; Fausnaugh et al. 2016; Pei et al. 2017; Horne et al. 2021; Lu et al. 2022; Prince et al. 2025) have revealed that the observed optical continuum is not solely emitted by the accretion disk. Korista & Goad (2001) first noted that radiation reprocessed by the BLR contributes not only to the formation of emission lines but also to the diffuse continuum emission. This finding was later confirmed by Fausnaugh et al. (2016) and further emphasized by Cackett et al. (2021); Netzer (2022), who demonstrated that the diffuse BLR contribution can significantly dominate the measured continuum time delays. This effect poses challenges for using continuum time delays as a method to determine the Hubble constant, H_0, as originally proposed by Collier et al. (1999). For instance, Cackett et al. (2007) derived an H_0 value of 15 ± 3 km s^{-1} Mpc^{-1}; however, at the time, not all aspects of the physical mechanisms driving continuum time delays were fully understood.

The contribution of the BLR to the continuum time delay implies that, in order to use photometric continuum RM of AGNs for measuring the Hubble constant, we require not only a reliable accretion disk model but also a robust model of the BLR structure. Importantly, such a BLR model must be fully determined by the absolute luminosity of the source. However, fully parametric BLR models (e.g. Baldwin et al. 1995; Li et al. 2013; Pancoast et al. 2014; Grier et al. 2017) may not be adequate in this context, as the ability to recover the absolute luminosity of the source can be compromised unless wavelength-resolved spectroscopic RM data are available. Without such spectral resolution, key constraints on the BLR geometry and its luminosity dependence may be lost, limiting the accuracy of distance measurements based on photometric continuum RM.

We thus propose the use of the Failed Radiatively Accelerated Dusty Outflow (FRADO) model of the BLR (Czerny & Hryniewicz 2011; Naddaf et al. 2021; Naddaf & Czerny 2022). The model assumes BLR formation based on radiation pressure acting on dust in disk regions where the disk atmosphere temperature falls below the sublimation threshold. It was proposed to explain the vertical rise of material responsible for low-ionization lines, such as Hβ. In this study, we thus investigate the reprocessing of central radiation through a combination of two reprocessors: the Keplerian disk, which we modify to include the warm corona in the innermost part, and the BLR, using the BLR response derived from the FRADO model. This approach provides a three-dimensional distribution of BLR clouds, which we then combine with a spectral shape model of the BLR generated using the CLOUDY code (version 23.00; Chatzikos et al. 2023a). We fit this model to the observed spectrum and time delays of NGC 5548 and evaluate its potential for determining the distance to the source and the Hubble constant. We test the model for a specific source, and we treat the results as the pilot study: a base for further model developments and the later use for other objects.

NGC 5548 ($z = 0.017175$), a Seyfert 1 galaxy, is among the most extensively studied AGNs. Its brightness, relatively close distance, and significant variability made it an early candidate for studying the inner, unresolved structure of an active nucleus (e.g., Clavel et al. 1991; Peterson et al. 1991; Krolik et al. 1991; Rokaki et al. 1993). The recent high-quality photometric monitoring (Fausnaugh et al. 2016), broad-band spectral analysis (Mehdipour et al. 2015), measured Hβ time delay from spectroscopic RM (Pei et al. 2017), and wavelength-resolved RM that captured the detailed response of the BLR (Horne et al. 2021) collectively make NGC 5548 an ideal laboratory for testing our methodology.

The structure of this paper is as follows. In Section 2, we describe the data used for fitting. Section 3 outlines our methodology, which involves generating the response function of the accretion disk using the lamp-post model and incorporating the BLR contribution via FRADO and CLOUDY to estimate the combined time delays. Section 4 presents the results obtained from different models, detailing the simultaneous fitting of the time lag and spectral energy distribution (SED) while assessing the strengths and limitations of each approach. Finally, in Section 5, we estimate the luminosity distance based on our best-fitting model. The discussion and conclusions are presented in Sections 6 and 7, respectively.

2. Spectral shape and continuum time delay data of NGC 5548

NGC 5548 (z = 0.017) is one of the most extensively studied AGNs across multiple wavelengths. It was the primary target of the AGN Watch international collaboration (Peterson et al. 2002), which began investigating its emission line variability as early as 1987. Over the years, its optical and UV variability has been the subject of numerous studies (Peterson et al. 1991; Korista et al. 1995; Peterson et al. 1992, 2002, 2004). Observations from both ground-based and space-based telescopes have provided critical insights into accretion disk dynamics and emission line variability. Notably, optical variability in both the continuum and emission lines was first reported by de Vaucouleurs & de Vaucouleurs (1972) in the 1970s, while early UV observations commenced in 1988 with the International Ultraviolet Explorer (IUE; Ulrich & Boisson 1983). More recently, intensive multi-wavelength monitoring campaigns (Edelson et al. 2015; De Rosa et al. 2015; Fausnaugh et al. 2016; Pei et al. 2017; Horne et al. 2021; Lu et al. 2022) have significantly deepened our understanding of the source.

These studies have revealed that the measured continuum time delays do not follow a simple power-law trend with wavelength. Instead, they show clear evidence of interaction with an extended BLR, where different emission lines originate. Consequently, these delays are often approximated by mean time delays, though some emission line delay profiles exhibit double-peaked features. This complexity opens up new avenues for testing specific models of the BLR structure, as well as for explaining the observed inter-band continuum time delays.

In this study, we utilize the broadband SED and global parameters from Mehdipour et al. (2015), covering the period from 2013 to 2014. The broadband SED, corrected for internal extinction, starlight contamination, the Balmer continuum, and the Fe II pseudo-continuum, was first presented by Mehdipour et al. (2015). Subsequently, Kubota & Done (2018) fitted this spectrum to an AGN spectral model, revealing that only the outermost part of the accretion flow corresponds to a standard disk. Their results further indicated that the optical/UV emission primarily originates from a region dominated by the warm corona (see their Figure 4).

Therefore, to systematically model the observed inter-band continuum time delays, we propose a step-by-step approach. We select three representative setups to illustrate how the spectral fit and time-delay measurements depend on the pre-set parameters and details of the geometry.

First, we assume a standard accretion disk model (Model A). This choice is motivated by the delay fitting for NGC 5548 done by Kammoun et al. (2021b). The source was fitted by Kammoun et al. (2021b) without assuming an inner hot flow, only with the corona height, black hole mass ($M_{\rm BH}$), spin, accretion rate, and the X-ray luminosity as free parameters. The color correction was set to 2.4. We modify the approach: we fix $M_{\rm BH}$ and the Eddington ratio, but we allow for the inner hot flow and the contribution of the BLR. Our color correction is the same, and no warm corona is present. Since we also fit the spectral shape, we include a starlight component in the model.

Next, we consider an alternative scenario (Model B) based on the spectral decomposition proposed by Kubota & Done (2018). In this case, the warm corona plays an important role in the spectral fit. We adopt the value of the warm corona temperature from the corresponding paper. In order to calculate the time delay caused by reprocessing, we assume that the optical/UV variability arises solely from the reprocessing of X-rays in the outer cold disk. This is motivated by the fact that warm corona with a temperature of approximately $\sim 10^6$ K, is too optically thick to absorb and re-emit incident hard X-rays in the UV/X-ray bands, although it still contributes to the UV continuum. The model is supplemented with the BLR contribution to the delays and the spectrum, and starlight is included.

Finally, we introduce Model C, a most general spectral decomposition based on Figure 5 of Mehdipour et al. (2015). Now a number of geometrical and physical parameters are optimized to fit the spectral and time delay data. This includes the warm corona temperature and its optical depth, as well as contribution from BLR and starlight.

The disk parameters used for Models A, B, and C are summarized in Table 1, with more detailed descriptions provided in Section 4.4.

To test these models, we utilize the continuum time delay data from Fausnaugh et al. (2016), obtained during the STORM campaign from December 2013 to August 2014. This campaign integrated optical light curves data from 16 ground-based observatories, across the B, V, R, I filters, as well as the SDSS $-u, g, r, i, z$ filters, coupled with ultraviolet data from the Hubble Space Telescope (HST) and Swift instruments. The inter-band time delays were measured relative to the HST light curve at 1367 Å, providing a crucial dataset for evaluating the proposed disk reprocessing scenarios.

3. Method

Understanding the origin of continuum time delays in AGNs is crucial for probing the structure of the central engine and its surrounding medium. However, fitting these delays solely as a result of accretion disk reprocessing has often led to the so-called disk-size problem, as discussed earlier. Motivated by previous studies (Korista & Goad 2001; Netzer 2022; Jaiswal et al. 2023; Beard et al. 2025), we extend this framework by considering the reprocessing of central flux by both the accretion disk and the BLR medium. Given our twofold motivation, we adopt a theoretical modeling approach that accounts for all relevant aspects. This allows us not only to test the BLR model we employ but also to explore the determination of the Hubble constant, as the relatively small number of model parameters enables us to treat the luminosity distance as an unknown parameter.

Building on this foundation, our model of an active nucleus comprises multiple key components: a standard accretion disk in the outer parts of the flow, a warm comptonizing corona, and a hot corona in the inner parts of the flow, the BLR region, and the contribution of the host galaxy to the total spectrum. In the following sections, we examine each of these components in detail.

3.1. Hot and warm corona

The hot corona, responsible for hard X-ray emission, was modeled by Mehdipour et al. (2015). In our approach, we adopt the proposed power-law shape and normalization for the observed spectrum when fitting the warm corona. We do not model the hot corona; instead, the power-law component is treated as part of the broadband spectrum that irradiates the BLR clouds, as discussed in the next section. It is also included in the fit to the global spectrum, in the X-ray region. However, we neglect the contribution of hard X-rays to the optical/UV part of the spectrum.

Unlike Mehdipour et al. (2015), we model the warm corona with a different approach. In our framework, the inner and outer

radii of the warm corona are treated as parameters. The outer radius of the warm corona coincides with the inner radius of the standard (outer) disk. The Comptonization process in the warm corona is computed using the analytical formulae from Sunyaev & Titarchuk (1980) and is parameterized by the optical depth and electron temperature. Since the warm corona covers the inner disk, we do not assume a single temperature for the soft photons. Instead, we determine the temperature of the underlying cold disk at each radius and adjust it by the Comptonization amplification factor. These calculations are performed iteratively, ensuring that the soft photon temperature spans a continuous range while preserving the total energy from the accretion flow. The coronal parameters (optical depth and the temperature) are assumed to be radius-independent as we do not have a firm predictions for these parameters from the warm corona physics. This methodology aligns closely with the approach of Kubota & Done (2018). The computational code used for this purpose was originally presented in Czerny et al. (2003). The warm corona is thus fully modeled, with its spectral shape and normalization determined by global fitted parameters, including the optical depth, temperature, the disk radius at which the warm corona develops, and the accretion rate. This is incorporated in the spectral fitting, but not included separately in BLR reprocessing where the incident radiation is made at the basis of the broad band SED, instead of a separate modeling of the disk and the warm corona. This choice avoids the computational complexity of calculating the reprocessed emission using the `CLOUDY` code (Chatzikos et al. 2023b) at every step of the simulation. It is stated explicitly later on.

Additionally, we do not include irradiation of the warm corona by hard X-rays, as the high temperature and large optical depth of the warm corona would cause the incident radiation to be predominantly scattered rather than absorbed and reprocessed. Consequently, no significant thermalization is expected, although some high-ionization lines, such as iron lines in the X-ray spectrum, may still be present (Petrucci et al. 2020; Ballantyne et al. 2024).

3.2. Cold disk reprocessing

The irradiating flux is thermalized only in the outer, cold regions of the standard accretion disk. To further explore this process, we simulate the lamp-post model to generate the disk's response function, assuming a pulse of short duration. In this simulation, we exclude corrections for general relativity (GR) and energy-dependent reflection effects, as introduced by Kammoun et al. (2023, 2024a); Papoutsis et al. (2024), to maintain a relatively simple code suitable for data fitting. As a result, the incident radiation from the corona is assumed to be fully absorbed by the cold disk, leading to a localized increase in temperature. We briefly comment on the implications and limitations of this simplification in Section 6.

To accurately model the disk reprocessing, we employ a non-uniform radial grid extending from the innermost stable circular orbit ($r_{\rm isco}$) to the outer disk radius ($r_{\rm out}$), ensuring sufficient resolution at smaller radii. The radial grid spacing follows the relation $dr = 0.085 \times (\frac{r}{r_{\rm isco}})^{0.85}$, where r is the radial distance from the central source in units of gravitational radius, r_g. For each radial position, the azimuthal angle ϕ is sampled using the relation $d\phi = \frac{1.57}{N_{\rm div}}$, where $N_{\rm div} = 3800$ ensures sufficient resolution across the entire radial range. The surface element for each (r, ϕ) coordinate is defined as $ds = r \cdot dr \cdot d\phi$ in units of r_g^2. To facilitate further calculations, we convert (r, ϕ) into Cartesian coordinates, assuming a geometrically thin disk with negligible height.

For each (x, y) coordinate, we compute the total time delay, $\tau_{\rm total}(x, y)$, as the sum of two components: the delay from the corona to the disk, $\tau_d(r)$, and the delay from the disk to the plane intersecting the equatorial plane at $(r = r_{out}, \phi = 0)$, denoted as $\tau_{\rm do}(x, y)$. The delay is influenced by key parameters, including lamp-luminosity (L_x), $M_{\rm BH}$, accretion rate ($\dot{M}$), the corona height (h), and the inclination angle of the system (i). By default, we assume a cold Keplerian disk extending down to the ISCO at $6\,r_g$, with an outer radius of $10^4\,r_g$. However, we also consider cases with different inner and outer radii, which can be set through the parameter $r_{\rm in}$.

The non-irradiated disk is characterized by its flux, $F_{\rm non\text{-}irradiated}$, and temperature, $T_{\rm disk}$, as defined in equations 1 and 2, respectively. When the contribution from the corona is included, the resulting total flux and temperature are given by equations 3 and 4. For a specified delay, we use the combined flux from both the disk emission and irradiation, $F_{\rm disk+irradiation}$, as described in equation 3. We then convert this total flux into an effective temperature, $T_{\rm eff}$, according to equation 4. This temperature is subsequently used to compute the blackbody emission.

$$F_{\rm non\text{-}irradiated}(r, t + \tau_d(r)) = \left(\frac{3GM\dot{M}}{8\pi r^3}\left(1 - \sqrt{\frac{r_{in}}{r}}\right)\right) \tag{1}$$

$$T_{\rm disk}(r, t + \tau_d(r)) = \left[\left(\frac{3GM\dot{M}}{8\pi r^3\sigma_B}\left(1 - \sqrt{\frac{r_{in}}{r}}\right)\right)\right]^{\frac{1}{4}} \tag{2}$$

$$F_{\rm disk+irradiation}(r, t+\tau_d(r)) = \left(\frac{3GM\dot{M}}{8\pi r^3}\left(1 - \sqrt{\frac{r_{in}}{r}}\right)\right)+\left(\frac{L_x(t)h}{4\pi r^3}\right) \tag{3}$$

$$T_{\rm eff}(r, t + \tau_d(r)) = \left[\left(\frac{3GM\dot{M}}{8\pi r^3\sigma_B}\left(1 - \sqrt{\frac{r_{in}}{r}}\right)\right) + \left(\frac{L_x(t)h}{4\pi r^3\sigma_B}\right)\right]^{\frac{1}{4}} \tag{4}$$

Additionally, we account for a color correction factor f_c to the disk temperature, which raises the temperature of the disk atmosphere to T_c, where $f_c = 1$ corresponds to no color correction applied, as described below (Shimura & Takahara 1995):

$$T_c = f_c T_{eff}. \tag{5}$$

To compute the full spectrum for a specific differential area, we use Planck's formula and store the results in a photon table, represented as a 2D matrix denoted as $\mathbf{P(t', \lambda)}$. This involves applying the calculated time delay corresponding to the disk position and wavelength. Each element in the photon table represents a unique delay and wavelength λ, with the λ values ranging from 1000 to 10000 Å and selected using a logarithmic scale grid for simulation. We also introduce a color correction as a free parameter of the model.

Next, we generate the response function by sending a very short light pulse of $\Delta_t = 0.05$ days duration and normalizing the result by the incident bolometric luminosity. The pulse duration is chosen to balance accuracy and temporal resolution: a very short pulse can introduce significant errors in the temperature enhancement, while a very long pulse tends to smear the signal and reduce time resolution, especially at the shortest wavelengths. The response function for a bare disk is given by the following equation:

$$\psi(t, \lambda) = \frac{1}{\Delta_t L_x}\frac{1}{f_c^4}\int_{S_{disk}} B_\lambda(T_c(r(t^{'} - \tau_{do}(x, y))))ds. \tag{6}$$

The time delay in the disk has been described previously by Jaiswal et al. (2023). Our adopted method, while simpler than the approaches presented by Kammoun et al. (2021b) and Kammoun et al. (2021a), which include corrections for GR and disk albedo, is sufficiently accurate for the current purpose of this pilot study.

3.3. BLR structure and reprocessing

To introduce the contribution from the BLR, we first describe its properties. In this study, we do not parameterize the structure of the BLR using arbitrary numbers or functions; instead, we calculate it based on the FRADO model, which was qualitatively proposed by Czerny & Hryniewicz (2011) and has been further developed in several subsequent studies (Czerny et al. 2017; Naddaf et al. 2021; Naddaf & Czerny 2022; Naddaf et al. 2023; Naddaf & Czerny 2024).

The basic idea behind the model is to associate the low-ionization parts of the BLR – responsible for emission lines, such as Hβ, Mg II, and Fe II, with dust-driven massive winds. In stellar environments, such winds are typically denser, possess higher optical depths, and exhibit significantly slower outflow velocities. Similarly, in AGNs, dust-driven winds are expected to be launched from the outer disk, where the effective temperature falls below the dust sublimation threshold. This temperature constraint naturally defines the inner radius of the BLR. The nature of the wind depends on $M_{\rm BH}$ and Eddington ratio: for sufficiently massive black holes and high accretion rates, the wind escapes, contributing to the BLR outflow structure; otherwise, it forms a failed wind, in which the material ultimately falls back onto the disk. Additionally, irradiation from the central parts of the disk plays an increasingly important role in shaping the dynamics and ionization state of the wind as the cloud elevates above the disk plane.

Specifically, we utilize the code from Naddaf et al. (2021), which provides a detailed numerical description of the wavelength-dependent cross-section for dusty particles. According to this model, radiatively dust-driven pressure lifts the clouds from the disk surface, while preserving their angular momentum derived from the Keplerian motion of the disk surface. As a cloud is lifted, it becomes increasingly illuminated by the inner parts of the disk. However, if the cloud becomes too hot, the dust evaporates, allowing the cloud to continue its motion along a ballistic orbit. The global parameters of the model, such as $M_{\rm BH}$, Eddington rate, and metallicity, govern the behavior of the BLR. For lower black hole masses, lower Eddington ratios, and lower metallicities, the clouds form a failed wind, while in the opposite case, a fraction of the clouds may form an escaping wind. Hence, we emphasize that the inner and outer radii of the BLR, along with the statistical distribution of the clouds, are governed by global parameters, such as $M_{\rm BH}$ and the Eddington ratio.

We assume a universal value of the dust sublimation temperature of 1500 K as representative for all grain species and sizes. It was suggested by Barvainis (1987) at the basis of the observational data for PG quasars. It is frequently used for zero order approximation, although it is well known that actually the sublimation temperature depends on the chemical composition as well as size of the dust grains (Draine & Lee 1984; Baskin & Laor 2018). However, calculating the range of evaporation temperature of each grain is time consuming and not appropriate for a pilot study. In addition, the chemical composition of grains in AGN is not firmly established, and the presence of the graphite with usual grain size distribution is highly unlikely (e.g. Czerny et al. 2004; Gaskell et al. 2004). We further discuss this issue in Section 6.3.

With knowledge of the global parameters of the source, we can determine the 3-D locations of statistically representative clouds within the BLR. The code calculates 3-D trajectories of clouds launched from the disk. As described in Naddaf et al. (2021), clouds are then located at these trajectories proportionally to time they spent at each part of the trajectory. This information is then combined with the emissivity law for specific emission lines, particularly low-ionization lines such as Hβ, Mg II, or Fe II. In our model, we assume that the emissivity weight of each cloud is influenced by its distance from the central disk: clouds closer to the center receive more radiation, resulting in a higher emissivity weight, while clouds farther away receive less radiation, leading to a lower weight, as defined in equation 7:

$$w \propto d^{-2}, \tag{7}$$

where d is the distance of a cloud from the center. This scaling of the emissivity, which inversely depends on the square of the distance, neglects the local efficiency of converting incident flux into BLR spectrum. However, since our model does not yet predict the local density, this simplification is reasonable at this stage of development. We fix the local density of the cloud at 10^{11} cm^{-3}, and the column density at 3×10^{23} cm^{-2}.

By supplementing the cloud distribution with emissivity, we can determine the emission line profile for any viewing angle relative to the observer, as demonstrated in Naddaf & Czerny (2022). Next, we focus on calculating the response function $\psi_{BLR}(t)$ for the BLR based on this distribution. This is accomplished by calculating the time delays for each representative cloud as observed, using a method analogous to that applied for disk emission. At this stage, we assume that the emissivity of the clouds is universal, though wavelength-dependent, which is determined through photoionization calculations for a representative cloud.

3.4. Photoionization calculations using CLOUDY

To determine the BLR spectral shape, we perform photoionization calculations using the code CLOUDY, version C23.00 (Chatzikos et al. 2023a). In these computations, we simplify the 3-D cloud distribution by replacing the entire ensemble of clouds with a single representative cloud, positioned at the radius inferred from the time delay. For the analysis at this established distance, we adopt an incident radiation luminosity of $\log L$ (erg/s) = 44, and a BLR distance from the central source of $\log r$ (cm) = 16 (Dalla Bontà et al. 2020), a constant hydrogen gas density of $\log n_H$ (cm^{-3}) = 11, and a column density of $\log N_H$ (cm^{-2}) = 23.5, following the prescriptions of (Korista & Goad 2001; Panda et al. 2022). The adopted distance in our representative case corresponds to the measured time delay of the Hβ line in NGC 5548. The assumed bolometric luminosity is also representative of this source, based on the redshift-inferred distance within the framework of standard cosmology. In this pilot study, we do not explore a wide range of gas densities or column densities in detail, as photoionization models, particularly single-zone models, still do not perfectly represent the full complexity of BLR properties (e.g. Netzer 2020; Pandey et al. 2025; Floris et al. 2025). We assume a metallicity five times higher than solar, as this was favored by comparisons between the FRADO model and quasar spectra (Naddaf et al. 2021). Independent studies of quasar metallicity also support super-solar values (e.g. Śniegowska et al. 2021), and in the specific case

of NGC 5548, high metallicity was advocated by Netzer (2020) based on line emissivity analysis. For simplicity, we neglect turbulence in the medium.

The shape of the incident SED is taken from the file "NGC5548.sed" available in the CLOUDY database, which corresponds to the SED derived by Mehdipour et al. (2015). Their study estimated the starlight contribution to NGC 5548 using HST observations, providing a well-constrained incident SED that we adopt for our calculations.

This is clearly an oversimplification, in two aspects. Each cloud receives the radiation of the same shape, only scaled down with the distance as specified in equation 7. This radiation includes both the hard X-ray radiation as well as the warm corona and the disk emission. Apart from the spectral shape, we also do not differentiate here between the arrival time from the hot corona, and warm extended corona. Accounting for such differences would require modeling the BLR response separately to the hard X-ray emission from the hot corona and to the emission from the warm corona, followed by merging several resulting transfer functions. As this is a pilot study, we have not undertaken that level of complexity at this stage, although it is feasible in principle, given that our spectral decomposition separates the contributions from all three components. For the current analysis, we adopt a fixed SED shape, a simplification that is unlikely to significantly affect our results. The hard X-ray power-law from the hot corona is consistent with SED, and the warm corona is also fitted in such way as to reproduce the spectrum. Slight error on the time delay introduced by the fact that some photons should come directly from the hot corona instead from the disk should not be essential, taking into account much larger size of the BLR than the disk.

The resulting BLR emissivity profile, $\epsilon(\lambda)$, is then incorporated into the final delay model. When we later account for the assumption of an unknown luminosity distance, the irradiating flux is adjusted accordingly to ensure consistency with the observed hard X-ray flux.

Since CLOUDY does not compute higher-order Balmer lines, we incorporate a scaled component into the spectrum, following the method of Kovačević et al. (2014). This modification improves the spectral fit, as demonstrated in Pandey et al. (2025), though it only affects the wavelength range between 3646Å and 4000Å in the rest-frame. The shape of this component is taken directly from Pandey et al. (2025); however, the emissivity still appears too low to fully capture the gradual decline observed beyond the Balmer edge in the data. More advanced modeling may be required to improve the fit in that region.

When we perform computations of the Model C for fixed luminosity distance the value of the incident flux in CLOUDY computations is fixed and corresponds to the observed luminosity and the time delay to the BLR as above. However, later on, in the Section 5 when the luminosity distance is treated as unknown, we scale the incident bolometric luminosity to the fitted accretion rate which is a function of the luminosity distance.

3.5. Starlight contribution

The starlight contribution in NGC 5548 was estimated by Mehdipour et al. (2015), and we adopt the same level in some of our models. However, in other models, we allow for flexibility in adjusting the starlight level. To represent the starlight profile, we use the template of an Sa galaxy from Kinney et al. (1996), which is available in the Kinney-Calzetti Spectral Atlas[1].

3.6. Combined time delay and NGC 5548 data fitting

After analyzing each component of the central regions assumed in our model for NGC 5548, we derive the final response function by incorporating both disk reprocessing and BLR contributions, as expressed in the following equation

$$\psi(\lambda, t) = (1 - f_{\rm BLR})\,\psi_d(\lambda, t) + f_{\rm BLR}\,\epsilon(\lambda) \int_{t_0}^{t_{\rm max}} \psi_d(\lambda, t - t')\,\psi_{\rm BLR}(t')\,dt' \quad (8)$$

where the parameter f_{BLR} defines the BLR fraction contributing to the continuum time delay.

As mentioned in Section 3.4, we do not treat separately photons reaching the BLR directly from the hot corona and/or from the warm corona, and from the disk. Photons from the hot and warm corona are included in BLR computations as the incident continuum (i.e. they are included in the $\epsilon(\lambda)$), but their arrival time is the same as for the photon disks under consideration. This is done for the efficiency of computations when fitting the data. Replacing the incident continuum adopted for photoionization modeling with three separate spectral components would additionally require repeating photoionization computations at every computational step.

We generate response functions for 100 wavelengths, covering the range from 1000 Å to 10000 Å. Using these response functions, we then compute the time delay at each wavelength using the following equation:

$$\tau(\lambda) = \frac{\int t\psi(t, \lambda)dt}{\int \psi(t, \lambda)dt} \quad (9)$$

To fit the data of NGC 5548, we utilize all the parameters listed in Table1, integrating the contributions from both the disk and the BLR as described in equation 8.

When searching for the optimal solution, we impose constraints from both the observed SED and the measured time delays. Specifically, we incorporate all 17 available time delay measurements and select 17 representative points, evenly distributed across the entire observed SED range. To systematically evaluate and compare different solutions, we integrate these constraints into a unified criterion:

$$\chi^2 = \sum \frac{(O_i - E_i)^2}{(\delta O_i)^2} \quad (10)$$

where O_i = observed data, δO_i = is the error in observed data, and E_i = value from the model. We assume the error in the spectral data of 7%, and the errors of the delay measurements are taken from Fausnaugh et al. (2016).

4. Results

In this section we concentrate on testing the FRADO model against the spectral and time-delay data for NGC 5548 and summarize the results obtained from our model fitting. We fix $M_{\rm BH}$

[1] https://www.stsci.edu/hst/instrumentation/reference-data-for-calibration-and-tools/astronomical-catalogs/the-kinney-calzetti-spetral-atlas

Table 1. Parameters utilized in modeling the delay and spectral energy distribution (SED) of NGC 5548 for the three Models A, B, and C. Some values were taken from the literature, others were derived as best fit values in the current work, as noted below.

Parameters	Model A	Model B	Model C
(1)	(2)	(3)	(4)
Black Hole Mass($M_{\rm BH}$)	$5 \times 10^{7(ref1)}$	$5.5 \times 10^{7(ref4)}$	$5 \times 10^{7(ref1)}$
Corona Height(h)	$20^{(a)}$	$43^{(ref4)}$	$48.29^{(a)}$
Inclination Angle(i)	$40^{(ref2)}$	$45^{(ref4)}$	$40^{(ref2)}$
Warm corona Inner Radius	–	$43^{(ref4)}$	$6^{(a)}$
Warm Corona Temperature	–	$1.98 \times 10^{6(ref4)}$	$6.58 \times 10^{6(a)}$
Warm corona optical depth/Photon index	–	$2.28^{(ref4)}$	$20.26^{(a)}$
Inner Cold Disk Radius(r_{in})	$35^{(a)}$	$151^{(ref4)}$	$94.87^{(a)}$
Outer Cold Disk Radius(r_{out})	$10000^{(a)}$	$282^{(ref4)}$	$10000^{(a)}$
Color Correction	$2.4^{(ref2)}$	$1.0^{(ref4)}$	$1.0^{(a)}$
BLR Contribution(f_{BLR})	$12\%^{(a)}$	$40\%^{(a)}$	$30\%^{(a)}$
Lamp Luminosity(L_x)	$1.26 \times 10^{44(a)}$	$1.247 \times 10^{44(ref4)}$	$9.68 \times 10^{43(a)}$
Eddington Ratio	$0.02^{(ref3)}$	$0.027^{(ref4)}$	$0.017^{(a)}$
Starlight	6.74×10^{-15}	5.39×10^{-15}	6.76×10^{-15}

Note. Columns are (1) name of the parameter used in the model, with values given in columns (2), (3) and (4) for Models A, B, and C, respectively. Black hole mass in unit of $M_\odot$, corona height in unit of r_g, inclination angle in degree, inner disk radius and outer disk radius in r_g, lamp luminosity in $erg\ s^{-1}$. Warm corona optical depth or a photon index are alternative (equivalent) parameters of Comptonization models. Starlight normalization is given in erg s^{-1} cm^{-2} $Å^{-1}$ at 5100 Å. References for the fixed parameters during fitting: (ref1) Netzer (2022); (ref2) Kammoun et al. (2021b); (ref3) Crenshaw et al. (2009); (ref4) Kubota & Done (2018); (a) fitted parameters. For model C we assume standard ΛCDM cosmology, with $H_0 = 70$ km s^{-1} Mpc^{-1}, $\Omega_m = 0.3$.

and the bolometric luminosity in our analysis. We assume that the distance to the source is known, and corresponds to the source redshift. The issue of the Hubble constant determination will be addressed separately in Section 5.

4.1. BLR properties from FRADO

The global model parameters adopted for NGC 5548, combined with the assumption of a dust sublimation temperature of 1500 K, allow us to uniquely determine the structure of the BLR. Notably, the FRADO model is specifically applicable to low-ionization lines such as Hβ, Mg II, and Fe II. In this framework, the cloud positions within the BLR are determined by the FRADO model, with parameters relevant to NGC 5548: $M_{\rm BH} = 5 \times 10^7 M_\odot$ (Netzer 2022), an Eddington ratio of 0.02 (Crenshaw et al. 2009), and an assumed metallicity 5 times solar.

We present the distribution of clouds forming the BLR in NGC 5548 in Figure 1. The upper panel presents the overall 3-D structure, revealing a complex cone-like configuration where no clouds escape to infinity due to the low Eddington rate. The lower panel provides a cross-section of this distribution, with the black line marking the thickness of the underlying Keplerian disk. This disk structure accounts for the effects of radiation pressure and opacity, as described by Różańska et al. (1999), both of which play a crucial role in shaping its complex geometry. A notable feature is the abrupt change in disk height, corresponding to the transition from the inner radiation pressure-dominated region to the outer gas-dominated region, which significantly impacts the cooling efficiency of the disk and its overall structure.

In this model, clouds are launched from the disk surface but remain relatively close to it, with the ratio of vertical height (z) to radial distance (r) staying below 5%. This limited height is a direct consequence of the low Eddington ratio, giving the BLR a geometry that closely resembles a puffed-up disk surface. The z/r ratio in the model peaks near the inner edge of the BLR, which is defined by the dust sublimation temperature reached at approximately $\sim 2260\ r_g$ for the adopted $M_{\rm BH}$, Eddington rate and metallicity. At this radius, the Keplerian velocity is ~ 6300 km s^{-1} for this $M_{\rm BH}$, implying that the full width at half maximum (FWHM) of the emission lines could reach up to twice this value. This result based on FRADO model is consistent with the Hβ FWHM of 10161 ± 587 km s^{-1} reported by Pei et al. (2017). However, contributions from larger radii act to moderate this broadening.

The position of the clouds and their velocity field allow us to construct a 2-D velocity-delay map (see Figure 2, upper panel) which we consider as representative for Hβ line, assuming a viewing angle of 40 degrees, which is likely representative of NGC 5548 (Pancoast et al. 2014; Cappi et al. 2016; Wildy et al. 2021; Horne et al. 2021). Our velocity–delay map closely resembles the predictions of a simple flat Keplerian disk model, as the vertical velocities are minimal, no outflows are included, and no selective shielding is assumed. It shows some similarity in the overall shape to the map derived observationally by Horne et al. (2021) (see their Figures 5 and 7).

However, the main inconsistency lies in the narrower velocity extent observed in our velocity-delay map, which shows emission up to $\sim \pm 4000$ km s^{-1}, while Horne et al. (2021) reported observed Hβ emission extending to $\sim \pm 8000 - 10000$ km s^{-1}, although the majority of the response is concentrated within $\sim \pm 5000$ km s^{-1}. Note that, FRADO

A&A proofs: manuscript no. main_rev3_no_color

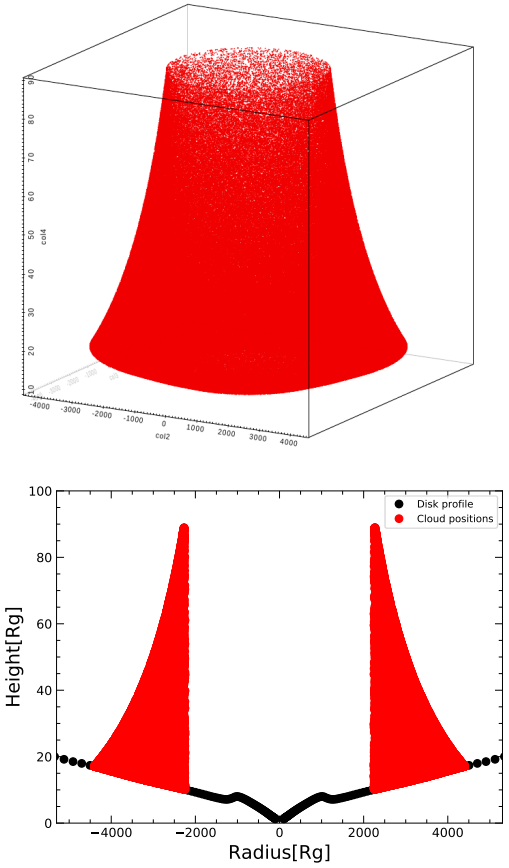

Fig. 1. Upper panel: 3-D plot of cloud positions from FRADO model for NGC 5548 with $M_{BH} = 5 \times 10^7 M_\odot$, $L/L_{Edd} = 0.02$, metallicity Z = 5 in solar units. The axes are in units of r_g. Bottom panel: a cross-section of cloud positions for $y > -300\, r_g$ and $y < 300\, r_g$. The black line indicates the thickness of the Keplerian disk. Clouds form a geometrically thin complex layer above the disk.

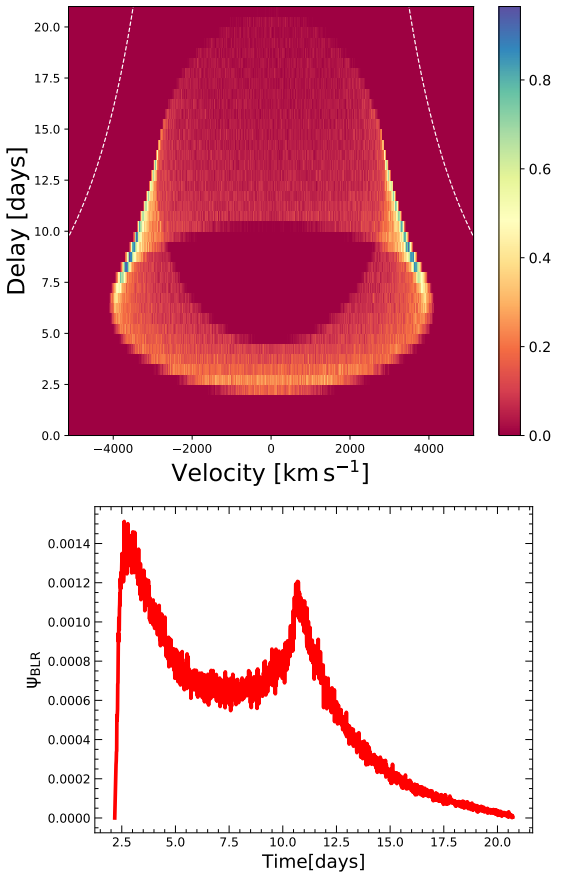

Fig. 2. Upper panel: Velocity–delay map of NGC 5548 constructed from FRADO model with inclination angle i = 40 degrees. Color coding represents the number density of BLR clouds in each velocity-delay bin. The white dashed line shows the virial envelope corresponding to Keplerian disk-like rotation for $v^2 \times \tau$ = constant with $M_{\rm BH} = 5{\times}10^7\, M_\odot$. Bottom panel: BLR response function generated using the cloud positions from the model shown in Figure 1, assuming an inclination angle of i = 40 degrees.

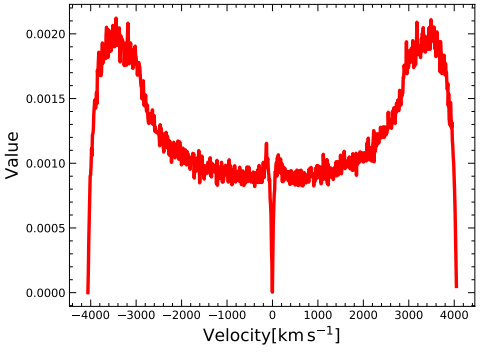

Fig. 3. Line profile generated by the FRADO model using the parameters from Figure 1.

inherently assumes that the BLR originates beyond the dust sublimation radius, which is appropriate for low-ionization lines like Hβ and thus naturally predicts narrower velocity distributions, consistent with emission from outer, slower-moving regions of the BLR. While, the broader velocity distributions observed by Horne et al. (2021) are shaped by contributions from the inner, dust-free high-ionization zones (dominated by CIV, He II lines) of the BLR, where gas orbits closer to the black hole at higher Keplerian speeds.

Nevertheless, the exact comparison is difficult since the observational Hβ map in Horne et al. (2021) seems to be strongly contaminated by He II emission. Notably, while the red wing of the observed Hβ shows a Keplerian structure, the blue wing appears significantly weaker, suggesting substantial He II contamination. In our model, in its present form, we cannot explain such asymmetry. However, such asymmetries in the Hβ line are well-documented and known to evolve over time in a quasi-periodic fashion (Shapovalova et al. 2004). Bon et al. (2016) explained

such phenomenon as caused by the presence of the secondary black hole, perturbing BLR, by precession of the outer part of the disk, or spiral waves in the disk. All such mechanisms will give asymmetry between blue and red-shifted wing of the flat BLR coexisting with the disk. In the future we could include the warped disk into FRADO model, but this is beyond the scope of the current paper.

Next, we derive the BLR response function by projecting the map onto time axis. The resulting shape, shown in Figure 2, lower panel, exhibits two distinct peaks: one at shorter time delays, around ~ 2.6 days, corresponding to the clouds on the same side as the observer, and the other peak arising from the clouds on the opposite side of the black hole. The shape of our modeled response function does not perfectly replicate the observed one reported by Horne et al. (2021). In their analysis using the MEMECHO software for Hβ (see Figure A.1 for comparison), the projected response exhibits two peaks: a prominent one at approximately 2 days and a second, much smaller peak at around 25 days. While our first peak aligns well with theirs at ~2 days, our second peak appears closer in time, at ~11 days, and is relatively stronger than the second peak reported by Horne et al. (2021). Despite these differences, it is important to emphasize that our model relies solely on global parameters, without introducing arbitrary values such as inner or outer BLR radii. This absence of free parameters enhances the significance of the observed similarity between the modeled and empirical response functions. Additionally, we assess the consistency between the BLR response function recovered from our FRADO model and the Hβ emission-line response function derived from spectroscopic RM data by Horne et al. (2021) in Section 7.

By integrating the BLR response profile derived from the FRADO model, we calculate a mean delay of 8.101 days for a viewing angle of 30 degrees and 8.105 days for a viewing angle of 40 degrees. This delay is measured relative to the X-rays. To compare it with delays at other wavelengths, such as the commonly used 5100 Å, it is essential to account for the net time delay between the X-rays and the specific wavelength of interest.

The measured time delay of the Hβ line relative to the 5100 Å continuum during the 2014 campaign (January to June) was reported by Pei et al. (2017) as $4.17^{+0.36}_{-0.3}$ days, which is shorter than predicted by the radius–luminosity relation. This Hβ delay ranks among the shortest ever recorded for NGC 5548. In contrast, the mean response function from the 1998−2001 campaign peaked around 20 days (Cackett & Horne 2006). Horne et al. (2021) later explored the nature of this shorter delay in detail, finding that the response function exhibited a secondary peak at approximately ~ 25 days but began with a high value near to zero time delay. Their observed map also supports the primary response originating from the near side of the BLR, facing the observer.

To compare the predicted and observed time delays, we need to add the delay of the 5100 Å continuum relative to X-rays to the observed data. Since the exact time delay at 5100 Å was not measured by Fausnaugh et al. (2016), we averaged their measurements around this wavelength and included the hard X-ray time delay, also provided in their study. This results in an estimated observed time delay for Hβ relative to X-rays of 6.83 ± 0.53 days. Our predicted delay is slightly longer. This discrepancy may stem from the long tail in the delay, which the model accounts for but may not be fully captured in the observations. Alternatively, the delay could be shorter if there is intervening material between the black hole and the BLR, potentially shielding part of the most distant flow. Another possibility is that the dust temperature in the BLR model, as discussed by Panda et al. (2020) and Naddaf et al. (2021), differs from the assumed 1500 K.

Additionally, the model predicts an upper limit for the covering factor of the BLR. If the cloud distribution is not transparent, the region intercepts all radiation emitted within inclinations greater than the aspect ratio z/r of the cloud distribution. As shown in Figure 1, the model suggests that less than 4% of the radiation can be intercepted by the BLR, as the cloud height is generally small compared to the radius. This is notably lower than the 10% to 30% covering factor typically expected from BLRs (e.g. Baldwin et al. 1995; Korista & Goad 2019; Panda 2021; Panda et al. 2022). In contrast, the yearly variations observed in the line profile of NGC 5548 suggest that the disk can be distorted and/or precessing (e.g., Shapovalova et al. 2009, see their Figure 2). Such a departure from the disk model strictly perpendicular to the symmetry axis may affect the irradiation of the launched clouds and this way to modify the BLR emissivity.

The distribution of BLR clouds enables us to roughly estimate the shape of the Hβ line predicted by the model. In this estimation, we neglect the vertical cloud velocities and only consider the projected rotational velocities towards the observer. The resulting line shape, shown in Figure 3, reveals a two-peak structure that is even more pronounced than that observed in the data. The FWHM predicted by our model approaches 8000 km s^{-1}. In comparison, the measured FWHM of the Hβ line from the rms spectrum was 10161 ± 587 km s^{-1} (Pei et al. 2017). Notably, the FWHM values have varied over the years, indicating the dynamic nature of the BLR. For instance, Peterson et al. (2004) reported an Hβ FWHM of 7202 ± 392 km s^{-1}, which is in good agreement with our model estimate. These variations suggest that our model captures a plausible state of the BLR, consistent with the historical range of observed line widths.

4.2. The BLR emissivity

To model the emission characteristics of photoionized clouds, we perform `CLOUDY` simulations that account for both line and continuum contributions. During our computations, we consider both line and continuum emissions, incorporating radiation from both inward and outward directions to ensure equal visibility of the illuminated and un-illuminated sides of the clouds. Among the most prominent features that emerge are the Balmer and Paschen edges, as illustrated in Figure 4. The depths of these edges are governed by the specific model parameters adopted (see the most recent study by Pandey et al. 2023).

The reprocessing calculations are performed for a single representative cloud, using the full shape of the SED as the incident radiation, as described in Section 3.4. This approach is admittedly a significant simplification, since in reality each cloud is exposed to a different incident spectrum depending on its location and orientation. This spectral variation is properly accounted for in the computation of the radiation force. However, generating comprehensive tables of local emissivity for the full range of incident spectra lies beyond the current scope of this work. Such an extension is essential for future studies to improve the physical realism of the model.

4.3. Exemplary shape of the response function

After deriving the BLR response function using FRADO model and the emissivity profile from `CLOUDY` for NGC 5548, we com-

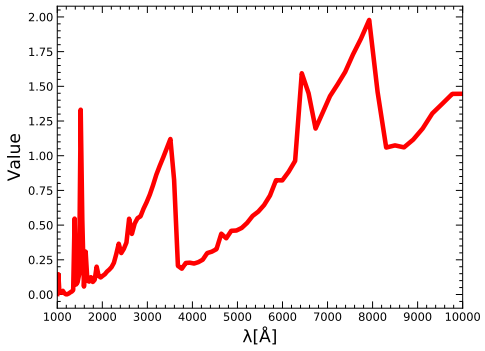

Fig. 4. Emissivity profile (ratio of the reprocessed to the incident continuum) of a BLR cloud for the adopted parameters: $\log n_H$ [cm^{-3}] = 11, $\log L$ [erg s^{-1}] = 44, and the BLR distance of 10^{16} cm.

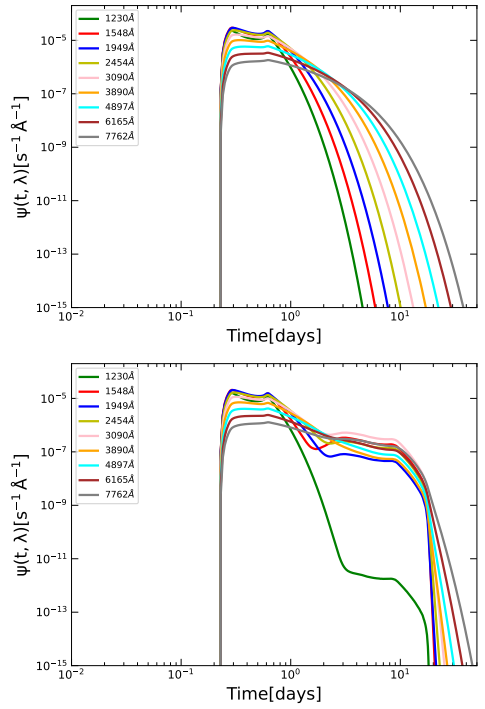

Fig. 5. Upper panel: Response functions of the disk at different wavelengths. Bottom panel: Combined response functions of the disk and BLR across the same wavelengths. These representative response functions are obtained for Model C. Parameters used: $M_{\rm BH} = 5.0 \times 10^7 M_\odot$, Eddington ratio = 0.015, $L_X = 9.68 \times 10^{43}$ erg s^{-1}, height: $h = 48.29 r_g$, $R_{in} = 94.87 r_g$, $R_{out} = 10000 r_g$, and viewing angle: $i = 40$ degrees.

pute the disk response function and the combined disk-BLR response function using equations 6 and 8, respectively. These results are presented for nine different wavelengths in the upper and bottom panels of Figure 5. The disk response function (upper) displays a single-peaked structure, whereas the combined response function (bottom) exhibits a bimodal shape, as expected, with the first peak corresponding to direct emission from the disk, and the second arises from delayed reprocessing by the BLR. Moreover, the overall time delay associated with the combined response function is significantly longer than that of the disk alone, consistent with the findings of Netzer (2022).

4.4. Time delays in representative models

This paper serves as a pilot study, focusing on three distinct global setups rather than exploring the full parameter space. In this section, we assume that the source distance can be determined from its redshift, enabling a unique conversion of bolometric luminosities to fluxes. We define these setups as Model A, Model B, and Model C, which were shortly introduced in Section 2. Each setup is characterized by different global parameters. In all cases $M_{\rm BH}$ was fixed (in Models A and C, the $M_{\rm BH}$ is derived from observational data (Netzer 2022)), whereas in Model B, it is adopted from the corresponding model reference (Kubota & Done 2018). All models are supplemented with the BLR components. A detailed discussion of each model follows in the subsequent sections.

4.4.1. Model A

To account for disk atmosphere effects, Model A employs a standard accretion disk framework with a fixed color correction. It uses well-established literature values for $M_{\rm BH}$ and Eddington ratio, and does not include the warm corona component. With only a few free parameters, the model incorporates the BLR contribution alongside the accretion disk emission to fit the observed continuum time delays and spectral energy distribution. We minimize the number of free parameters by relying on the basic parameter values from the literature, including the $M_{\rm BH}$, Eddington rate, color correction, and viewing angle (see Table 1 for the adopted values). Specifically, the adopted color correction of 2.4 comes from the studies of Kammoun et al. (2021b, 2023). The model does not include the warm corona, and the cold disk extends down to the ISCO (6 r_g). The BLR model is then directly determined based on the assumed $M_{\rm BH}$, Eddington rate, and a fixed metallicity of 5, but the covering factor is left as a free parameter of the model. The other key parameter is the corona height. The resulting predictions are presented in Figure 6.

The model reproduces the time delay quite well, the Balmer edge at ∼ 3600 Å is well reproduced, the region of the Paschen jump is not so well fitted. The covering factor and the corona height optimizing the fit of the time delay are given in Table 1.

Below, we outline the key advantages and limitations of this model.

Model advantages:

- three free parameters: starlight level, inner disk radius, BLR fraction
- the Hβ delay is approximately recovered
- the double peak shape is approximately recovered
- the time delay is well modeled

Model limitations:

- The optical/UV SED is inconsistent with the observed data

In Model A, the discrepancy between the observed and modeled SED is substantial in the blue part, and cannot be resolved by adjusting any model parameters without making the time delay fit worse. The required lamp height lead to a very blue spectrum in the UV due to the color correction applied. The time delay is primarily driven by the disk response, with the BLR contribution appearing only near the Balmer edge−contrary to the

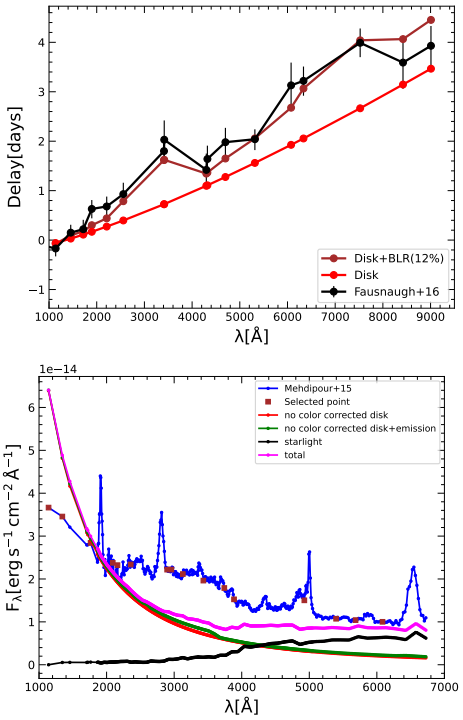

Fig. 6. Model A. Upper panel:The observed delay from Fausnaugh et al. (2016) is represented in black. The delay calculated from the disk response function alone is shown in red, while the delay calculated from the combined response function of the disk and BLR is shown in brown. Bottom panel: The observed SED from Mehdipour et al. (2015) is shown in blue. The disk SED is represented in red, while green illustrates the disk SED combined with the emission lines. The starlight contribution is shown in black color. The final SED, incorporating contributions from the disk, star, and emission lines, is shown in purple. The selected points used for estimating the χ^2 value are represented by brown squares. Parameters: $M_{\rm BH} = 5.0{\times}10^7 M_\odot$, Eddington ratio = 0.02, $L_X = 1.26 \times 44$ erg s^{-1}, height: $h = 20r_g$, $R_{in} = 35r_g$, $R_{out} = 10000r_g$, color correction= 2.4, viewing angle: $i = 40$ degrees.

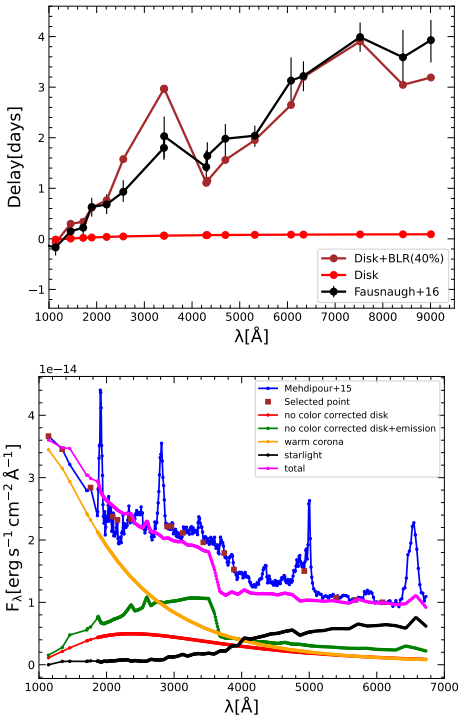

Fig. 7. Model B. Upper panel: The observed delay from Fausnaugh et al. (2016) is represented in black. The delay calculated from the disk response function alone is shown in red, while the delay calculated from the combined response function of the disk and BLR is shown in brown. Bottom panel: The observed SED from Mehdipour et al. (2015) is shown in blue. The disk SED is represented in red, while green illustrates the disk SED combined with the emission lines. The starlight contribution is represented in black, while the warm corona is shown in orange. The final SED, incorporating contributions from the disk, star, warm corona, and emission lines, is shown in purple. The selected points used for estimating the χ^2 value are represented by brown squares. Parameters: $M_{\rm BH} = 5.5{\times}10^7 M_\odot$, Eddington ratio = 0.02, $L_X = 1.247 \times 44$ erg s^{-1}, height: $h = 43r_g$, $R_{in} = 151r_g$, $R_{out} = 282r_g$, color correction= 1.0, viewing angle: $i = 45$ degrees.

findings of Netzer (2022). This discrepancy arises because the disk contribution is underestimated due to the fixed color correction being set too high. While this increases the time delay by pushing the fixed-color emission outward, it simultaneously shifts the disk spectrum toward the far-UV. Consequently, we do not include the SED fit from Model A in the χ^2 minimization, as further adjustments would not improve the fit.

The starlight contribution in our decomposition is 6.74×10^{-15} erg s^{-1} cm^{-2} Å^{-1}, comparable to reported value of 6.2×10^{-15} erg s^{-1} cm^{-2} Å^{-1} (Mehdipour et al. 2015). Furthermore, this model fails to reproduce both soft and hard X-rays, as it includes only a cold disk. As a result, there is an inconsistency between the shape of the incident continuum assumed in the CLOUDY modeling and the continuum produced by the model itself.

4.4.2. Model B

In Model B, we adopt the framework of Kubota & Done (2018), where the innermost part of the accretion disk is replaced by a hot corona. In our setup, the standard accretion disk extends from 151 r_g to 282 r_g, and we do not apply any color correction since the disk in this region remains cold. The global system parameters and the inclination angle are consistently taken from Kubota & Done (2018). The free parameters in the model are the BLR contribution, f_{BLR}, and the level of starlight. The corona height is fixed at the value of the inner radius of the warm corona, i.e., 43 r_g.

The results of this model are presented in Figure 7. As in Model A, we employ the same BLR response function (see Section 4.1). However, this approach may introduce minor inconsistencies due to slight differences in $M_{\rm BH}$ and accretion rate. While the time delay fit remains broadly satisfactory, the SED is again not well reproduced. The reduced inner disk radius results in a steep decline in the disk spectrum at shorter wavelengths.

In this configuration, the total time delay is predominantly influenced by the BLR, with only a minimal contribution from the accretion disk. Consequently, the contribution from BLR to the time delay is significantly higher than in Model A. Addition-

A&A proofs: manuscript no. main_rev3_no_color

Table 2. Time delay measurements.

Wavelength (Å)	$\tau_{centroid}$ (days)	τ_{model} (days)
1158	$-0.17^{+0.16}_{-0.16}$	−0.14
1479	$0.15^{+0.18}_{-0.16}$	0.13
1746	$0.22^{+0.16}_{-0.19}$	0.39
1928	$0.63^{+0.19}_{-0.18}$	0.78
2246	$0.68^{+0.19}_{-0.20}$	0.60
2600	$0.93^{+0.20}_{-0.23}$	1.62
3467	$1.80^{+0.24}_{-0.24}$	2.23
3472	$2.03^{+0.43}_{-0.39}$	2.73
4369	$1.42^{+0.36}_{-0.33}$	1.12
4392	$1.64^{+0.31}_{-0.27}$	1.15
4776	$1.98^{+0.34}_{-0.29}$	1.51
5404	$2.04^{+0.22}_{-0.20}$	1.95
6176	$3.13^{+0.41}_{-0.46}$	2.61
6440	$3.22^{+0.30}_{-0.29}$	2.92
7648	$3.99^{+0.29}_{-0.29}$	4.03
8561	$3.59^{+0.53}_{-0.54}$	3.64
9157	$3.93^{+0.44}_{-0.40}$	3.58

Note. Columns are (1) pivot-wavelength of the filters in the observed-frame, (2) measured inter-band delays from Fausnaugh et al. (2016) in the rest-frame, (3) recovered inter-band delays from Model C. The inter-band delays are with respect to HST 1367 Å.

ally, the amount of starlight in this case is 5.39×10^{-15} erg s^{-1} cm^{-2} Å^{-1}, less than corresponding value in Model A.

Model advantages:

- only two free parameters: starlight level, BLR fraction
- the Hβ delay is approximately recovered
- the double peak shape is approximately recovered
- the time delay is reasonably well modeled

Model limitations:

- Although the high-energy portion of the SED is reasonably well recovered, this model fails to accurately fit the 3000–4000 Å wavelength range, which includes the Balmer jump, and shows some inconsistencies at longer wavelengths in the optical regime. This is related to the limited flexibility due to a small number of free parameters.
- The modeled time-delay spectrum is predominantly influenced by the BLR, with negligible contribution from the accretion disk, in contrast to observed AGN time-delay spectra that exhibit significant contributions from both the accretion disk and the BLR (Mandal et al. 2025).

4.4.3. Model C

This model represents a generalization of Model B. Rather than fixing certain parameters to the values derived by Kubota & Done (2018), we treat them as free parameters and allow the data to constrain them through fitting. First, we allow for the variation of the radii dividing the zones of hot corona, warm corona and outer disk. We assume that the outer radius of the cold disk is large. Then, we vary the warm corona parameters (optical depth, temperature) as well as the Eddington rate, to achieve the best fit to the broad band spectrum (including X-rays), and to time delays. Model parameters are listed in Table 1.

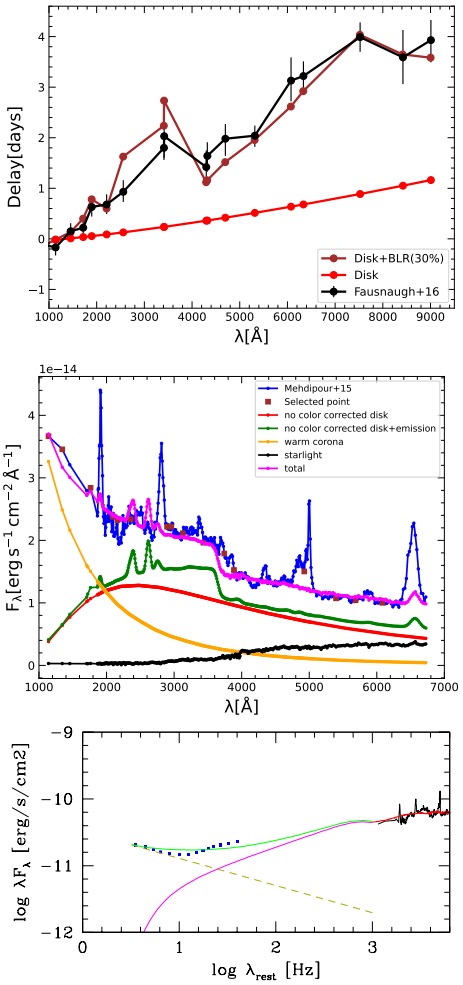

Fig. 8. Model C. Upper panel: The observed delay from Fausnaugh et al. (2016) is represented in black. The delay calculated from the disk response function alone is shown in red, while the delay calculated from the combined response function of the disk and BLR is shown in brown. Middle panel: The observed SED from Mehdipour et al. (2015) is shown in blue. The disk SED is represented in red, while green illustrates the disk SED combined with the emission lines.The starlight contribution is represented in black, while the warm corona is shown in orange. The final SED, incorporating contributions from the disk, star, warm corona, and emission lines, is shown in purple. The selected points used for estimating the χ^2 value are represented by brown squares. Parameters used: $M_{\rm BH} = 5.0 \times 10^7 M_\odot$, Eddington ratio = 0.015, $L_X = 9.68 \times 10^{43}$ erg s^{-1}, height: $h = 48.29 r_g$, $R_{in} = 94.87 r_g$, $R_{out} = 10000 r_g$, and viewing angle: $i = 40$ degrees. Bottom panel: X-ray–UV-optical SED fitting. The warm corona is represented by the magenta line, the hard X-ray power law is shown in dashed gold, the green line represents the sum of the two, and the black line displays the optical data.

The time delays recovered from this model, along with the observed inter-band delays from Fausnaugh et al. (2016), are presented in Table 2. The corresponding fitted SEDs, are displayed in the upper, middle, and bottom panels of Figure 8,

respectively. The Balmer edge is well reproduced in the lag-spectrum. Paschen edge is expected to be less prominent, as shown by Pandey et al. (2023) at the basis of CLOUDY simulations.

Additionally, the broad-band SED is now well represented, with the starlight continuum of 6.76×10^{-15} erg s^{-1} cm^{-2} Å^{-1}, which is nearly identical to the value of 6.2×10^{-15} erg s^{-1} cm^{-2} Å^{-1} reported by Mehdipour et al. (2015). The middle panel of the figure provides a detailed view of the optical/UV portion of the spectrum, consistent with previous presentations. Furthermore, the bottom panel displays the full X-ray-UV-optical spectral range on a logarithmic scale, allowing for clearer visualization of the broad-band fit. In this representation, both the hard X-ray component and the contribution of the warm corona to the X-ray band are clearly visible. This contrasts with Model A, which lacked a warm corona and therefore failed to reproduce the observed soft X-ray data. In comparison, Model B, by construction from Kubota & Done (2018), is consistent with the X-ray band and thus its X-ray spectral range is not plotted in this figure. However, it is important to note that Kubota & Done (2018) did not fit the spectroscopic optical data, and as a result, the discrepancy between their model and the actual optical observations was not apparent in their analysis.

The disk contribution to the time delay in this model falls between the contributions in Model A and Model B. Overall, the time delay is reproduced much more accurately compared to the other two models, providing a better fit to the observed data. The contribution of the corona to the spectrum is dominating the part of the spectrum below ~ 2000 Å.

Model advantages:

- limited number of parameters (although larger than in Model B)
- the Hβ delay is approximately recovered
- the double peak shape is approximately recovered
- the time delay is well modeled
- We successfully reproduce the Balmer jump in the observed SED, and our modeled SED is consistent with the observed spectrum.

In conclusion, this model offers a significant improvement in both time delay and SED fitting, with a more realistic representation of the BLR contribution to the observed continuum time delays and a better overall alignment with the observed spectral features.

5. Distance Estimation from generalized Model C

Having considered the final fit from Model C as successful, we now assess whether our model improves the determination of the Hubble constant for this source, as done by Cackett et al. (2007). To begin, we first explore analytical estimates and subsequently evaluate the method that should be employed for actual data fitting.

5.1. Analytical estimate of H_0

Collier et al. (1999) proposed a method for determining H_0 based on continuum time delays, under the assumption that the inter-band time delays are a result of a classical accretion disk structure, as given by the following equation

$$H_0 = 89.6 \left(\frac{\lambda}{10^4}\right)^{3/2} \left(\frac{z}{0.001}\right) \left(\frac{\tau}{day}\right)^{-1} \left(\frac{f_\nu / cosi}{Jy}\right)^{1/2} \left(\frac{\chi}{4}\right)^{4/3} \left[\frac{\text{km}}{\text{s Mpc}}\right] \quad (11)$$

where τ is the time delay measured at the wavelength λ, z is the source redshift, f_ν is the measured flux at the frequency ν corresponding to the wavelength λ, and χ is the parameter which is used to account for systematic discrepancies due to conversion of annulus temperature to the corresponding wavelength λ at a given radius. According to Wien's law, $\chi = 4.97$ (Netzer 2022); however, under the assumption of a flux-weighted radius, χ is typically taken to be 2.49 (Edelson et al. 2024). In our analysis, considering the AGN accretion disk SED as a multicolored blackbody spectrum, we adopt $\chi = 4$.

We can test the model using this formula, but it is important to use the disk delay rather than the total combined disk plus BLR time delay. The disk delay from Model C is $\tau_{5100} = 1.008$ days at $\lambda = 5100$ Å relative to the X-ray source. For a corona height of $h = 0$, this delay becomes $\tau_{5100} = 0.898$ days (i.e., 1.008 − 0.110 days), and this value is therefore used in equation (11). We convert the flux from Lu et al. (2022), $F_\lambda = 5.22 \times 10^{-15}$ erg s^{-1}cm^{-2}Å^{-1}, to $f_\nu = 4.590 \times 10^{-26}$ erg s^{-1}cm^{-2}Hz^{-1}. Assuming an inclination angle of $i = 40$ degrees for the source, we derive H_0 of 47.54 km s^{-1}Mpc^{-1}. This represents a considerable improvement over the value of $H_0 = 15$ km s^{-1} Mpc^{-1} obtained by Cackett et al. (2007) for the same source. The difference is largely due to the fact that we are using only the disk delay. If we had used the total time delay (disk + BLR) of 2.00 days, we would have obtained a much lower value of $H_0 = 21.34$ km s^{-1} Mpc^{-1}, closer to the result from Cackett et al. (2007).

However, adopting $\chi = 2.49$ yields a derived H_0 of 25.27 km s^{-1} Mpc^{-1} for the disk delay, or 11.34 km s^{-1} Mpc^{-1} when including both the disk+BLR delay. Since there is no universally accepted value of χ, equation 11 inherently carries additional uncertainty associated with this parameter.

5.2. Direct method to measure the distance to the source and H_0 from combined spectral and time delay fitting

The Model C in the version described in Section 4.4.3 is based on the known distance which in turn constraints the accretion rate and the bolometric luminosity of the source. Therefore, if we indeed want to measure the distance to the source we cannot rely on quantities that were determined knowing its distance. We thus must allow the Eddington rate to cover a broad range, reflecting the possibly broad range of the luminosity distance of the source. However, we keep $M_{\rm BH}$ fixed, as it is derived from spectral fitting−using the FWHM/line dispersion (σ) of the Hβ line and the time delay measured from RM, making it independent of the luminosity distance. We also fix the viewing angle.

In this Section, we present a series of computations using a grid of pre-selected luminosity distances. For each luminosity distance, we fit several model parameters by minimizing the χ^2 value. The parameters we vary when fitting the spectrum include the Eddington ratio ($\dot{m}$), the cold disk inner radius (r_{in}), the height of the corona (h), the optical depth of the warm corona ($\tau_{\rm op-depth}$), the temperature of the hot corona (T_e), the covering factor of the BLR (f_{BLR}), and the normalization of the starlight (A_{star}).

The incident radiation in the `CLOUDY` computations is determined by the choice of the luminosity distance, as the incident radiation must match the observed hard X-ray flux. Therefore, for each value of the luminosity distance, we use a different spectral shape for the BLR component. Figure 9 illustrates exemplary shapes corresponding to different normalizations of the incident flux. It is important to note that the distance to the BLR and the

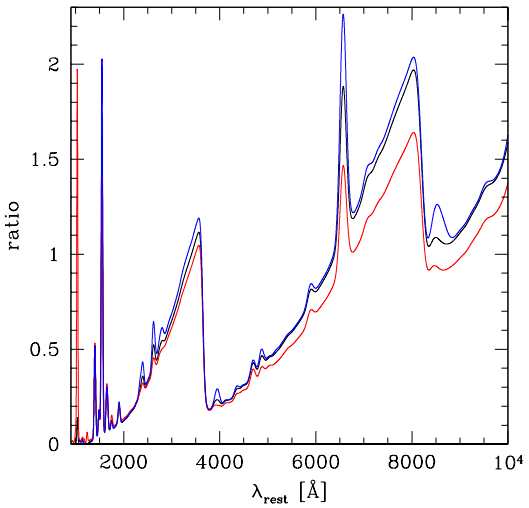

Fig. 9. Examples of the BLR emission profile for three values of the logarithm of the bolometric luminosity $\log L$ [erg s^{-1}] = 44.0 (black line), 43.8 (blue line), and 44.2 (red line) corresponding to the three values of the luminosity distance, D_L = 70, 56, and 84 Mpc, respectively.

internal parameters of the clouds remain unchanged throughout these computations.

The dependence of the BLR shape on the incident flux is not monotonic. However, the changes are relatively small, as the range of the considered flux amplitude variation is limited. It is important to emphasize that we do not modify the spectral shape of the incident radiation, as it was derived from observations rather than the model. During spectral fitting, we construct the final model spectrum based on absolute luminosity and compare it to the observed flux, taking into account the adopted distance as

$$F_\lambda = \frac{L_\lambda}{4\pi D_L^2} \tag{12}$$

The value of χ^2 is calculated at several wavelengths, excluding the intense emission lines. Soft X-ray data points, taken from Mehdipour et al. (2015), are also included in the calculation. We assume a 10% error in the spectral fitting process. For the time delay, the χ^2 value is based on the errors complementing the time delay measurements (Fausnaugh et al. 2016).

The results of the combined delay and spectra fitting are shown in the upper panel of Figure 10 in luminosity distance space. Now, in the χ^2–D_L plane, each point in the sequence corresponds to the same Eddington ratio and other parameters in both the time delay and spectral fitting. The minimum occurs at D_L = 74 Mpc in our grid, though the minimum is relatively shallow. The best fits for both the spectrum and the time delay at this grid are also presented in Figure 8.

The accretion rate predictably increases along the sequence, from 0.008 to 0.038, while the covering factor remain roughly the same, at ∼ 30 %. The results are weakly sensitive to the lamp height, which remains close to ∼ $25r_g$, as well as to the inner radius of the cold disk, which is located at ∼ $90r_g$ in all fits.

The value of the luminosity distance can be directly translated into the Hubble constant using the expression $H_0 = zc/D_L$, given that the redshift to the source is small. Thus, the same result, but as a function of the implied H_0, is shown in the lower panel of Figure 10. The distance of D_L = 74 Mpc corresponds to a Hubble constant of 66.8 km s^{-1} Mpc^{-1}. Interpolating between the grid points we find the minimum location at 73.96 Mpc. Since the minimum is shallow, the error is large, leading to our constraint of D_L as $D_L = 74.0^{+2.4}_{-10.0}$ Mpc. This translates to Hubble constant constraints: $H_0 = 66.9^{+10.5}_{-2.1}$ km s^{-1}Mpc^{-1}.

The error estimate presented here is necessarily approximate, as it is based on a qualitative assessment of the effective number of independent degrees of freedom (dof) in the model. Our dataset includes 17 measurements of time delays and we sample the spectrum in the same number of wavelengths. The model involves 7 free parameters, in addition to 4 parameters that are held fixed: $M_{\rm BH}$, viewing angle, local cloud density, and column density. Each model realization is computed for a fixed luminosity distance. This setup yields 23 dof. We simply determine the 1 sigma error of the reduced χ^2 as $\chi^2/dof \leq \chi^2_{\rm min}/dof + 1/23$. We did not perform tests whether all these measurements are statistically independent.

A more robust approach to error estimation would be to use a bootstrap resampling method, which could account for eventual correlations. Unfortunately, our current implementation is not optimized for such computationally intensive analysis, which would require at least 100 realizations to obtain reliable error estimates. Code optimization is underway, as we view this methodology as promising for future studies.

Note that, in this analysis, we do not vary all the parameters involved in Model C when calculating the spectral and time delay fits, as described above. Therefore, the derived constraint should be interpreted as an indication that the methodology is working, with further progress expected to reduce the error.

The value is well within the error range of the expected values (Abdalla et al. 2022; Freedman et al. 2024). The measurement error may decrease with improved modeling of the continuum in this source. Additionally, combining measurements from more sources will help further reduce the error. This value is higher than the 47.54 km s^{-1}Mpc^{-1} obtained from the analytical formula, which suggests that the proper methodology – avoiding forced power-law solutions and the extra χ parameter – is essential.

To illustrate the necessity of combining delay and spectral fitting, we also present the results obtained when only one type of data, either delays or spectra is used independently.

In experiments where only the time delay is fitted, we vary four parameters ($\dot{m}$, r_{in}, h, f_{BLR}), while the other three (T_e, $\tau_{\rm op-depth}$, A_{star}) are fixed at the values determined by the spectral best-fit, as these parameters have a negligible impact on the time delay. This strategy is motivated by the fact that spectral fitting is computationally efficient, whereas time delay fitting is considerably more time-consuming. Moreover, when fitting the SED, all parameters must be optimized simultaneously.

The χ^2 values in the luminosity distance space for the SED-only fit are shown in the upper panel of Figure 11. The key parameter that changes with D_L is the accretion rate. The formal minimum of χ^2 occurs at D_L = 58 Mpc, with the Eddington ratio varying from ∼ 0.008 at D_L = 50 Mpc to ∼ 0.034 at D_L = 102

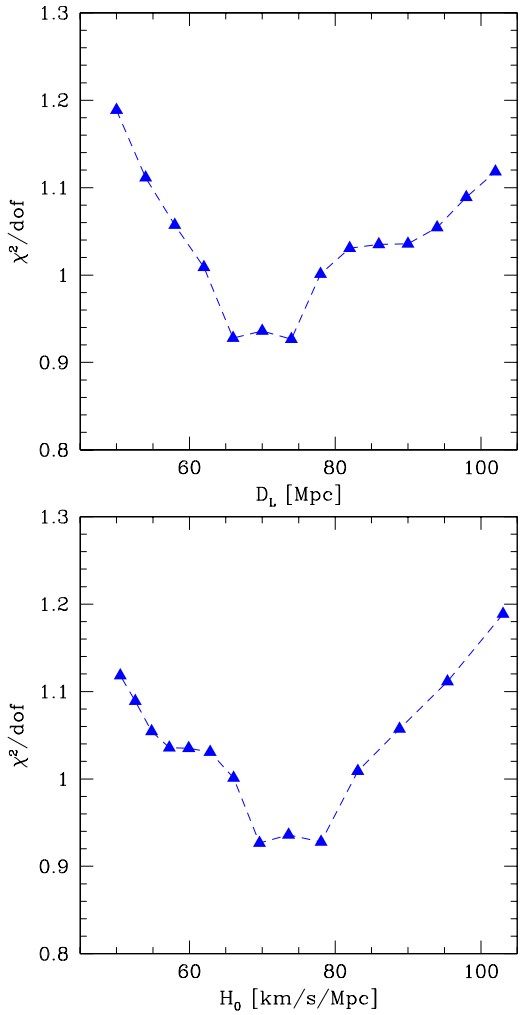

Fig. 10. Upper panel: The sequence of best fits of both the spectrum and the delay as a function of the luminosity distances, marginalized for other model parameters. Bottom panel: The same plot as a function of the resulting Hubble constant.

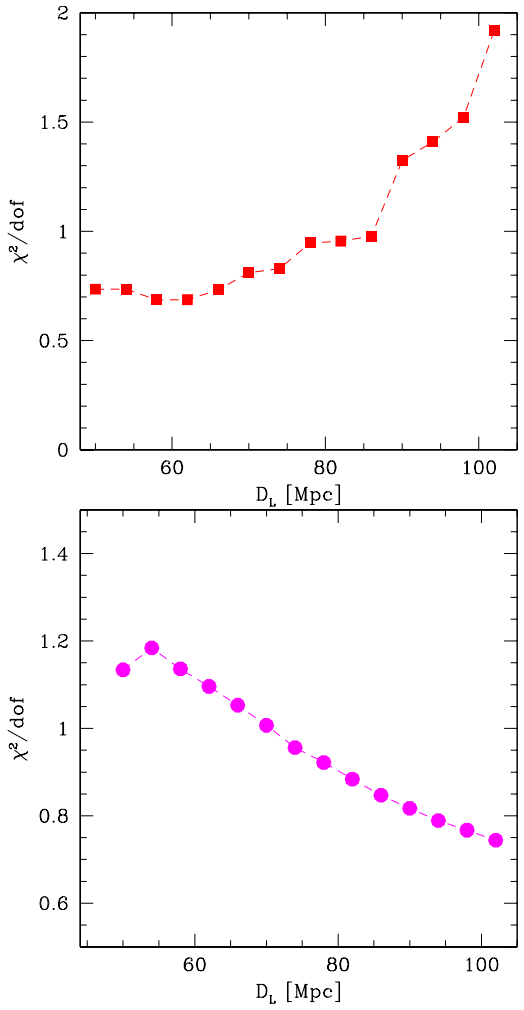

Fig. 11. Upper panel: The sequence of best fits of the spectrum as a function of the luminosity distances, marginalized for other model parameters. Bottom panel: The same plot for the time-delay fitting.

Mpc. Along with this change in the accretion rate, the corona height increases from 16.5 r_g to 53.0 r_g. The covering factor of the BLR, f_{BLR}, remains roughly the same, $\sim$ 0.30. The stellar contribution also decreases by a factor of 4 as D_L increases. Despite these variations, the optical depth of the hot corona remains roughly unchanged at 20, while the electron temperature increases slightly with D_L, from 6.6×10^6 K to 8.0×10^6 K. The reduced χ^2 is of order of 1, suggesting that the adopted spectral errors of 7% are realistic.

The χ^2 values for the case when we fit only the delay data set in the lag-spectrum, are shown in the lower panel of Figure 11. The dependence of χ^2 on D_L is relatively weak, exhibiting an almost monotonic decrease in χ^2 values with increasing luminosity distance. This sequence exhibits very different properties compared to the spectral sequence. The Eddington ratio remains constant at 0.03, independent of D_L, since there is no direct coupling between the delay, the distance, and the source luminosity. The lamp height is monotonically increasing with D_L. Additionally, the weak variation in the irradiation flux does not lead to a substantial change in the model structure.

Therefore, the combined fitting of both the SED and the time lag-spectrum is essential. Spectral fitting enforces a change in the best-fit Eddington ratio with D_L, which, in turn, affects the delay fitting. A small Eddington ratio implies a smaller source size and shorter time delays as expected from standard disk.

6. Discussion

The aim of this paper is two-fold: first, to test the FRADO model for the formation of the BLR, and second, to attempt the estimation of the Hubble constant from such a self-consistent model by determining the redshift-independent distance to the source NGC 5548. While this remains a pilot study, our results demonstrate that the method holds significant potential.

The model itself involves very few parameters. $M_{\rm BH}$ has been fixed, and we have not yet tested its dependence on the results.

However, it is worth noting that $M_{\rm BH}$ can be considered independent from cosmology since it is based on line kinematic width and the measured time delay. The key parameters – Eddington ratio, BLR contribution, and cold disk inner radius are fitted using the observed mean spectrum and the continuum time delays measured in the continuum–RM campaign by Fausnaugh et al. (2016). The best fit favors a redshift-independent distance of ∼ 74 Mpc to the source. This distance, when converted to the Hubble constant, implies a value of $H_0 = 66.9^{+10.5}_{-2.1}$ km s^{-1} Mpc^{-1}. Additionally, the model successfully reproduces the Hβ time delay. One hidden parameter in the FRADO model is the dust sublimation temperature, $T_{\rm sub}$, which we adopt as 1500 K. Variations in this temperature would directly influence the favored distance, roughly following the relationship $r \propto (T_{\rm sub}/1500K)^{-4/3}$.

The multi-wavelength time delays in NGC 5548 have also been modeled in other studies. The original work by Fausnaugh et al. (2016), which provided the delay measurements, employed only power-law parametric modeling. More recently, Kammoun et al. (2023) fitted the NGC 5548 time delay using a new model that incorporates relativistic effects, such as the X-ray reflection component and albedo, while also exploring the influence of black hole spin and corona height. Their SED fitting yielded a higher Eddington ratio (0.05) than our solution, along with a higher $M_{\rm BH}$, resulting in a significantly greater bolometric luminosity for the source compared to our model. However, we cannot analyze this discrepancy in detail, as their best-fit SED was not explicitly presented. While Kammoun et al. (2023) strongly advocate for the inclusion of color correction, they do not account for the BLR contribution in their model. Notably, in both of these studies, the distance to NGC 5548 was determined using redshift measurements.

The recent study by Netzer et al. (2024) shares several key elements with our work. However, their BLR model is not based on a dynamical framework like ours, requiring additional arbitrary parameters to define the dynamics and geometry. At the same time, their study addresses important factors, such as obscuration, which are not considered in our analysis. Despite successfully fitting both the spectra and time delays for their target, Mrk 817, they did not attempt to interpret their results in terms of a redshift-independent distance or derive an estimate for the Hubble constant.

Constructing a complete model of the BLR remains a significant challenge, with progress being made along several fronts. For instance, Long & Dexter (2025) analyzed the STORM data for NGC 5548 and, by combining a few representative geometries with table models that span a range of cloud ionization properties, concluded that none of the simplest models adequately reproduce the observed data. This highlights the limitations of overly simplified assumptions. Additionally, parametric approaches, such as those implemented in the BELMAG code (Rosborough et al. 2024, 2025), exemplify the complexity and richness required to capture the full diversity of BLR structures.

Our approach does not yet incorporate a detailed treatment of the ionization levels of individual clouds, as our objective is more modest and thus we do not aim to reproduce all features of the available data for the NGC 5548 source. Instead, we begin by establishing the dynamics based on the FRADO model, which alone enables us to roughly reproduce key observables such as the Hβ time delay, the transfer function, and the mean spectrum (apart from intensities of all lines), as well as the overall time-delay spectrum.

The geometry adopted in our model naturally leads to double-peaked emission lines. This is consistent with the observed double-peaked structure of the Hβ line, particularly in the rms profile (e.g. Lu et al. 2016; Shapovalova et al. 2009; Long & Dexter 2025). Moreover, other emission lines also exhibit double-peaked profiles (Horne et al. 2021), and the velocity-resolved time delays further support this structure (Long & Dexter 2025). Our model recovered transfer function similarly displays a double-peaked profile, consistent with an axially symmetric geometry dominated by Keplerian motion. In contrast, Horne et al. (2021) obtained an almost single-peaked transfer function for Hβ, which may indicate the presence of cloud emission anisotropy, an effect already considered by Ferland et al. (1979), as well as possible selective shielding of parts of the BLR by outflowing material located within the region.

There remains considerable room for advancement in the coming years, particularly in refining the physical details of BLR modeling. Furthermore, the potential application of continuum time-delay measurements to cosmology provides an additional strong motivation for continued progress in this area.

Taken together, these comparisons highlight the unique strengths of our approach. Unlike previous studies that either relied on power-law fitting, incorporated relativistic effects without addressing the BLR contribution, or did not pursue an independent distance determination, our method integrates spectral fitting and time delay modeling within a self-consistent framework. By leveraging the FRADO model, we obtain a redshift-independent distance to NGC 5548. While further refinements–such as improved continuum modeling and broader sample studies–are needed to reduce uncertainties, our results demonstrate the potential of this methodology in offering an alternative approach to cosmic distance measurements.

6.1. Covering factor

Although we refer to our disk-plus-BLR model as self-consistent, not all of its components are fully self-consistent yet. In principle, for a given $M_{\rm BH}$ and Eddington ratio, the BLR covering factor should be determined by the model. Some tests of the predicted covering factor have been performed for relatively high Eddington ratios (Naddaf et al. 2023; Naddaf & Czerny 2024). However, at lower Eddington ratios, the clouds are located too close to the disk, leading to inconsistencies.

The aspect ratio of the cloud distribution, as shown in Figure 1, implies a covering factor of approximately 5%, whereas the value favored by time delay and spectral fitting is 36%. While the BLR location is well represented, the vertical motion of the clouds appears insufficient when considering only radiation pressure from dust. This suggests that line driving likely plays a role, but it is not yet included in the FRADO model.

Incorporating line driving, such as by combining FRADO with the QWIND model of Risaliti & Elvis (2010), is highly complex. The improved version of the QWIND software (Quera-Bofarull et al. 2023) is publicly available, providing a strong foundation for future work. However, it still lacks dust physics, which is crucial for determining the radial structure of the BLR at low luminosities. Future developments integrating these elements will be essential for achieving a fully self-consistent model.

6.2. Relativistic effects and X-ray albedo

Currently our model does not account for the effects of GR, which are critically important for phenomena within the inner 10 r_g. In these inner regions, spacetime curvature significantly influences both the propagation of photons from the lamppost

(a point-like X-ray source) to the accretion disk and their subsequent travel from the disk to the observer. Additionally, the energy dissipation profile in the cold disk depends on the black hole spin (see e.g., Novikov & Thorne 1973).

However, the lamppost geometry itself is a considerable simplification, and in the case of NGC 5548, the cold accretion disk does not extend all the way to the ISCO. As a result, the reprocessing primarily occurs at larger radii, where GR effects are less dominant.

Another important consideration is the disk albedo, which is a complex function of the density in the disk atmosphere and the ionization parameter, both of which are likely to vary with radius. This issue is best addressed in systems that exhibit broad, relativistically smeared X-ray Fe Kα lines, where model assumptions can be more directly tested (e.g., Ballantyne et al. 2001; Dovčiak et al. 2004; García et al. 2013). Even models of reprocessing by the warm corona were studied recently by Petrucci et al. (2020).

For the case of continuum time delays, GR effects have been specifically studied for NGC 5548 by Kammoun et al. (2024b). However, these models do not include contributions from the BLR and fail to reproduce features such as the Balmer and Paschen edges in the time-delay spectrum.

In the future, it may become possible to integrate these various components into a single model. However, full GR-based computations are computationally expensive and require the inclusion of additional free functions (radial profile of the ionization parameter, disk geometrical height, hard X-ray source geometry) to model the reprocessing accurately. Overall, as demonstrated by Kammoun et al. (2021a), the disk response is indeed sensitive to both relativistic effects and albedo. Nonetheless, those models do not incorporate an inner warm corona and therefore cannot be used for direct comparison in our case.

6.3. Dust sublimation temperature

In this work, we adopt a universal dust sublimation temperature of 1500 K, which plays a crucial role in the FRADO model as it sets the onset of BLR cloud launching. This choice directly influences the analytical expression for the Hubble constant derived in equation 11. Given the temperature profile in the standard accretion disk that underlies this formula, our inferred values for the Hubble constant scale approximately as:

$$H_0 \propto \left(\frac{T_{sub}}{1500K}\right)^{4/3}. \quad (13)$$

However, the dust sublimation temperature is not firmly established. While Barvainis (1987) originally recommended 1500 K as a representative value, more recent papers recommend 1500 K for standard mixture of silicate/graphite dust (e.g. Mor & Netzer 2012), but for pure graphite, higher values such as 1800 K are proposed (e.g., Mor & Netzer 2012). A broader, density-dependent range was presented by Baskin & Laor (2018), whose Figure 1 shows that at densities around 10^{11}cm^{-3}, sublimation temperatures for silicate and graphite grains could reach 1600 K and 2000 K, respectively.

Nonetheless, graphite is unlikely to be present in the nuclear parts of AGN, as the 2175 Å feature is generally not seen in absorption (Laor & Draine 1993; Gaskell et al. 2004), which rather suggests the presence of amorphous carbon grains (e.g. Czerny et al. 2004). However, there are no reliable estimates for the sublimation temperature of amorphous carbon in AGN environments. Stellar measurements from AGB stars give a temperature of 1170 ± 60 K, very close to the sublimation temperature of silicate in these surroundings.

An alternative constraint was proposed by Vazquez et al. (2015), who argued for dust temperatures as high as 1800 K based on dust time-delay measurements rather than direct spectral analysis. However, their interpretation may be affected by an incomplete subtraction of the accretion disk contribution to the observed dust-delays (Mandal et al. 2024).

Given these uncertainties, we adopt 1500 K as a conservative and widely used value, but we acknowledge a plausible error margin of ±100 K. Based on the scaling relation above, this translates into a $\sim$ 9% uncertainty in the inferred Hubble constant, representing an important systematic contribution to our results.

The presence of dust, particularly of dust with atypical properties, may additionally imply problems with establishing the intrinsic SED. For example, Gaskell et al. (2023) argue that, based on their extinction curve, the UV flux of NGC 5548 may be underestimated by a factor of seven. Tests of such issues can be performed in the future.

6.4. Other fixed parameters as sources of systematic errors

It would be computationally very time consuming to move the other fixed parameters to the parameters fitted to the data, and to study the degeneracy between all these parameters. However, we can easily discuss their expected importance looking at the analytical formula for the Hubble constant of Collier et al. (1999) (see equation 11). Those extra fixed parameters are: $M_{\rm BH}$, inclination angle, gas density, and column density. The black hole mass does not enter into equation 11. The monochromatic flux f_ν is not sensitive on $M_{\rm BH}$ as long as the optical spectrum does not show strong departure from a power law (Shakura & Sunyaev 1973). This happens only in the far UV. The presence of the warm corona complicates the reasoning. Also the shape of the structure function shows some dependence on $M_{\rm BH}$ (see e.g. Naddaf et al. 2025, for most recent study), and not just on local monochromatic flux which is actually fitted. The onset of the BLR does not depend on $M_{\rm BH}$, as it is set by the dust sublimation temperature, but the vertical velocities increase with $M_{\rm BH}$. Overall, it should not lead to significant effect. The viewing angle is important, as it is present in equation 11. For the viewing angle of 30 degrees, the Hubble constant would be lower by 6 %, and for 50 degrees it would be higher by 8 %. Therefore, this effect is important for any specific source. On the other hand, if the method is later applied to a large sample of objects at different redshifts, the viewing angle effects will average out, as there is no strong evidence for a redshift-dependent trend in the viewing angle or the dusty torus opening angle (e.g. Prince et al. 2022; Rałowski et al. 2024). However, assessing the influence of the local density and column density of the BLR clouds is considerably more challenging, as both parameters impact the ionization state and the effective optical depth of the region. These quantities can be effectively constrained by analyzing the shape of the delay enhancement near the Balmer and Paschen edges. Moreover, any reduction in effective optical depth can be compensated for by adjusting the covering factor, which is treated as a free parameter in the model. We certainly plan to refine and improve the model in future work.

6.5. FRADO vs LOC models as a method to reproduce the BLR transfer function

FRADO is a dynamical model which aims to reproduce the physical origin of the clouds, their location and their velocities. The model is not yet fully matured, but there are clear prospects for the model further development. For the dynamics, the addition of the line driving, mentioned above, should be included as its importance is increasing with the height of the clouds. Next, the emissivity of each clouds should be calculated individually, according to its location. Finally, there are two even more complex problems. One is a good realistic description of the shielding of clouds by themselves, important at low heights from the disk. The second one is determination of the density distribution of material based on thermal instability of the medium, as described already by Krolik et al. (1981). The wind is launched as a continuous medium, with clouds forming out of this wind in short thermal timescale.

Locally Optimally Emitting Cloud (LOC) models, on the other hand, by their concept (power law distribution of clouds in radius and in density, with the limiting densities and limiting radii, and power law slopes as parameters) are better suited for accurately reproducing the line ratios observed in AGN spectra. The additional parameters are still required if the distribution is flat, concentrated around the accretion disk, instead of a spherical distribution as in the original model of Baldwin et al. (1995). This model is mature, but its parameters must be controlled by the data. However, to derive the BLR response, additional assumptions are required. Lawther et al. (2018) combined a spherically symmetric approach with the continuity equation to constrain the radial distribution of clouds, and were thereby able to predict the expected time delays for all emission lines. Additionally, using LOC model, Korista & Goad (2019) pioneered the study of the disk continuum contamination by BLR continuum. However, it remains to be seen whether LOC models can be applied in the same way as FRADO to simultaneously fit both the spectra and time delays, and thereby enable determination of the Hubble constant. This has not been achieved so far.

6.6. Other distance measurements to the source

The heliocentric redshift of NGC 5548 ($z = 0.017175 \pm 2.30 \times 10^{-5}$; de Vaucouleurs et al. 1991) corresponds to a distance of 79.05 ± 5.54 Mpc. It is different when the motion of the source is measured relative to the Cosmic Microwave Background (CMB)[2]. The proper motion of the source is thus not negligible, as indicated by the difference between its heliocentric and CMB-based velocities reported by NED (5149 ± 7 km s^{-1} vs. 5359 ± 16 km s^{-1}).

In addition to redshift-based estimates, several independent distance measurements exist for this source. Two estimates rely on the Tully-Fisher method: an older measurement of 103 Mpc (Bottinelli et al. 1984) and a more recent one that closely aligns with the redshift-based value (82.2 ± 16.4 Mpc; Robinson et al. 2021). Meanwhile, the AGN continuum time lag method yielded a significantly higher distance of 341 ± 62 Mpc (Cackett et al. 2007). In contrast, dust reverberation mapping provided a distance of 92.5 ± 1.5 Mpc (Yoshii et al. 2014), which, despite its small uncertainty, is not consistent with the redshift-based value.

Applying a velocity correction from the heliocentric frame to the CMB frame shifts the redshift from 0.017175 to 0.017876. This adjustment would, in turn, modify our estimated value of the Hubble constant to $69.6^{+11.0}_{-2.2}$ km s^{-1} Mpc^{-1}. However, given the relatively large uncertainties involved, achieving a highly precise correction for the proper motion is not crucial in this context.

[2] https://ned.ipac.caltech.edu/

6.7. The Hubble tension

The recent measurements of the Hubble constant generally highlight a persistent tension between early- and late-Universe determinations (see Abdalla et al. 2022, for a review). A key issue in this debate is the determination of measurement uncertainties. For example, studies by Riess et al. (2016) and Planck Collaboration et al. (2016) suggest a significant discrepancy, while the baryon acoustic oscillation (BAO) measurements by Wang et al. (2017) are consistent with both within their reported errors. However, the overall tension remains unresolved, as indicated by the most recent results from Riess et al. (2024), Uddin et al. (2024), and Planck Collaboration et al. (2020).

In response to this discrepancy, several independent methods have been proposed to confirm or address the tension (e.g., see de Jaeger et al. 2022; Wong et al. 2024; Trefoloni et al. 2024; Liu et al. 2024; Bargiacchi et al. 2025, for some of the latest examples). Notably, some local measurements yield lower values of H_0 (e.g., Grillo et al. 2024). The latest findings from the clustering of galaxies, quasars, and Lyman-α forest tracers, based on the first year of observations from the Dark Energy Spectroscopic Instrument (DESI Data Release 1; DESI Collaboration et al. 2024), support a lower Hubble constant of 68.40 ± 0.27 km s^{-1} Mpc^{-1} for a flat ΛCDM model, with remarkably small uncertainty. Their results, incorporating constraints from Big Bang nucleosynthesis and acoustic angular scale measurements from the CMB, suggest $H_0 = 68.52 \pm 0.62$ km s^{-1} Mpc^{-1}, while a joint analysis of CMB anisotropies and CMB lensing from Planck+ACT yields $H_0 = 67.97 \pm 0.38$ km s^{-1} Mpc^{-1}. Most recent measurements from the Dark Energy Survey (DES) experiment yields an H_0 value of $67.81^{+0.96}_{-0.86}$ km s^{-1} Mpc^{-1} (DES Collaboration et al. 2025).

Although our method lacks the precision needed to decisively address this tension, it represents a significant improvement over the results obtained by Cackett et al. (2007) for this object. This progress is both substantial and encouraging.

Interestingly, distance-ladder-based measurements tend to yield higher values of H_0 compared to single-step methods, with Perivolaropoulos (2024) reporting an average of $H_0 = 69.0 \pm 0.48$ km s^{-1} Mpc^{-1}. Our target source, at a redshift of $z = 0.017175$, lies near the boundary of $z \sim 0.01$, where some studies suggest a possible transition in cosmological behavior (e.g., Gavas et al. 2025; Verde et al. 2024). However, given the current uncertainties in our results, we cannot yet distinguish between competing interpretations. Future efforts should focus on reducing measurement errors and extending the analysis to AGN at both lower and higher redshifts to further explore this issue.

6.8. Prospects for continuum reverberation from LSST

The standard six-color photometry provided by the Legacy Survey of Space and Time (LSST), soon to be available from the Vera Rubin Observatory, may not achieve the same level of precision in time delay measurements as combined SWIFT/ground-based monitoring. However, there remain promising opportunities for detecting continuum time delays, particularly for AGNs with larger black hole masses with high luminosities (Pozo Nuñez et al. 2023, 2024; Panda et al. 2024).

For the most massive quasars, however, the contribution of the BLR to the observed time delay may be less significant. This is suggested by results for *PG*2308 + 098, a quasar with $M_{\rm BH}$ of $10^{9.6\pm0.1}\,M_{\odot}$, as reported by Kokubo (2018). To better understand this effect, we can also investigate a potential scaling relation between BLR continuum contamination and emission line intensities, which may provide further insight into the role of the BLR in time delay measurements.

7. Conclusions

Our pilot study aims to test the FRADO model for the BLR structure and estimate the Hubble constant based on the mean spectrum data and continuum time delay measurements for NGC 5548. The study has been highly successful, yielding several key outcomes:

- The time delay of the Hβ line is approximately recovered, even though our model does not allow for direct adjustments of the inner and outer radii of BLR. Instead, these parameters emerge naturally from computations of radiation pressure acting on dust and the dust sublimation temperature.
- By using the redshift-based distance of NGC 5548 and its known luminosity, we successfully model the overall spectrum, incorporating contributions from both the accretion disk and the BLR. Additionally, we accurately reproduce the time-delay pattern, emphasizing the crucial role played by the Balmer and Paschen edges.
- Relaxing the assumption of a known redshift-based luminosity, we model the spectrum and time-delay data across a range of Eddington ratios. For each value, we optimize the source distance, ultimately identifying a best-fit Eddington ratio and corresponding distance, which in turn provide an estimate of the Hubble constant.
- Although the uncertainty in the Hubble constant remains relatively large ($66.9^{+10.5}_{-2.1}$ km s^{-1} Mpc^{-1}), our method demonstrates potential for refinement. Further improvements, both for this source and for similar determinations using other AGNs with dense monitoring could lead to significantly more precise measurements.

Our results validate the viability of using AGN continuum time delays and spectral modeling as an independent method for measuring cosmic distances and estimating the Hubble constant. While the current uncertainty is still substantial, the methodology holds promise for future applications. Expanding the sample to include additional AGNs with well-sampled continuum–RM data will be crucial for reducing uncertainties and improving the accuracy of this approach.

Acknowledgements. We thank the anonymous referee for valuable comments and suggestions. This project has received funding from the European Research Council (ERC) under the European Union's Horizon 2020 research and innovation program (grant agreement No. [951549]). VKJ acknowledges the OPUS-LAP/GA ˇCR-LA bilateral project (2021/43/I/ST9/01352/OPUS 22 and GF23-04053L). MHN also acknowledges the financial support by the University of Liege under Special Funds for Research, IPD-STEMA Program. SP is supported by the international Gemini Observatory, a program of NSF NOIRLab, which is managed by the Association of Universities for Research in Astronomy (AURA) under a cooperative agreement with the U.S. National Science Foundation, on behalf of the Gemini partnership of Argentina, Brazil, Canada, Chile, the Republic of Korea, and the United States of America. BC acknowledges the support from COST Action CA21136 - Addressing observational tensions in cosmology with systematics and fundamental physics (CosmoVerse), supported by COST (European Cooperation in Science and Technology). FPN gratefully acknowledges the generous and invaluable support of the Klaus Tschira Foundation. We thank Dr. Missagh Mehdipour for sharing the broadband SED data points with us.

References

Abdalla, E., Abellán, G. F., Aboubrahim, A., et al. 2022, Journal of High Energy Astrophysics, 34, 49
Baldwin, J., Ferland, G., Korista, K., & Verner, D. 1995, ApJ, 455, L119
Ballantyne, D. R., Ross, R. R., & Fabian, A. C. 2001, MNRAS, 327, 10
Ballantyne, D. R., Sudhakar, V., Fairfax, D., et al. 2024, MNRAS, 530, 1603
Bargiacchi, G., Dainotti, M. G., & Capozziello, S. 2025, New A Rev., 100, 101712
Barvainis, R. 1987, ApJ, 320, 537
Baskin, A. & Laor, A. 2018, MNRAS, 474, 1970
Beard, M. W. J., McHardy, I. M., Horne, K., et al. 2025, MNRAS, 537, 293
Blandford, R. D. & McKee, C. F. 1982, ApJ, 255, 419
Bon, E., Zucker, S., Netzer, H., et al. 2016, ApJS, 225, 29
Bottinelli, L., Gouguenheim, L., Paturel, G., & de Vaucouleurs, G. 1984, A&AS, 56, 381
Cackett, E. M., Bentz, M. C., & Kara, E. 2021, iScience, 24, 102557
Cackett, E. M., Chiang, C.-Y., McHardy, I., et al. 2018, ApJ, 857, 53
Cackett, E. M. & Horne, K. 2006, MNRAS, 365, 1180
Cackett, E. M., Horne, K., & Winkler, H. 2007, MNRAS, 380, 669
Cao, S., Mandal, A. K., Zajaček, M., Czerny, B., & Ratra, B. 2025, Phys. Rev. D, 111, 083545
Cao, S., Zajaček, M., Czerny, B., Panda, S., & Ratra, B. 2024, MNRAS, 528, 6444
Cao, S., Zajaček, M., Panda, S., et al. 2022, MNRAS, 516, 1721
Cappi, M., De Marco, B., Ponti, G., et al. 2016, A&A, 592, A27
Chatzikos, M., Bianchi, S., Camilloni, F., et al. 2023a, Rev. Mexicana Astron. Astrofis., 59, 327
Chatzikos, M., Bianchi, S., Camilloni, F., et al. 2023b, Rev. Mexicana Astron. Astrofis., 59, 327
Clavel, J., Reichert, G. A., Alloin, D., et al. 1991, ApJ, 366, 64
Collier, S., Horne, K., Wanders, I., & Peterson, B. M. 1999, MNRAS, 302, L24
Crenshaw, D. M., Kraemer, S. B., Schmitt, H. R., et al. 2009, ApJ, 698, 281
Czerny, B., Beaton, R., Bejger, M., et al. 2018, Space Sci. Rev., 214, 32
Czerny, B. & Hryniewicz, K. 2011, A&A, 525, L8
Czerny, B., Li, J., Loska, Z., & Szczerba, R. 2004, MNRAS, 348, L54
Czerny, B., Li, Y.-R., Hryniewicz, K., et al. 2017, ApJ, 846, 154
Czerny, B., Nikołajuk, M., Różańska, A., et al. 2003, A&A, 412, 317
Dalla Bontà, E., Peterson, B. M., Bentz, M. C., et al. 2020, ApJ, 903, 112
de Jaeger, T., Galbany, L., Riess, A. G., et al. 2022, MNRAS, 514, 4620
De Rosa, G., Peterson, B. M., Ely, J., et al. 2015, ApJ, 806, 128
de Vaucouleurs, G. & de Vaucouleurs, A. 1972, Astrophys. Lett., 12, 1
de Vaucouleurs, G., de Vaucouleurs, A., Corwin, Herold G., J., et al. 1991, Third Reference Catalogue of Bright Galaxies
DES Collaboration, Abbott, T. M. C., Acevedo, M., et al. 2025, arXiv e-prints, arXiv:2503.06712
DESI Collaboration, Adame, A. G., Aguilar, J., et al. 2024, arXiv e-prints, arXiv:2404.03002
Dovčiak, M., Karas, V., & Yaqoob, T. 2004, ApJS, 153, 205
Draine, B. T. & Lee, H. M. 1984, ApJ, 285, 89
Edelson, R., Gelbord, J. M., Horne, K., et al. 2015, ApJ, 806, 129
Edelson, R., Peterson, B. M., Gelbord, J., et al. 2024, ApJ, 973, 152
Fausnaugh, M. M., Denney, K. D., Barth, A. J., et al. 2016, ApJ, 821, 56
Ferland, G. J., Netzer, H., & Shields, G. A. 1979, ApJ, 232, 382
Floris, A., Pandey, A., Czerny, B., et al. 2025, A&A, 697, A23
Freedman, W. L., Madore, B. F., Jang, I. S., et al. 2024, arXiv e-prints, arXiv:2408.06153
García, J., Dauser, T., Reynolds, C. S., et al. 2013, ApJ, 768, 146
Gaskell, C. M., Anderson, F. C., Birmingham, S. Á., & Ghosh, S. 2023, MNRAS, 519, 4082
Gaskell, C. M., Goosmann, R. W., Antonucci, R. R. J., & Whysong, D. H. 2004, ApJ, 616, 147
Gavas, S., Bagla, J. S., & Khandai, N. 2025, Phys. Rev. D, 111, 043516
Grier, C. J., Pancoast, A., Barth, A. J., et al. 2017, ApJ, 849, 146
Grillo, C., Pagano, L., Rosati, P., & Suyu, S. H. 2024, A&A, 684, L23
Guo, H., Barth, A. J., & Wang, S. 2022, ApJ, 940, 20
Homayouni, Y., Trump, J. R., Grier, C. J., et al. 2019, ApJ, 880, 126
Horne, K., De Rosa, G., Peterson, B. M., et al. 2021, ApJ, 907, 76
Jaiswal, V. K., Prince, R., Panda, S., & Czerny, B. 2023, A&A, 670, A147
Kammoun, E., Papadakis, I. E., Dovčiak, M., & Panagiotou, C. 2024a, A&A, 686, A69
Kammoun, E., Papadakis, I. E., Dovčiak, M., & Panagiotou, C. 2024b, A&A, 686, A69
Kammoun, E. S., Dovčiak, M., Papadakis, I. E., Caballero-García, M. D., & Karas, V. 2021a, ApJ, 907, 20
Kammoun, E. S., Papadakis, I. E., & Dovčiak, M. 2021b, MNRAS, 503, 4163
Kammoun, E. S., Robin, L., Papadakis, I. E., Dovčiak, M., & Panagiotou, C. 2023, MNRAS, 526, 138
Kinney, A. L., Calzetti, D., Bohlin, R. C., et al. 1996, ApJ, 467, 38
Kokubo, M. 2018, PASJ, 70, 97

Korista, K. T., Alloin, D., Barr, P., et al. 1995, ApJS, 97, 285
Korista, K. T. & Goad, M. R. 2001, ApJ, 553, 695
Korista, K. T. & Goad, M. R. 2019, MNRAS, 489, 5284
Kovačević, J., Popović, L. Č., & Kollatschny, W. 2014, Advances in Space Research, 54, 1347
Krolik, J. H. 1999a, Active galactic nuclei : from the central black hole to the galactic environment
Krolik, J. H. 1999b, Active galactic nuclei : from the central black hole to the galactic environment
Krolik, J. H., Horne, K., Kallman, T. R., et al. 1991, ApJ, 371, 541
Krolik, J. H., McKee, C. F., & Tarter, C. B. 1981, ApJ, 249, 422
Kubota, A. & Done, C. 2018, MNRAS, 480, 1247
Laor, A. & Draine, B. T. 1993, ApJ, 402, 441
Lawther, D., Goad, M. R., Korista, K. T., Ulrich, O., & Vestergaard, M. 2018, MNRAS, 481, 533
Li, Y.-R., Shangguan, J., Wang, J.-M., et al. 2025, arXiv e-prints, arXiv:2502.18856
Li, Y.-R., Wang, J.-M., Ho, L. C., Du, P., & Bai, J.-M. 2013, ApJ, 779, 110
Li, Y.-R., Wang, J.-M., Songsheng, Y.-Y., et al. 2022, ApJ, 927, 58
Liu, T., Cao, S., Biesiada, M., Zhang, Y., & Wang, J. 2024, ApJ, 965, L11
Long, K. & Dexter, J. 2025, ApJ, 987, 196
Lu, K.-X., Bai, J.-M., Wang, J.-M., et al. 2022, ApJS, 263, 10
Lu, K.-X., Du, P., Hu, C., et al. 2016, ApJ, 827, 118
Lusso, E., Risaliti, G., & Nardini, E. 2025, arXiv e-prints, arXiv:2504.02040
Mandal, A. K., Woo, J.-H., & Wang, S. 2025, ApJ, 985, 30
Mandal, A. K., Woo, J.-H., Wang, S., et al. 2024, ApJ, 968, 59
Martínez-Aldama, M. L., Czerny, B., Kawka, D., et al. 2019, ApJ, 883, 170
McHardy, I. M., Cameron, D. T., Dwelly, T., et al. 2014, MNRAS, 444, 1469
Mehdipour, M., Kaastra, J. S., Kriss, G. A., et al. 2015, A&A, 575, A22
Mor, R. & Netzer, H. 2012, MNRAS, 420, 526
Morgan, C. W., Kochanek, C. S., Morgan, N. D., & Falco, E. E. 2010, ApJ, 712, 1129
Mudd, D., Martini, P., Zu, Y., et al. 2018, ApJ, 862, 123
Naddaf, M. H. & Czerny, B. 2022, A&A, 663, A77
Naddaf, M.-H. & Czerny, B. 2024, Universe, 10, 29
Naddaf, M.-H., Czerny, B., & Szczerba, R. 2021, ApJ, 920, 30
Naddaf, M. H., Martinez-Aldama, M. L., Hutsemekers, D., Savic, D., & Czerny, B. 2025, arXiv e-prints, arXiv:2506.01159
Naddaf, M. H., Martinez-Aldama, M. L., Marziani, P., et al. 2023, A&A, 675, A43
Netzer, H. 2020, MNRAS, 494, 1611
Netzer, H. 2022, MNRAS, 509, 2637
Netzer, H., Goad, M. R., Barth, A. J., et al. 2024, ApJ, 976, 59
Novikov, I. D. & Thorne, K. S. 1973, in Black Holes (Les Astres Occlus), ed. C. Dewitt & B. S. Dewitt, 343–450
Pancoast, A., Brewer, B. J., & Treu, T. 2014, MNRAS, 445, 3055
Panda, S. 2021, A&A, 650, A154
Panda, S., Bon, E., Marziani, P., & Bon, N. 2022, Astronomische Nachrichten, 343, e210091
Panda, S., Martínez-Aldama, M. L., Marinello, M., et al. 2020, ApJ, 902, 76
Panda, S., Pozo Nuñez, F., Bañados, E., & Heidt, J. 2024, ApJ, 968, L16
Pandey, A., Czerny, B., Panda, S., et al. 2023, A&A, 680, A102
Pandey, A., Martínez-Aldama, M. L., Czerny, B., et al. 2025, ApJS, 277, 36
Papoutsis, M., Papadakis, I. E., Panagiotou, C., Dovčiak, M., & Kammoun, E. 2024, A&A, 691, A60
Pei, L., Fausnaugh, M. M., Barth, A. J., et al. 2017, ApJ, 837, 131
Perivolaropoulos, L. 2024, Phys. Rev. D, 110, 123518
Peterson, B. M. 1993, PASP, 105, 247
Peterson, B. M., Alloin, D., Axon, D., et al. 1992, ApJ, 392, 470
Peterson, B. M., Balonek, T. J., Barker, E. S., et al. 1991, ApJ, 368, 119
Peterson, B. M., Berlind, P., Bertram, R., et al. 2002, ApJ, 581, 197
Peterson, B. M., Ferrarese, L., Gilbert, K. M., et al. 2004, ApJ, 613, 682
Petrucci, P. O., Gronkiewicz, D., Rozanska, A., et al. 2020, A&A, 634, A85
Planck Collaboration, Ade, P. A. R., Aghanim, N., et al. 2016, A&A, 594, A13
Planck Collaboration, Aghanim, N., Akrami, Y., et al. 2020, A&A, 641, A6
Pozo Nuñez, F., Bruckmann, C., Deesamutara, S., et al. 2023, MNRAS, 522, 2002
Pozo Nuñez, F., Czerny, B., Panda, S., et al. 2024, Research Notes of the American Astronomical Society, 8, 47
Prince, R., Hernández Santisteban, J. V., Horne, K., et al. 2025, arXiv e-prints, arXiv:2506.06731
Prince, R., Hryniewicz, K., Panda, S., Czerny, B., & Pollo, A. 2022, ApJ, 925, 215
Quera-Bofarull, A., Done, C., Lacey, C. G., Nomura, M., & Ohsuga, K. 2023, MNRAS, 518, 2693
Rałowski, M., Hryniewicz, K., Pollo, A., & Stawarz, Ł. 2024, A&A, 682, A120
Riess, A. G., Macri, L. M., Hoffmann, S. L., et al. 2016, ApJ, 826, 56
Riess, A. G., Scolnic, D., Anand, G. S., et al. 2024, ApJ, 977, 120
Risaliti, G. & Elvis, M. 2010, A&A, 516, A89
Risaliti, G. & Lusso, E. 2015, ApJ, 815, 33
Robinson, J. H., Bentz, M. C., Courtois, H. M., et al. 2021, ApJ, 912, 160
Rokaki, E., Collin-Souffrin, S., & Magnan, C. 1993, A&A, 272, 8
Rosborough, S., Robinson, A., Almeyda, T., Humphrey, D., & Noll, M. 2025, arXiv e-prints, arXiv:2507.14337
Rosborough, S. A., Robinson, A., Almeyda, T., & Noll, M. 2024, ApJ, 965, 35
Różańska, A., Czerny, B., Życki, P. T., & Pojmański, G. 1999, MNRAS, 305, 481
Schmidt, M. 1963, Nature, 197, 1040
Sergeev, S. G., Doroshenko, V. T., Golubinskiy, Y. V., Merkulova, N. I., & Sergeeva, E. A. 2005, ApJ, 622, 129
Seyfert, C. K. 1943, ApJ, 97, 28
Shakura, N. I. & Sunyaev, R. A. 1973, A&A, 24, 337
Shapovalova, A. I., Doroshenko, V. T., Bochkarev, N. G., et al. 2004, A&A, 422, 925
Shapovalova, A. I., Popović, L. Č., Bochkarev, N. G., et al. 2009, New A Rev., 53, 191
Shappee, B. J., Prieto, J. L., Grupe, D., et al. 2014, ApJ, 788, 48
Shimura, T. & Takahara, F. 1995, ApJ, 445, 780
Śniegowska, M., Marziani, P., Czerny, B., et al. 2021, ApJ, 910, 115
Sunyaev, R. A. & Titarchuk, L. G. 1980, A&A, 86, 121
Suyu, S. H., Goobar, A., Collett, T., More, A., & Vernardos, G. 2024, Space Sci. Rev., 220, 13
Trefoloni, B., Lusso, E., Nardini, E., et al. 2024, A&A, 689, A109
Uddin, S. A., Burns, C. R., Phillips, M. M., et al. 2024, ApJ, 970, 72
Ulrich, M. H. & Boisson, C. 1983, ApJ, 267, 515
Vazquez, B., Galianni, P., Richmond, M., et al. 2015, ApJ, 801, 127
Verde, L., Schöneberg, N., & Gil-Marín, H. 2024, ARA&A, 62, 287
Wang, Y., Xu, L., & Zhao, G.-B. 2017, ApJ, 849, 84
Wildy, C., Landt, H., Ward, M. J., Czerny, B., & Kynoch, D. 2021, MNRAS, 500, 2063
Wong, K. C., Dux, F., Shajib, A. J., et al. 2024, A&A, 689, A168
Yoshii, Y., Kobayashi, Y., Minezaki, T., Koshida, S., & Peterson, B. A. 2014, ApJ, 784, L11
Yu, Z., Martini, P., Davis, T. M., et al. 2020, ApJS, 246, 16
Zajaček, M., Panda, S., Pandey, A., et al. 2024, A&A, 683, A140

Appendix A: H_0 based on observationally determined response function

We employ an alternative method to validate the results obtained from the FRADO model. In rare cases, NGC 5548 being one notable example, the transfer function for Hβ was directly determined from the data using densely sampled spectroscopic RM. For this purpose, we use the results presented by Horne et al. (2021). These observations were conducted in 2014, roughly during the same period with the photometric time-delay measurements. The study provides response functions for various emission lines, but we focus on those corresponding to the Hβ line, as they are most representative of the regions in the BLR where the Balmer and Paschen continua originate and play a dominant role in shaping the observed time delays. Specifically, we consider two versions of the Hβ response functions presented by Horne et al. (2021): one that encompasses the full Hβ line and another centered narrowly around 4863 Å. A comparison between our model-derived BLR response function and the two response functions from Horne et al. (2021) is shown in the upper panel of Figure A.1.

Both observed response functions lack a double-peak structure, which, however, is present in the case of the CIV line (see Figure 4 of Horne et al. 2021). More importantly, these response functions exhibit a significantly longer tail, with this extended tail being notably stronger in the full-Hβ response profile than in the narrower 4863 Å case. This long tail is also clearly visible in the 4830 Å bin shown in Figure 9 of Horne et al. (2021), suggesting that the extended delay may arise from contamination by Fe II emission. On average, the optical and UV Fe II delays tend to be longer than those of typical low-ionization lines such as Mg II and Hβ (Zajaček et al. 2024).

Having an observationally derived transfer function significantly reduces our dependence on the FRADO model summarized in Section 3.3. However, we still require CLOUDY computations to determine the wavelength-dependent efficiency of reemission by the BLR, as well as a disk/corona model.

Therefore, we perform fitting of both the mean spectrum and the wavelength-dependent time delay as before, for a set of values of the luminosity distance. For each luminosity distance D_L, the model parameters are refitted accordingly.

In the case of the entire Hβ transfer function, we are unable to tightly constrain the luminosity distance (blue data points in the bottom panel of A.1); the monotonic trend continues up to 98 Mpc, with marginal rise at 102 Mpc. We did not perform computations beyond this distance. However, for the transfer function centered around 4863 Å , a broad minimum is observed from 82 Mpc till 94 Mpc (red data points), which is shifted compared to the 74 Mpc value obtained using the theoretical FRADO model for the transfer function (black data points). Interestingly, the overall fit is the best for the FRADO model. The resulting constraint on the Hubble constant H_0 from the 4863 Å bin is $60.3^{+2.0}_{-9.1}$ km s^{-1} Mpc^{-1}, generally lower than the FRADO-derived range but only marginally outside the 1 sigma error value due to relatively large uncertainty, further supporting the applicability of the FRADO model in such analyses.

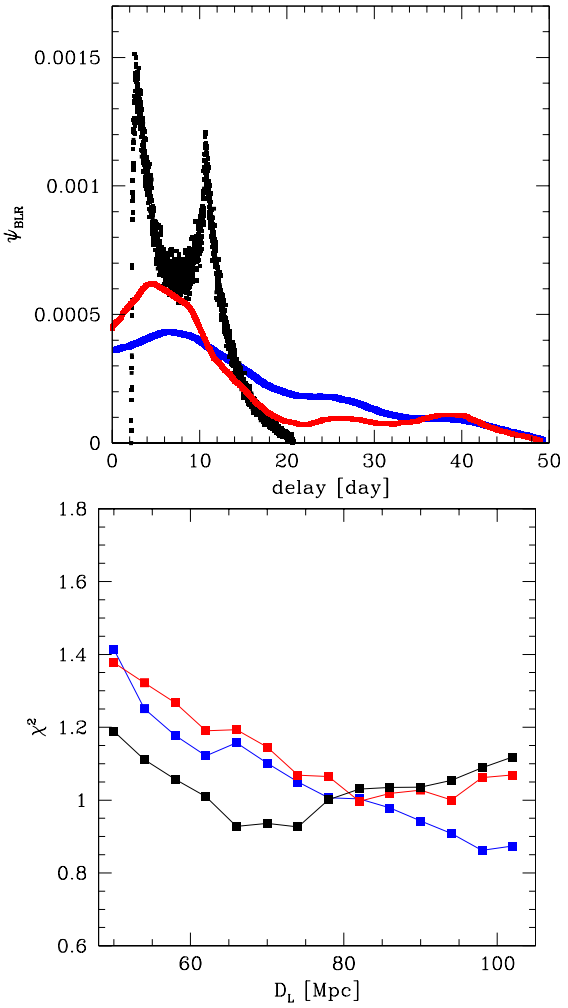

Fig. A.1. Upper panel: the response function from the FRADO model (black), total Hβ response (blue) presented in Figure 4 of Horne et al. (2021), and the response at 4863 Å (red) shown in Figure 9 of the same paper. Lower panel: The χ^2 values as a function of luminosity distance for the three response functions are shown in their respective colors.

Chapter 6

Paper-3

6.1 Introduction

This paper tests the extended corona model using optical/UV reverberation mapping of accretion disks. Instead of a single compact lamppost source, the corona is modeled as two emitting regions placed at different heights along the axis. Response functions and simulated light curves are generated to study the wavelength-dependent delays. The results show that the two-lamp configuration produces delay curves very similar to a single lamppost, with differences up to 20% for specific luminosity ratios. Cross-correlation analysis also indicates that present monitoring campaigns are not sensitive enough to distinguish the two cases. The study concludes that current optical/UV reverberation mapping is only weakly sensitive to vertical extension of the corona, and much denser observations would be required.

Astronomy & Astrophysics manuscript no. main
January 3, 2025

Testing the extended corona model with the optical/UV reverberation mapping of the accretion disk

Vikram K. Jaiswal[1] and Bożena Czerny[1]

Center for Theoretical Physics, Polish Academy of Sciences, Al. Lotników 32/46, 02-668 Warsaw, Poland

Received ....

ABSTRACT

Context. The illumination of the accretion disks is frequently studied assuming that the incident X-ray flux is a point-like source. The approach is referred as lamppost model.
Aims. The most recent computations of the X-ray reprocessing by the disk take into account the departure from the simple lamppost models. However, in computations of the incident flux thermalization and subsequent re-emission in the optical-UV band the lamppost approximation is most frequently assumed. We test if the UV-optical reverberation mapping and time delay measurements are sensitive to this assumption.
Methods. We assume that the incident radiation originates from a region extended along the symmetry axis. To model this, we adopt a simple setup by representing the emission as two lamps irradiating the disk simultaneously from two different heights. We then compare the resulting predictions with those obtained for a single lamppost located at an intermediate height.
Results. We show at the basis of the transfer function that the deviation of the wavelength-dependent delay curve shows at most a difference of 20 % in comparison to a single lamppost, assuming the black hole mass of $10^8 M_\odot$, Eddington ratio 1, and the location of the lamps at 5 and 100 rg. The maximum deviation happens for the lamp luminosity ratio $\sim$ 3. When simulating light curves for a two-lamp setup and a standard lamppost with the same black hole mass and a sampling rate of 0.1 days, we find no measurable differences in the ICCF profiles between the two setups. Larger black hole mass and considerably lower Eddington ratio would allow to see larger differences between a single lamppost and a two-lampost model.
Conclusions. UV/optical reverberation mapping is not very sensitive to the vertical extension of the corona. To detect such extension we would need small errors in the time delay (below 20 % in optimized setup, and much less otherwise), and the sampling of the lightcurves must be very dense. The effective position of the lamp is given by the luminosity-weighted position of the emitting components.

Key words. giant planet formation – κ-mechanism – stability of gas spheres

1. Introduction

Active Galactic Nuclei (AGN) are highly variable systems powered by accretion onto supermassive black holes. Most of the energy is released in the innermost regions of the accretion flow, deep within the gravitational potential well of the central black hole. This complex and dynamic region undergoes rapid variations (see, e.g., Krolik 1999). The UV and X-ray emission generated in these inner regions irradiates the more distant parts of the accretion flow, which, in efficiently accreting systems, typically takes the form of a geometrically thin, optically thick accretion disk.

The production of the X-ray continuum involves seed photons from the accretion disk being Comptonized by high-energy electrons in the corona. This interaction up-scatters the photons to higher energies, resulting in an X-ray spectrum. A portion of these X-ray photons interacts with the accretion disk, illuminating it, while the rest travel unimpeded directly to the observer. The phenomenon of X-ray irradiation of the accretion disk has been extensively studied in AGN over the years (e.g., Nandra et al. 1989; Pounds et al. 1990; George & Fabian 1991). This irradiation leads to the formation of characteristic X-ray features, such as the iron Kα line and the Compton hump. These features originate in the accretion disk close to the black hole, where relativistic effects become significant (Iwasawa et al. 1996; Fabian et al. 2000; Dovčiak et al. 2004).

The first measurement of a delay in reprocessed X-rays, known as a reverberation lag, was made in the source Ark 564 using XMM-Newton observations, as reported by McHardy et al. (2007). Subsequently, Fabian et al. (2009) measured the lag between the soft X-ray energy band (0.3–1 keV) and the hard band (1–4 keV) in the AGN 1H 0707−495. Since then, numerous reverberation lags have been detected in AGN (Emmanoulopoulos et al. 2011; Kara et al. 2013; Zoghbi et al. 2013; Cackett et al. 2013, 2014; Kara et al. 2016a,b; Ursini et al. 2020a). For a detailed review, see De Marco & Ponti (2019), and for a broader discussion of light echo studies, refer to Cackett et al. (2021).

More distant regions of the accretion disk are also illuminated by X-rays and UV radiation. In these regions, most of the radiation is absorbed, temporarily increasing the local disk temperature. This process results in observable time delays between subsequent optical bands due to the light travel time effect. Early studies of the optical/UV continuum focused on measuring interband time delays (e.g., Collier et al. 1998, 1999; Oknyanskij et al. 2003; Sergeev et al. 2005; Cackett et al. 2007; Poindexter et al. 2008; Fausnaugh et al. 2016; Montano et al. 2022). More recently, reverberation mapping campaigns utilizing HST, SWIFT, and ground-based telescopes have extended the spectral coverage to include the X-ray and far-UV regions alongside optical bands (McHardy et al. 2014, 2018; Cackett et al. 2018, 2020; Vincentelli et al. 2021; Cackett et al. 2023; Edelson et al. 2024;

Liu et al. 2024). This multi-band, broad-wavelength photometric approach provides a powerful tool for independently probing the geometry of the hot corona and the inner accretion flow.

Despite extensive observations and studies, the exact geometry of the corona remains poorly understood. Historically, three primary models have been proposed to describe the hot corona:

- Flat Disk Atmosphere Model: This model describes the corona as a hot, thin atmosphere that lies above the flat, geometrically thin accretion disk. Soft UV photons emitted vertically from the disk interact with the corona's relativistic electrons, where they are upscattered via inverse Compton scattering, producing the observed hard X-rays. (Haardt & Maraschi 1993; Haardt et al. 1994; Galeev et al. 1979).
- Hot, Thick Accretion Flow Model: Here, the corona is envisioned as a hot, optically thin accretion flow surrounding the black hole (Ichimaru 1977; Narayan & Yi 1994; Esin et al. 1997).
- Lamppost Model: This model posits that the corona is a compact source located along the black hole's spin axis, often approximated as a point source at a height h above the disk (Matt et al. 1991; Rokaki et al. 1993; Beloborodov 1999). It may also be associated with the base of a relativistic jet (Henri & Pelletier 1991; Markoff et al. 2005).

Advances in spectral modeling have shown that the first scenario cannot produce the observed hard X-ray spectral slopes, and the relative importance of the second and third models appears to correlate with the source's Eddington ratio (see, e.g., Różańska et al. 2015; Giustini & Proga 2019; Ballantyne et al. 2024; Palit et al. 2024). Recent theoretical work, such as the broad-band spectral energy distribution (SED) models by Kubota & Done (2018), integrates contributions from the hot corona, a warm corona, and an outer cold disk. These models address the energy budget but do not resolve the geometric details of the corona.

In this study, we focus on sources radiating above a few percent of the Eddington luminosity, where the inner hot flow is unlikely to dominate. For such sources, the lamppost geometry provides a plausible approximation. While the Comptonization process requires the corona to have an extended structure to effectively intercept disk photons, the lamppost model remains a reasonable simplification if radial extent of corona is small compared to its height. Nevertheless, this approximation needs to be rigorously tested against observational data.

In recent years, researchers have increasingly explored the possibility of an extended hot corona using observational data. Several X-ray reprocessing studies have incorporated the effects of an extended, contracting, or moving corona (Wilkins & Fabian 2012; Wilkins et al. 2016; Kara et al. 2019; Chainakun 2019; You et al. 2021). Szanecki et al. (2020) introduced a new extended lamppost model that considers the spatial extent and rotational motion of the X-ray source, applying it to the AGN 1H 0707−495. However, their study did not yield definitive evidence for the size of the corona. Building on this, Hancock et al. (2023) developed a two-corona model for the sources 1H 0707−495 and IRAS 13224−3809, suggesting that the corona could extend up to approximately 20 r_g for IRAS 13224−3809, where rg refers gravitational radius.. Similarly, Lucchini et al. (2023) investigated the same source and demonstrated that the two-corona model can successfully reproduce its spectral and timing properties. Additionally, Ursini et al. (2020b) proposed a complex structure to explain both the hard and soft X-ray emission in the AGN HE 1143-1810. Their model incorporates two components: a hot, hard X-ray-emitting corona and a warm corona, consistent with the multi-component framework discussed earlier.

These findings underscore the growing interest in refining corona models to better understand their spatial and physical properties. The issue of the corona height also plays a crucial role in modeling the variable X-ray radiation incident on and absorbed by the outer regions of the accretion disk. This irradiation drives UV and optical variability, which serves as a key tool for probing the structure of the cold outer accretion disk and the broad line region (BLR). Such as, the reverberation mapping technique, has been extensively utilized in numerous studies, primarily to measure black hole masses by establishing the radius-luminosity relationship for strong emission lines (Peterson 1988, 1993; Peterson et al. 2004; Bentz et al. 2013; Zajaček et al. 2021; Shen et al. 2024).

While the height of the corona is not a significant factor for BLR mapping, it has emerged as a critical parameter in recent accretion disk reverberation mapping models (Kammoun et al. 2021a, 2023). Representative values for the corona height have been derived through data fitting in these studies (Kammoun et al. 2021b), highlighting its importance in understanding disk irradiation and variability.

One of the most intriguing findings from these two lines of research is the apparent discrepancy in the inferred heights of the corona across X-ray and optical/UV delay studies. In X-ray studies, the corona height is typically small, varying from 5 r_g to 39 r_g. In contrast, optical/UV studies suggest a significantly larger height, varying from 22 r_g to 74 r_g

This disparity raises important questions about the nature of the X-ray source. It is unclear whether the position of the X-ray source genuinely varies between the studied objects or if the corona is vertically extended, causing the inner and outer regions of the disk to respond to irradiation from different parts of this structure. Further investigation is essential to reconcile these findings and to understand the complex interplay between the corona's geometry and the multiwavelength variability it induces.

This paper aims to explore the potential impact of a vertically extended corona on UV/optical reverberation mapping. To model this scenario, we approximate the corona as two distinct lamppost-like sources positioned along the symmetry axis, rather than a single point source. Using this setup, we simulate the irradiation of the accretion disk to investigate how the extended corona influences the observed variability. Our objective is to assess whether optical/UV data can effectively differentiate between a single lamppost corona and a vertically extended corona, providing new insights into the geometry of the X-ray emitting region.

2. Method

We simulate the reprocessing of the coronal emission extended along the symmetry axis in a very simple way. We assume that instead of a single point-like source located at the symmetry axis we have two point-like sources located at a different heights, h_1 and h_2. The average bolometric luminosities of the two components are assumed to be L_1, and L_2, and in general they can be different. The setup is illustrated in Figure 1.

In addition, we illustrate the stationary incident flux as a function of the radius in the case of two coronas of the same luminosity, and compare it with the disk flux from dissipation. At large distances all fluxes are proportional to r^{-3} but at small radii the distributions are quite different. As shown in middle and

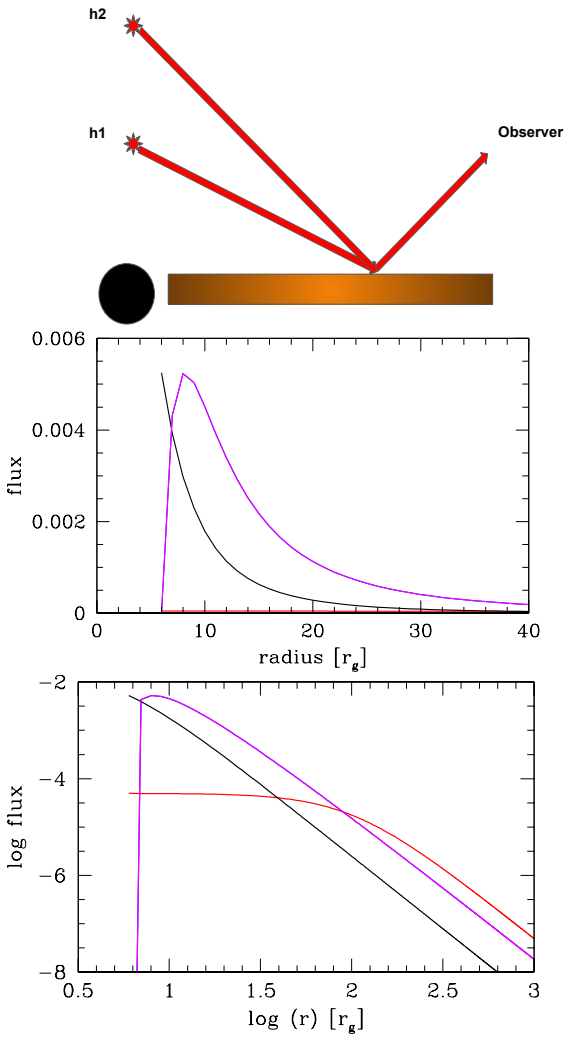

Fig. 1. A schematic representation of the geometry is shown in the upper panel, along with an example of the stationary incident flux for this geometrical setup presented in linear scale (middle panel) and logarithmic scale (lower panel). The corona heights are 5 r_g (black line) and 100 r_g (red line), each contributing approximately 30% of the total disk luminosity. The disk flux is represented in magenta.

bottom panel of Figure 1, in the case of small height the irradiation dominates close to ISCO, and before the peak of the disk emission drops below and remains proportional to the disk flux. For larger height the incident flux is flat at to the radius of the order of the lamp height, well below the disk emission, and then starts to dominate by a small factor, decreasing with the radius in proportion to the disk flux.

2.1. reprocessing of the radiation by the accretion disk

We use a simple accretion disk model of Shakura & Sunyaev (1973) for this purpose, and geometrical optics for light propagation. It is a reasonable approximation for sources with Eddington rate above a few percent. In such sources the cold optically thick geometrically thin disk extends down to innermost stable circular orbit (ISCO). In Shakura-Sunyaev model ISCO is located at 6 r_g (where $r_g = GM_{BH}/c^2$), and M_{BH} is the black hole mass, while G and c are gravitational constant and the light velocity). We neglect all general relativity effects, which is a good approximation for a non-rotating black hole. We concentrate on the relative effects of having two instead of one lampost sources, and our simplified treatment shows the direction of the change.

The disk is divided into zones as in Jaiswal et al. (2023). In order to calculate the effect of incident radiation, in the first step we set a quasi-logarithmic radial grid that covers the accretion disk between R_{isco} and R_{out}, with a variable density to ensure proper resolution at the inner parts. Specifically, we define the radial bin size using the formula: $dR = 0.085 * (\frac{R}{R_{\rm isco}})^{0.85}$. For each value of "R," we also increase the grid step in the angular (ϕ) direction by $d\phi = \frac{1.5700}{N_{div}}$, where $N_{div} = 1000$. Once we have a given "R" and ϕ value, we calculate the (x,y) Cartesian coordinate in the disk plane and the surface element, $ds = R*dR*d\phi$ in a unit of Rg^2. We neglect the disk's height and assume $z = 0$. For a given (x,y) coordinate, we calculate the total delay $\tau_{total}(x, y)$, which is the sum of the time $\tau_d(r)$ taken by a photon to reach a given disk location from the bottom corona located at height h_1 along the symmetry axis to the accretion disk and the time taken to reach the observer after reprocessing by the disk, $\tau_{do}(x, y)$. We define this time delay with respect to the plane crossing the equatorial plane at R_{out}, $\phi = 0$, and perpendicular to the direction towards the observer. This delay thus depends on the inclination angle i, the corona height, the position on the accretion disk, and the black hole mass. Similarly, we calculate the delay for the top corona located at h_2.

The disk temperature is calculated from the sum of the flux generated by the disk (parametrized by M_{BH} and accretion rate, $\dot{M}$, or, equivalently, the Eddington rate) and the incident flux. We assume black body local radiation, not applying any color-corrections.

We are assuming that the incident radiation is perfectly thermally absorbed. Whenever an X-ray photon strikes the disk, all the radiation it carries is absorbed by the disk, causing a local increase in the disk temperature. Therefore, in our model, we have ignored any energy-dependent reflection, as discussed in Kammoun et al. (2019) and Kammoun et al. (2021a), and have instead considered that all the incident radiation is absorbed by the disk and then reprocessed, i.e. considering perfect thermalization of incident X-ray flux.

2.2. Transfer function

The computation of the transfer function involves using a short impulse of light and determining the corresponding reprocessed flux as a function of time. The exact width of the pulse is not critical; a typical value is 0.05 days. For a black hole mass of $10^8 M_\odot$, often adopted as a reference, this pulse duration corresponds to a light travel time of $1.76 r_g$, which is well within the $10 r_g$ limit recommended by Kammoun et al. (2021a). To calculate the response function for two lamps, a pulse is sent from each corona for a duration of 0.05 days. At any given radius (r) and angle (ϕ), there are two possible scenarios: the pulses either overlap or they do not. If the pulses do not overlap, we calculate the total flux separately, as the two pulses will arrive independently. However, when the pulses do overlap, we first calculate the flux from corona 1, then we compute the combined flux from both coronas, and finally, we calculate the flux from corona-2. This method allows us to generate the response function.

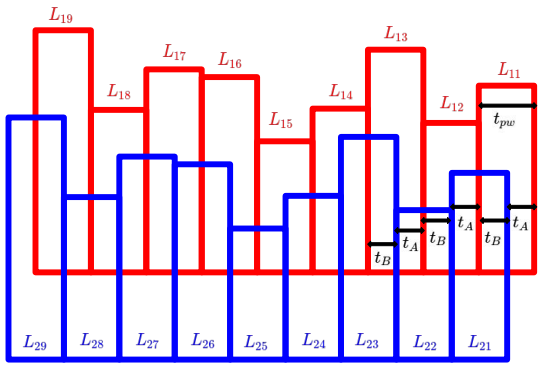

Fig. 2. The diagram illustrates the light curves from Corona-1 (red) and Corona-2 (blue) at a specific location on the disk. Here, t_{pw} represents the pulse width of the light curves, t_A denotes the temporal shift between the two for a given (r, ϕ), which varies based on the disk location, and t_C is the result of subtracting the shift (t_A) from the pulse width (t_{pw}).

2.3. Creation of corona and reprocessed lightcurves

The use of the response function requires that the variability be of small amplitude, ensuring that a single response function can describe all the disk luminosity states. In numerical method we do not require that the variable irradiating flux creates only a small amplitude variations. We generate the variable flux in some timestep bins, and we calculated the reprocessing of the incident radiation in each disk element and time bin independently. This is a much more time-consuming method but it reflects well the reality, including all the sampling issues.

We start with creating a single long equal-step lightcurve representing the corona using the Timmer & Koenig (1995) algorithm which is parameterized by three slopes and two frequency breaks. Such description is more general than damped random walk model applied to AGN by Kelly et al. (2009) which is equivalent to the fixed slopes, 0 and -2, and a single break. The random curve is additionally parameterized by the total variance which sets the fractional amplitude of the variability. The corona light curve is produced by multiplying the fixed luminosity with the dimensionless random number series, and the resulting series is utilized as the irradiation source for the accretion disk. In the next step we apply the observationally motivated sampling of the dense lightcurve. In this paper we assumed 0.1 day sampling, and the duration of the lightcurve 200 days.

In the case of two coronal sources we usually use the same dense curve, without any intrinsic delay between the coronal points. Next we calculate the reprocessing of the incident radiation at every timestep. As illustrated in Figure 2, the accretion disk receives radiation at any radius r and azimuthal angle ϕ from two distinct radiation sources, referred to as corona1 and corona2. These sources emit light that reaches different locations on the disk at different times due to their varying spatial positions and distances from the disk. For a specific point on the disk, (r, ϕ), the light pulse from corona1 arrives at time t_0, while the light pulse from corona2 reaches the same location later, at time $t_0 + t_A$. Here, t_A represents the additional time delay caused by the difference in light travel paths from corona2 to the disk location. To simplify calculations, the red pulse ('L_{11}') emitted by corona1 is ignored during the initial phase because the blue pulse ('L_{21}') from corona2 is absent in this period. The analysis begins at time $t_0 + t_{pw}$, where t_{pw} pulse width. During the time interval from $t_0 + t_{pw}$ to $t_0 + t_{pw} + t_A$, the total flux $F_{\rm irr}$ and the corresponding effective temperature $T_{\rm irr}$ at the location (r, ϕ) are computed as:

$$F_{\rm irr}(r,\phi) = \frac{3GM\dot{M}}{8\pi r^3}\left(1-\sqrt{\frac{6}{r}}\right) + \frac{L_{12}h_1}{4\pi r_1^3} + \frac{L_{21}h_2}{4\pi r_2^3} \tag{1}$$

$$T_{\rm irr}(r,\phi) = \left[\frac{3GM\dot{M}}{8\pi r^3\sigma_B}\left(1-\sqrt{\frac{6}{r}}\right) + \frac{L_{12}h_1}{4\pi r_1^3\sigma_B} + \frac{L_{21}h_2}{4\pi r_2^3\sigma_B}\right]^{\frac{1}{4}} \tag{2}$$

where $r_1 = \sqrt{r^2+h_1^2}$, $r_2 = \sqrt{r^2+h_2^2}$, L_{12} and L_{21} are luminosities associated with the two sources, and h_1 and h_2 represent their respective heights above the disk. For the subsequent time interval from $t_0 + t_{pw} + t_A$ to $t_0 + t_{pw} + t_A + t_B$, the conditions change as the sources evolve. During this phase, the flux and temperature are updated to:

$$F_{\rm irr}(r,\phi) = \frac{3GM\dot{M}}{8\pi r^3}\left(1-\sqrt{\frac{6}{r}}\right) + \frac{L_{12}h_1}{4\pi r_1^3} + \frac{L_{22}h_2}{4\pi r_2^3} \tag{3}$$

$$T_{\rm irr}(r,\phi) = \left[\frac{3GM\dot{M}}{8\pi r^3\sigma_B}\left(1-\sqrt{\frac{6}{r}}\right) + \frac{L_{12}h_1}{4\pi r_1^3\sigma_B} + \frac{L_{22}h_2}{4\pi r_2^3\sigma_B}\right]^{\frac{1}{4}} \tag{4}$$

Once the effective temperature $T_{\rm irr}$ is determined, it becomes possible to compute the emitted intensity across wavelengths using the Planck function. This is expressed as:

$$I_{\rm irr}(\lambda) = \frac{2\pi hc^2}{\lambda^5}\frac{1}{e^{\frac{hc}{\lambda k_B T_{\rm irr}}}-1} \tag{5}$$

For a non-irradiated disk (without external illumination from the coronal sources), the flux $F_{\rm disk}$, effective temperature $T_{\rm disk}$, and intensity $I_{\rm disk}(\lambda)$ are given by:

$$F_{\rm disk}(r,\phi) = \frac{3GM\dot{M}}{8\pi r^3}\left(1-\sqrt{\frac{6}{r}}\right) \tag{6}$$

$$T_{\rm disk}(r,\phi) = \left[\frac{3GM\dot{M}}{8\pi r^3\sigma_B}\left(1-\sqrt{\frac{6}{r}}\right)\right]^{\frac{1}{4}} \tag{7}$$

$$I_{\rm disk}(\lambda) = \frac{2\pi hc^2}{\lambda^5}\frac{1}{e^{\frac{hc}{\lambda k_B T_{\rm disk}}}-1} \tag{8}$$

The impact of the external illumination by the coronae can be studied by subtracting the contribution of the intrinsic disk emission from the total irradiated intensity. This yields the net effective intensity as:

$$I_{\rm eff}(\lambda) = I_{\rm irr}(\lambda) - I_{\rm disk}(\lambda) \tag{9}$$

Finally, the monochromatic luminosity L_λ can be computed by multiplying the net effective intensity $I_{\rm eff}(\lambda)$ by the corresponding surface area of the emitting region:

$$L_\lambda = \int I_{\rm eff}(\lambda)\, dA \tag{10}$$

This approach allows us to analyze how the external radiation sources contribute to the observed flux, temperature, and spectral properties of the disk, enabling a deeper understanding of the physical processes at play.

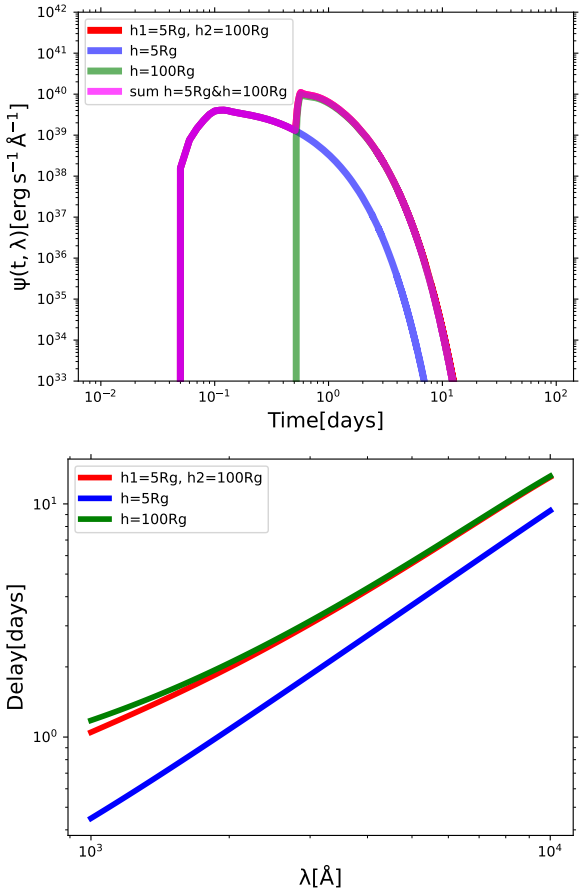

Fig. 3. The upper plot shows the response functions for a single corona with a height of $5r_g$ (blue) and $100r_g$ (green), as well as for two corona (red). The summed response function for the single corona at $5r_g$ and $100r_g$ is shown in pink. The combined response function closely overlaps with the two-corona response function for the given parameters. The bottom plot displays the corresponding delay plot. For the single corona, the parameters are: black hole mass $10^8 M_\odot$, incident luminosity $L_X = 1.0 \times 10^{46}$ erg s^{-1}, Eddington ratio = 1.0, heights $h = 5r_g$ (blue) and $h = 100r_g$ (green), and viewing angle $i = 30°$. For the two coronae, the parameters are: black hole mass $10^8 M_\odot$, luminosities L_1 and $L_2 = 1.0 \times 10^{46}$ erg s^{-1}, Eddington ratio = 1.0, heights $h_1 = 5r_g$ and $h_2 = 100r_g$, and viewing angle $i = 30°$.

3. Results

We first analysed the response function from the extended corona model and compare the resulting time delay pattern to see if this geometry can be distinguish from a simple lamppost model in the data.

3.1. response function from the extended corona

We have computed the response function for the two-lamppost corona model. An example for the wavelength $\lambda = 1000$ Å is presented in Figure 3(top), which illustrates four response functions, each distinguished by a unique color. The blue curve represents a single corona positioned at a height of $5\,R_g$, while the green curve corresponds to a single corona at a height of $100\,R_g$. The response for the two-lamp model is depicted in red. Both the combined response function and the two-point corona response function begin at the same time. Each single-corona response function exhibits a distinct peak that depends on the corona's height. However, the two-lamppost model produces a broader, two-peak response function, reflecting the travel time of light from both lamps to the disk and subsequently to the observer. For the given parameters, the two-lamp corona's response function can be approximated by summing the red and blue single-corona response functions (indicated in pink). Notably, the shape of the time delay curve in the two-corona case generally aligns with that of the single-corona case. .

3.2. time delays from the extended corona

Having the response functions for a range of wavelengths, we determined the the time delay for those three cases: two single lamp models and for a two-lamp model. The delay profiles are displayed in the bottom plot of figure 3. Single lamp solutions are equivalent to those created in Jaiswal et al. (2023). They are consistent with the standard $\lambda^{4/3}$ trend when the corona height is small, and show systematic departure with the rise of the corona height (Kammoun et al. 2021a). The delay from the two-lamp model is roughly following the same trend. We do not see any sub-structure related to the two-component character of the transfer function. There is a small departure in the overall shape.

If we analyse the actual data, we do not know the lamp position. Therefore, in order to find a criterion for the presence of two lamps instead of one we must compare the two-lamp setup with the option of a single lamp setup, most similar in properties. To ensure accurate comparison, we adjusted the height of the single corona so that it matched the delay of the 2-corona for the longest wavelength, and measured the departure at the shortest wavelengths. We could not simply measure the departure from the $\lambda^{4/3}$ trend since the curvature effect is always present.

We perfomed the computations for a range of luminosity ratios between the lower corona's luminosity to the upper corona's luminosity. The results are shown in Figure 4, the blue line represents the delay profile of 2-corona while the red line represents the delay profile of a single corona with combined luminosity and the height optimized as described above. Then, we determined the maximum deviation in delay between the two plots for a given wavelength as shown in Figure 5. The results are summarized in Table 1.

We see that the maximum deviation from a single lamp model is at the lamp luminosity ratio 3, and it reaches 20 %.Such a measurement would, of course, require coverage over a wide range of time delays, from 1000Å to 10000Å, with no contamination from BLR scattering. However, with excellent data, these tests can be successfully performed. Overall, large deviations are seen for the lamp luminosity ratio from 2 to 4, and departures are expected to be much lower outside this range.

The effective lamp position is well approximated by the arithmetic average of the assumed lamp positions weighted with the lamp luminosity

$$h = \frac{h_1 L_1 + h_2 L_2}{L_1 + L_2}. \tag{11}$$

A&A proofs: manuscript no. main

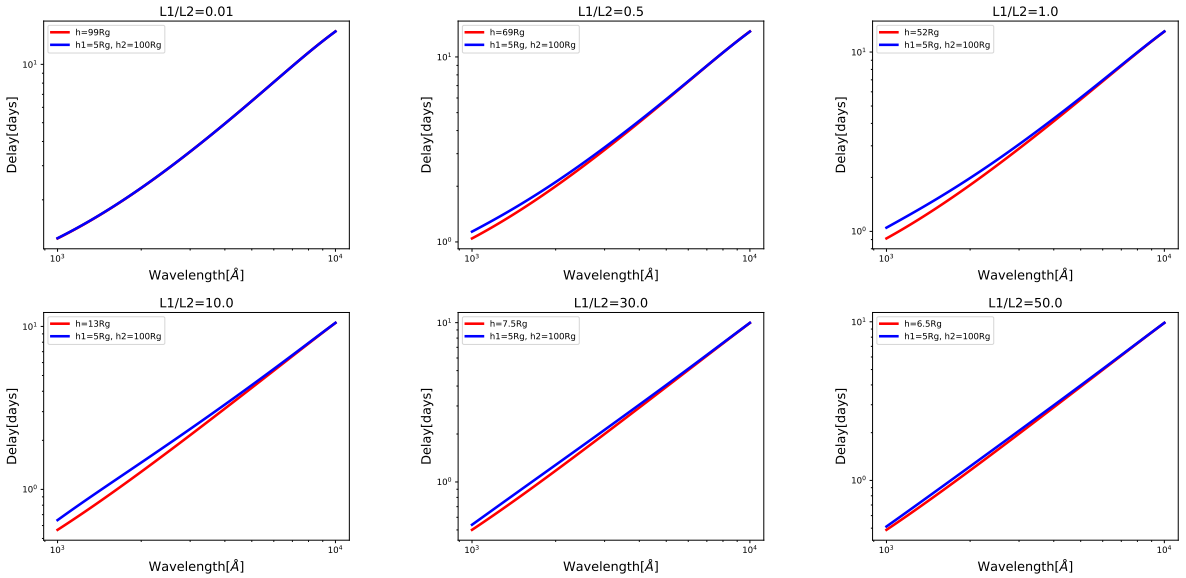

Fig. 4. The plots show the variation in the delay as the luminosity ratio between the two corona is changed. The luminosity for the single corona is fixed at 2×10^{46} erg/s, while the height is adjusted such that the delay for the longest wavelength matches the delay for the two corona. The delay from the single corona is represented in red, while the delay from the two corona is shown in blue for different luminosity ratios.

Luminosity Ratio	Deviation[days]	Deviation[%]
0.01	0.0035	0.276
0.10	0.0313	2.593
0.5	0.0922	8.826
1.0	0.1351	14.78
2.0	0.1407	17.79
2.5	0.1422	19.01
3.0	0.1432	20.10
4.0	0.1254	18.56
10.0	0.0832	14.73
20.0	0.0507	9.77
30.0	0.0382	7.63
40.0	0.0279	5.64
50.0	0.0241	4.93

Table 1. Difference in delay between single and 2-corona for 1000Å from Figure 4.

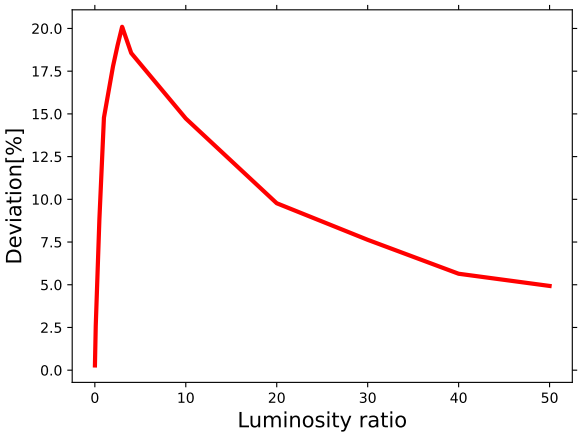

Fig. 5. Deviation in delay for wavelength 1000Å for different luminosity ratios as shown in table 1.

3.3. cross-correlation function from the two lamp model

In the case of the two-lamp geometry, the response function has a two-peak shape, hence in principle two timescales from two lamps are present in the process. Therefore, we aimed to check if this could be also present in cross-correlation function, and help to differentiate between a point-like and extended corona.

We conducted simulations to distinguish between the single corona and two corona models. We generated X-ray light curves using the Timmer & Koenig (1995) algorithm. We then used these light curves to create reprocessed light curves from the disk (see Section 2.3).

Next, we calculated the Interpolated Cross-Correlation Function (ICCF) between the two wavelengths, 1000Å and 7923Å. This process was repeated for 10 random realizations of the initial light curve, while maintaining the same statistical setup. We used exactly the same lightcurve for a single-lamp corona and for two-lamp model. The 10 ICCF plots are shown in the figure 6. All curves should be statistically equivalent, and the difference shows the expected statistical error for the adopted sampling. The overall shape varies between the different realizations of the process, particularly at the longest timescales. We observe that the ICCF for two corona is consistently broader than that of the single corona, but the differences between individual realizations dominate.

These 10 exemplary statistical realizations of the lightcurve can be used as a qualitative test whether the two-lamp corona can be differentiated from a single-lamp corona. With this aim, we calculated the mean shape of the ICCF shown in Figure 6, and

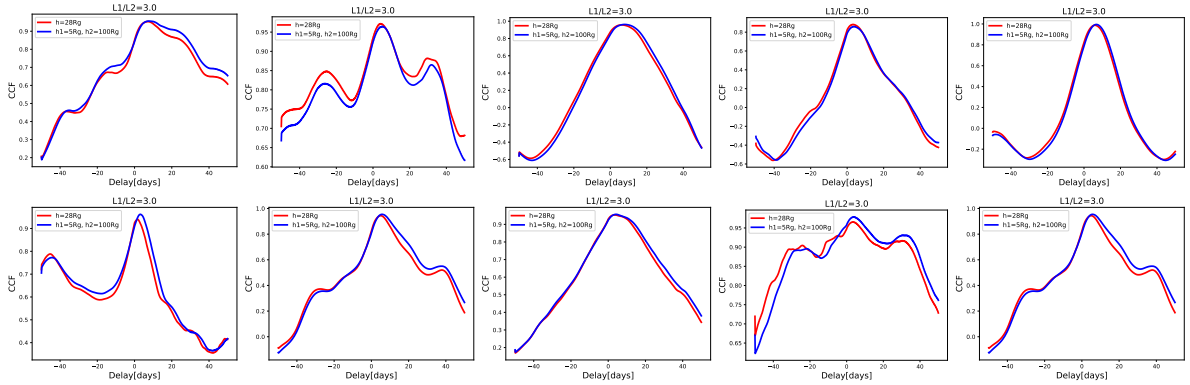

Fig. 6. Examples of the ICCF results for statistically equivalent light curves are shown. The blue line represents the ICCF for the two-corona case, while the red line represents the ICCF for the single-corona case. In this simulation, the luminosity ratio between the two coronae is set to 3. Stochastic variability dominates under the adopted parameters: a light curve duration of 200 days and a sampling interval of 0.1 days.For the single corona, the parameters are: black hole mass $10^8 M_\odot$, incident luminosity $L_X = 2.0 \times 10^{46}$ erg s^{-1}, Eddington ratio = 1.0, heights $h = 28 r_g$, and viewing angle $i = 30°$. For the two coronae, the parameters are: black hole mass $10^8 M_\odot$, luminosities $L_1 = 1.5 \times 10^{46}$ and $L_2 = 0.5 \times 10^{46}$ erg s^{-1}, Eddington ratio = 1.0, heights $h_1 = 5 r_g$ and $h_2 = 100 r_g$, and viewing angle $i = 30°$.

Luminosity Ratio	$(t_{peak})_{1-corona}$ [days]	$(t_{peak})_{2-corona}$ [days]
1.0	4.69	5.69
3.0	4.19	5.19

Table 2. Table summarizing the peak delay from figure 7.

the contour plot shows the dispersion. The result for the lamp luminosity ratio 1:1(top panel) and 1:3(bottom panel) are shown in Figure 7. We observe that the two mean curves lie well within the dispersion, making it difficult to distinguish between them based on a single measurement. The error of the mean would be by a factor of $\sqrt{N}$ lower than the dispersion, but even 10 lightcurves for a given source would not allow us to see the difference. Denser monitoring than 10 observation per day is unlikely, but eventually much longer observations (several seasons) could help.

3.4. comparison of ICCF time delay with respect to single corona

In Figure 7, we present the averaged values and standard deviations of all 10 ICCFs for both single and double corona configurations. Simulations were conducted for luminosity ratios of 1 and 3, with the results summarized in Table 2. For a luminosity ratio of 1, the peak occurs at 4.69 days for the single corona configuration and at 5.69 days for the double corona configuration. Similarly, for a luminosity ratio of 3, the peak is observed at 4.19 days for the single corona and at 5.19 days for the double corona. Thus, extended corona increases statistically the mean time delay but fluctuations are large.

4. Discussion

We presented a simulated setup for irradiation of the disk by the vertically extended hot corona. We aimed to see if the optical/UV reverberation mapping of the accretion disk can reveal such an geometry. The simulations were performed for a black hole mass $10^8 M_\odot$, dense (0.1 day sampling) and long (200 days) monitoring. The expected delays for such setup were from fraction of a day at short wavelengths to 10 days at $\sim$ 10000 Å. The location of the two lamps were extreme, at $5 r_g$ and $100 r_g$. When one of the lamps dominates, the wavelength-dependent delay pattern is like for a single lamppost model. When the two sources have comparable luminosity there is a deviation between the two-source pattern and a single-source (intermediate height) pattern but smaller than 20 %. Therefore, it is not very likely to resolve the vertical extension of the hot corona with the current studies of the continuum time delays. The eventual traces of the vertical extension of the corona in the shape of ICCF are even harder to detect under the discussed setup.

The two lamps are roughly equivalent to a single lamppost model with the location determined as the luminosity-weighted average height (see Equation 11). This is simply related to the fact that most reprocessing observed in optical/UV happens at a distance larger than the largest corona height. In this case the local ratio of the incident radiation from all N lamps to the disk emission is independent from the radius, and given by the ratio

$$\frac{F_{inc}}{F_{disk}} \propto \sum_{i=1}^{N} L_i H_i, \tag{12}$$

as implied by the ratio of the lamp terms to the first term corresponding to non-illuminated disk in Equation 6. Similar condition holds for a continuum distribution, then the sum would be replaced with the integral.

When the two lamps have the same luminosity the effective height is practically just half of the higher lamp position. Therefore, the upper extension of the corona in this sense dominates. This is due to the simple fact, that the irradiation due to the higher lamp dominates at distances larger than $\sim 30 r_g$, as illustrated in Figure 1 where the emission at longer wavelengths is produced.

In our standard model the emission above 2000 Å originates at a distance larger than the maximum height of the corona, 100 r_g , as illustrated by Figure 8. However, this value depends on the black hole mass as well as on the Eddington ratio. We may have better prospects to see the effect of extended corona not equivalent to a mean position when the Eddington ratio is lower,

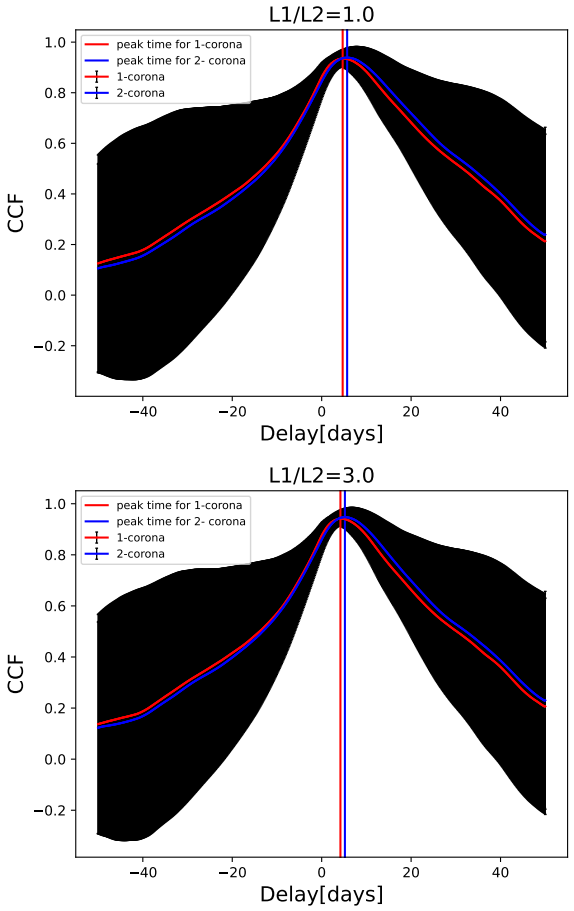

Fig. 7. Upper panel: The mean and dispersion of 10 statistical realizations of the ICCF for a lamp luminosity ratio of 1:1. Bottom panel: The mean and dispersion of 10 statistical realizations of the ICCF for a lamp luminosity ratio of 1:3. The red line represents the mean ICCF for a 1-corona, while the blue line represents the mean ICCF for 2-corona. The shaded region indicates the dispersion in the 2-corona model.

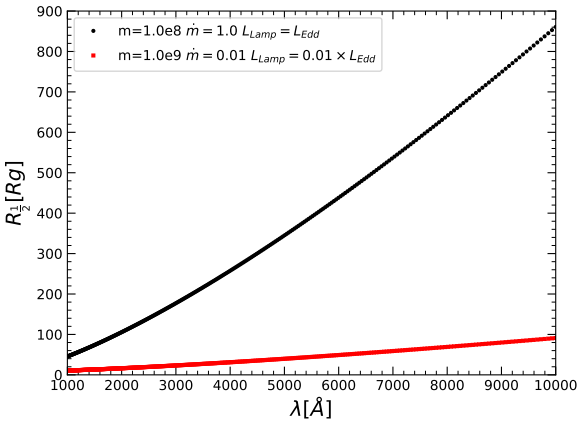

Fig. 8. The dependence of the mid-radius, where 50% of the radiation is emitted, on the emission wavelength is shown for two models: one with a black hole mass of $10^8 M_\odot$ and an Eddington rate of $\dot{m} = 1$ (black line), and another with a black hole mass of $10^9 M_\odot$ and an Eddington rate of $\dot{m} = 0.01$ (red line).

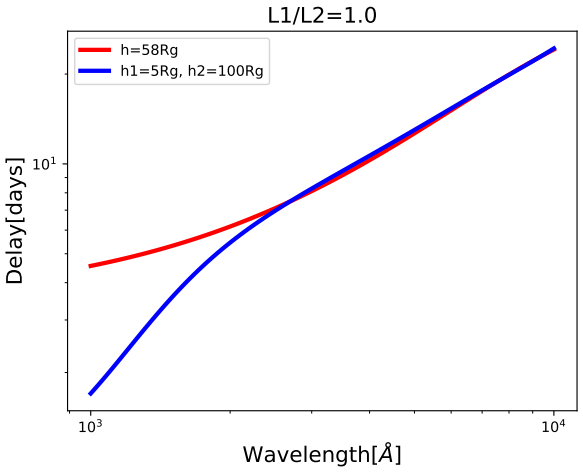

Fig. 9. The plot compare the delays for a 1-corona and 2-corona (with a luminosity ratio of 1). The height of the single corona is selected such that the delay for the longest wavelength matches that of the 2-corona model. For the single corona, the parameters are: black hole mass $10^9 M_\odot$, incident luminosity $L_X = 2.0 \times 10^{46}$ erg s^{-1}, Eddington ratio = 0.01, height $h = 58 r_g$, and viewing angle $i = 30°$. For the two coronae, the parameters are: black hole mass $10^9 M_\odot$, luminosities $L_1 = 1.0 \times 10^{46}$ erg s^{-1} and $L_2 = 1.0 \times 10^{46}$ erg s^{-1}, Eddington ratio = 0.01, heights $h_1 = 5 r_g$ and $h_2 = 100 r_g$, and viewing angle $i = 30°$.

and the black hole mass is higher. This is illustrated in Figure 8 with the red line. In this case the reprocessing takes place at the radii lower or comparable to the height of the upper corona. This opens a prospect to see the difference between a single lamppost and an extended corona. We check that showing the expected time delay.

The delay from the two-corona model in the case of the large black hole mass and low Eddington rate is shown in Figure 9. The delay now does not follow the standard $\lambda^{4/3}$ law any more, as it bends rapidly at the shortest wavelengths. Due to the irradiation, the temperature is almost constant at small radii where radiation at the shortest wavelengths is produces (see the schematic picture in the lower panel of Figure 1). Therefore, the time delay almost disappears. However, most of the reverberation-measured sources do not have such high masses and low Eddington ratios. In addition, our assumptions underlying the model may not be satisfied in this case. We assume (see Section 2.1) that the standard disk extends down to ISCO while this is not true for lower values of the Eddington ratio, and the transition to an inner hot flow is not well described. In addition, since in such case all reprocessing takes place closer to the black hole, the effects of General Relativity become important, and the use of geometrical optics is not justified. If there is a suitable observational data then much more advanced modeling would have to be performed, and the methodology of Langis et al. (2024) would be an excellent starting point.

5. Conclusions

- **Sensitivity of UV/Optical Reverberation Mapping:** The study reveals that UV/optical reverberation mapping has limited sensitivity to the vertical extension of the corona. Detecting such an extension requires highly precise time delay measurements (with errors below 20%) and exceptionally dense sampling of lightcurves.
- **Effective Position of the Corona:** The effective position of the corona is well approximated by a luminosity-weighted average height of the emitting components. This result underscores that the impact of vertical extension on reverberation mapping is minimal under typical observational conditions.
- **Comparison of Two-Lamp and Single-Lamp Models:** The differences in wavelength-dependent delays between the two-lamp corona model and the single-lamp model are relatively small, with a maximum deviation of 20%, observed for a lamp luminosity ratio of about 3. These differences remain challenging to detect with current observational techniques.
- **Insights from Cross-Correlation Function (ICCF) Analysis:** Simulations demonstrate that ICCFs for single-lamp and two-lamp corona configurations are statistically similar. Differentiating the two geometries would require significantly extended monitoring periods or much denser observational sampling.
- **Role of Black Hole Mass and Eddington Ratio:** The study suggests that larger black hole masses and lower Eddington ratios enhance the likelihood of detecting the effects of an extended corona. These conditions result in more pronounced deviations from single-lamp model predictions, but would require much more advanced modelling.

Acknowledgments

We are thankful to Amit Kumar Mandal for helpful suggestions in the text. This project has received funding from the European Research Council (ERC) under the European Union's Horizon 2020 research and innovation program (grant agreement No. [951549]). VKJ acknowledges the OPUS-LAP/GAČR-LA bilateral project (2021/43/I/ST9/01352/OPUS 22 and GF23-04053L).

References

Ballantyne, D. R., Sudhakar, V., Fairfax, D., et al. 2024, MNRAS, 530, 1603
Beloborodov, A. M. 1999, ApJ, 510, L123
Bentz, M. C., Denney, K. D., Grier, C. J., et al. 2013, ApJ, 767, 149
Cackett, E. M., Bentz, M. C., & Kara, E. 2021, iScience, 24, 102557
Cackett, E. M., Chiang, C.-Y., McHardy, I., et al. 2018, ApJ, 857, 53
Cackett, E. M., Fabian, A. C., Zogbhi, A., et al. 2013, ApJ, 764, L9
Cackett, E. M., Gelbord, J., Barth, A. J., et al. 2023, ApJ, 958, 195
Cackett, E. M., Gelbord, J., Li, Y.-R., et al. 2020, ApJ, 896, 1
Cackett, E. M., Horne, K., & Winkler, H. 2007, MNRAS, 380, 669
Cackett, E. M., Zoghbi, A., Reynolds, C., et al. 2014, MNRAS, 438, 2980
Chainakun, P. 2019, The Astrophysical Journal, 878, 20
Collier, S., Horne, K., Wanders, I., & Peterson, B. M. 1999, MNRAS, 302, L24
Collier, S. J., Horne, K., Kaspi, S., et al. 1998, ApJ, 500, 162
De Marco, B. & Ponti, G. 2019, Astronomische Nachrichten, 340, 290
Dovčiak, M., Karas, V., & Yaqoob, T. 2004, ApJS, 153, 205
Edelson, R., Peterson, B. M., Gelbord, J., et al. 2024, ApJ, 973, 152
Emmanoulopoulos, D., McHardy, I. M., & Papadakis, I. E. 2011, MNRAS, 416, L94
Esin, A. A., McClintock, J. E., & Narayan, R. 1997, ApJ, 489, 865
Fabian, A. C., Iwasawa, K., Reynolds, C. S., & Young, A. J. 2000, PASP, 112, 1145
Fabian, A. C., Zoghbi, A., Ross, R. R., et al. 2009, Nature, 459, 540
Fausnaugh, M. M., Denney, K. D., Barth, A. J., et al. 2016, ApJ, 821, 56
Galeev, A. A., Rosner, R., & Vaiana, G. S. 1979, ApJ, 229, 318
George, I. M. & Fabian, A. C. 1991, MNRAS, 249, 352
Giustini, M. & Proga, D. 2019, A&A, 630, A94
Haardt, F. & Maraschi, L. 1993, ApJ, 413, 507
Haardt, F., Maraschi, L., & Ghisellini, G. 1994, ApJ, 432, L95
Hancock, S., Young, A. J., & Chainakun, P. 2023, MNRAS, 520, 180
Henri, G. & Pelletier, G. 1991, ApJ, 383, L7
Ichimaru, S. 1977, ApJ, 214, 840
Iwasawa, K., Fabian, A. C., Reynolds, C. S., et al. 1996, MNRAS, 282, 1038
Jaiswal, V. K., Prince, R., Panda, S., & Czerny, B. 2023, A&A, 670, A147
Kammoun, E. S., Dovčiak, M., Papadakis, I. E., Caballero-García, M. D., & Karas, V. 2021a, ApJ, 907, 20
Kammoun, E. S., Papadakis, I. E., & Dovčiak, M. 2019, ApJ, 879, L24
Kammoun, E. S., Papadakis, I. E., & Dovčiak, M. 2021b, MNRAS, 503, 4163
Kammoun, E. S., Robin, L., Papadakis, I. E., Dovčiak, M., & Panagiotou, C. 2023, MNRAS, 526, 138
Kara, E., Alston, W. N., Fabian, A. C., et al. 2016a, MNRAS, 462, 511
Kara, E., Fabian, A. C., Cackett, E. M., et al. 2013, MNRAS, 434, 1129
Kara, E., Miller, J. M., Reynolds, C., & Dai, L. 2016b, Nature, 535, 388
Kara, E., Steiner, J. F., Fabian, A. C., et al. 2019, Nature, 565, 198
Kelly, B. C., Bechtold, J., & Siemiginowska, A. 2009, ApJ, 698, 895
Krolik, J. H. 1999, Active Galactic Nuclei. From the Central Black Hole to the Galactic Environment
Kubota, A. & Done, C. 2018, MNRAS, 480, 1247
Langis, D. A., Papadakis, I. E., Kammoun, E., Panagiotou, C., & Dovčiak, M. 2024, A&A, 691, A252
Liu, T., Edelson, R., Hernández Santisteban, J. V., et al. 2024, ApJ, 964, 167
Lucchini, M., Mastroserio, G., Wang, J., et al. 2023, ApJ, 951, 19
Markoff, S., Nowak, M. A., & Wilms, J. 2005, ApJ, 635, 1203
Matt, G., Perola, G. C., & Piro, L. 1991, A&A, 247, 25
McHardy, I. M., Arévalo, P., Uttley, P., et al. 2007, MNRAS, 382, 985
McHardy, I. M., Cameron, D. T., Dwelly, T., et al. 2014, MNRAS, 444, 1469
McHardy, I. M., Connolly, S. D., Horne, K., et al. 2018, MNRAS, 480, 2881
Montano, J. W., Guo, H., Barth, A. J., et al. 2022, ApJ, 934, L37
Nandra, K., Pounds, K. A., Stewart, G. C., Fabian, A. C., & Rees, M. J. 1989, MNRAS, 236, 39P
Narayan, R. & Yi, I. 1994, ApJ, 428, L13
Oknyanskij, V. L., Horne, K., Lyuty, V. M., et al. 2003, in Astronomical Society of the Pacific Conference Series, Vol. 290, Active Galactic Nuclei: From Central Engine to Host Galaxy, ed. S. Collin, F. Combes, & I. Shlosman, 119
Palit, B., Rozanska, A., Petrucci, P. O., et al. 2024, arXiv e-prints, arXiv:2406.14378
Peterson, B. M. 1988, Publications of the Astronomical Society of the Pacific, 100, 18
Peterson, B. M. 1993, PASP, 105, 247
Peterson, B. M., Ferrarese, L., Gilbert, K. M., et al. 2004, The Astrophysical Journal, 613, 682
Poindexter, S., Morgan, N., & Kochanek, C. S. 2008, ApJ, 673, 34
Pounds, K. A., Nandra, K., Stewart, G. C., George, I. M., & Fabian, A. C. 1990, Nature, 344, 132
Rokaki, E., Collin-Souffrin, S., & Magnan, C. 1993, A&A, 272, 8
Różańska, A., Malzac, J., Belmont, R., Czerny, B., & Petrucci, P. O. 2015, A&A, 580, A77
Sergeev, S. G., Doroshenko, V. T., Golubinskiy, Y. V., Merkulova, N. I., & Sergeeva, E. A. 2005, ApJ, 622, 129
Shakura, N. I. & Sunyaev, R. A. 1973, A&A, 500, 33
Shen, Y., Grier, C. J., Horne, K., et al. 2024, ApJS, 272, 26
Szanecki, M., Niedźwiecki, A., Done, C., et al. 2020, A&A, 641, A89
Timmer, J. & Koenig, M. 1995, A&A, 300, 707
Ursini, F., Dovčiak, M., Zhang, W., et al. 2020a, A&A, 644, A132
Ursini, F., Petrucci, P. O., Bianchi, S., et al. 2020b, A&A, 634, A92
Vincentelli, F. M., McHardy, I., Cackett, E. M., et al. 2021, Monthly Notices of the Royal Astronomical Society, 504, 4337–4353
Wilkins, D. R., Cackett, E. M., Fabian, A. C., & Reynolds, C. S. 2016, MNRAS, 458, 200
Wilkins, D. R. & Fabian, A. C. 2012, MNRAS, 424, 1284
You, B., Tuo, Y., Li, C., et al. 2021, Nature Communications, 12, 1025
Zajaček, M., Czerny, B., Martinez-Aldama, M. L., et al. 2021, ApJ, 912, 10
Zoghbi, A., Reynolds, C., Cackett, E. M., et al. 2013, ApJ, 767, 121

Appendix A

Lag and SED fitting IN NGC 5548

High quality time delay measurements and spectral data are required to constrain the luminosity distance to the source. We determined that the best fit sets the luminosity distance for NGC 5548 at 74 Mpc (see Chapter 5) but we show here for comparison the fit of the spectrum and the time delay pattern for two extreme luminosity distances considered in the paper: 50 and 102 Mpc. They are visually not very different as the change in the luminosity distance is compensated by the change of the fitted parameters like accretion rate, coronal height, or starlight contamination.

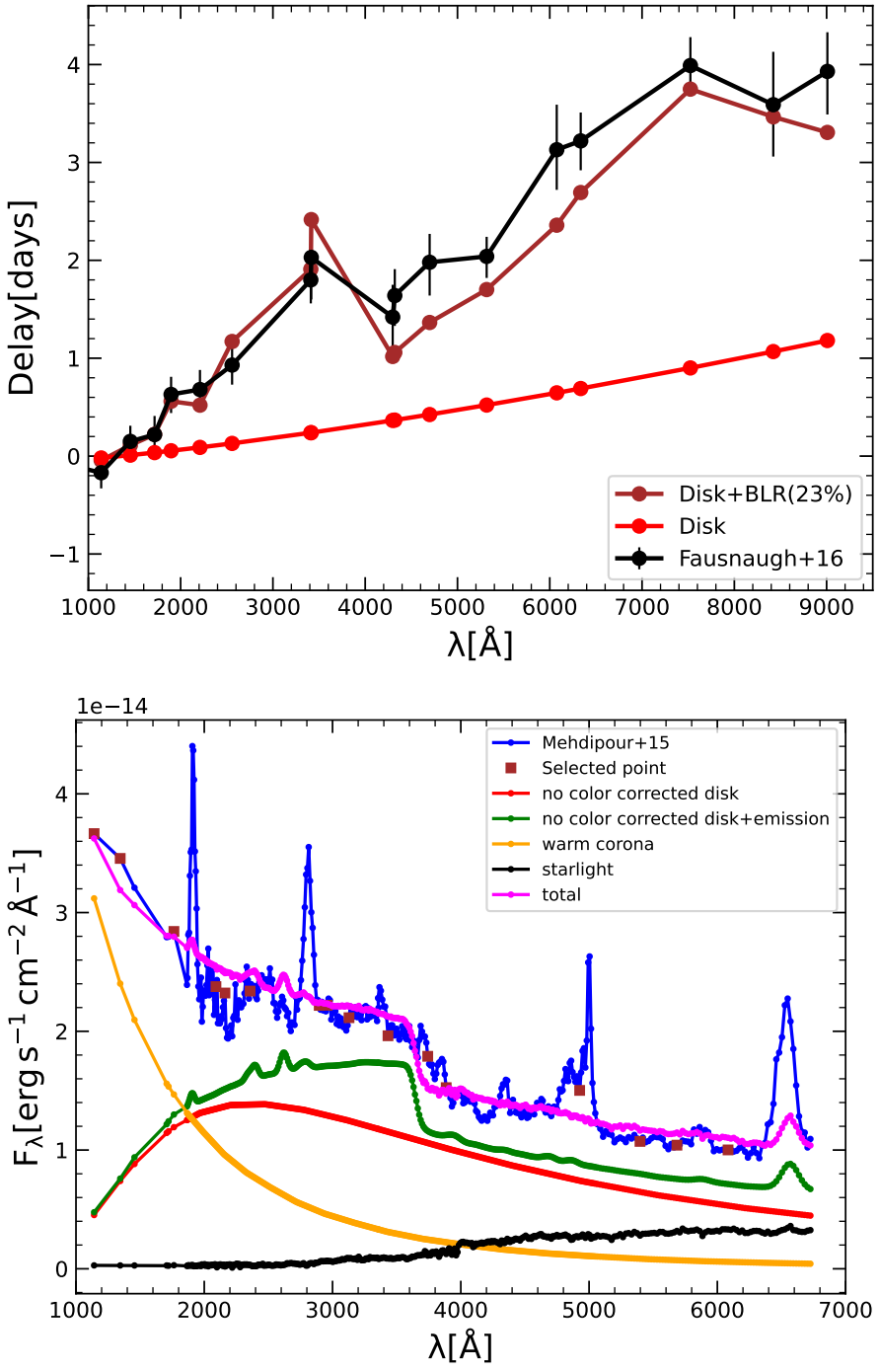

FIGURE A.1: Simultaneous fitting of the lag spectrum and spectral energy distribution (SED) of NGC 5548, under the assumption of a luminosity distance of 50 Mpc.

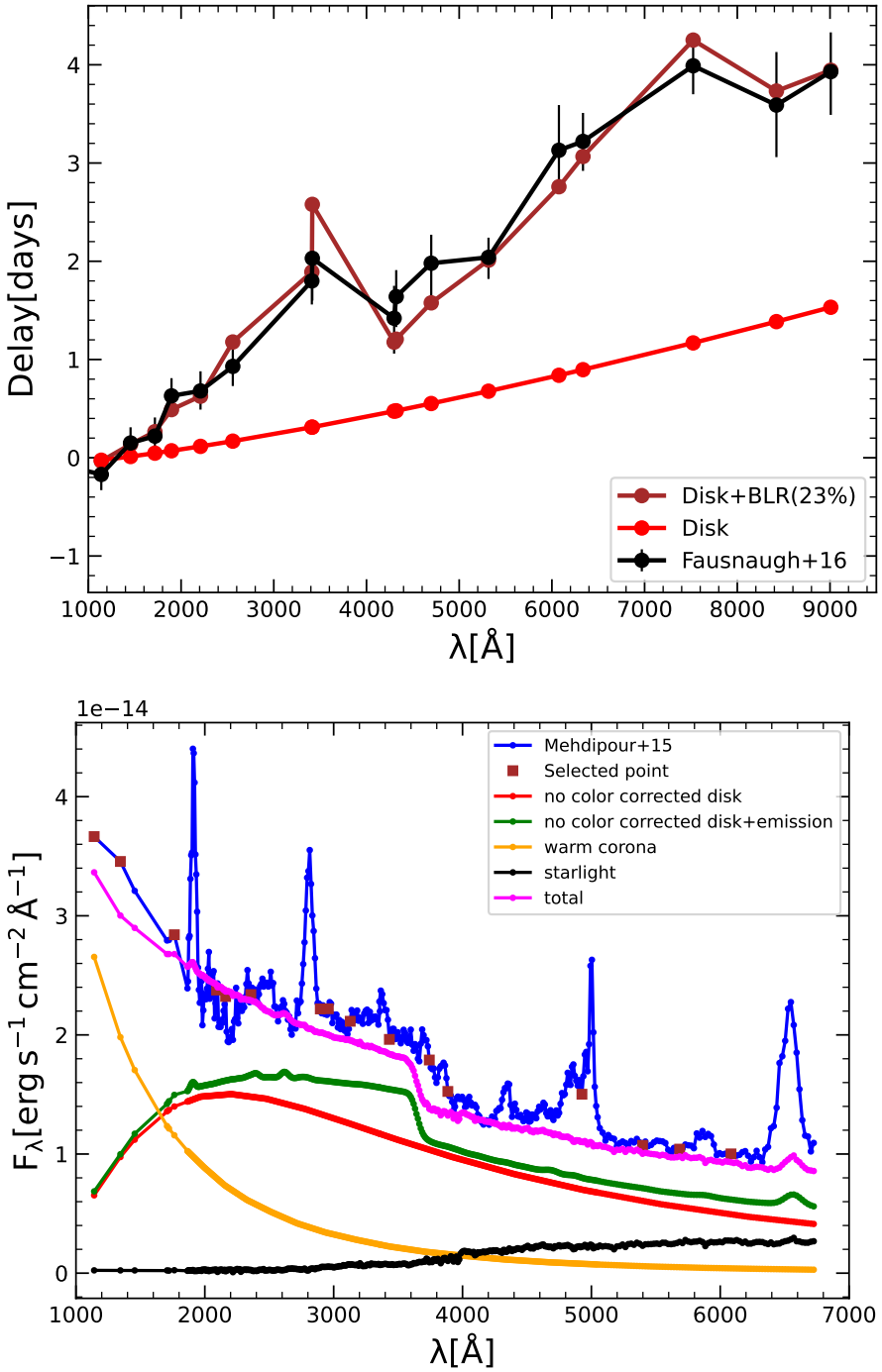

FIGURE A.2: Simultaneous fitting of the lag spectrum and spectral energy distribution (SED) of NGC 5548, under the assumption of a luminosity distance of 102 Mpc.

Appendix B

Shielding effect in the Broad Line Region

It is sometimes suggested (e.g. Horne et al., 2021) that the observer does not see the entire Broad Line Region, and the appearance may be dominated by the clouds close to the observer. Clouds themselves or strong outflow from the disk inside the inner BLR radius can selectively shield part of the BLR from our view. If so, we would indeed preferentially see the BLR part closer to the observer. This effect can shorten the time delay as the most distant clouds would not contribute to the emission. In Figure B.1 I show the response function for NGC 5548 calculated assuming that clouds opposite to the direction towards observed, within a certain arbitrary angle, as shielded. The shortening effect depends clearly on this angle, so in principle, shorter delay could be explained even with larger radius of the BLR than in the original model without shielding. However, shielding would also imply a considerable change in the line profile, as I show in Figure B.2. With moderate shielding, the line of more strongly double-peaked than without shielding. This issue was not included in my papers but should be studied in the future.

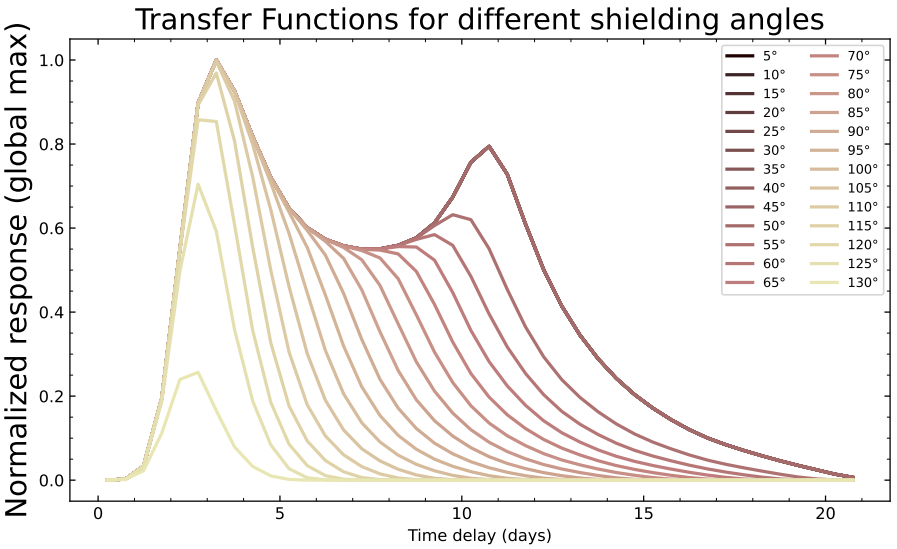

FIGURE B.1: Response functions of the broad-line region (BLR) for different shielding angles. The comparison highlights how changes in shielding geometry alter the strength and timing of the BLR response to continuum variability.

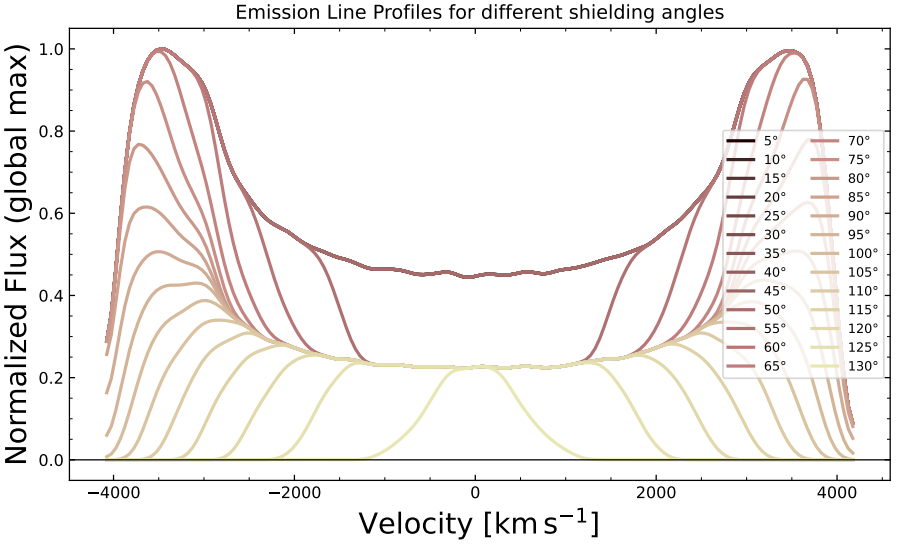

FIGURE B.2: Broad-line emission profiles for a range of shielding angles, illustrating how the shielding geometry alters the observed profile.

References

Abbott, R., et al., 2023. Constraints on the Cosmic Expansion History from GWTC–3. 949, 76. doi:10.3847/1538-4357/ac74bb, arXiv:2111.03604.

Abdalla, E., et al., 2022. Cosmology intertwined: A review of the particle physics, astrophysics, and cosmology associated with the cosmological tensions and anomalies. Journal of High Energy Astrophysics 34, 49–211. doi:10.1016/j.jheap.2022.04.002, arXiv:2203.06142.

Abramowicz, M., Jaroszynski, M., Sikora, M., 1978. Relativistic, accreting disks. 63, 221–224.

Abramowicz, M.A., Czerny, B., Lasota, J.P., Szuszkiewicz, E., 1988. Slim Accretion Disks. 332, 646. doi:10.1086/166683.

Alston, W.N., Done, C., Vaughan, S., 2014. X-ray time delays in the narrow line Seyfert 1 galaxy PG 1244+026. 439, 1548–1555. doi:10.1093/mnras/stu005, arXiv:1311.5165.

Alston, W.N., Fabian, A.C., Kara, E., Parker, M.L., Dovciak, M., Pinto, C., Jiang, J., Middleton, M.J., Miniutti, G., Walton, D.J., Wilkins, D.R., Buisson, D.J.K., Caballero-Garcia, M.D., Cackett, E.M., De Marco, B., Gallo, L.C., Lohfink, A.M., Reynolds, C.S., Uttley, P., Young, A.J., Zogbhi,

A., 2020. A dynamic black hole corona in an active galaxy through X-ray reverberation mapping. Nature Astronomy 4, 597–602. doi:10.1038/s41550-019-1002-x, arXiv:2001.06454.

Antonucci, R., 1993. Unified models for active galactic nuclei and quasars. 31, 473–521. doi:10.1146/annurev.aa.31.090193.002353.

Antonucci, R.R.J., Cohen, R.D., 1983. Time development of the emission lines and continuum of NGC 4151. 271, 564–574. doi:10.1086/161223.

Antonucci, R.R.J., Miller, J.S., 1985. Spectropolarimetry and the nature of NGC 1068. 297, 621–632. doi:10.1086/163559.

Assef, R.J., Stern, D., Kochanek, C.S., Blain, A.W., Brodwin, M., Brown, M.J.I., Donoso, E., Eisenhardt, P.R.M., Jannuzi, B.T., Jarrett, T.H., Stanford, S.A., Tsai, C.W., Wu, J., Yan, L., 2013. Mid-infrared Selection of Active Galactic Nuclei with the Wide-field Infrared Survey Explorer. II. Properties of WISE-selected Active Galactic Nuclei in the NDWFS Boötes Field. 772, 26. doi:10.1088/0004-637X/772/1/26, arXiv:1209.6055.

Aubourg, É., et al., 2015. Cosmological implications of baryon acoustic oscillation measurements. 92, 123516. doi:10.1103/PhysRevD.92.123516, arXiv:1411.1074.

Balbus, S.A., Hawley, J.F., 1991. A Powerful Local Shear Instability in Weakly Magnetized Disks. I. Linear Analysis. 376, 214. doi:10.1086/170270.

Balbus, S.A., Hawley, J.F., 1998. Turbulent transport in accretion disks, in: Holt, S.S., Kallman, T.R. (Eds.), Accretion processes in Astrophysical Systems: Some like it hot! - eigth AstroPhysics Conference, pp. 79–88. doi:10.1063/1.55947.

Baldwin, J., Ferland, G., Korista, K., Verner, D., 1995. Locally Optimally Emitting Clouds and the Origin of Quasar Emission Lines. 455, L119. doi:10.1086/309827, arXiv:astro-ph/9510080.

Bambi, C., 2020. Astrophysical Black Holes: A Review, in: Multifrequency Behaviour of High Energy Cosmic Sources - XIII. 3-8 June 2019. Palermo, p. 28. doi:10.22323/1.362.0028, arXiv:1906.03871.

Barvainis, R., 1987. Hot Dust and the Near-Infrared Bump in the Continuum Spectra of Quasars and Active Galactic Nuclei. 320, 537. doi:10.1086/165571.

Beloborodov, A.M., 1999. Plasma Ejection from Magnetic Flares and the X-Ray Spectrum of Cygnus X-1. 510, L123–L126. doi:10.1086/311810, arXiv:astro-ph/9809383.

Bennert, N., Falcke, H., Schulz, H., Wilson, A.S., Wills, B.J., 2002. Size and Structure of the Narrow-Line Region of Quasars. 574, L105–L109. doi:10.1086/342420, arXiv:astro-ph/0206334.

Bentz, M.C., Denney, K.D., Grier, C.J., Barth, A.J., Peterson, B.M., Vestergaard, M., Bennert, V.N., Canalizo, G., De Rosa, G., Filippenko, A.V., Gates, E.L., Greene, J.E., Li, W., Malkan, M.A., Pogge, R.W., Stern, D., Treu, T., Woo, J.H., 2013. The Low-luminosity End of the Radius-Luminosity Relationship for Active Galactic Nuclei. 767, 149. doi:10.1088/0004-637X/767/2/149, arXiv:1303.1742.

Bentz, M.C., Peterson, B.M., Netzer, H., Pogge, R.W., Vestergaard, M., 2009. The Radius-Luminosity Relationship for Active Galactic Nuclei: The Effect of Host-Galaxy Starlight on Luminosity Measurements. II. The Full Sample

of Reverberation-Mapped AGNs. 697, 160–181. doi:10.1088/0004-637X/697/1/160, arXiv:0812.2283.

Bentz, M.C., Peterson, B.M., Pogge, R.W., Vestergaard, M., Onken, C.A., 2006. The Radius-Luminosity Relationship for Active Galactic Nuclei: The Effect of Host-Galaxy Starlight on Luminosity Measurements. 644, 133–142. doi:10.1086/503537, arXiv:astro-ph/0602412.

Birrer, S., Shajib, A.J., Galan, A., Millon, M., Treu, T., Agnello, A., Auger, M., Chen, G.C.F., Christensen, L., Collett, T., Courbin, F., Fassnacht, C.D., Koopmans, L.V.E., Marshall, P.J., Park, J.W., Rusu, C.E., Sluse, D., Spiniello, C., Suyu, S.H., Wagner-Carena, S., Wong, K.C., Barnabè, M., Bolton, A.S., Czoske, O., Ding, X., Frieman, J.A., Van de Vyvere, L., 2020. TDCOSMO. IV. Hierarchical time-delay cosmography - joint inference of the Hubble constant and galaxy density profiles. 643, A165. doi:10.1051/0004-6361/202038861, arXiv:2007.02941.

Blandford, R., Meier, D., Readhead, A., 2019. Relativistic Jets from Active Galactic Nuclei. 57, 467–509. doi:10.1146/annurev-astro-081817-051948, arXiv:1812.06025.

Blandford, R.D., Payne, D.G., 1982. Hydromagnetic flows from accretion disks and the production of radio jets. 199, 883–903. doi:10.1093/mnras/199.4.883.

Blandford, R.D., Znajek, R.L., 1977. Electromagnetic extraction of energy from Kerr black holes. 179, 433–456. doi:10.1093/mnras/179.3.433.

Bochkarev, N.G., 1984. Search for one-day variability of the broad components of emission line profile for the NGC 4151 Seyfert galaxy nucleus. Pisma v Astronomicheskii Zhurnal 10, 574–582.

Bolton, C.T., 1972. Identification of Cygnus X-1 with HDE 226868. 235, 271–273. doi:10.1038/235271b0.

Burtscher, L., Hönig, S., Jaffe, W., Kishimoto, M., Lopez-Gonzaga, N., Meisenheimer, K., Tristam, K.R.W., 2016. Infrared interferometry and AGNs: Parsec-scale disks and dusty outflows, in: Malbet, F., Creech-Eakman, M.J., Tuthill, P.G. (Eds.), Optical and Infrared Interferometry and Imaging V, p. 99070R. doi:10.1117/12.2231077, arXiv:1607.04533.

Cackett, E.M., Chiang, C.Y., McHardy, I., Edelson, R., Goad, M.R., Horne, K., Korista, K.T., 2018. Accretion Disk Reverberation with Hubble Space Telescope Observations of NGC 4593: Evidence for Diffuse Continuum Lags. 857, 53. doi:10.3847/1538-4357/aab4f7, arXiv:1712.04025.

Cackett, E.M., Fabian, A.C., Zogbhi, A., Kara, E., Reynolds, C., Uttley, P., 2013. A Soft X-Ray Reverberation Lag in the AGN ESO 113-G010. 764, L9. doi:10.1088/2041-8205/764/1/L9, arXiv:1210.7874.

Cackett, E.M., Gelbord, J., Li, Y.R., Horne, K., Wang, J.M., Barth, A.J., Bai, J.M., Bian, W.H., Carroll, R.W., Du, P., Edelson, R., Goad, M.R., Ho, L.C., Hu, C., Khatu, V.C., Luo, B., Miller, J., Yuan, Y.F., 2020. Supermassive Black Holes with High Accretion Rates in Active Galactic Nuclei. XI. Accretion Disk Reverberation Mapping of Mrk 142. 896, 1. doi:10.3847/1538-4357/ab91b5, arXiv:2005.03685.

Cackett, E.M., Zoghbi, A., Reynolds, C., Fabian, A.C., Kara, E., Uttley, P., Wilkins, D.R., 2014. Modelling the broad Fe Kα reverberation in the AGN NGC 4151. 438, 2980–2994. doi:10.1093/mnras/stt2424, arXiv:1311.2997.

Camarena, D., Marra, V., 2021. On the use of the local prior on the absolute magnitude of Type Ia supernovae in cosmological inference. 504, 5164–5171. doi:10.1093/mnras/stab1200, arXiv:2101.08641.

Chartas, G., Kochanek, C.S., Dai, X., Moore, D., Mosquera, A.M., Blackburne, J.A., 2012. Revealing the Structure of an Accretion Disk through Energy-dependent X-Ray Microlensing. 757, 137. doi:10.1088/0004-637X/757/2/137, arXiv:1204.4480.

Chartas, G., Kochanek, C.S., Dai, X., Poindexter, S., Garmire, G., 2009. X-Ray Microlensing in RXJ1131-1231 and HE1104-1805. 693, 174–185. doi:10.1088/0004-637X/693/1/174, arXiv:0805.4492.

Chatzikos, M., Bianchi, S., Camilloni, F., Chakraborty, P., Gunasekera, C.M., Guzmán, F., Milby, J.S., Sarkar, A., Shaw, G., van Hoof, P.A.M., Ferland, G.J., 2023. The 2023 Release of Cloudy. 59, 327–343. doi:10.22201/ia.01851101p.2023.59.02.12, arXiv:2308.06396.

Cherepashchuk, A.M., Lyutyi, V.M., 1973. Rapid Variations of Hα Intensity in the Nuclei of Seyfert Galaxies NGC 4151, 3516, 1068. 13, 165.

Clavel, J., Wamsteker, W., Glass, I.S., 1989. Hot Dust on the Outskirts of the Broad-Line Region in Fairall 9. 337, 236. doi:10.1086/167100.

Clavel, J., et al., 1991. Steps toward Determination of the Size and Structure of the Broad-Line Region in Active Galactic Nuclei. I. an 8 Month Campaign of Monitoring NGC 5548 with IUE. 366, 64. doi:10.1086/169540.

Collinson, J.S., Ward, M.J., Landt, H., Done, C., Elvis, M., McDowell, J.C., 2017. Reaching the peak of the quasar spectral energy distribution - II.

Exploring the accretion disc, dusty torus and host galaxy. 465, 358–382. doi:10.1093/mnras/stw2666, arXiv:1610.04221.

Crummy, J., Fabian, A.C., Gallo, L., Ross, R.R., 2006. An Explanation for the Soft X-ray Excess in AGN, in: Wilson, A. (Ed.), The X-ray Universe 2005, p. 497.

Czerny, B., Hryniewicz, K., 2011. The origin of the broad line region in active galactic nuclei. 525, L8. doi:10.1051/0004-6361/201016025, arXiv:1010.6201.

Davidson, K., Netzer, H., 1979. The emission lines of quasars and similar objects. Reviews of Modern Physics 51, 715–766. doi:10.1103/RevModPhys.51.715.

De Marco, B., Ponti, G., Cappi, M., Dadina, M., Uttley, P., Cackett, E.M., Fabian, A.C., Miniutti, G., 2013. Discovery of a relation between black hole mass and soft X-ray time lags in active galactic nuclei. 431, 2441–2452. doi:10.1093/mnras/stt339, arXiv:1201.0196.

De Rosa, G., Peterson, B.M., Ely, J., Kriss, G.A., Crenshaw, D.M., Horne, K., Korista, K.T., Netzer, H., Pogge, R.W., Arévalo, P., Barth, A.J., Bentz, M.C., Brandt, W.N., Breeveld, A.A., Brewer, B.J., Dalla Bontà, E., De Lorenzo-Cáceres, A., Denney, K.D., Dietrich, M., Edelson, R., Evans, P.A., Fausnaugh, M.M., Gehrels, N., Gelbord, J.M., Goad, M.R., Grier, C.J., Grupe, D., Hall, P.B., Kaastra, J., Kelly, B.C., Kennea, J.A., Kochanek, C.S., Lira, P., Mathur, S., McHardy, I.M., Nousek, J.A., Pancoast, A., Papadakis, I., Pei, L., Schimoia, J.S., Siegel, M., Starkey, D., Treu, T., Uttley, P., Vaughan, S., Vestergaard, M., Villforth, C., Yan, H., Young, S., Zu, Y., 2015. Space Telescope and Optical Reverberation Mapping Project.I.

Ultraviolet Observations of the Seyfert 1 Galaxy NGC 5548 with the Cosmic Origins Spectrograph on Hubble Space Telescope. 806, 128. doi:10.1088/0004-637X/806/1/128, arXiv:1501.05954.

Dexter, J., Agol, E., 2011. Quasar Accretion Disks are Strongly Inhomogeneous. 727, L24. doi:10.1088/2041-8205/727/1/L24, arXiv:1012.3169.

Di Valentino, E., Mena, O., Pan, S., Visinelli, L., Yang, W., Melchiorri, A., Mota, D.F., Riess, A.G., Silk, J., 2021. In the realm of the Hubble tension-a review of solutions. Classical and Quantum Gravity 38, 153001. doi:10.1088/1361-6382/ac086d, arXiv:2103.01183.

Edelson, R., Gelbord, J., Cackett, E., Connolly, S., Done, C., Fausnaugh, M., Gardner, E., Gehrels, N., Goad, M., Horne, K., McHardy, I., Peterson, B.M., Vaughan, S., Vestergaard, M., Breeveld, A., Barth, A.J., Bentz, M., Bottorff, M., Brandt, W.N., Crawford, S.M., Dalla Bontà, E., Emmanoulopoulos, D., Evans, P., Figuera Jaimes, R., Filippenko, A.V., Ferland, G., Grupe, D., Joner, M., Kennea, J., Korista, K.T., Krimm, H.A., Kriss, G., Leonard, D.C., Mathur, S., Netzer, H., Nousek, J., Page, K., Romero-Colmenero, E., Siegel, M., Starkey, D.A., Treu, T., Vogler, H.A., Winkler, H., Zheng, W., 2017. Swift Monitoring of NGC 4151: Evidence for a Second X-Ray/UV Reprocessing. 840, 41. doi:10.3847/1538-4357/aa6890, arXiv:1703.06901.

Edelson, R., Gelbord, J., Cackett, E., Peterson, B.M., Horne, K., Barth, A.J., Starkey, D.A., Bentz, M., Brandt, W.N., Goad, M., Joner, M., Korista, K., Netzer, H., Page, K., Uttley, P., Vaughan, S., Breeveld, A., Cenko, S.B., Done, C., Evans, P., Fausnaugh, M., Ferland, G., Gonzalez-Buitrago, D., Gropp, J., Grupe, D., Kaastra, J., Kennea, J., Kriss, G., Mathur, S., Mehdipour, M., Mudd, D., Nousek, J., Schmidt, T., Vestergaard, M.,

Villforth, C., 2019. The First Swift Intensive AGN Accretion Disk Reverberation Mapping Survey. 870, 123. doi:10.3847/1538-4357/aaf3b4, arXiv:1811.07956.

Edelson, R., Gelbord, J.M., Horne, K., McHardy, I.M., Peterson, B.M., Arévalo, P., Breeveld, A.A., De Rosa, G., Evans, P.A., Goad, M.R., Kriss, G.A., Brandt, W.N., Gehrels, N., Grupe, D., Kennea, J.A., Kochanek, C.S., Nousek, J.A., Papadakis, I., Siegel, M., Starkey, D., Uttley, P., Vaughan, S., Young, S., Barth, A.J., Bentz, M.C., Brewer, B.J., Crenshaw, D.M., Dalla Bontà, E., De Lorenzo-Cáceres, A., Denney, K.D., Dietrich, M., Ely, J., Fausnaugh, M.M., Grier, C.J., Hall, P.B., Kaastra, J., Kelly, B.C., Korista, K.T., Lira, P., Mathur, S., Netzer, H., Pancoast, A., Pei, L., Pogge, R.W., Schimoia, J.S., Treu, T., Vestergaard, M., Villforth, C., Yan, H., Zu, Y., 2015. Space Telescope and Optical Reverberation Mapping Project. II. Swift and HST Reverberation Mapping of the Accretion Disk of NGC 5548. 806, 129. doi:10.1088/0004-637X/806/1/129, arXiv:1501.05951.

Efstathiou, G., 2025. Challenges to the Λ CDM cosmology. Philosophical Transactions of the Royal Society of London Series A 383, 20240022. doi:10.1098/rsta.2024.0022, arXiv:2406.12106.

Elvis, M., 2000. A Structure for Quasars. 545, 63–76. doi:10.1086/317778, arXiv:astro-ph/0008064.

Emmering, R.T., Blandford, R.D., Shlosman, I., 1992. Magnetic Acceleration of Broad Emission-Line Clouds in Active Galactic Nuclei. 385, 460. doi:10.1086/170955.

Espey, B.R., Carswell, R.F., Bailey, J.A., Smith, M.G., Ward, M.J., 1989. H alpha Emission Lines in High-Redshift Quasars. 342, 666. doi:10.1086/167627.

Event Horizon Telescope Collaboration, Akiyama, K., et al., 2019a. First M87 Event Horizon Telescope Results. I. The Shadow of the Supermassive Black Hole. 875, L1. doi:10.3847/2041-8213/ab0ec7, arXiv:1906.11238.

Event Horizon Telescope Collaboration, Akiyama, K., et al., 2019b. First M87 Event Horizon Telescope Results. VI. The Shadow and Mass of the Central Black Hole. 875, L6. doi:10.3847/2041-8213/ab1141, arXiv:1906.11243.

Fabian, A.C., Rees, M.J., Stella, L., White, N.E., 1989. X-ray fluorescence from the inner disc in Cygnus X-1. 238, 729–736. doi:10.1093/mnras/238.3.729.

Fabian, A.C., Zoghbi, A., Ross, R.R., Uttley, P., Gallo, L.C., Brandt, W.N., Blustin, A.J., Boller, T., Caballero-Garcia, M.D., Larsson, J., Miller, J.M., Miniutti, G., Ponti, G., Reis, R.C., Reynolds, C.S., Tanaka, Y., Young, A.J., 2009. Broad line emission from iron K- and L-shell transitions in the active galaxy 1H0707-495. 459, 540–542. doi:10.1038/nature08007.

Fanaroff, B.L., Riley, J.M., 1974. The morphology of extragalactic radio sources of high and low luminosity. 167, 31P–36P. doi:10.1093/mnras/167.1.31P.

Fath, E.A., 1909. The spectra of some spiral nebulae and globular star clusters. Lick Observatory Bulletin 149, 71–77. doi:10.5479/ADS/bib/1909LicOB.5.71F.

Fausnaugh, M.M., et al., 2016. Space Telescope and Optical Reverberation Mapping Project. III. Optical Continuum Emission and Broadband

Time Delays in NGC 5548. 821, 56. doi:10.3847/0004-637X/821/1/56, arXiv:1510.05648.

Fausnaugh, M.M., et al., 2018. Continuum Reverberation Mapping of the Accretion Disks in Two Seyfert 1 Galaxies. 854, 107. doi:10.3847/1538-4357/aaaa2b, arXiv:1801.09692.

Ferrarese, L., Merritt, D., 2000. A Fundamental Relation between Supermassive Black Holes and Their Host Galaxies. 539, L9–L12. doi:10.1086/312838, arXiv:astro-ph/0006053.

Freedman, W.L., Madore, B.F., Gibson, B.K., Ferrarese, L., Kelson, D.D., Sakai, S., Mould, J.R., Kennicutt, Jr., R.C., Ford, H.C., Graham, J.A., Huchra, J.P., Hughes, S.M.G., Illingworth, G.D., Macri, L.M., Stetson, P.B., 2001. Final Results from the Hubble Space Telescope Key Project to Measure the Hubble Constant. 553, 47–72. doi:10.1086/320638, arXiv:astro-ph/0012376.

Freedman, W.L., Madore, B.F., Hoyt, T., Jang, I.S., Beaton, R., Lee, M.G., Monson, A., Neeley, J., Rich, J., 2020a. Calibration of the Tip of the Red Giant Branch. 891, 57. doi:10.3847/1538-4357/ab7339, arXiv:2002.01550.

Freedman, W.L., Madore, B.F., Hoyt, T., Jang, I.S., Beaton, R., Lee, M.G., Monson, A., Neeley, J., Rich, J., 2020b. Calibration of the Tip of the Red Giant Branch. 891, 57. doi:10.3847/1538-4357/ab7339, arXiv:2002.01550.

Freedman, W.L., Madore, B.F., Hoyt, T.J., Jang, I.S., Lee, A.J., Owens, K.A., 2025. Status Report on the Chicago-Carnegie Hubble Program (CCHP): Measurement of the Hubble Constant Using the Hubble and James Webb Space Telescopes. 985, 203. doi:10.3847/1538-4357/adce78, arXiv:2408.06153.

Fritz, J., Franceschini, A., Hatziminaoglou, E., 2006. Revisiting the infrared spectra of active galactic nuclei with a new torus emission model. 366, 767–786. doi:10.1111/j.1365-2966.2006.09866.x, arXiv:astro-ph/0511428.

Gallo, L.C., Gonzalez, A.G., Miller, J.M., 2021. Eclipsing the X-Ray Emitting Region in the Active Galaxy NGC 6814. 908, L33. doi:10.3847/2041-8213/abdcb5, arXiv:2101.05433.

Gao, F., Braatz, J.A., Reid, M.J., Lo, K.Y., Condon, J.J., Henkel, C., Kuo, C.Y., Impellizzeri, C.M.V., Pesce, D.W., Zhao, W., 2016. The Megamaser Cosmology Project. VIII. A Geometric Distance to NGC 5765b. 817, 128. doi:10.3847/0004-637X/817/2/128, arXiv:1511.08311.

Gaskell, C.M., 2009. What broad emission lines tell us about how active galactic nuclei work. 53, 140–148. doi:10.1016/j.newar.2009.09.006, arXiv:0908.0386.

Gaskell, C.M., Sparke, L.S., 1986. Line Variations in Quasars and Seyfert Galaxies. 305, 175. doi:10.1086/164238.

Gierliński, M., Done, C., 2004. Is the soft excess in active galactic nuclei real? 349, L7–L11. doi:10.1111/j.1365-2966.2004.07687.x, arXiv:astro-ph/0312271.

Giommi, P., Padovani, P., Polenta, G., Turriziani, S., D'Elia, V., Piranomonte, S., 2012. A simplified view of blazars: clearing the fog around long-standing selection effects. 420, 2899–2911. doi:10.1111/j.1365-2966.2011.20044.x, arXiv:1110.4706.

GRAVITY Collaboration, Amorim, A., Bauböck, M., Brandner, W., Bolzer, M., Clénet, Y., Davies, R., de Zeeuw, P.T., Dexter, J., Drescher, A., Eckart,

A., Eisenhauer, F., Förster Schreiber, N.M., Gao, F., Garcia, P.J.V., Genzel, R., Gillessen, S., Gratadour, D., Hönig, S., Kaltenbrunner, D., Kishimoto, M., Lacour, S., Lutz, D., Millour, F., Netzer, H., Ott, T., Paumard, T., Perraut, K., Perrin, G., Peterson, B.M., Petrucci, P.O., Pfuhl, O., Prieto, M.A., Rouan, D., Sanchez-Bermudez, J., Shangguan, J., Shimizu, T., Schartmann, M., Stadler, J., Sternberg, A., Straub, O., Straubmeier, C., Sturm, E., Tacconi, L.J., Tristram, K.R.W., Vermot, P., von Fellenberg, S., Waisberg, I., Widmann, F., Woillez, J., 2021. The central parsec of NGC 3783: a rotating broad emission line region, asymmetric hot dust structure, and compact coronal line region. 648, A117. doi:10.1051/0004-6361/202040061, arXiv:2102.00068.

Gravity Collaboration, Amorim, A., Bourdarot, G., Brandner, W., Cao, Y., Clénet, Y., Davies, R., de Zeeuw, P.T., Dexter, J., Drescher, A., Eckart, A., Eisenhauer, F., Fabricius, M., Feuchtgruber, H., Förster Schreiber, N.M., Garcia, P.J.V., Genzel, R., Gillessen, S., Gratadour, D., Hönig, S., Kishimoto, M., Lacour, S., Lutz, D., Millour, F., Netzer, H., Ott, T., Perraut, K., Perrin, G., Peterson, B.M., Petrucci, P.O., Pfuhl, O., Prieto, A., Rabien, S., Rouan, D., Santos, D.J.D., Shangguan, J., Shimizu, T., Sternberg, A., Straubmeier, C., Sturm, E., Tacconi, L.J., Tristram, K.R.W., Widmann, F., Woillez, J., 2024. VLTI/GRAVITY interferometric measurements of the innermost dust structure sizes around active galactic nuclei. 690, A76. doi:10.1051/0004-6361/202450746, arXiv:2407.13458.

GRAVITY Collaboration, Dexter, J., Shangguan, J., Hönig, S., Kishimoto, M., Lutz, D., Netzer, H., Davies, R., Sturm, E., Pfuhl, O., Amorim, A., Bauböck, M., Brandner, W., Clénet, Y., de Zeeuw, P.T., Eckart, A., Eisenhauer, F., Förster Schreiber, N.M., Gao, F., Garcia, P.J.V., Genzel, R., Gillessen,

S., Gratadour, D., Jiménez-Rosales, A., Lacour, S., Millour, F., Ott, T., Paumard, T., Perraut, K., Perrin, G., Peterson, B.M., Petrucci, P.O., Prieto, M.A., Rouan, D., Schartmann, M., Shimizu, T., Sternberg, A., Straub, O., Straubmeier, C., Tacconi, L.J., Tristram, K., Vermot, P., Waisberg, I., Widmann, F., Woillez, J., 2020. The resolved size and structure of hot dust in the immediate vicinity of AGN. 635, A92. doi:10.1051/0004-6361/201936767, arXiv:1910.00593.

Gravity Collaboration, Sturm, E., Dexter, J., Pfuhl, O., Stock, M.R., Davies, R.I., Lutz, D., Clénet, Y., Eckart, A., Eisenhauer, F., Genzel, R., Gratadour, D., Hönig, S.F., Kishimoto, M., Lacour, S., Millour, F., Netzer, H., Perrin, G., Peterson, B.M., Petrucci, P.O., Rouan, D., Waisberg, I., Woillez, J., Amorim, A., Brandner, W., Förster Schreiber, N.M., Garcia, P.J.V., Gillessen, S., Ott, T., Paumard, T., Perraut, K., Scheithauer, S., Straubmeier, C., Tacconi, L.J., Widmann, F., 2018a. Spatially resolved rotation of the broad-line region of a quasar at sub-parsec scale. 563, 657–660. doi:10.1038/s41586-018-0731-9, arXiv:1811.11195.

Gravity Collaboration, Sturm, E., Dexter, J., Pfuhl, O., Stock, M.R., Davies, R.I., Lutz, D., Clénet, Y., Eckart, A., Eisenhauer, F., Genzel, R., Gratadour, D., Hönig, S.F., Kishimoto, M., Lacour, S., Millour, F., Netzer, H., Perrin, G., Peterson, B.M., Petrucci, P.O., Rouan, D., Waisberg, I., Woillez, J., Amorim, A., Brandner, W., Förster Schreiber, N.M., Garcia, P.J.V., Gillessen, S., Ott, T., Paumard, T., Perraut, K., Scheithauer, S., Straubmeier, C., Tacconi, L.J., Widmann, F., 2018b. Spatially resolved rotation of the broad-line region of a quasar at sub-parsec scale. 563, 657–660. doi:10.1038/s41586-018-0731-9, arXiv:1811.11195.

Greene, J.E., Ho, L.C., 2005. Estimating Black Hole Masses in Active Galaxies Using the Hα Emission Line. 630, 122–129. doi:10.1086/431897, arXiv:astro-ph/0508335.

Guerras, E., Mediavilla, E., Jimenez-Vicente, J., Kochanek, C.S., Muñoz, J.A., Falco, E., Motta, V., 2013. Microlensing of Quasar Broad Emission Lines: Constraints on Broad Line Region Size. 764, 160. doi:10.1088/0004-637X/764/2/160, arXiv:1207.2042.

Haardt, F., Maraschi, L., 1991. A Two-Phase Model for the X-Ray Emission from Seyfert Galaxies. 380, L51. doi:10.1086/186171.

Haardt, F., Maraschi, L., 1993. X-Ray Spectra from Two-Phase Accretion Disks. 413, 507. doi:10.1086/173020.

Hall, P.B., Sarrouh, G.T., Horne, K., 2018. Non-blackbody Disks Can Help Explain Inferred AGN Accretion Disk Sizes. 854, 93. doi:10.3847/1538-4357/aaa768, arXiv:1705.05467.

Häring, N., Rix, H.W., 2004. On the Black Hole Mass-Bulge Mass Relation. 604, L89–L92. doi:10.1086/383567, arXiv:astro-ph/0402376.

Harris, D.E., Krawczynski, H., 2006. X-Ray Emission from Extragalactic Jets. 44, 463–506. doi:10.1146/annurev.astro.44.051905.092446, arXiv:astro-ph/0607228.

Hasinger, G., 2008. Absorption properties and evolution of active galactic nuclei. 490, 905–922. doi:10.1051/0004-6361:200809839, arXiv:0808.0260.

Hickox, R.C., Alexander, D.M., 2018. Obscured Active Galactic Nuclei. 56, 625–671. doi:10.1146/annurev-astro-081817-051803, arXiv:1806.04680.

Ho, L.C., 2009. Origin and Dynamical Support of Ionized Gas in Galaxy Bulges. 699, 638–648. doi:10.1088/0004-637X/699/1/638, arXiv:0906.4103.

Hönig, S.F., Kishimoto, M., 2017. Dusty Winds in Active Galactic Nuclei: Reconciling Observations with Models. 838, L20. doi:10.3847/2041-8213/aa6838, arXiv:1703.07781.

Horne, K., et al., 2021. Space Telescope and Optical Reverberation Mapping Project. IX. Velocity-Delay Maps for Broad Emission Lines in NGC 5548. 907, 76. doi:10.3847/1538-4357/abce60, arXiv:2003.01448.

Hu, J.P., Wang, F.Y., 2023. Hubble Tension: The Evidence of New Physics. Universe 9, 94. doi:10.3390/universe9020094, arXiv:2302.05709.

Huang, C.D., 2024. The Mira Distance Ladder. arXiv e-prints , arXiv:2401.09581doi:10.48550/arXiv.2401.09581, arXiv:2401.09581.

Jiang, J., Fabian, A.C., Dauser, T., Gallo, L., García, J.A., Kara, E., Parker, M.L., Tomsick, J.A., Walton, D.J., Reynolds, C.S., 2019. High Density Reflection Spectroscopy - II. The density of the inner black hole accretion disc in AGN. 489, 3436–3455. doi:10.1093/mnras/stz2326, arXiv:1908.07272.

Jiang, Y.F., Green, P.J., Greene, J.E., Morganson, E., Shen, Y., Pancoast, A., MacLeod, C.L., Anderson, S.F., Brandt, W.N., Grier, C.J., Rix, H.W., Ruan, J.J., Protopapas, P., Scott, C., Burgett, W.S., Hodapp, K.W., Huber, M.E., Kaiser, N., Kudritzki, R.P., Magnier, E.A., Metcalfe, N., Tonry, J.T., Wainscoat, R.J., Waters, C., 2017. Detection of Time Lags between Quasar Continuum Emission Bands Based On Pan-STARRS Light Curves. 836, 186. doi:10.3847/1538-4357/aa5b91, arXiv:1612.08747.

Kammoun, E.S., Dovčiak, M., Papadakis, I.E., Caballero-García, M.D., Karas, V., 2021a. UV/Optical Disk Thermal Reverberation in Active Galactic Nuclei: An In-depth Study with an Analytic Prescription for Time-lag Spectra. 907, 20. doi:10.3847/1538-4357/abcb93, arXiv:2011.08563.

Kammoun, E.S., Papadakis, I.E., Dovčiak, M., 2019. A Hard Look at Thermal Reverberation and Optical/Ultraviolet Lags in NGC 5548. 879, L24. doi:10.3847/2041-8213/ab2a72, arXiv:1906.07692.

Kammoun, E.S., Papadakis, I.E., Dovčiak, M., 2021b. Modelling the UV/optical continuum time-lags in AGN. 503, 4163–4171. doi:10.1093/mnras/stab725, arXiv:2103.04892.

Kara, E., Alston, W.N., Fabian, A.C., Cackett, E.M., Uttley, P., Reynolds, C.S., Zoghbi, A., 2016. A global look at X-ray time lags in Seyfert galaxies. 462, 511–531. doi:10.1093/mnras/stw1695, arXiv:1605.02631.

Kara, E., Fabian, A.C., Cackett, E.M., Miniutti, G., Uttley, P., 2013a. Revealing the X-ray source in IRAS 13224-3809 through flux-dependent reverberation lags. 430, 1408–1413. doi:10.1093/mnras/stt024, arXiv:1301.1924.

Kara, E., Fabian, A.C., Cackett, E.M., Uttley, P., Wilkins, D.R., Zoghbi, A., 2013b. Discovery of high-frequency iron K lags in Ark 564 and Mrk 335. 434, 1129–1137. doi:10.1093/mnras/stt1055, arXiv:1306.2551.

Kara, E., Steiner, J.F., Fabian, A.C., Cackett, E.M., Uttley, P., Remillard, R.A., Gendreau, K.C., Arzoumanian, Z., Altamirano, D., Eikenberry, S., Enoto, T., Homan, J., Neilsen, J., Stevens, A.L., 2019. The corona contracts in a black-hole transient. 565, 198–201. doi:10.1038/s41586-018-0803-x, arXiv:1901.03877.

Kara, E., Zoghbi, A., Marinucci, A., Walton, D.J., Fabian, A.C., Risaliti, G., Boggs, S.E., Christensen, F.E., Fuerst, F., Hailey, C.J., Harrison, F.A., Matt, G., Parker, M.L., Reynolds, C.S., Stern, D., Zhang, W.W., 2015. Iron K and Compton hump reverberation in SWIFT J2127.4+5654 and NGC 1365 revealed by NuSTAR and XMM-Newton. 446, 737–749. doi:10.1093/mnras/stu2136, arXiv:1410.3357.

Kaspi, S., Maoz, D., Netzer, H., Peterson, B.M., Vestergaard, M., Jannuzi, B.T., 2005. The Relationship between Luminosity and Broad-Line Region Size in Active Galactic Nuclei. 629, 61–71. doi:10.1086/431275, arXiv:astro-ph/0504484.

Kaspi, S., Smith, P.S., Netzer, H., Maoz, D., Jannuzi, B.T., Giveon, U., 2000. Reverberation Measurements for 17 Quasars and the Size-Mass-Luminosity Relations in Active Galactic Nuclei. 533, 631–649. doi:10.1086/308704, arXiv:astro-ph/9911476.

Kishimoto, M., Hönig, S.F., Beckert, T., Weigelt, G., 2007. The innermost region of AGN tori: implications from the HST/NICMOS type 1 point sources and near-IR reverberation. 476, 713–721. doi:10.1051/0004-6361:20077911, arXiv:0709.0431.

Kollatschny, W., 2003. Accretion disk wind in the AGN broad-line region: Spectroscopically resolved line profile variations in Mrk 110. 407, 461–472. doi:10.1051/0004-6361:20030928, arXiv:astro-ph/0306389.

Kollatschny, W., Bischoff, K., Robinson, E.L., Welsh, W.F., Hill, G.J., 2001. Short-term emission line and continuum variations in Mrk 110. 379, 125–135. doi:10.1051/0004-6361:20011323, arXiv:astro-ph/0109470.

Kollatschny, W., Ulbrich, K., Zetzl, M., Kaspi, S., Haas, M., 2014. Broad-line region structure and kinematics in the radio galaxy 3C 120. 566, A106. doi:10.1051/0004-6361/201423901, arXiv:1405.1588.

Koratkar, A.P., Gaskell, C.M., 1991. Radius-Luminosity and Mass-Luminosity Relationships for Active Galactic Nuclei. 370, L61. doi:10.1086/185977.

Koshida, S., Minezaki, T., Yoshii, Y., Kobayashi, Y., Sakata, Y., Sugawara, S., Enya, K., Suganuma, M., Tomita, H., Aoki, T., Peterson, B.A., 2014. Reverberation Measurements of the Inner Radius of the Dust Torus in 17 Seyfert Galaxies. 788, 159. doi:10.1088/0004-637X/788/2/159, arXiv:1406.2078.

Kwan, J., Krolik, J.H., 1981. The formation of emission lines in quasars and Seyfert nuclei. 250, 478–507. doi:10.1086/159395.

Lacy, M., Ridgway, S.E., Sajina, A., Petric, A.O., Gates, E.L., Urrutia, T., Storrie-Lombardi, L.J., 2015. The Spitzer Mid-infrared AGN Survey. II. The Demographics and Cosmic Evolution of the AGN Population. 802, 102. doi:10.1088/0004-637X/802/2/102, arXiv:1501.04118.

LaMassa, S.M., Cales, S., Moran, E.C., Myers, A.D., Richards, G.T., Eracleous, M., Heckman, T.M., Gallo, L., Urry, C.M., 2015. The Discovery of the First "Changing Look" Quasar: New Insights Into the Physics and Phenomenology of Active Galactic Nucleus. 800, 144. doi:10.1088/0004-637X/800/2/144, arXiv:1412.2136.

Landt, H., Elvis, M., Ward, M.J., Bentz, M.C., Korista, K.T., Karovska, M., 2011. The near-infrared broad emission line region of active galactic nuclei - II. The 1-μm continuum. 414, 218–240. doi:10.1111/j.1365-2966.2011.18383.x, arXiv:1101.3342.

Landt, H., Ward, M.J., Kynoch, D., Packham, C., Ferland, G.J., Lawrence, A., Pott, J.U., Esser, J., Horne, K., Starkey, D.A., Malhotra, D., Fausnaugh, M.M., Peterson, B.M., Wilman, R.J., Riffel, R.A., Storchi-Bergmann, T., Barth, A.J., Villforth, C., Winkler, H., 2019. The first spectroscopic dust reverberation programme on active galactic nuclei: the torus in NGC 5548. 489, 1572–1589. doi:10.1093/mnras/stz2212, arXiv:1908.01627.

Lawrence, A., 1991. The relative frequency of broad-lined and narrow-lined active galactic nuclei : implications for unified schemes. 252, 586. doi:10.1093/mnras/252.4.586.

Li, Y.R., Songsheng, Y.Y., Qiu, J., Hu, C., Du, P., Lu, K.X., Huang, Y.K., Bai, J.M., Bian, W.H., Yuan, Y.F., Ho, L.C., Wang, J.M., 2018. Supermassive Black Holes with High Accretion Rates in Active Galactic Nuclei. VIII. Structure of the Broad-line Region and Mass of the Central Black Hole in Mrk 142. 869, 137. doi:10.3847/1538-4357/aaee6b, arXiv:1811.06302.

Li, Y.R., Wang, J.M., Ho, L.C., Du, P., Bai, J.M., 2013. A Bayesian Approach to Estimate the Size and Structure of the Broad-line Region in Active Galactic Nuclei Using Reverberation Mapping Data. 779, 110. doi:10.1088/0004-637X/779/2/110, arXiv:1310.3907.

Madejski, G.G., Sikora, M., 2016. Gamma-Ray Observations of Active Galactic Nuclei. 54, 725–760. doi:10.1146/annurev-astro-081913-040044.

Madore, B.F., Freedman, W.L., 2020. Astrophysical Distance Scale: The AGB J-band Method. I. Calibration and a First Application. 899, 66. doi:10.3847/1538-4357/aba045, arXiv:2005.10792.

Magorrian, J., Tremaine, S., Richstone, D., Bender, R., Bower, G., Dressler, A., Faber, S.M., Gebhardt, K., Green, R., Grillmair, C., Kormendy, J.,

Lauer, T., 1998. The Demography of Massive Dark Objects in Galaxy Centers. 115, 2285–2305. doi:10.1086/300353, arXiv:astro-ph/9708072.

Marinucci, A., Matt, G., Kara, E., Miniutti, G., Elvis, M., Arevalo, P., Ballantyne, D.R., Baloković, M., Bauer, F., Brenneman, L., Boggs, S.E., Cappi, M., Christensen, F.E., Craig, W.W., Fabian, A.C., Fuerst, F., Hailey, C.J., Harrison, F.A., Risaliti, G., Reynolds, C.S., Stern, D.K., Walton, D.J., Zhang, W., 2014. Simultaneous NuSTAR and XMM-Newton 0.5-80 keV spectroscopy of the narrow-line Seyfert 1 galaxy SWIFT J2127.4+5654. 440, 2347–2356. doi:10.1093/mnras/stu404, arXiv:1402.7245.

Markoff, S., Nowak, M.A., Wilms, J., 2005. Going with the Flow: Can the Base of Jets Subsume the Role of Compact Accretion Disk Coronae? 635, 1203–1216. doi:10.1086/497628, arXiv:astro-ph/0509028.

Martocchia, A., Matt, G., 1996. Iron Kalpha line intensity from accretion discs around rotating black holes. 282, L53–L57. doi:10.1093/mnras/282.4.L53.

Mateos, S., Carrera, F.J., Alonso-Herrero, A., Hernán-Caballero, A., Barcons, X., Asensio Ramos, A., Watson, M.G., Blain, A., Caccianiga, A., Ballo, L., Braito, V., Ramos Almeida, C., 2016. X-Ray Absorption, Nuclear Infrared Emission, and Dust Covering Factors of AGNs: Testing Unification Schemes. 819, 166. doi:10.3847/0004-637X/819/2/166, arXiv:1601.04439.

Mathur, S., 2000. Narrow-line Seyfert 1 galaxies and the evolution of galaxies and active galaxies. 314, L17–L20. doi:10.1046/j.1365-8711.2000.03530.x, arXiv:astro-ph/0003111.

Matt, G., Guainazzi, M., Maiolino, R., 2003. Changing look: from Compton-thick to Compton-thin, or the rebirth of fossil active galactic nuclei. 342, 422–426. doi:10.1046/j.1365-8711.2003.06539.x, arXiv:astro-ph/0302328.

McHardy, I.M., Cameron, D.T., Dwelly, T., Connolly, S., Lira, P., Emmanoulopoulos, D., Gelbord, J., Breedt, E., Arevalo, P., Uttley, P., 2014. Swift monitoring of NGC 5548: X-ray reprocessing and short-term UV/optical variability. 444, 1469–1474. doi:10.1093/mnras/stu1636, arXiv:1407.6361.

McLure, R.J., Jarvis, M.J., 2002. Measuring the black hole masses of high-redshift quasars. 337, 109–116. doi:10.1046/j.1365-8711.2002.05871.x, arXiv:astro-ph/0204473.

Mehdipour, M., Kaastra, J.S., Kriss, G.A., Cappi, M., Petrucci, P.O., Steenbrugge, K.C., Arav, N., Behar, E., Bianchi, S., Boissay, R., Branduardi-Raymont, G., Costantini, E., Ebrero, J., Di Gesu, L., Harrison, F.A., Kaspi, S., De Marco, B., Matt, G., Paltani, S., Peterson, B.M., Ponti, G., Pozo Nuñez, F., De Rosa, A., Ursini, F., de Vries, C.P., Walton, D.J., Whewell, M., 2015. Anatomy of the AGN in NGC 5548. I. A global model for the broadband spectral energy distribution. 575, A22. doi:10.1051/0004-6361/201425373, arXiv:1501.01188.

Miller, J.S., Goodrich, R.W., 1990. Spectropolarimetry of High-Polarization Seyfert 2 Galaxies and Unified Seyfert Theories. 355, 456. doi:10.1086/168780.

Millon, M., Galan, A., Courbin, F., Treu, T., Suyu, S.H., Ding, X., Birrer, S., Chen, G.C.F., Shajib, A.J., Sluse, D., Wong, K.C., Agnello, A.,

Auger, M.W., Buckley-Geer, E.J., Chan, J.H.H., Collett, T., Fassnacht, C.D., Hilbert, S., Koopmans, L.V.E., Motta, V., Mukherjee, S., Rusu, C.E., Sonnenfeld, A., Spiniello, C., Van de Vyvere, L., 2020. TDCOSMO. I. An exploration of systematic uncertainties in the inference of H_0 from time-delay cosmography. 639, A101. doi:10.1051/0004-6361/201937351, arXiv:1912.08027.

Miniutti, G., Fabian, A.C., 2004. A light bending model for the X-ray temporal and spectral properties of accreting black holes. 349, 1435–1448. doi:10.1111/j.1365-2966.2004.07611.x, arXiv:astro-ph/0309064.

Miyoshi, M., Moran, J., Herrnstein, J., Greenhill, L., Nakai, N., Diamond, P., Inoue, M., 1995. Evidence for a black hole from high rotation velocities in a sub-parsec region of NGC4258. 373, 127–129. doi:10.1038/373127a0.

Moresco, M., 2023. Addressing the Hubble tension with cosmic chronometers. arXiv e-prints , arXiv:2307.09501doi:10.48550/arXiv.2307.09501, arXiv:2307.09501.

Morgan, C.W., Kochanek, C.S., Morgan, N.D., Falco, E.E., 2010. The Quasar Accretion Disk Size-Black Hole Mass Relation. 712, 1129–1136. doi:10.1088/0004-637X/712/2/1129, arXiv:1002.4160.

Mosquera, A.M., Kochanek, C.S., Chen, B., Dai, X., Blackburne, J.A., Chartas, G., 2013. The Structure of the X-Ray and Optical Emitting Regions of the Lensed Quasar Q 2237+0305. 769, 53. doi:10.1088/0004-637X/769/1/53, arXiv:1301.5009.

Mudd, D., et al., 2018. Quasar Accretion Disk Sizes from Continuum Reverberation Mapping from the Dark Energy Survey. 862, 123. doi:10.3847/1538-4357/aac9bb, arXiv:1711.11588.

Naddaf, M.H., Czerny, B., Szczerba, R., 2021. The Picture of BLR in 2.5D FRADO: Dynamics and Geometry. 920, 30. doi:10.3847/1538-4357/ac139d, arXiv:2102.00336.

Narayan, R., Igumenshchev, I.V., Abramowicz, M.A., 2003. Magnetically Arrested Disk: an Energetically Efficient Accretion Flow. 55, L69–L72. doi:10.1093/pasj/55.6.L69, arXiv:astro-ph/0305029.

Narayan, R., Yi, I., 1994. Advection-dominated Accretion: A Self-similar Solution. 428, L13. doi:10.1086/187381, arXiv:astro-ph/9403052.

Nenkova, M., Sirocky, M.M., Ivezić, Ž., Elitzur, M., 2008a. AGN Dusty Tori. I. Handling of Clumpy Media. 685, 147–159. doi:10.1086/590482, arXiv:0806.0511.

Nenkova, M., Sirocky, M.M., Nikutta, R., Ivezić, Ž., Elitzur, M., 2008b. AGN Dusty Tori. II. Observational Implications of Clumpiness. 685, 160–180. doi:10.1086/590483, arXiv:0806.0512.

Netzer, H., 2015. Revisiting the Unified Model of Active Galactic Nuclei. 53, 365–408. doi:10.1146/annurev-astro-082214-122302, arXiv:1505.00811.

Netzer, H., Shemmer, O., Maiolino, R., Oliva, E., Croom, S., Corbett, E., di Fabrizio, L., 2004. Near-Infrared Spectroscopy of High-Redshift Active Galactic Nuclei. II. Disappearing Narrow-Line Regions and the Role of Accretion. 614, 558–567. doi:10.1086/423608, arXiv:astro-ph/0406560.

Novikov, I.D., Thorne, K.S., 1973. Astrophysics of black holes., in: Dewitt, C., Dewitt, B.S. (Eds.), Black Holes (Les Astres Occlus), pp. 343–450.

Oknyanskij, V.L., Horne, K., 2001. Reverberation Radii of Dust Holes in Active Galactic Nuclei, in: Peterson, B.M., Pogge, R.W., Polidan, R.S. (Eds.), Probing the Physics of Active Galactic Nuclei, p. 149.

Onken, C.A., Kollmeier, J.A., 2008. An Improved Method for Using Mg II to Estimate Black Hole Masses in Active Galactic Nuclei. 689, L13. doi:10.1086/595746, arXiv:0810.1950.

Osterbrock, D.E., 1989. Active galactic nuclei. Annals of the New York Academy of Sciences 571, 99–109. doi:10.1111/j.1749-6632.1989.tb50500.x.

Osterbrock, D.E., Pogge, R.W., 1985. The spectra of narrow-line Seyfert 1 galaxies. 297, 166–176. doi:10.1086/163513.

Packham, C., Radomski, J.T., Roche, P.F., Aitken, D.K., Perlman, E., Alonso-Herrero, A., Colina, L., Telesco, C.M., 2005. The Extended Mid-Infrared Structure of the Circinus Galaxy. 618, L17–L20. doi:10.1086/427691.

Padovani, P., 2011. The microjansky and nanojansky radio sky: source population and multiwavelength properties. 411, 1547–1561. doi:10.1111/j.1365-2966.2010.17789.x, arXiv:1009.6116.

Padovani, P., 2016. The faint radio sky: radio astronomy becomes mainstream. 24, 13. doi:10.1007/s00159-016-0098-6, arXiv:1609.00499.

Page, D.N., Thorne, K.S., 1974. Disk-Accretion onto a Black Hole. Time-Averaged Structure of Accretion Disk. 191, 499–506. doi:10.1086/152990.

Parker, M.L., Wilkins, D.R., Fabian, A.C., Grupe, D., Dauser, T., Matt, G., Harrison, F.A., Brenneman, L., Boggs, S.E., Christensen, F.E., Craig, W.W., Gallo, L.C., Hailey, C.J., Kara, E., Komossa, S., Marinucci, A.,

Miller, J.M., Risaliti, G., Stern, D., Walton, D.J., Zhang, W.W., 2014. The NuSTAR spectrum of Mrk 335: extreme relativistic effects within two gravitational radii of the event horizon? 443, 1723–1732. doi:10.1093/mnras/stu1246, arXiv:1407.8223.

Perez, E., Penston, M.V., Tadhunter, C., Mediavilla, E., Moles, M., 1988. An accretion disc in the broad-line radio galaxy 3C 390.3 ? 230, 353–362. doi:10.1093/mnras/230.3.353.

Perivolaropoulos, L., 2024. Hubble tension or distance ladder crisis? 110, 123518. doi:10.1103/PhysRevD.110.123518, arXiv:2408.11031.

Peterson, B.M., 1993. Reverberation Mapping of Active Galactic Nuclei. 105, 247. doi:10.1086/133140.

Peterson, B.M., 2001. Variability of Active Galactic Nuclei, in: Aretxaga, I., Kunth, D., Mújica, R. (Eds.), Advanced Lectures on the Starburst-AGN, p. 3. doi:10.1142/9789812811318_0002, arXiv:astro-ph/0109495.

Peterson, B.M., Denney, K.D., De Rosa, G., Grier, C.J., Pogge, R.W., Bentz, M.C., Kochanek, C.S., Vestergaard, M., Kilerci-Eser, E., Dalla Bontà, E., Ciroi, S., 2013. The Size of the Narrow-line-emitting Region in the Seyfert 1 Galaxy NGC 5548 from Emission-line Variability. 779, 109. doi:10.1088/0004-637X/779/2/109, arXiv:1309.1468.

Peterson, B.M., Ferrarese, L., Gilbert, K.M., Kaspi, S., Malkan, M.A., Maoz, D., Merritt, D., Netzer, H., Onken, C.A., Pogge, R.W., Vestergaard, M., Wandel, A., 2004. Central Masses and Broad-Line Region Sizes of Active Galactic Nuclei. II. A Homogeneous Analysis of a Large Reverberation-Mapping Database. 613, 682–699. doi:10.1086/423269, arXiv:astro-ph/0407299.

Peterson, B.M., Meyers, K.A., Carpriotti, E.R., Foltz, C.B., Wilkes, B.J., Miller, H.R., 1985. The variability of the spectrum of Arakelian 120. II. Evidence for a small broad line emitting region. 292, 164–171. doi:10.1086/163142.

Peterson, B.M., Wandel, A., 1999. Keplerian Motion of Broad-Line Region Gas as Evidence for Supermassive Black Holes in Active Galactic Nuclei. 521, L95–L98. doi:10.1086/312190, arXiv:astro-ph/9905382.

Peterson, B.M., Wandel, A., 2000. Evidence for Supermassive Black Holes in Active Galactic Nuclei from Emission-Line Reverberation. 540, L13–L16. doi:10.1086/312862, arXiv:astro-ph/0007147.

Peterson, B.M., et al., 1991. Steps toward Determination of the Size and Structure of the Broad-Line Region in Active Galactic Nuclei. II. an Intensive Study of NGC 5548 at Optical Wavelengths. 368, 119. doi:10.1086/169675.

Peterson, B.M., et al., 2002. Steps toward Determination of the Size and Structure of the Broad-Line Region in Active Galactic Nuclei. XVI. A 13 Year Study of Spectral Variability in NGC 5548. 581, 197–204. doi:10.1086/344197, arXiv:astro-ph/0208064.

Petrucci, P.O., Ursini, F., De Rosa, A., Bianchi, S., Cappi, M., Matt, G., Dadina, M., Malzac, J., 2018. Testing warm Comptonization models for the origin of the soft X-ray excess in AGNs. 611, A59. doi:10.1051/0004-6361/201731580, arXiv:1710.04940.

Phillips, M.M., 1993. The Absolute Magnitudes of Type IA Supernovae. 413, L105. doi:10.1086/186970.

Pier, E.A., Krolik, J.H., 1992. Infrared Spectra of Obscuring Dust Tori around Active Galactic Nuclei. I. Calculational Method and Basic Trends. 401, 99. doi:10.1086/172042.

Planck Collaboration, Aghanim, N., et al., 2020. Planck 2018 results. VI. Cosmological parameters. 641, A6. doi:10.1051/0004-6361/201833910, arXiv:1807.06209.

Pozo Nuñez, F., Gianniotis, N., Blex, J., Lisow, T., Chini, R., Polsterer, K.L., Pott, J.U., Esser, J., Pietrzyński, G., 2019. Optical continuum photometric reverberation mapping of the Seyfert-1 galaxy Mrk509. 490, 3936–3951. doi:10.1093/mnras/stz2830, arXiv:1912.10319.

Radomski, J.T., Packham, C., Levenson, N.A., Perlman, E., Leeuw, L.L., Matthews, H., Mason, R., De Buizer, J.M., Telesco, C.M., Orduna, M., 2008. Gemini Imaging of Mid-Infrared Emission from the Nuclear Region of Centaurus A. 681, 141–150. doi:10.1086/587771, arXiv:0802.4119.

Rauch, K.P., Blandford, R.D., 1991. Microlensing and the Structure of Active Galactic Nucleus Accretion Disks. 381, L39. doi:10.1086/186191.

Reynolds, C.S., 2019. Observing black holes spin. Nature Astronomy 3, 41–47. doi:10.1038/s41550-018-0665-z, arXiv:1903.11704.

Riess, A.G., Casertano, S., Yuan, W., Bowers, J.B., Macri, L., Zinn, J.C., Scolnic, D., 2021. Cosmic Distances Calibrated to 1% Precision with Gaia EDR3 Parallaxes and Hubble Space Telescope Photometry of 75 Milky Way Cepheids Confirm Tension with ΛCDM. 908, L6. doi:10.3847/2041-8213/abdbaf, arXiv:2012.08534.

Riess, A.G., Macri, L.M., Hoffmann, S.L., Scolnic, D., Casertano, S., Filippenko, A.V., Tucker, B.E., Reid, M.J., Jones, D.O., Silverman, J.M., Chornock, R., Challis, P., Yuan, W., Brown, P.J., Foley, R.J., 2016. A 2.4% Determination of the Local Value of the Hubble Constant. 826, 56. doi:10.3847/0004-637X/826/1/56, arXiv:1604.01424.

Riess, A.G., Yuan, W., Macri, L.M., Scolnic, D., Brout, D., Casertano, S., Jones, D.O., Murakami, Y., Anand, G.S., Breuval, L., Brink, T.G., Filippenko, A.V., Hoffmann, S., Jha, S.W., D'arcy Kenworthy, W., Mackenty, J., Stahl, B.E., Zheng, W., 2022. A Comprehensive Measurement of the Local Value of the Hubble Constant with 1 km s^{-1} Mpc^{-1} Uncertainty from the Hubble Space Telescope and the SH0ES Team. 934, L7. doi:10.3847/2041-8213/ac5c5b, arXiv:2112.04510.

Risaliti, G., Harrison, F.A., Madsen, K.K., Walton, D.J., Boggs, S.E., Christensen, F.E., Craig, W.W., Grefenstette, B.W., Hailey, C.J., Nardini, E., Stern, D., Zhang, W.W., 2013. A rapidly spinning supermassive black hole at the centre of NGC 1365. 494, 449–451. doi:10.1038/nature11938, arXiv:1302.7002.

Santos, D.J.D., Shimizu, T., Davies, R., Cao, Y., Dexter, J., de Zeeuw, P.T., Eisenhauer, F., Förster Schreiber, N.M., Feuchtgruber, H., Genzel, R., Gillessen, S., Kuhn, L., Lutz, D., Ott, T., Rabien, S., Shangguan, J., Sturm, E., Tacconi, L.J., 2025. Spectroscopic active galactic nucleus survey at z $\sim$ 2 with NTT/SOFI for GRAVITY+ observations. 696, A30. doi:10.1051/0004-6361/202453292, arXiv:2503.02942.

Schmidt, M., 1963. 3C 273 : A Star-Like Object with Large Red-Shift. 197, 1040. doi:10.1038/1971040a0.

Schmitt, H.R., Donley, J.L., Antonucci, R.R.J., Hutchings, J.B., Kinney, A.L., 2003. A Hubble Space Telescope Survey of Extended [O III] λ5007 Emission in a Far-Infrared Selected Sample of Seyfert Galaxies: Observations. 148, 327–352. doi:10.1086/377440, arXiv:astro-ph/0307254.

Seyfert, C.K., 1943. Nuclear Emission in Spiral Nebulae. 97, 28. doi:10.1086/144488.

Shakura, N.I., Sunyaev, R.A., 1973. Black holes in binary systems. Observational appearance. 24, 337–355.

Shappee, B.J., Prieto, J.L., Grupe, D., Kochanek, C.S., Stanek, K.Z., De Rosa, G., Mathur, S., Zu, Y., Peterson, B.M., Pogge, R.W., Komossa, S., Im, M., Jencson, J., Holoien, T.W.S., Basu, U., Beacom, J.F., Szczygieł, D.M., Brimacombe, J., Adams, S., Campillay, A., Choi, C., Contreras, C., Dietrich, M., Dubberley, M., Elphick, M., Foale, S., Giustini, M., Gonzalez, C., Hawkins, E., Howell, D.A., Hsiao, E.Y., Koss, M., Leighly, K.M., Morrell, N., Mudd, D., Mullins, D., Nugent, J.M., Parrent, J., Phillips, M.M., Pojmanski, G., Rosing, W., Ross, R., Sand, D., Terndrup, D.M., Valenti, S., Walker, Z., Yoon, Y., 2014. The Man behind the Curtain: X-Rays Drive the UV through NIR Variability in the 2013 Active Galactic Nucleus Outburst in NGC 2617. 788, 48. doi:10.1088/0004-637X/788/1/48, arXiv:1310.2241.

Shen, Y., Richards, G.T., Strauss, M.A., Hall, P.B., Schneider, D.P., Snedden, S., Bizyaev, D., Brewington, H., Malanushenko, V., Malanushenko, E., Oravetz, D., Pan, K., Simmons, A., 2011. A Catalog of Quasar Properties from Sloan Digital Sky Survey Data Release 7. 194, 45. doi:10.1088/0067-0049/194/2/45, arXiv:1006.5178.

Shuder, J.M., 1982. On the physical conditions and the velocity fields in Seyfert 1 galaxies and QSOs. 259, 48–54. doi:10.1086/160145.

Simpson, C., 2005. The luminosity dependence of the type 1 active galactic nucleus fraction. 360, 565–572. doi:10.1111/j.1365-2966.2005.09043.x, arXiv:astro-ph/0503500.

Slipher, V.M., 1917. The spectrum and velocity of the nebula N.G.C. 1068 (M 77). Lowell Observatory Bulletin 3, 59–62.

Stalevski, M., Ricci, C., Ueda, Y., Lira, P., Fritz, J., Baes, M., 2016. The dust covering factor in active galactic nuclei. 458, 2288–2302. doi:10.1093/mnras/stw444, arXiv:1602.06954.

Suganuma, M., Yoshii, Y., Kobayashi, Y., Minezaki, T., Enya, K., Tomita, H., Aoki, T., Koshida, S., Peterson, B.A., 2006. Reverberation Measurements of the Inner Radius of the Dust Torus in Nearby Seyfert 1 Galaxies. 639, 46–63. doi:10.1086/499326, arXiv:astro-ph/0511697.

Tchekhovskoy, A., Narayan, R., McKinney, J.C., 2011. Efficient generation of jets from magnetically arrested accretion on a rapidly spinning black hole. 418, L79–L83. doi:10.1111/j.1745-3933.2011.01147.x, arXiv:1108.0412.

Thorne, J., Robotham, A., Davies, L., Bellstedt, S., 2022. Agn unification diagram. URL: https://doi.org/10.5281/zenodo.6381013, doi:10.5281/zenodo.6381013.

Tran, H.D., Miller, J.S., Kay, L.E., 1992. Detection of Obscured Broad-Line Regions in Four Seyfert 2 Galaxies. 397, 452. doi:10.1086/171801.

Tremaine, S., Gebhardt, K., Bender, R., Bower, G., Dressler, A., Faber, S.M., Filippenko, A.V., Green, R., Grillmair, C., Ho, L.C., Kormendy, J., Lauer, T.R., Magorrian, J., Pinkney, J., Richstone, D., 2002. The Slope of the Black Hole Mass versus Velocity Dispersion Correlation. 574, 740–753. doi:10.1086/341002, arXiv:astro-ph/0203468.

Tripp, R., 1998. A two-parameter luminosity correction for Type IA supernovae. 331, 815–820.

Turner, T.J., Pounds, K.A., 1988. Variability of the soft excess in the Seyfert I galaxy MKN 335. 232, 463–471. doi:10.1093/mnras/232.2.463.

Urry, C.M., Padovani, P., 1995. Unified Schemes for Radio-Loud Active Galactic Nuclei. 107, 803. doi:10.1086/133630, arXiv:astro-ph/9506063.

Vestergaard, M., 2002. Determining Central Black Hole Masses in Distant Active Galaxies. 571, 733–752. doi:10.1086/340045, arXiv:astro-ph/0204106.

Vestergaard, M., Peterson, B.M., 2006. Determining Central Black Hole Masses in Distant Active Galaxies and Quasars. II. Improved Optical and UV Scaling Relationships. 641, 689–709. doi:10.1086/500572, arXiv:astro-ph/0601303.

Victoria-Ceballos, C.I., González-Martín, O., Fritz, J., Ramos Almeida, C., López-Rodríguez, E., García-Burillo, S., Alonso-Herrero, A., Martínez-Paredes, M., Esparza-Arredondo, D., Osorio-Clavijo, N., 2022. The Complex Infrared Dust Continuum Emission of NGC 1068: Ground-based N- and Q-band Spectroscopy and New Radiative Transfer Models. 926, 192. doi:10.3847/1538-4357/ac441a, arXiv:2201.11869.

Vincentelli, F.M., Mastroserio, G., McHardy, I., Ingram, A., Pahari, M., 2020. X-ray reverberation lags from the 1.5 Seyfert galaxy NGC 5273. 492, 1135–1141. doi:10.1093/mnras/stz3511, arXiv:1912.06196.

Walton, D.J., Risaliti, G., Harrison, F.A., Fabian, A.C., Miller, J.M., Arevalo, P., Ballantyne, D.R., Boggs, S.E., Brenneman, L.W., Christensen, F.E., Craig, W.W., Elvis, M., Fuerst, F., Gandhi, P., Grefenstette, B.W., Hailey, C.J., Kara, E., Luo, B., Madsen, K.K., Marinucci, A., Matt, G., Parker, M.L., Reynolds, C.S., Rivers, E., Ross, R.R., Stern, D., Zhang, W.W., 2014. NuSTAR and XMM-NEWTON Observations of NGC 1365: Extreme Absorption Variability and a Constant Inner Accretion Disk. 788, 76. doi:10.1088/0004-637X/788/1/76, arXiv:1404.5620.

Wandel, A., Peterson, B.M., Malkan, M.A., 1999. Central Masses and Broad-Line Region Sizes of Active Galactic Nuclei. I. Comparing the Photoionization and Reverberation Techniques. 526, 579–591. doi:10.1086/308017, arXiv:astro-ph/9905224.

Wang, J.G., Dong, X.B., Wang, T.G., Ho, L.C., Yuan, W., Wang, H., Zhang, K., Zhang, S., Zhou, H., 2009. Estimating Black Hole Masses in Active Galactic Nuclei Using the Mg II λ2800 Emission Line. 707, 1334–1346. doi:10.1088/0004-637X/707/2/1334, arXiv:0910.2848.

Webster, B.L., Murdin, P., 1972. Cygnus X-1-a Spectroscopic Binary with a Heavy Companion ? 235, 37–38. doi:10.1038/235037a0.

Wilkes, B.J., 1984. Studies of broad emission line profiles in QSOs - I. Observed, high-resolution profiles. 207, 73–98. doi:10.1093/mnras/207.1.73.

Wilkins, D.R., Gallo, L.C., Silva, C.V., Costantini, E., Brandt, W.N., Kriss, G.A., 2017. Revealing structure and evolution within the corona of the

Seyfert galaxy I Zw 1. 471, 4436–4451. doi:10.1093/mnras/stx1814, arXiv:1707.05782.

Winn, J.N., Rusin, D., Kochanek, C.S., 2004. The central image of a gravitationally lensed quasar. 427, 613–615. doi:10.1038/nature02279, arXiv:astro-ph/0312136.

Woo, J.H., Le, H.A.N., Karouzos, M., Park, D., Park, D., Malkan, M.A., Treu, T., Bennert, V.N., 2018. Calibration and Limitations of the Mg II Line-based Black Hole Masses. 859, 138. doi:10.3847/1538-4357/aabf3e, arXiv:1804.02798.

Young, P.J., Westphal, J.A., Kristian, J., Wilson, C.P., Landauer, F.P., 1978. Evidence for a supermassive object in the nucleus of the galaxy M87 from SIT and CCD area photometry. 221, 721–730. doi:10.1086/156076.

Zoghbi, A., Cackett, E.M., Reynolds, C., Kara, E., Harrison, F.A., Fabian, A.C., Lohfink, A., Matt, G., Balokovic, M., Boggs, S.E., Christensen, F.E., Craig, W., Hailey, C.J., Stern, D., Zhang, W.W., 2014. Observations of MCG-5-23-16 with Suzaku, XMM-Newton and NuSTAR: Disk Tomography and Compton Hump Reverberation. 789, 56. doi:10.1088/0004-637X/789/1/56, arXiv:1405.3674.

Zoghbi, A., Fabian, A.C., Reynolds, C.S., Cackett, E.M., 2012. Relativistic iron K X-ray reverberation in NGC 4151. 422, 129–134. doi:10.1111/j.1365-2966.2012.20587.x, arXiv:1112.1717.

Zoghbi, A., Uttley, P., Fabian, A.C., 2011. Understanding reverberation lags in 1H0707-495. 412, 59–64. doi:10.1111/j.1365-2966.2010.17883.x, arXiv:1010.3744.